

Spring 1995

Identification and Characterization of the Iron-Zinc Intermetallics Formed in Galvanneal steel

Richard Frederick George Grant
Old Dominion University

Follow this and additional works at: https://digitalcommons.odu.edu/physics_etds



Part of the [Metallurgy Commons](#), and the [Physics Commons](#)

Recommended Citation

Grant, Richard F.. "Identification and Characterization of the Iron-Zinc Intermetallics Formed in Galvanneal steel" (1995). Doctor of Philosophy (PhD), Dissertation, Physics, Old Dominion University, DOI: 10.25777/jj8g-nr96
https://digitalcommons.odu.edu/physics_etds/43

This Dissertation is brought to you for free and open access by the Physics at ODU Digital Commons. It has been accepted for inclusion in Physics Theses & Dissertations by an authorized administrator of ODU Digital Commons. For more information, please contact digitalcommons@odu.edu.

IDENTIFICATION AND CHARACTERIZATION
OF THE
IRON-ZINC INTERMETALLICS FORMED
IN GALVANNEAL STEEL.

by

Richard Frederick George Grant
B.Sc. November 1988, University of Toronto
M.S. June 1990, Florida Institute of Technology
M.S. May 1992, Old Dominion University

A Dissertation submitted to the Faculty of Old Dominion University in Partial
Fulfillment of the Requirement for the Degree of

DOCTOR OF PHILOSOPHY
PHYSICS

OLD DOMINION UNIVERSITY
May, 1995

Approved:

Desmond C. Cook (Director)

UMI Number: 9530660

UMI Microform 9530660

Copyright 1995, by UMI Company. All rights reserved.

**This microform edition is protected against unauthorized
copying under Title 17, United States Code.**

UMI

**300 North Zeeb Road
Ann Arbor, MI 48103**

ABSTRACT

The demand to improve the corrosion resistance of steel sheet, particularly for use within the automotive industry, has led to a dramatic increase in the use of coated steels in place of cold-rolled sheet steel. Galvanneal steel results from the post annealing of the zinc-coated steel sheet, in which iron and zinc are interdiffused to form an iron-zinc alloy coating. Within this alloy coating, four main iron-zinc phases, Zeta, Delta, Gamma-1, and Gamma may be present. Manufacture of the most suitable coating requires identifying which phases form during the galvannealing process, an understanding of the properties of each phase and knowing how to control the formation of any particular phase or phases in order to obtain optimum material performance. Positive identification of each phase and the fraction present in a galvanneal coating is very difficult. The primary cause of this difficulty has been the lack of high quality data on the crystal structure and the related microstructure of the separate iron-zinc phases. Therefore, through a detailed investigation of the iron-zinc alloys, we have compiled a database of their microstructural properties and used this information to study commercially produced galvanneal steel coatings.

A series of high purity iron-zinc alloys with iron concentrations in the range 5-30 at.% Fe were prepared and characterized. Bulk iron concentration of the samples were determined by chemical titration and induction coupled plasma spectroscopy. Sample homogeneity was analyzed with an electron microprobe and a scanning transmission electron

microscope. Finally, Mössbauer spectroscopy and X-ray diffraction were employed to characterize the microstructural properties of the alloys as a function of iron concentration across each phase.

Next, a new Mössbauer detector capable of analyzing commercial produced galvanized coatings in-situ was constructed and tested. The detector is able to simultaneously detect the γ -rays, X-rays, and conversion electrons which are emitted from the galvanized coatings following the resonant absorption of a γ -ray. The detector probes the full coating depth allowing the complete coating composition to be determined.

Finally, the database of the crystallographic and hyperfine parameters of the iron-zinc intermetallics along with the new detector were used to study several commercially produced galvanized coatings. The detailed analysis of the coatings has enabled the positive identification of the phases as layers within the coatings. Phase fractions and relative iron concentrations were determined for each coating. Furthermore, the Mössbauer spectral areas showed a linear correlation with the weight of iron in the coatings. Lastly, the effect of aluminum impurity in the galvanized bath on phase formation was investigated.

ACKNOWLEDGMENTS

Many thanks go to my thesis advisor Dr. Desmond C. Cook. I have learned a great deal from Des over the years, both the academic and administrative sides of research. He has taught me the finer points of experimental physics and kept me involved in the proposal and paper writing, budget spending, and the presenting of our work at conferences. I am thankful for his guidance and value the friendship we have developed.

I would like to acknowledge the financial assistance of the International Lead Zinc Research Organization, Inc. (ILZRO), and Virginia's Center for Innovative Technology. Without their support this work would not have been possible.

Special thanks to Dr. Gary E. Copeland, Dr. Gilbert R. Hoy, Dr. Larry B. Weinstein, Dr. John B. Cooper, and Dr. Herbert E. Townsend for sitting on my dissertation committee. Particular thanks are due to Dr. Townsend from Bethlehem Steel Corporation Inc., who has been an active contributor to this research from the beginning. Furthermore, Bethlehem Steels' financial contributions through ILZRO are greatly appreciated.

I would also like to thank Mr. Ed Bower from Bethlehem Steel Corporation, for the computerized milling of the "donut" portion of the detector and Dr. Waldemar Ferdanowicz also from B.S.C. for performing the STEM analysis.

To Mr. Thurman Gardner, Mr. Robert Kizziar, and Mr. Bobby Powell of the O.D.U. science shop I am greatly indebted. Their skill, precision, and hard work produced the parts and equipment necessary to complete my work. In particular, the expert machining of the toroidal detector by Mr. Kizziar produced a working detector with just one prototype.

Thanks are due to Patricia Cook for giving up several weekends to skillfully perform the chemical titration analysis.

Through the years spent at O.D.U. I have made many new friends and colleagues whose help and encouragement have made this an experience I will always remember.

I would like to thank my parents for their understanding and support over the years. My father can finally retire, I'm no longer a professional student!

Last but certainly not least, a very special thanks to my wife Michele. These last few months have been difficult for her having to tolerate my grumpy attitude. She managed to maintain the household, attend veterinary medical school, and keep a smile on her face while I remained locked away in front of the computer. Her love and support have made a difficult period much easier.

TABLE OF CONTENTS

LIST OF TABLES	Page vi
LIST OF FIGURES	vii
PART I: IRON-ZINC INTERMETALLICS	1
Chapter 1. Preparation of Iron-Zinc Intermetallics	4
1.1 Materials Used	6
1.2 Alloy Production	8
1.3 Induction Coupled Plasma Spectroscopy	11
1.4 Wet Chemical Titration	15
1.5 Electron Microprobe Spectroscopy	19
1.6 Scanning Transmission Electron Microscopy	21
1.7 Summary of Sample Analysis	22
Chapter 2. Characterization of the Iron-Zinc Intermetallics	29
2.1 X-Ray Diffraction Analysis	31
2.1.1 Experimental Technique	31
2.1.2 Crystal Structure of the Four Phases	32
2.1.3 Lattice Parameters of the Four Phases	40
2.1.4 Analysis of Mixed Phase Regions	60
2.1.5 Summary of XRD Analysis	61
2.2 Mössbauer Effect Analysis	66
2.2.1 Experimental Technique	66
2.2.2 Mössbauer Parameters of the Four Phases	67
2.2.3 Analysis of Mixed Phase Regions	84
2.2.4 Summary of Mössbauer Effect Analysis	88

PART II: GALVANNEAL STEEL COATINGS	Page 90
Chapter 3. Galvanneal Steel	92
3.1 Processing of Galvanneal Steel Coatings	93
3.2 Properties of Galvanneal Steel Coatings	95
3.2.1 Corrosion	97
3.2.2 Formability	97
3.2.3 Paintability	98
3.2.4 Weldability	99
3.3 Summary	99
Chapter 4. Mössbauer Detector for Characterization of Galvanneal Steel Coatings	101
4.1 Toroidal Detector	102
4.1.1 Mössbauer Spectroscopy and Detector Theory	102
4.1.2 Detector Design	106
4.1.3 Construction	108
4.1.4 General Operation	112
4.2 Evaluation of the Mössbauer Detector	123
4.2.1 Mössbauer Analysis of Standard Foils	123
4.2.2 Test on Galvanneal Steel Coatings	129
4.3 Summary	155
Chapter 5. Galvanneal Steel Coating Analysis	156
5.1 Sample Preparation and Experimental Procedure	158
5.2 Comparison of Mössbauer Findings with the Metallographic Properties	159
5.3 Coating Iron Weight Compared with Coating Spectral Area	187
5.4 Effect of Aluminum in the Galvannealing Bath	189
5.5 Summary	192
Chapter 6. Conclusions and Recommendations for Further Study	195
REFERENCES	201
APPENDICES	203

LIST OF TABLES

	Page
Table I. Composition data of some of the commercially available high purity iron and zinc powders	7
Table II. Electron microprobe analysis of the iron-zinc phases	20
Table III. Summary of the iron concentration in the Fe-Zn intermetallics using the different analytical techniques	27
Table IV. Summary of XRD data published prior to this study	33
Table V. Structural parameters for the ζ phase iron-zinc intermetallic	35
Table VI. Structural parameters for the Γ_1 phase iron-zinc intermetallic	37
Table VII. Structural parameters for the Γ phase iron-zinc intermetallic	39
Table VIII. XRD data for the ζ sample FZ007F from 10° to 120° two-theta	42
Table IX. XRD data for the δ sample FZ034F from 10° to 120° two-theta	44
Table X. XRD data for the Γ_1 sample FZ025G from 10° to 120° two-theta	46
Table XI. XRD data for the Γ sample FZ035D from 10° to 120° two-theta	48
Table XII. Summary of the major emissions during the decay of 14.4 keV excited state of ^{57}Fe	104
Table XIII. Toroidal detector resolution for three different gas mixtures	118

LIST OF FIGURES

	Page
Figure 1.1 Iron-zinc binary phase diagram	5
Figure 1.2 Iron-zinc binary phase diagram showing the prepared samples	10
Figure 1.3 ICP results measuring the iron concentration of raw powders and iron-zinc intermetallics	13
Figure 1.4 ICP results measuring the zinc concentration of raw powders and iron-zinc intermetallics	14
Figure 1.5 Wet chemical titration results measuring the iron concentration of raw powders and intermetallics	18
Figure 1.6 SEM photograph and corresponding STEM analysis of a sample prepared in the ζ phase	23
Figure 1.7 SEM photograph and corresponding STEM analysis of a sample prepared in the δ phase	24
Figure 1.8 SEM photograph and corresponding STEM analysis of a sample prepared in the Γ_1 phase	25
Figure 1.9 SEM photograph and corresponding STEM analysis of a sample prepared in the Γ phase.	26
Figure 2.1 Drawing of the ζ structure as viewed along the [011] direction	34
Figure 2.2 Drawing of the 26 atom cluster forming the Γ structure	39
Figure 2.3 XRD spectrum of the ζ sample FZ007F from 10° to 120° two-theta	41
Figure 2.4 XRD spectrum of the δ sample FZ034F from 10° to 120° two-theta	43

	Page
Figure 2.5 XRD spectrum of the Γ_1 sample FZ025G from 10° to 120° two-theta .	45
Figure 2.6 XRD spectrum of the Γ sample FZ035D from 10° to 120° two-theta .	47
Figure 2.7 Overlap of the XRD spectra of the four phases	49
Figure 2.8 Cell parameters of ζ as a function of iron concentration	51
Figure 2.9 Cell parameters of δ as a function of iron concentration	54
Figure 2.10 Cell parameters of Γ_1 as a function of iron concentration	56
Figure 2.11 Cell parameters of Γ as a function of iron concentration	58
Figure 2.12 Overlap of the XRD spectra for three Γ samples with identical iron concentrations but prepared at different sintering temperatures	59
Figure 2.13 Overlap of the XRD spectra for samples prepared in the Γ - δ region .	62
Figure 2.14 Overlap of the XRD spectra for samples prepared in the Γ_1 - δ region .	62
Figure 2.15 Overlap of the XRD spectra of a Γ_1 sample and of a δ sample	64
Figure 2.16 XRD spectra of a δ sample as a function of the sintering time	64
Figure 2.17 Overlap of the XRD spectra of a Γ_1 sample and of a Γ sample	65
Figure 2.18 Mössbauer spectrum of the ζ sample FZ007F	68
Figure 2.19 Overlap of the Mössbauer spectra for samples in the ζ phase	69
Figure 2.20 Mössbauer spectrum of the δ sample FZ033D	71
Figure 2.21 Overlap of the Mössbauer spectra for samples in the δ phase	72
Figure 2.22 Mössbauer parameters as a function of iron concentration for samples produced in the δ phase	74
Figure 2.23 Mössbauer spectrum of the Γ_1 sample FZ025G	76
Figure 2.24 Overlap of the Mössbauer spectra for samples in the Γ_1 phase	77

	Page
Figure 2.25 Mössbauer parameters as a function of iron concentration for samples produced in the Γ_1 phase	78
Figure 2.26 Mössbauer spectrum of the Γ sample FZ018D	80
Figure 2.27 Overlap of the Mössbauer spectra for samples in the Γ phase	81
Figure 2.28 Mössbauer parameters as a function of iron concentration for samples produced in the Γ phase	82
Figure 2.29 Overlap of the Mössbauer spectra for samples in the δ - Γ region	85
Figure 2.30 Mössbauer spectrum of a sample in the Γ_1 - Γ region	86
Figure 2.31 Overlap of the Mössbauer spectra for samples in the δ - Γ_1 region	87
Figure 3.1 Schematic of a continuous hot-dip galvannealing line	94
Figure 3.2 Cross sectional micrograph of a galvanneal coating	96
Figure 4.1 The decay modes of the first nuclear excited state of ^{57}Fe	103
Figure 4.2 Geometries and instrumentation for transmission and scattering Mössbauer spectroscopy	105
Figure 4.3 Cross sectional view of the toroidal and CEMS detectors	107
Figure 4.4 Photographs of the toroidal detector	110
Figure 4.5 Gas absorption characteristics for X-rays in argon and krypton	113
Figure 4.6 Comparison of the PHA spectra of ^{57}Co + ^{73}Ar sources with ^{57}Co	115
Figure 4.7 PHA spectra of a ^{57}Co source for three different gas mixtures	117
Figure 4.8 PHA spectra of a ^{57}Co source as a function of time	119
Figure 4.9 Comparison of the PHA spectra for four different samples	122
Figure 4.10 Schematic showing the two layered foils used to test the detector	124
Figure 4.11 Comparison of the Mössbauer spectra for the SSFE configuration	126

	Page
Figure 4.12 Comparison of the Mössbauer spectra for the FESS configuration . . .	128
Figure 4.13 Overlap of the XRD spectra of the three coatings	131
Figure 4.14 Schematic of the fracturing technique used to strip the coatings cleanly off the substrate	132
Figure 4.15 CEMS spectrum of the surface of Sample A	135
Figure 4.16 CEMS spectrum of the underside of Sample A	136
Figure 4.17 TMS spectrum of Sample A	137
Figure 4.18 XMS spectrum of Sample A	138
Figure 4.19 XMS spectrum of Sample A with the iron base signal removed . . .	139
Figure 4.20 Comparison of the XMS and TMS spectra of Sample A	140
Figure 4.21 CEMS spectrum of the surface of Sample A	142
Figure 4.22 CEMS spectrum of the underside of Sample A	143
Figure 4.23 TMS spectrum of Sample A	144
Figure 4.24 XMS spectrum of Sample A	145
Figure 4.25 XMS spectrum of Sample A with the iron base signal removed . . .	146
Figure 4.26 Comparison of the XMS and TMS spectra of Sample A	147
Figure 4.27 CEMS spectrum of the surface of Sample A	149
Figure 4.28 CEMS spectrum of the underside of Sample A	150
Figure 4.29 TMS spectrum of Sample A	151
Figure 4.30 XMS spectrum of Sample A	152
Figure 4.31 XMS spectrum of Sample A with the iron base signal removed . . .	153
Figure 4.32 Comparison of the XMS and TMS spectra of Sample A	154

	Page
Figure 5.1 Metallurgical analysis of commercial galvanneal sample #1	163
Figure 5.2 Mössbauer analysis of commercial galvanneal sample #1	164
Figure 5.3 XRD analysis of commercial galvanneal sample #1	165
Figure 5.4 Metallurgical analysis of commercial galvanneal sample #2	167
Figure 5.5 Mössbauer analysis of commercial galvanneal sample #2	168
Figure 5.6 XRD analysis of commercial galvanneal sample #2	169
Figure 5.7 Metallurgical analysis of commercial galvanneal sample #3	171
Figure 5.8 Mössbauer analysis of commercial galvanneal sample #3	172
Figure 5.9 XRD analysis of commercial galvanneal sample #3	173
Figure 5.10 Metallurgical analysis of commercial galvanneal sample #4	175
Figure 5.11 Mössbauer analysis of commercial galvanneal sample #4	176
Figure 5.12 XRD analysis of commercial galvanneal sample #4	177
Figure 5.13 Metallurgical analysis of commercial galvanneal sample #5	179
Figure 5.14 Mössbauer analysis of commercial galvanneal sample #5	180
Figure 5.15 XRD analysis of commercial galvanneal sample #5	181
Figure 5.16 Metallurgical analysis of commercial galvanneal sample #6	183
Figure 5.17 Mössbauer analysis of commercial galvanneal sample #6	184
Figure 5.18 XRD analysis of commercial galvanneal sample #6	185
Figure 5.19 Comparison of the coating and substrate spectral areas	188
Figure 5.20 Comparison of the coating spectral area and weight of iron	188
Figure 5.21 Comparison of Al free and Al added galvanneal coatings	191

IRON-ZINC INTERMETALLICS

Part 1: Iron-Zinc Intermetallics

The demand to improve the corrosion resistance of steel sheet, particularly for use within the automotive industry, has led to a dramatic increase in the use of coated steels in place of cold-rolled sheet steel. Consequently, industrial interest in the processing of zinc alloy coatings has risen over the past decade. Hot-dip galvanized and galvanized sheet steel are two products in use today. These processes involve the use of zinc and zinc-alloy coatings to protect the steel through the sacrificial or galvanic mechanism, and are an economic way to apply the zinc. Subsequently, today's continuous coating lines are capable of producing materials having well controlled coating thickness and uniformity. In contrast to galvanized steel, galvanized steel results from the post annealing of the zinc-coated steel sheet, in which iron and zinc are interdiffused to form an iron-zinc alloy coating. Within this alloy coating, the four main iron-zinc phases may be present.

Manufacture of the most suitable coating requires identifying which phases form during the galvannealing process, an understanding of the properties of each phase and knowing how to control the formation of any particular phase or phases in order to obtain optimum material performance. Positive identification of each phase and the fraction present in a galvanized coating is very difficult. The primary cause of this difficulty is the lack of high quality data on the crystal structure and the related microstructure of the separate iron-zinc phases. This research has been undertaken to address the problem of phase identification in commercial galvanized coatings through the careful production and characterization of high purity iron-zinc alloys.

The main body of this dissertation is divided into two distinct sections. The first part,

entitled Iron-Zinc Intermetallics, covers Chapters 1 and 2 and deals with the production and characterization of high purity iron-zinc alloys. In Chapter 1 we discuss the preparation of iron-zinc intermetallics through a slow diffusion process. The prepared samples are analyzed for their bulk iron concentration using two techniques, induction coupled plasma spectroscopy and wet chemical titration. The homogeneity of the iron-zinc alloys is determined with an electron microprobe and a scanning transmission electron microscope. The second chapter discusses the microstructural characterization of the iron-zinc alloys using X-ray diffraction and Mössbauer spectroscopy. Specifically, the crystal structure and hyperfine parameters are monitored as a function of iron concentration across each of the four main iron-zinc phases. The aim of this work is to compile a database of the microstructural parameters of the iron-zinc phases in order to aid in the identification of the phases in commercial galvaneal coatings.

The second part of this dissertation, entitled Galvaneal Steel Coatings, covers Chapters 3-5 and deals with the identification of the iron-zinc phases in commercially produced galvaneal steel. Chapter 3 involves the general properties of galvaneal steel in comparison to galvanized and uncoated sheet steel. The construction and testing of a toroidal scattering Mössbauer detector is discussed in detail in Chapter 4. This detector was developed to study galvaneal coatings in-situ; i.e., without removing them from the steel substrate. Finally, in Chapter 5 several commercially produced galvaneal coatings are studied in order to identify the phases present in the coatings and compare the results with the metallurgical properties. Coating analysis is performed with the new detector, using the database of the microstructural parameters developed in the first part of this dissertation.

CHAPTER ONE

Preparation of Iron-Zinc Intermetallics

To accurately study the microstructural properties of the iron-zinc intermetallic alloys, it is necessary to produce high quality samples which are representative of any chosen point on the phase diagram. These phases (see Figure 1.1)¹ are called Gamma, Γ (18.0-31.0 at.% Fe), Gamma-1, Γ_1 (18.9-24.0 at.% Fe), Delta, δ (8.1-13.2 at.% Fe), and Zeta, ζ (5.9-7.1 at.% Fe). An accurate study requires the samples to be homogeneous and have an iron content measured to an accuracy of $\frac{1}{2}$ at.%. At the same time, the samples must be very pure, containing no substitutional or interstitial elements which would effect the crystal structure and general microstructural properties. Although several publications discuss the preparation of some iron-zinc intermetallics,²⁻¹³ to date none report on the preparation of the alloys having the rigidly controlled parameters mentioned above. In preparation of our iron-zinc alloys, we have developed a well controlled technique which produces high quality samples whose iron content is nearly identical to that of the original mixture. This accuracy allows us to select any point on the phase diagram at which to study a sample.

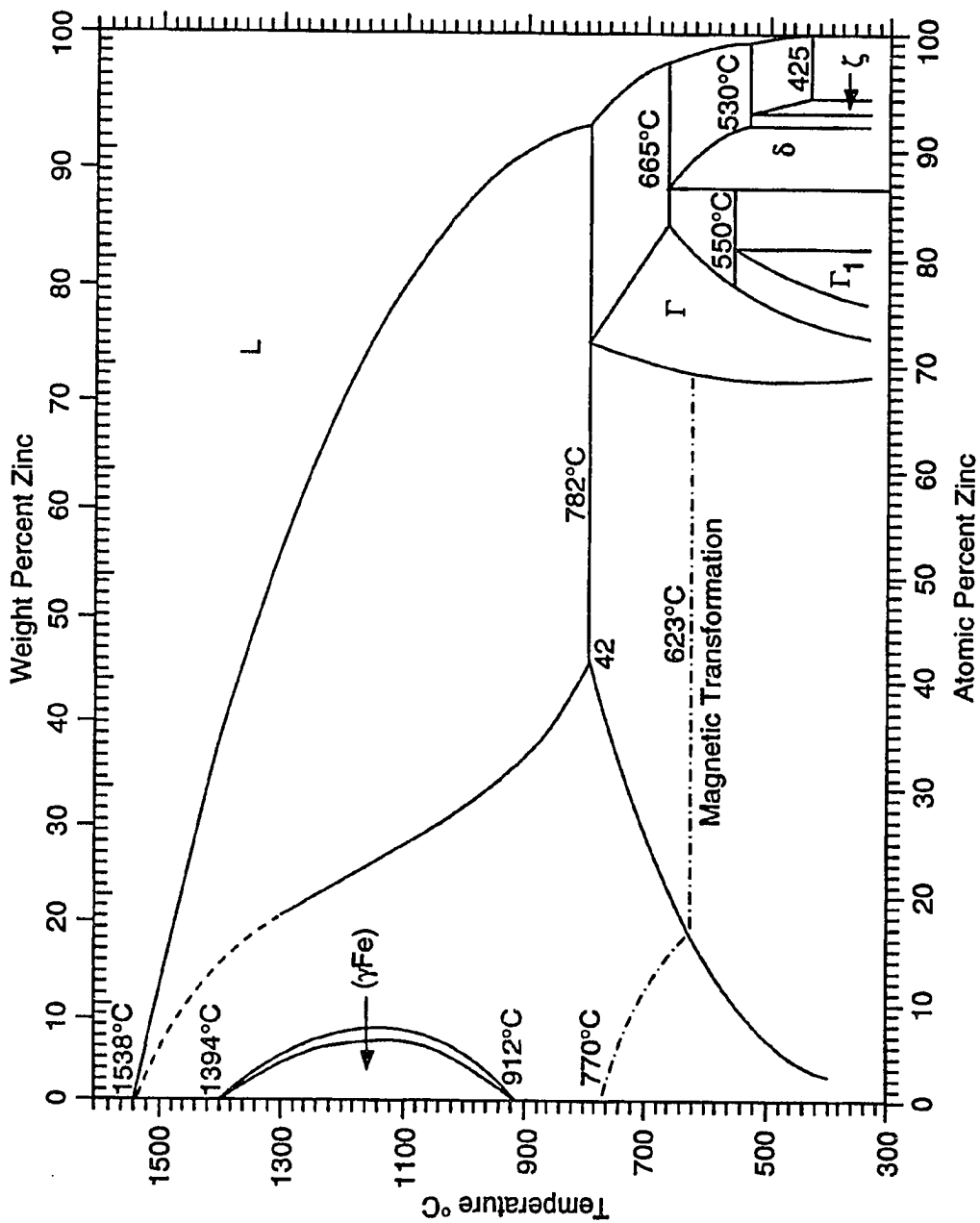


Figure 1.1. Iron-zinc phase diagram (from Kubaschewski).¹

1.1 Materials Used

Many iron and zinc powders are commercially available with different purity and particle size. Generally, the smaller the particle size, the lower the purity. The objective was to produce high purity iron-zinc alloys in each of the four phases. Table I shows some of the powders commercially available, along with their purity and particle size. The selection of the iron and zinc powders was made using different criteria. Since the zinc diffuses into the iron during alloy formation, choosing iron powder having small particle size is important even at the expense of the powder purity. However, use of iron powders containing more than 0.1 at.% of carbon or oxygen was avoided due to the possible formation of iron carbides or oxides. SCM Metal Products A-131 Electrolytic Iron Micropowder was selected. The average particle size for this powder is 4 microns and therefore the diffusing zinc is expected to easily penetrate to the center of the iron particle. Although the iron content is documented to be only 98.2 at.%, an appreciable amount of hydrogen, 1.5 at.%, makes up the majority of impurity elements present. Of importance is the very low fraction of carbon and nitrogen present in the powder, 0.025 at.%. It is known from the early research at Old Dominion University,¹⁴ that these interstitial elements adversely effect the quality of the samples. The particle size for the zinc powder is not as important since its diffusion is high, particularly for alloys prepared above 420 °C. Therefore, the highest purity zinc was chosen. OBRON Atlantic Corporation's stock number AS-081 zinc powder was used with a purity of 99.9% and particle size of 20 microns. All powders were purchased in sealed containers, and once opened, were stored in an evacuated container to prevent oxidation and moisture uptake.

TABLE I. Composition data of some of the commercially available high purity iron and zinc powders.

			Elemental Fractions at. %				Particle Size		
Manufacturer	Item	Number	Fe/Zn	C	O	H	Min	Ave	Max
SCM	Iron Micropowder	A-131	98.20	0.02		1.5	3.6 μ m (99%)		45 μ m (1%)
SCM	Iron Chip (Electrolytic)	1-276	99.97	0.0005	0.01		500 μ m (35%)		850 μ m (62%)
GAF	Iron Micropowder	R-1430	99.70	0.12					
OBRON	Zinc Powder	AS-081	99.90					20 μ m	
OBRON	Zinc Flake	31129/G	99.00					15 μ m	
ZCA	Zinc Dust	122	97.00		3.00			5 μ m	
ZCA	Zinc Powder	1213	98.00		2.00			150 μ m	

Code: SCM - SCM Metal Products, Inc.

GAF - GAF Chemicals Corporation

OBRON- OBRON Atlantic Corporation

ZCA - Zinc Corporation of America

1.2 Alloy Preparation

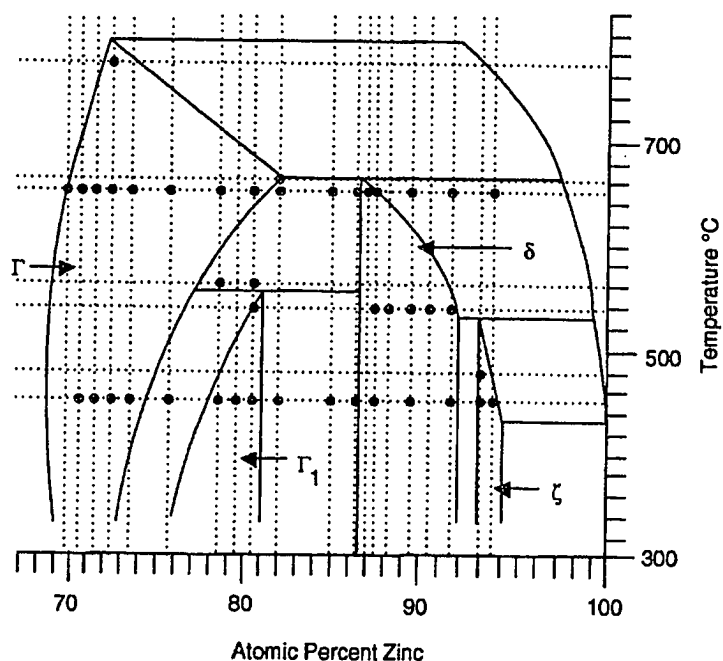
There are several different methods for producing iron-zinc intermetallics.²⁻¹³ Most of these incorporate sintering in a vacuum or an inert atmosphere for long periods of time at very high temperatures. However, since the melting temperatures of iron and zinc are very different, 1535 °C and 420 °C respectively, sintering at relatively low temperatures is preferred in order to prevent the evaporation of zinc. Using the following technique, we were able to produce high purity, homogeneous intermetallics at specific points on the phase diagram.

Samples were prepared by carefully weighing out 20-30 grams total of iron and zinc followed by encapsulation and a thorough mixing of the two metals by rotation for at least 24 hours. All masses were weighed to an accuracy of 0.0004 grams. A small quantity of each sample, 1.0-1.5 grams, was placed into a ½" press tool and subjected to 50 tsi to form a tablet approximately 1-2 mm thick. This produced samples with press densities greater than 6.5 g cm⁻³ which is close to the maximum possible press densities of 7.1-7.4 g cm⁻³ for these mixtures. The tablets were sealed into an evacuated quartz tube, 12 cm long and 1.5 cm inside diameter. Generally two tablets of the same mixture and up to eleven different mixtures were placed in the same quartz tube. Each tablet was separated by a small quartz disc, 1mm thick and 12 mm in diameter to prevent them from touching. The samples were then sintered in an Applied Test Systems, Inc. computer controlled tube furnace for varying times and temperatures depending on the desired sample. Care was taken to ensure that the evacuated quartz tube was completely inside the furnace thereby allowing the entire tube to

reach a uniform temperature. The sintering temperature was determined from the phase diagram for the particular sample required. In order to minimize thermal stress within the pressed tablet and to prevent zinc loss, the temperature was increased over a period of 2 hours until the final sintering temperature was reached.

Following sintering, the samples were quenched in liquid nitrogen to maintain the microstructural properties present at the particular sintering temperature. Next, the tablets were removed from the quartz tube, finely crushed, individually encapsulated in another evacuated quartz tube, and annealed at the same temperature and for the same time as the original sinter. Each sample was annealed separately during this stage of production.

Figure 1.2 shows the high zinc concentration end of the most commonly used iron-zinc binary phase diagram.¹ This area contains the four main iron-zinc phases, Gamma, Gamma-1, Delta and Zeta. Using the above mentioned technique, samples were produced at several points within each phase and in the regions between the main phases as indicated. Samples were produced across each of the four phases to investigate the dependence on the iron concentration of the crystal structure and hyperfine parameters. Fourteen samples were prepared within the Gamma phase since it spans the widest range of iron concentrations. To study the effect the sintering temperature has on the crystal structure of the phases, samples were produced at different temperatures but at the same iron concentration within a phase. Furthermore, samples were prepared in the mixed phase areas of the phase diagram to investigate the nature of these regions. These mixed phase samples are labeled with the letter M in Figure 1.2.



Sample	Zinc at. %	Iron at. %	Temp °C	Phase	Sample	Zinc at. %	Iron at. %	Temp °C	Phase
FZ007C	92.96	7.04	480	ζ	FZ024J	80.65	19.35	530	Γ ₁
FZ007F	92.96	7.04	450	ζ	FZ025G	78.46	21.54	450	Γ ₁
FZ010D	93.6	6.4	450	ζ	FZ026H	86.48	13.52	450	M
FZ010H	93.6	6.4	650	M	FZ026K	86.48	13.52	650	M
FZ011G	89.63	10.37	540	δ	FZ027H	84.99	15.01	450	M
FZ012J	79.56	20.44	450	Γ ₁	FZ027K	84.99	15.01	650	M
FZ013K	69.76	30.24	650	Γ	FZ028H	81.96	18.04	450	M
FZ015L	73.51	26.49	650	Γ	FZ028K	81.96	18.04	650	M
FZ015S	73.51	26.49	450	Γ	FZ028N	81.96	18.04	665	Γ
FZ016J	80.64	19.36	650	Γ	FZ030G	86.99	13.01	650	δ
FZ016N	80.64	19.36	560	M	FZ031D	70.67	29.33	450	Γ
FZ017D	78.23	21.77	650	Γ	FZ031G	70.67	29.33	650	Γ
FZ017F	78.23	21.77	560	M	FZ032D	87.24	12.76	450	δ
FZ018D	75.78	24.22	650	Γ	FZ032G	87.24	12.76	650	δ
FZ018I	75.78	24.22	450	M	FZ033D	89.62	10.38	450	δ
FZ019D	71.61	28.39	650	Γ	FZ033G	89.62	10.38	650	M
FZ019I	71.61	28.39	450	Γ	FZ034F	91.59	8.41	450	δ
FZ020D	91.59	8.41	540	δ	FZ034I	91.59	8.41	650	M
FZ021D	90.64	9.36	540	δ	FZ035D	72.37	27.63	450	Γ
FZ022D	88.21	11.79	540	δ	FZ035G	72.37	27.63	650	Γ
FZ023C	87.25	12.75	540	δ	FZ035J	72.37	27.63	770	Γ
FZ024G	80.65	19.35	450	Γ ₁					

Figure 1.2. The iron-zinc phase diagram showing the atomic percent zinc and the sintering temperatures of the prepared samples.

1.3 Induction Coupled Plasma Spectroscopy

Induction Coupled Plasma spectroscopy (ICP) was used to measure the iron and zinc fractions of the iron-zinc powders prior to alloying and of the fully annealed intermetallics. By comparing the ICP results of samples before and after the sintering process, we were able to ascertain if there was any iron or zinc lost during the alloying process. ICP analysis was performed with an Applied Research Laboratories, Inc. Model 3410 ICP Spectrometer. Absolute atomic concentration was determined using standard solutions commercially available for ICP analysis,¹⁵ as well as using calibration solutions prepared from our own iron and zinc powders. Sample preparation involved dissolving a known mass of the sample, ~100 mg, in concentrated nitric acid by heating to approximately 100 °C in a fume hood for 30 minutes. A watch glass was placed over the beaker to prevent solution evaporation. Following cooling, the solution was diluted to 2 liters in a volumetric flask using highly purified de-ionized water. The total atomic concentration was maintained at about 50 ppm so as not to exceed the upper saturation limit of the ICP unit. The analysis was performed by setting the spectrometer on the 213.856 nm and 202.551 nm emission lines of zinc and the 259.940 nm and 273.955 nm emission lines of iron. The number of iron and zinc atoms per unit volume were measured at the original solution concentrations and at dilutions of 1:1 and 1:9. This procedure minimizes errors due to background counting.

Both the raw-mixed and the intermetallic iron-zinc powders were analyzed by ICP. Figures 1.3 (a) and 1.3 (b) indicate the measured fraction of iron in the raw powders and the intermetallics plotted against the expected fraction as determined from the initial masses of

iron and zinc before the metals were mixed. Figures 1.4 (a) and 1.4 (b) show the corresponding plots of the ICP data for the fraction of zinc in each raw powder and alloy. For each figure the iron or zinc fraction is an average of the atomic concentration in ppm at the two different iron or zinc absorption wavelengths and at three solution concentrations. On each graph is a straight line showing the 1:1 correspondence expected if the ICP atomic percentage was to agree with the expected atomic percentage in the original mix before sintering. Also shown is the slope of a least squares fit of the data for each figure. As can be seen from the figures, the fraction of iron measured in the raw powders and intermetallics was less than that expected. In contrast, the fraction of zinc was generally higher than expected. Furthermore, Figures 1.4 (a) and 1.4 (b) indicate scatter in the zinc data is much greater than that for iron. The data suggests that the differences are due to loss of iron during the sintering and annealing processes and that the alloys are deficient in iron. In fact, a loss of zinc rather than iron would be expected from the heating process.

Shown in Figures 1.3 (c) and 1.4 (c) are the ICP data of the measured iron and zinc fractions for the iron-zinc intermetallics plotted against those of the raw powders. Now it can be seen that the 1:1 correspondence line is a reasonable fit of the data thereby indicating that iron and zinc were not lost during sintering and annealing. The results indicate that ICP was not capable of measuring the absolute concentrations to the accuracy of ± 0.5 at.% Fe which we desired. However, ICP was able to confirm that no zinc or iron was lost during the sintering or annealing processes.

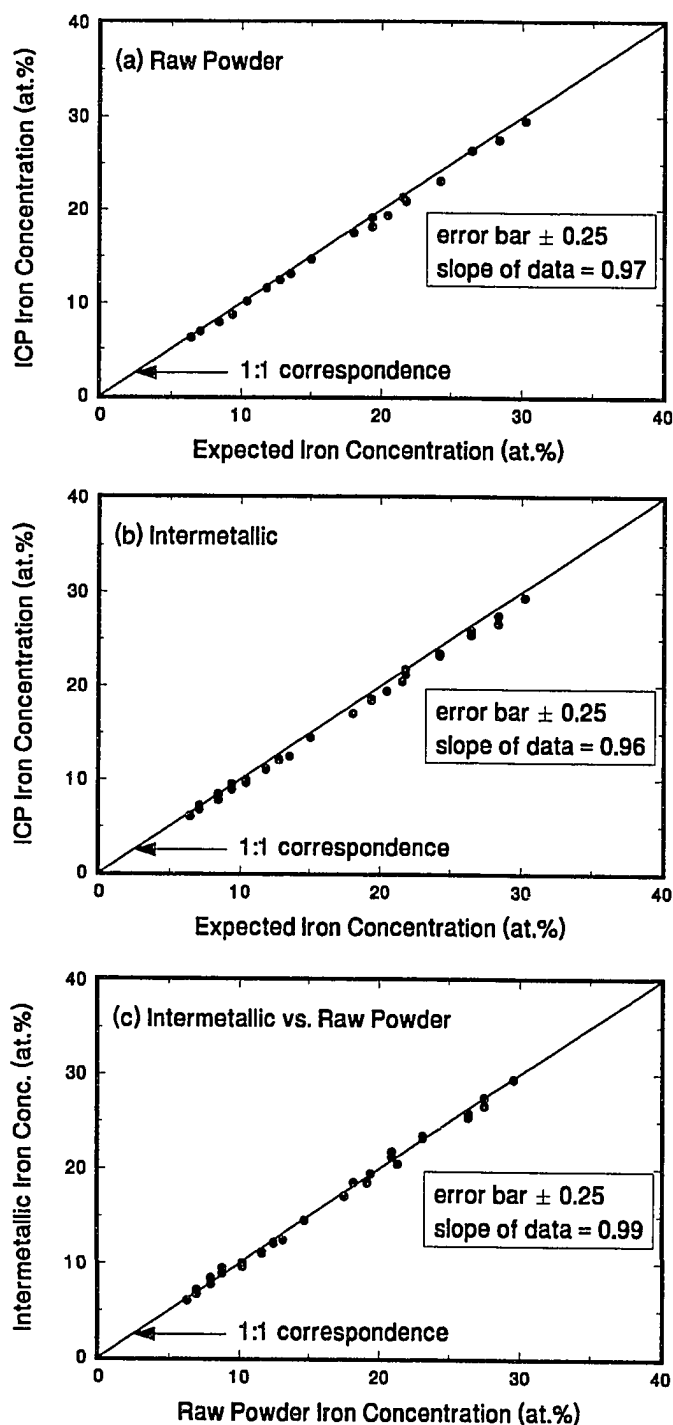


Figure 1.3. ICP results showing the measured iron concentration compared to the expected value for (a) the raw powders, (b) the intermetallics, and (c) a comparison of the intermetallics and raw powders.

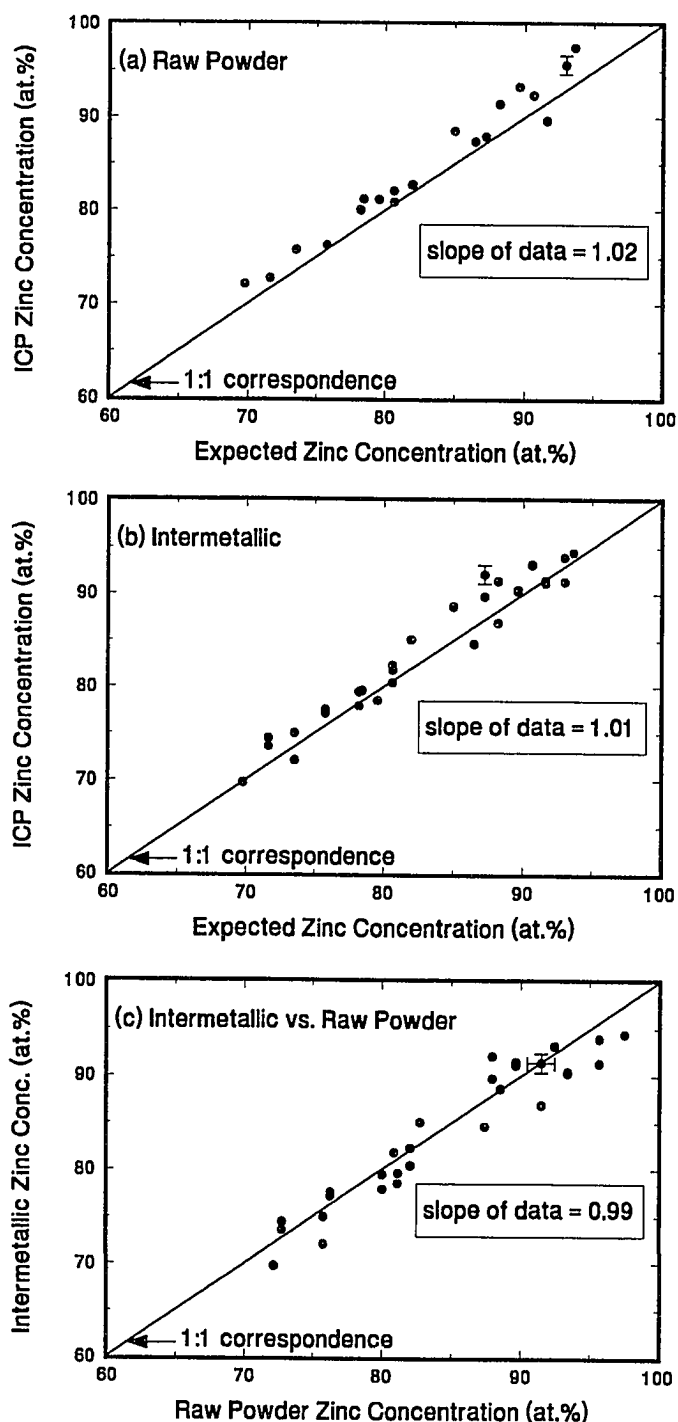
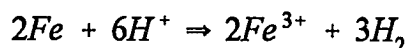


Figure 1.4. ICP results showing the measured zinc concentration compared to the expected value for (a) the raw powders, (b) the intermetallics, and (c) a comparison of the intermetallics and raw powders.

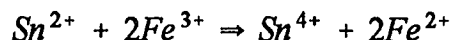
1.4 Wet chemical titration

There are several titration techniques available for determining the fraction of iron in a material.^{16,17} It was important to choose a technique whose titration end point would not be affected by the presence of zinc. A common method uses a permanganate solution to oxidize the iron.^{16,17} However, the permanganate solution is not stable in air and no reports have been made on the effect of zinc on this solution. Hence, it was decided to develop another oxidation-reduction standard whose end point is not effected by the zinc in the solution.

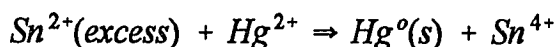
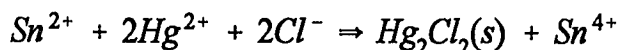
To accurately determine the fraction of iron in each sample, the following titration technique was performed three times on the same material. Samples were first reacted with 10-15 milliliters of concentrated hydrochloric acid and heated below the boiling point for 20-40 minutes. Iron(II) and iron(III) formed as products depicted in the following equations:



The solution became yellow/orange due to the presence of iron(III). Since iron(II) is oxidized to iron(III) during titration, all of the iron(III) must initially be reduced to iron(II). For this we used tin(II) chloride which reduces iron(III) to iron(II) and changes the solution from yellow/orange to nearly colorless, as shown in the following equation:



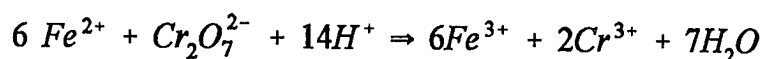
Serious errors can result if a large excess of tin(II) chloride is added because the tin(II) will also be oxidized during the titration to erroneously give high values of iron content. Therefore, tin(II) chloride was added dropwise to the yellow/orange solution until it became pale green or nearly colorless. A slight excess (2 drops) was added to ensure the complete reduction of iron(III). In order to prevent interference with the titration, this slight excess of tin(II) was oxidized by adding a solution of mercury(II) chloride. Essentially, a slight excess of tin(II) causes a white precipitate of mercury(I) chloride to form when mercury(II) chloride is added. However, if too much tin(II) chloride is used to reduce the iron(III), a black precipitate of mercury forms when the mercury(II) chloride solution is added. This difference in precipitates provides an excellent method of checking whether the reduction of iron(III) has been correctly performed. These reactions are shown below.



If no precipitate formed or if the precipitate was black upon the addition of mercury(II) chloride solution, the sample was discarded. Furthermore, because the air slowly oxidizes iron(II), one sample was reduced and titrated before reducing the next sample.

Once the reduction of iron(III) was complete, sulfuric and phosphoric acids were

added to allow for a more complete reaction during the titration and to potentiate a sharper endpoint of the indicator. The indicator, barium diphenylamine sulfonate, was added and the solution was titrated with standardized potassium dichromate solution. The color change at the endpoint proceeded from a blue-green to grey to purple through the following reaction:



The procedure described was first used to standardize the titrant. A pure iron powder sample of known mass was then used to measure the molarity of the titrant. Once the volume of titrant needed to oxidize the iron had been measured, the molarity of the titrant was calculated as follows:

$$\text{Molarity of titrant} = \frac{\text{mass of Fe powder}}{55.85 \times 6 \times \text{volume of titrant}}$$

Depending on the amount of sample being analyzed, the molarity of the titrant ranged from 0.006670 M to 0.01696 M.

After titrant standardization, the iron-zinc powders were tested. Sample sizes of the mixed raw powders and the iron-zinc intermetallics ranged from nearly 3 grams to 0.13 gram depending on the percentage of iron and the amount of the sample available for testing. The experimental percentage of iron was determined through the following calculations:

$$\text{Mass of Fe} = \text{molarity of titrant} \times 55.85 \times 6 \times \text{volume of titrant}$$

$$\text{Fe (w\%)} = \frac{\text{mass of Fe (calculated above)}}{\text{mass of sample}}$$

The fraction of iron in the raw powders and alloys, as determined from wet chemical analysis are shown plotted in Figure 1.5 as a function of the expected fraction. Accordance between the two fractions is demonstrated. The wet chemical analysis technique establishes that the iron content in our samples was generally low by only about 0.2 at.%. This was established by comparing the standard deviation of the three titrations for each sample with the expected iron content. In addition, there was no noticeable difference in iron fraction between the raw powders and their corresponding alloys.

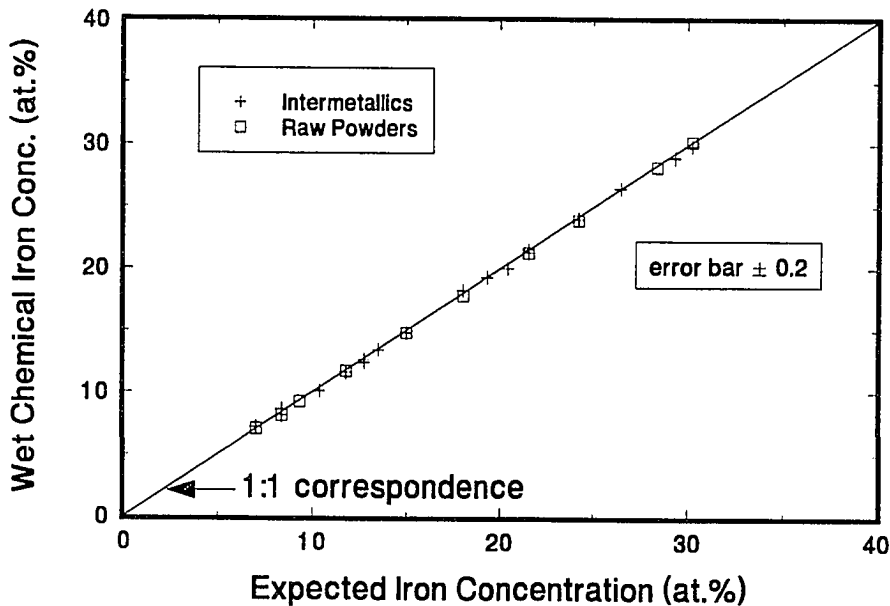


Figure 1.5. Wet chemical titration results showing the measured iron concentration compared to the expected value for the raw powders and the intermetallics.

1.5 Electron Microprobe Spectroscopy

Samples were studied for homogeneity using an ETEC Autoprobe with a beryllium window, a Kevex Energy Dispersive System, and Krisel automation system. X-ray counts were collected for 200 sec with a beam current of 215 pAmp and data corrected to atomic percent using ZAF correction.¹⁸ Typical probe volumes were about 10 cubic microns thus allowing 1-2 probes to be made in most particles. Both the iron and zinc peak positions were determined (re-peaked) before each measurement in order to compensate for any electronic drift of the equipment. Small amounts of each sample (<50 mg) were mounted in a 2.5 mm diameter epoxy plug with up to four different samples per plug. The plugs were then placed in an oven for 2 hours at 75 °C to cure the epoxy. Once cooled, the mounted samples were carefully polished with 600 μm , 6 μm , 1 μm , and finally $\frac{1}{4}$ μm pads. Finally, the polished samples were coated with a thin layer of carbon to improve the electrical conductivity and reduce charge build-up on the sample while in the microprobe. Pure iron and zinc standards¹⁹ as well as our iron and zinc powders were used for calibration standards since no known iron-zinc intermetallic standards existed at that time. Table II shows the microprobe analysis for four samples, one from each of the main iron-zinc phases. It should be noted that since pure iron and zinc powders were used for calibration, the atomic percentages are not considered to be accurate to better than 2 at.%. Using calibration standards of the same structure, i.e., iron-zinc alloys, would lead to a more accurate composition analysis, however, until this work none were available. The variation in the composition from particle to particle, as indicated by the standard deviation, is a good measure of the homogeneity of the

TABLE II. Electron microprobe results of samples produced in each of the four main iron-zinc phases.

Sample	Point of Analysis	Normalized at.% Fe	Average at.% Fe and Standard Deviation
Zeta	Particle #1 - point #1	6.84	Average at.% Fe = 6.79 Standard Deviation = 0.12
	- point #2	6.88	
	- point #3	6.74	
	- point #4	6.85	
	Particle #2 - point #1	6.62	
	Particle #3 - point #1	6.98	
	Particle #4 - point #1	6.70	
	Particle #5 - point #1	6.68	
Delta	Particle #1 - point #1	9.46	Average at.% Fe = 9.43 Standard Deviation = 0.09
	- point #2	9.31	
	- point #3	9.37	
	Particle #2 - point #1	9.51	
	Particle #3 - point #1	9.40	
	Particle #4 - point #1	9.53	
Gamma-1	Particle #1 - point #1	23.42	Average at.% Fe = 21.03 Standard Deviation = 1.40
	- point #2	21.22	
	Particle #2 - point #1	19.70	
	Particle #3 - point #1	22.86	
	Particle #4 - point #1	20.01	
	Particle #5 - point #1	19.96	
	Particle #6 - point #1	20.83	
	Particle #7 - point #1	20.20	
Gamma	Particle #1 - point #1	26.69	Average at.% Fe = 27.24 Standard Deviation = 0.33
	- point #2	26.85	
	Particle #2 - point #1	27.50	
	Particle #3 - point #1	27.20	
	Particle #4 - point #1	27.24	
	Particle #5 - point #1	27.36	
	Particle #6 - point #1	27.42	
	Particle #7 - point #1	27.67	

sample. As indicated in Table II, several points within a particle were analyzed, as well as many different particles for each sample. In general, measurements on many particles of the same sample indicated an iron homogeneity of greater than 93%, as indicated by the standard deviation.

1.6 Scanning Transmission Electron Microscopy

Some samples were further analyzed for homogeneity using a scanning transmission electron microscope. In general, the resolution of the STEM is approximately 20 nm with a probe volume of $\approx 0.02 \mu\text{m}^3$. Therefore, sample homogeneity can be determined over smaller sampling volumes than with the electron microprobe or using chemical analysis. Between 10-30 points were analyzed across each particle at 30-60 nm intervals. A small amount of each sample was embedded in the tip of a BEEM Capsule (size 00) in an epoxy of low vapor pressure. The epoxy plug was trimmed to a 20 μm pyramid and then 30-50 nm sections were cut dry using a Diatome 45° diamond knife which was sharpened to a 10 nm edge. The sections were then attached to a collodion/Formvar/carbon coated grid²⁰ which was inserted into a Vacuum Generators HB501 STEM for microanalysis. The sample was tilted 10°-15° towards the detector in order to minimize absorption and shadowing by the grid bars. The STEM contained an AN 10,000 EDS system equipped with a 30 mm² windowless detector having 148 eV resolution.

The composition profile across a particle was determined using a list of tracking points generated prior to automated acquisition. Again, since pure iron and zinc powders

were used for calibration, the atomic percentages are not considered to be as accurate as the variation in the atomic percentage across a given particle. Figures 1.6-1.9 show the STEM particle profiles and SEM photographs indicating the sampling positions for typical grains from samples prepared in each of the four main iron-zinc phases. The atomic percentage remains relatively constant across each grain, demonstrating good homogeneity and sample diffusion. However, at the very edge of some of the grains, regions of high zinc, and therefore, low iron concentration, were observed. We believe this is due to a small amount of zinc oxide being present in the initial zinc powder preventing total diffusion. Nonetheless, the change in overall composition due to these regions is very small.

1.7 Summary of Sample Analysis

The preparation and chemical analysis of the high purity, homogeneous iron-zinc alloys reported in this chapter, form a basis of information necessary to allow further detailed microstructural characterization of iron-zinc alloys to be undertaken. In particular, the next chapter deals with the X-ray diffraction and Mössbauer spectroscopic analysis of these samples. Furthermore, the production of these standards allows commercial producers of galvanized steel to calibrate their monitoring instrumentation and more accurately analyze galvanized steel.

Induction coupled plasma spectroscopy is a popular technique for determining the average iron content in a galvanized coating. However, our results show that ICP tends to underestimate the iron while overestimate the zinc fraction in the iron-zinc intermetallics.

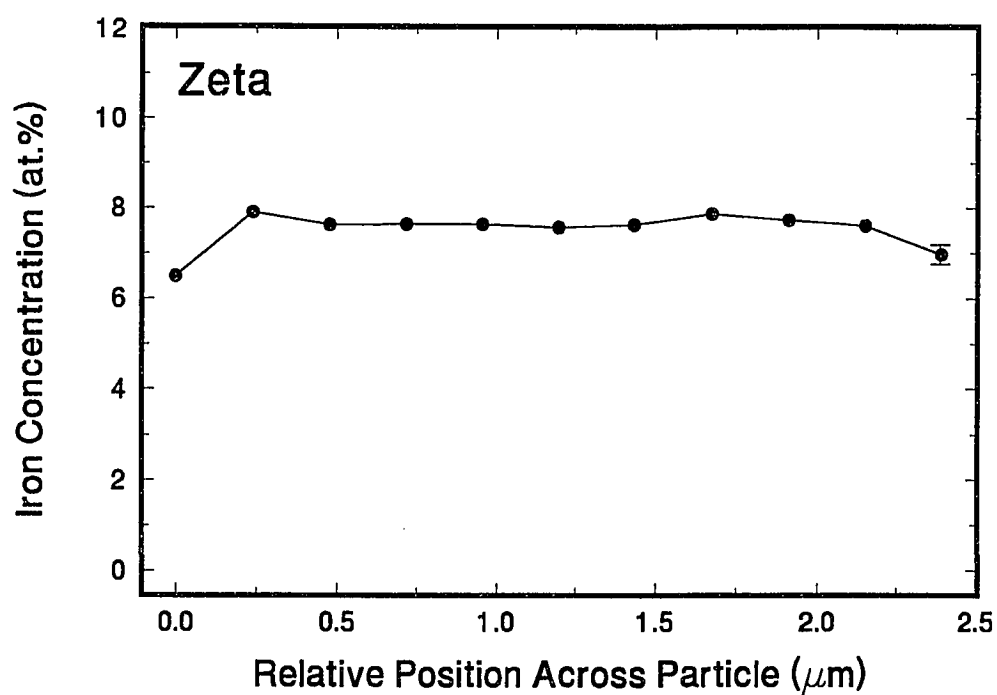
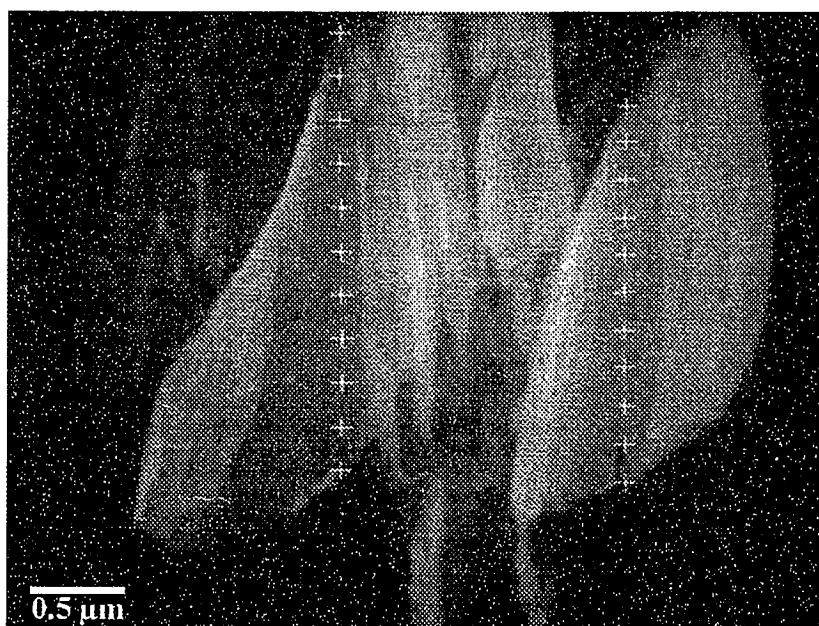


Figure 1.6. SEM photograph and corresponding STEM particle profile of a typical sample produced in the Zeta phase. The plus marks in the SEM photo show the probe points of the STEM.

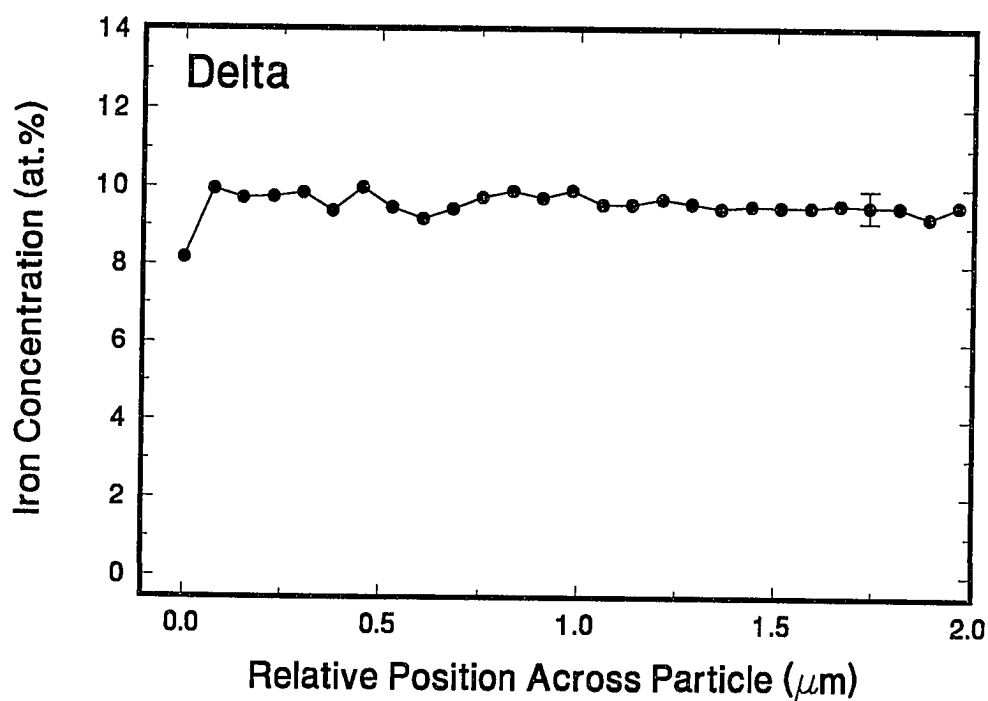
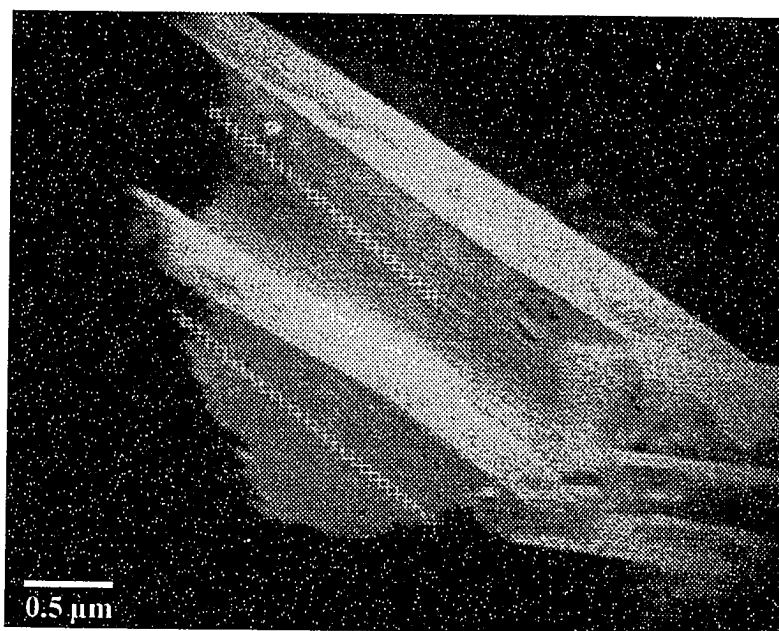


Figure 1.7. SEM photograph and corresponding STEM particle profile of a typical sample produced in the Delta phase. The plus marks in the SEM photo show the probe points of the STEM.

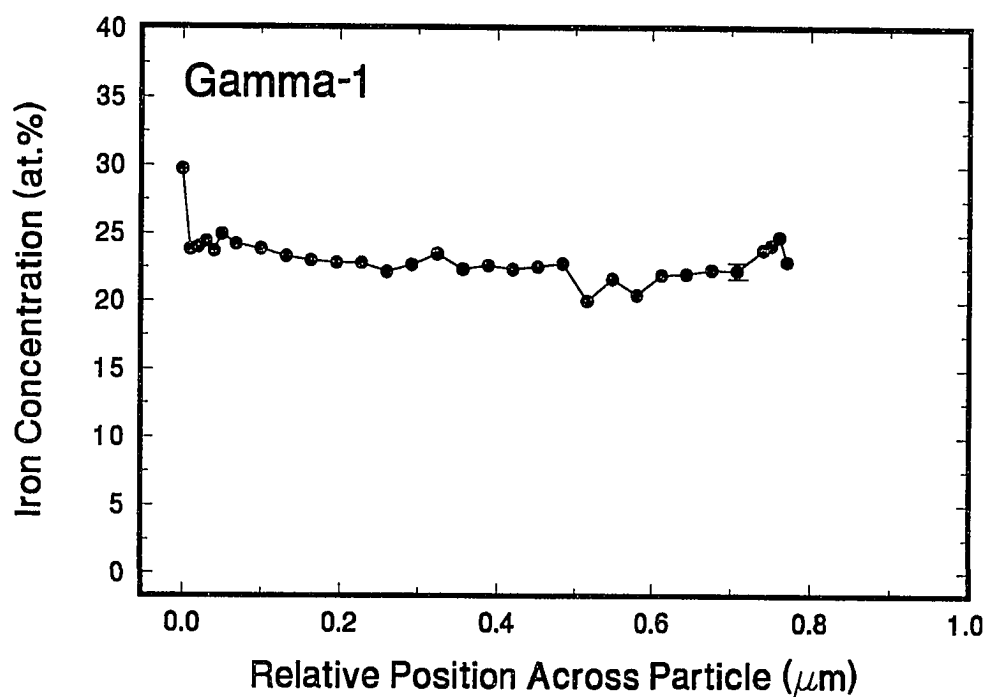
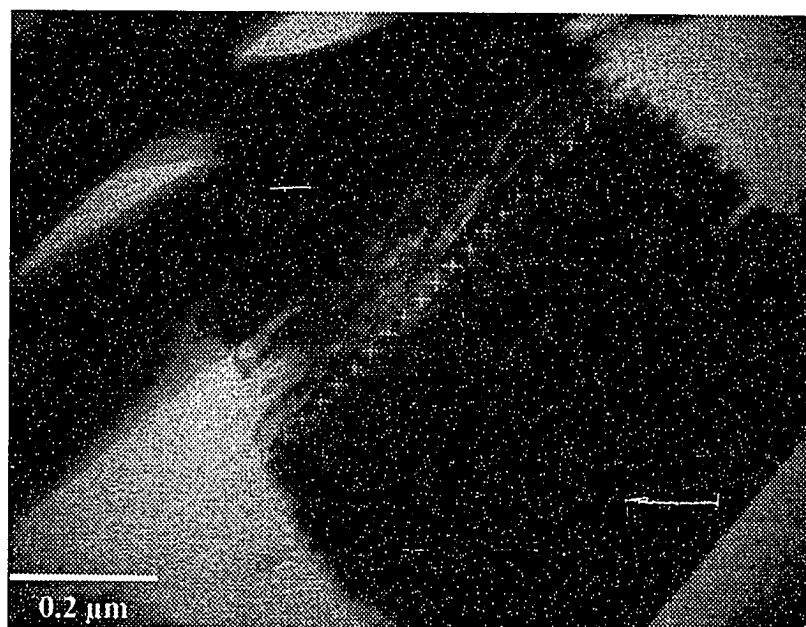


Figure 1.8. SEM photograph and corresponding STEM particle profile of a typical sample produced in the Gamma-1 phase. The plus marks in the SEM photo show the probe points of the STEM.

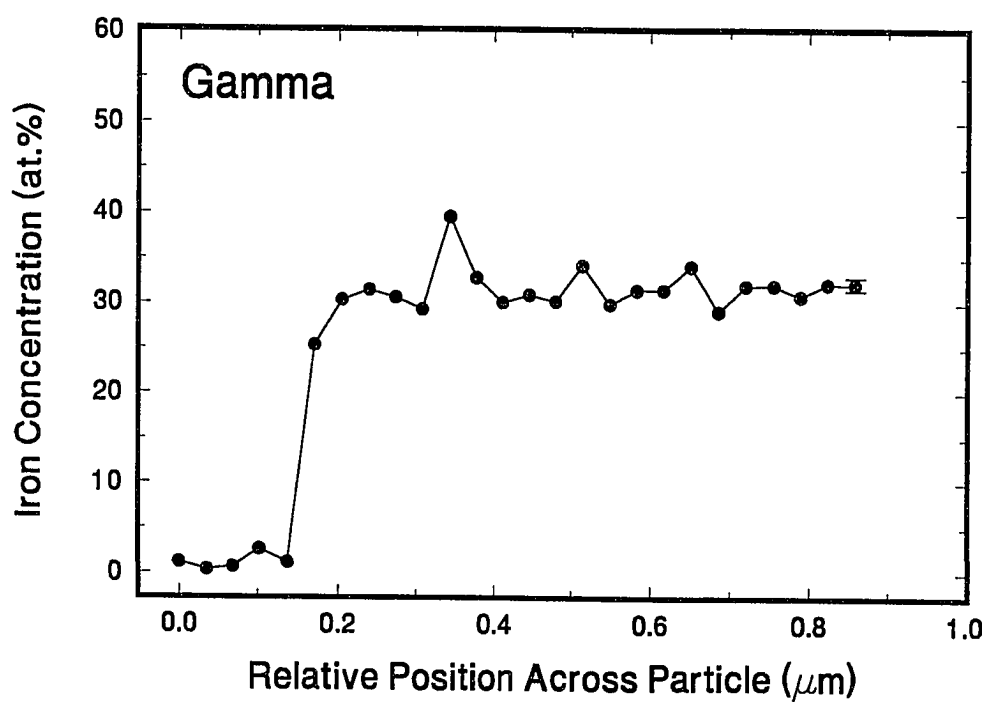
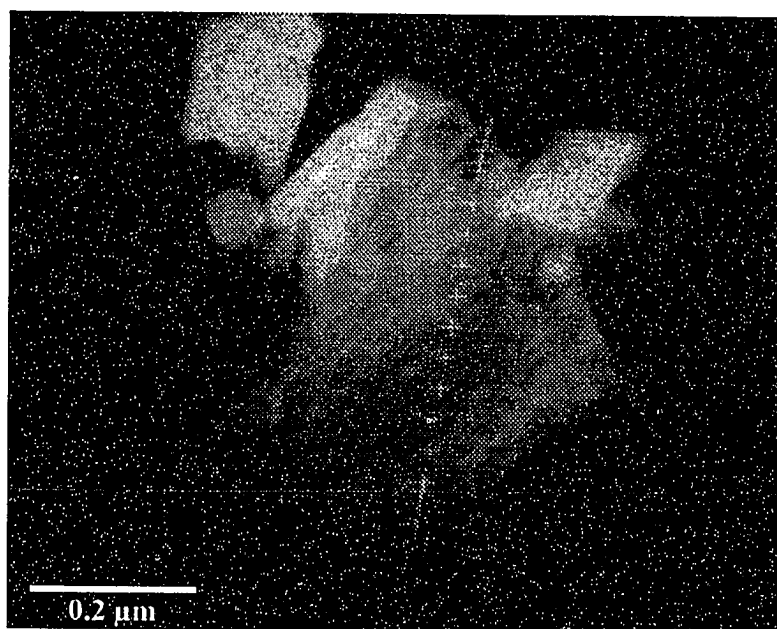


Figure 1.9. SEM photograph and corresponding STEM particle profile of a typical sample produced in the Gamma phase. The plus marks in the SEM photo show the probe points of the STEM.

In addition, the ICP results are not reproducible. Table III compares the measured iron concentration of four iron-zinc intermetallics (one from each of the four phases) using the different analytical techniques discussed in sections 1.3-1.6. As indicated, the ICP results are consistently lower than the expected values.

In comparison, the wet chemical analytical method for measuring the iron concentration of iron-zinc intermetallics has proven to be very accurate. Although the technique is lengthy and involved, it provides accuracies in bulk iron concentration to within 0.5 at.% of the expected value. Furthermore, the uncertainty in the wet chemical measurement is consistently less than ± 0.2 at.% producing a greater than 99% confidence level of being within two standard deviation units of the actual bulk iron concentration. The electron microprobe and STEM analysis of the prepared iron-zinc intermetallics indicate

TABLE III. Comparison of the measured iron concentrations of four iron-zinc alloys (one from each of the four phases), using the different analytical techniques.

	Expected	ICP	Wet Chemical	Electron Microprobe	STEM
Zeta	7.04	6.77 \pm 0.05	7.20 \pm 0.01	6.79 \pm 0.12 Homog.=98%	7.62 \pm 0.25 Homog.=97%
Delta	10.37	10.01 \pm 0.21	10.11 \pm 0.03	9.43 \pm 0.09 Homog.=99%	9.65 \pm 0.21 Homog.=98%
Gamma-1	20.44	19.49 \pm 0.48	20.03 \pm 0.10	21.03 \pm 1.40 Homog.=93%	23.60 \pm 1.67 Homog.=93%
Gamma	29.33	28.08 \pm 0.58	28.91 \pm 0.07	27.24 \pm 0.33 Homog.=99%	31.73 \pm 2.30 Homog.=93%

sample homogeneity is typically greater than 93%. Furthermore, the sample homogeneity as determined by STEM is generally less than that of the electron microprobe. This difference is expected since the probe volumes of the two techniques are significantly different.

Using the method of slow diffusion of zinc in iron, we have been able to prepare high purity, homogeneous alloys within the four main iron-zinc phases, as well as, in the mixed phase regions of the phase diagram. This technique allows samples to be prepared at specific points in the iron-zinc phase diagram. The bulk iron concentrations of the prepared alloys were measured with induction coupled plasma spectroscopy and wet chemical titration. Furthermore, sample homogeneity was measured with an electron microprobe and a scanning transmission electron microscope.

Once the production of high quality iron-zinc intermetallics was demonstrated, their microstructural characterization could proceed. Specifically, samples were prepared at varying iron concentrations within each phase so that the crystallographic and other microstructural properties of the phases could be monitored as function of iron concentration across each phase. The next chapter focuses on the analysis of the prepared iron-zinc alloys using X-ray diffraction and transmission Mössbauer spectroscopy.

The availability and characterization of high quality iron-zinc intermetallics will lead to a better understanding of some of the microstructural properties of commercial galvanized steel. This will result in improved coating quality whose properties may be tailored to specific applications.

CHAPTER TWO

Characterization of the Iron-Zinc Intermetallics

The need to fully characterize the crystalline and microstructural properties of iron-zinc intermetallics was prompted by the difficulty in identifying the phases formed in galvanized steel coatings. Primarily, this was due to the fact that X-ray techniques, X-ray Diffraction (XRD) and X-ray Fluorescence, had been reported as unable to separately identify the Delta and Gamma-1 phases. It has been known for several years that Mössbauer spectroscopy can separately identify the four main iron-zinc phases.^{12,14,21,22} However, application of Mössbauer spectroscopy to the study of galvanized coatings, produces very complex spectra making the unique determination of the phases present, and their relative fractions, difficult. Accurate determination of the phases present in galvanized coatings is further complicated by the lack of high quality data on the microstructural properties of the pure iron-zinc intermetallics. Therefore, to aid in the analysis of the galvanized coatings, a detailed study of the iron-zinc intermetallics, listed in Figure 1.2, was accomplished using X-ray diffraction and transmission Mössbauer spectroscopy. All samples were prepared in

accordance with the method outlined in Chapter 1. Also, the bulk iron concentration and homogeneity of the samples were determined as described previously. This study was performed in order to compile a database of the crystalline and microstructural properties of the iron-zinc intermetallics to perpetuate phase identification in galvaneal steel coatings. Characterization involved monitoring the changes in the lattice and hyperfine parameters across each phase as a function of the iron concentration. Furthermore, samples were prepared and analyzed between the main iron-zinc phases in order to determine their characteristics so that their possible presence in coatings could be determined. In the following chapter, the X-ray diffraction and transmission Mössbauer spectroscopic techniques are described. Also, the crystal structure of the four iron-zinc phases is discussed as well as their characterization using the XRD and Mössbauer analytical methods. The lattice parameters of the four phases have been calculated and the Miller indices for the observed X-ray diffraction peaks have been determined.

2.1 X-ray Diffraction Analysis

Published X-ray diffraction data on the four iron-zinc phases is very limited and in most cases is over 30 years old. The most recent update to the X-ray Powder Diffraction Standards published by the International Center for Diffraction Data, I.C.D.D.²³ was for the Zeta phase which references work performed in 1979.⁴ However, the I.C.D.D. standard of the most complex phase, Delta, is compiled using data recorded in 1928 and 1938.^{6,7} This work was performed well before the discovery of the neighboring Gamma-1 phase in 1974.¹⁰ Hence, some doubt must exist as to the quality of the data presented in the early publications. Since an accurate determination of the structure of each phase and their atomic positions would require single crystals to be grown, it was decided that the earlier publications would be used as a starting point for the present study. In other words, the structures of the four phases, as determined by previous studies, would be used for our study unless obvious discrepancies were observed.

2.1.1 Experimental Technique

The XRD patterns of the iron-zinc intermetallics were recorded using a Philips model APD3720 automated powder diffractometer. Data was recorded using a Cu anode X-ray tube operating at 40kV and 25mA. The wavelength of the Cu-K _{α 1} line is 1.540598 Å. General goniometer scans between the angles of 10° and 120° two-theta were used with step increments of 0.020° and a sample time of 1 s. The intermetallic samples were finely powdered and annealed, as discussed in section 1.2, before being packed into a standard

holder. Approximately 1 gram of sample was required to fill the sample holder creating a sample 1 mm thick. The X-ray illumination length across the sample was 12.5 mm. Extreme care was taken when loading the powder to ensure that the top of the sample was exactly the same as that of the holder. This eliminates errors in the diffraction angles which arise when alignment is not precise. The goniometer was calibrated using a quartz standard. Diffraction peak positions were determined using the standard peak search routine provided by Philips. Specifically, each peak position was resolved from the centroid of the peak indicated by the second derivative of the spectrum. Lattice parameters for each phase were determined using software written specifically for this research. X-ray spectra were analyzed using the Cu-K $_{\alpha 1}$ and Cu-K $_{\alpha 2}$ diffraction peaks.

2.1.2 Crystal Structure of the Four Iron-Zinc Phases

Much controversy exists over the crystal structure of the iron-zinc phases. Particularly, the division of the Delta phase into two different morphologies was proposed by Ghoniem et al.²⁴ in 1972. However, other publications conclude that the Delta phase remains a single morphology across the entire range of homogeneity.^{25,26} This discrepancy in part is due to the complex X-ray spectrum for this phase. Table IV is a summary of the crystallographic data which has been published to date on the four iron-zinc phases. Included is the I.C.D.D. reference patterns which are presently in use. However, most of these patterns appear to be only partially complete. Furthermore, there are conflicting results as to the site occupancies within the Gamma structure as will be discussed later in this section.

TABLE IV. Summary of XRD data published prior to the present study.

Phase	Zeta (ζ)	Delta (δ)	Gamma-1 (Γ_1)	Gamma (Γ)
Stoichiometric Equation	FeZn_{13}	FeZn_{10}	$\text{Fe}_3\text{Zn}_{21}$	$\text{Fe}_3\text{Zn}_{10}$
Crystal Structure	monoclinic	hexagonal	fcc	bcc
Symmetry Group	C2/m	P6 ₃ mc	F $\bar{4}$ 3m	I $\bar{4}$ 3m
I.C.D.D. Ref. Pattern #	34-1314	13-578	32-478	33-697
Iron at. %	7.14	9.09	19.24	23.08
Iron Range at. %	5.9-7.1	8.1-13.2	18.9-24.0	18.0-31.0
Iron Range wt. %	5.2-6.1	7.0-11.5	16.6-21.2	15.8-27.7
Atoms/Unit Cell	28	555	408	52
Lattice Parameters	a=10.862Å	a=12.83Å	a=17.98Å	a=8.98Å
	b=7.608Å	c=57.72Å		
	c=5.061Å			
	$\beta=100.53^\circ$			
Cell Volume (Å³)	412	8228	5813	724
References	a,b,c	a,d,e,f,g,h	a,i,j	a,i,k,l,m

References

- a. I.C.D.D., International Center for Diffraction Data, publishers of the Powder Diffraction File, Newtown Square, PA, U.S.A..
- b. P.J. Brown, *Acta Cryst.* **15**, 608-612 (1962).
- c. P.J. Gellings, E.W. de Bree and G. Gierman, *Z. Metallkde* **70**, 315-317 (1979).
- d. A. Osawa and Y. Ogawa, *Z. Krist.* **68**, 177-188 (1928).
- e. H. Bablik, F. Gotzl and F. Halla, *Z. Metallkde* **8**, 249-252 (1938).
- f. G.F. Bastin, F.J.J. van Loo and G.D. Rieck, *Z. Metallkde* **67**, 694-699 (1976).
- g. G.F. Bastin, F.J.J. van Loo and G.D. Rieck, *Z. Metallkde* **68**, 359-361 (1977).
- h. P.J. Gellings, E.W. de Bree and G. Gierman, *Z. Metallkde* **70**, 312-314 (1979).
- i. G.F. Bastin, F.J.J. van Loo and G.D. Rieck, *Z. Metallkde* **65**, 665-660 (1974).
- j. A.S. Koster and J.C. Schoone, *Acta Cryst.* **B37**, 1905-1907 (1981).
- k. A. Johansson, H. Ljung and S. Westman, *Acta. Chem. Scand.* **22**, 2743-2753 (1968).
- l. J.K. Brandon, R.Y. Brizard, P.C. Chieh, R.K. McMillan and W.B. Pearson, *Acta. Cryst.* **B30**, 1412-1417 (1974).
- m. P.J. Gellings, G. Gierman, D. Koster and J. Kuit, *Z. Metallkde* **70**, 70-75 (1971).

Zeta Phase: The Zeta phase spans a narrow iron concentration range between 5.9 at.% - 7.1 at.%, (5.1 wt.% - 6.1 wt.%), as shown in Figure 1.2. It has a peritectic melting point at 530 °C. It crystallizes in the monoclinic structure,² $a \neq b \neq c$, $\beta \neq 90^\circ$, with space group C2/m and has the stoichiometry FeZn_{13} . The Zeta structure, as proposed by Brown,² consists of an iron atom surrounded by twelve zinc atoms at the vertices of a slightly distorted icosahedron. These icosahedrons then link together to form chains which run parallel to the c-axis. The chains group to form an approximate hexagonal array illustrated in Figure 2.1. The lattice parameters were determined by Brown² to be, $a = 13.424 \pm 0.005 \text{ \AA}$, $b = 7.608 \pm 0.001 \text{ \AA}$, $c = 5.061 \pm 0.003 \text{ \AA}$, and $\beta = 127^\circ 18' \pm 2'$. More recent work by Gellings et al.⁴ confirmed Brown's results, taking into account the preferred choice of the axes. Using the international convention for choosing the axes such that the angle β is as close as possible to 90° , Gellings et al. found the lattice parameters to be, $a = 10.862 \text{ \AA}$, $b = 7.608 \text{ \AA}$, $c = 5.061 \text{ \AA}$, and $\beta = 100^\circ 32'$. The atomic positions and site occupancies for the structure proposed by Brown are shown in Table V.

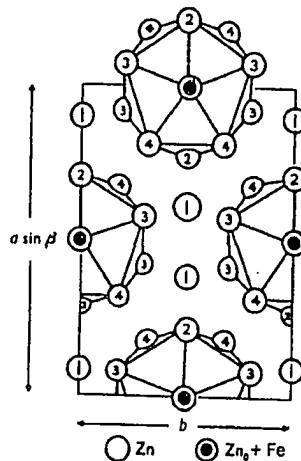


Figure 2.1. Drawing of the Zeta structure as viewed along the [001] direction.²

TABLE V. Atomic positions for the ζ phase iron-zinc alloy.²

Atomic Position	Atomic Parameter	Occupation
2(a) (0,0,0)	---	2Fe or 2Zn
2(c) (0,0,½)	---	2Zn or 2Fe
4(i) (x,0,z)	x=0.1120 z=0.2920	Zn
4(i) (x,0,z)	x=0.2195 z=0.0730	Zn
8(j) (x,y,z)	x=0.0770 y=0.2920 z=0.8350	Zn
8(j) (x,y,z)	x=0.1760 y=0.1780 z=0.5450	Zn

Delta Phase: The Delta phase forms with iron concentration between 8.1 at.% - 13.2 at.%, (7.0 wt.% - 11.5 wt.%). It has a peritectic melting point at 672 °C and crystallizes in a hexagonal structure, $a = b \neq c$, $\gamma = 120^\circ$, with space group $P6_3mc$.⁷ The nominal stoichiometry is $FeZn_{10}$ although it can vary between $Fe_{0.89}Zn_{10.11}$ and $Fe_{1.45}Zn_{9.55}$. The unit cell is very large, containing 555 ± 8 atoms;⁷ however, the atomic arrangement within the unit cell is not known. Bastin et al.⁹ determined the lattice parameters for Delta to range from, $a=12.80-12.77 \text{ \AA}$ and $c=57.30-56.96 \text{ \AA}$ as one moves across the phase. This unusually long columnar cell has a volume of approximately 8100 \AA^3 . Although several papers have reported on the existence of two different morphologies within the Delta phase when formed in galvanneal coatings, none have observed this in the pure alloys. Specifically, Bastin et al.⁹ prepared single crystals of the δ phase with compositions covering the entire range of homogeneity and observed no discontinuities in the lattice parameters.

Gamma-1 Phase: The Gamma-1 phase was first discovered by Bastin et al.¹⁰ in 1974 and led to the modification of the iron-zinc phase diagram. The Gamma-1 phase forms between the iron concentrations of 18.9 at.% and 24 at.%, (16.0 wt.% - 21.3 wt.%). It has a peritectic melting point at 550 °C and a nominal stoichiometry of Fe₃Zn₂₁. It crystallizes in a cubic structure with space group $F\bar{4}3m$. The structure is described¹¹ as having 408 atoms per unit cell, $a=17.963 \text{ \AA}$, and a cell volume of $V=5796 \text{ \AA}^3$. The single crystal X-ray diffraction work of Koster and Schoone¹¹ describes the Gamma-1 structure as being related to the Gamma structure in that if eight cells of the Gamma structure were stacked together and the cell dimensions were doubled, then a large Gamma-1 cell with space group $F\bar{4}3m$ would be formed. As will be discussed in section 2.1.5 of this dissertation, the relationship between the structures of Gamma-1 and Gamma results in an overlap of the X-ray diffraction peaks from each phase. This complicates the separate identification of the Gamma-1 and Gamma phases in galvanneal steel coatings using XRD. Table VI shows the atomic positions and site occupancies proposed by Koster and Schoone.¹¹ The second column in Table VI indicates the site symmetries as Cubo-Octahedral (CO), Octahedral (OH), Outer-Tetrahedral (OT), and Inner-Tetrahedral (IT).

TABLE VI. Structural parameters for the Γ_1 phase iron-zinc intermetallic.

Atomic Position	Site Geometry	Atomic Parameters	Occupation
48(h) (x,x,z)	CO	x=0.0944 (5) z=0.2285 (6)	Zn
48(h) (x,x,z)		x=0.0578 (4) z=0.7268 (6)	Zn
48(h) (x,x,z)	CO	x=0.1495 (4) z=0.9643 (7)	Zn
48(h) (x,x,z)		x=0.1425 (4) z=0.4669 (7)	Zn
48(h) (x,x,z)		x=0.2001 (4) z=0.5880 (6)	Zn
24(f) (x,0,0)	OH	x=0.1615 (14)	Fe
24(f) (x,0,0)		x=0.3940 (10)	Zn
24(g) (x,1/4,1/4)	OH	x=0.0649 (10)	Zn
16(e) (x,x,x)	OT	x=0.0845 (7)	Fe, Zn
16(e) (x,x,x)	IT	x=0.1986 (10)	Fe, Zn
16(e) (x,x,x)	OT	x=0.3317 (11)	Fe, Zn
16(e) (x,x,x)		x=0.6014 (10)	Fe
16(e) (x,x,x)		x=0.8097 (9)	Zn
16(e) (x,x,x)	IT	x=0.9527 (10)	Fe

Gamma Phase: The Gamma phase forms between the iron concentrations of 18 at.% - 31 at.%, (15.8 wt.% - 27.8 wt.%). It has a peritectic melting point at 782 °C. The nominal stoichiometry is $\text{Fe}_3\text{Zn}_{10}$ but is quite often written as Fe_5Zn_8 for samples at the high iron side of the phase diagram. It crystallizes in the cubic γ -brass structure with space group $\text{I}\bar{4}3\text{m}$. Each lattice point on the bcc Bravais lattice contains a 26 atom cluster. Therefore, there are 52 atoms per unit cell.²⁶ Figure 2.2 shows the cluster of atoms which is situated at the body centered position. The clusters at the eight corner positions have been omitted for simplicity. Each cluster is identical and contains four crystallographically unique sites. They are labeled Inner Tetrahedral (IT), Outer Tetrahedral (OT), Octahedral (OH) and Cubo-Octahedral (CO). These four sites contain 4, 4, 6 and 12 atoms respectively per cluster (see Figure 2.2). Previous neutron and X-ray diffraction studies^{25,26} have been unable to conclusively ascertain which of the four sites are occupied by the iron atoms. Table VII compares the atomic positions and site occupancies reported by Brandon et al.²⁶ with the previously reported work of Johansson et al.²⁵ Although the atomic positions are similar, Johansson et al. determined that the iron is occupying the IT and OH sites whereas Brandon et al. concluded the iron must occupy the IT and OT sites. As will be discussed in section 2.2.2, the Mössbauer effect analysis of many samples produced within the Gamma phase enabled us to determine that the iron occupies the IT and OH sites, in agreement with Johansson et al.

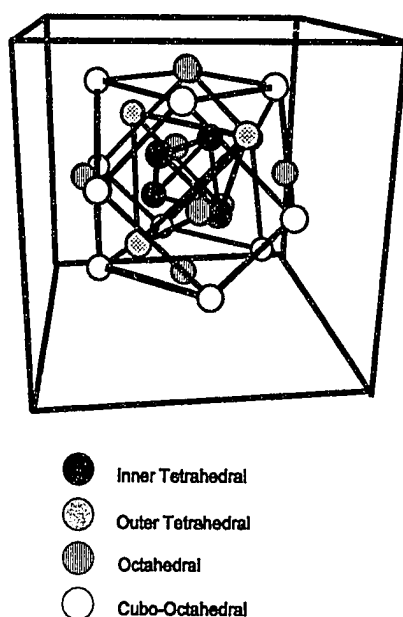


Figure 2.2. The bcc structure of the Γ phase showing the 26 atom cluster at the body centered lattice point. This cluster is also repeated at the 8 corner positions giving 52 atoms per unit cell.

TABLE VII. Comparison of the structural data for the Γ phase iron-zinc alloy.

		Johansson et al. (1968)	Brandon et al. (1974)
Atomic Positions	IT 8(c) (xxx)	$x=0.0973\pm15$	$x=0.1028\pm5$
	OT 8(c) (xxx)	$x=-0.1638\pm13$	$x=-0.1673\pm4$
	OH 12(e) (x00)	$x=0.3551\pm15$	$x=0.3538\pm4$
	CO 24(g) (xxz)	$x=0.3029\pm8$ $z=0.0508\pm12$	$x=0.3045\pm2$ $z=0.0491\pm3$
Site Occupancy	IT	Fe	4Fe+4Zn
	OT	Zn	Fe
	OH	8Fe+4Zn	Zn
	CO	Zn	Zn

2.1.3 Lattice Parameters of the Four Phases

In order to completely document the lattice parameters of the four phases, spectra were recorded over the large range of angles, 10° to 120° two-theta. However, as will be shown, only a small range of angles is required to differentiate between the four phases. General X-ray diffraction spectra of the Zeta, Delta, Gamma-1 and Gamma phases are shown in Figures 2.3-2.6. These spectra were recorded over the full range of angles, and the lattice parameters and Miller indices were calculated by the methods described below. The characteristics for these spectra are listed in Tables VIII-XI, respectively. As will be discussed below, the diffraction spectra change within one phase as a function of iron concentration. However, the changes in peak positions are small and do not effect the major features of each of the four spectra in Figures 2.3-2.6.

Figure 2.7 shows the overlap of XRD spectra of the four phases plotted between the angles of 30° and 50° two-theta. This figure provides better visual information on the diffraction peak positions and provides for easy comparison between the four phases. Furthermore, low and high iron concentration spectra have been plotted for the Delta and Gamma phases illustrating the subtle changes in the spectra as the iron concentration increases across these phases. As will be discussed in more detail in the following sections, no changes in the spectra as a function of iron concentration were observed for the Zeta and Gamma-1 phases.

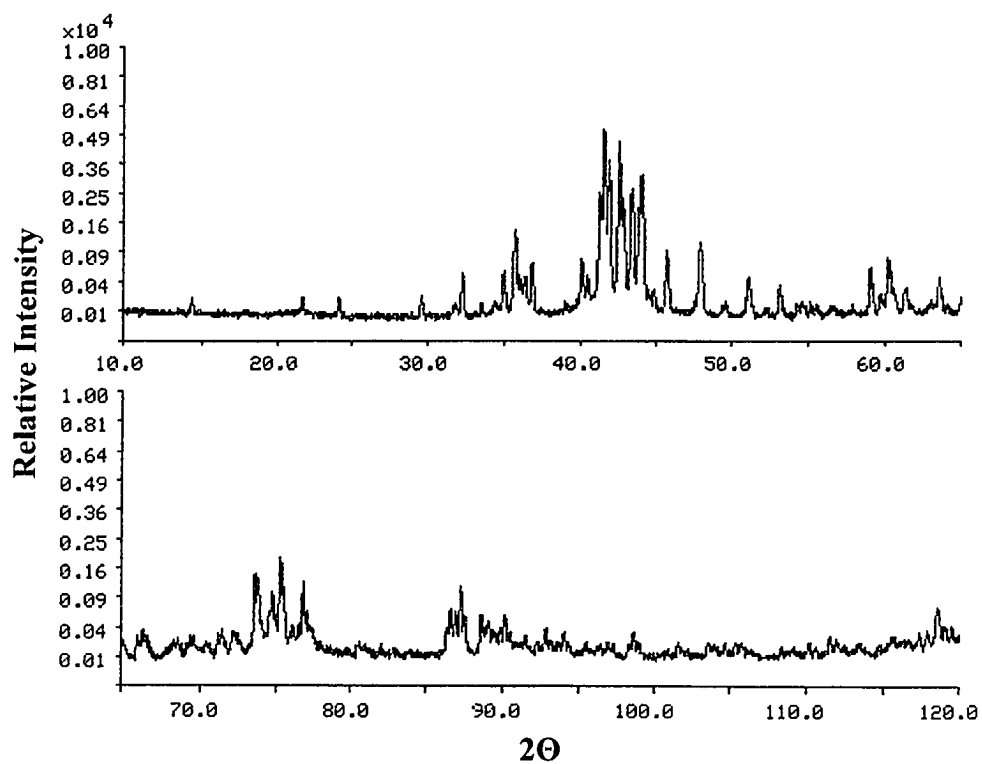


Figure 2.3. XRD spectrum of the ζ sample FZ007F from 10° to 120° two-theta.

TABLE VIII. XRD data for the ζ sample FZ007F from 10° to 120° two-theta.

2Theta	I/I _o	d (Å)	hkl	2Theta	I/I _o	d (Å)	hkl
14.3980	2.37	6.1471	110	72.1400	4.34	1.3083	730
21.6400	2.69	4.1034	111	72.4000	3.93	1.3043	152
24.1080	2.69	3.6887	111	73.6300	25.94	1.2855	532
29.5380	3.23	3.0218	021	74.5800	10.67	1.2714	623
32.3130	8.89	2.7683	221	74.7930	17.95	1.2684	204
33.5370	1.84	2.6699	400	75.3000	36.76	1.2611	352
35.0020	9.32	2.5615	401	75.9300	4.70	1.2522	043
35.7250	26.67	2.5113	221	76.5300	6.74	1.2438	732
36.0020	7.42	2.4926	002	76.8000	21.23	1.2401	550
36.7720	12.22	2.4421	202	77.4750	5.08	1.2310	713
40.0180	13.03	2.2513	131	77.9780	2.33	1.2243	642
40.4250	8.14	2.2295	112	78.6680	1.44	1.2153	822
41.2150	48.46	2.1886	401	79.8020	1.24	1.2008	443
41.5070	100.00	2.1738	131	80.5430	1.84	1.1917	513
41.8220	72.53	2.1582	312	80.9850	1.84	1.1863	261
42.4900	86.51	2.1258	421	82.0350	1.69	1.1737	551
42.7830	43.62	2.1120	202	82.9050	1.03	1.1636	514
43.3530	52.10	2.0855	022	83.8650	0.45	1.1527	803
43.7800	37.98	2.0661	330	86.3200	4.58	1.1261	262
43.9720	61.56	2.0575	510	86.9520	10.21	1.1195	733
44.4520	4.16	2.0364	511	87.3230	20.71	1.1157	224
44.7800	4.34	2.0223	402	88.6700	9.67	1.1022	153
45.6100	16.53	1.9874	331	89.1400	7.58	1.0976	461
47.7570	15.84	1.9029	040	89.5820	4.16	1.0934	840
47.8900	19.43	1.8980	421	90.1880	9.32	1.0876	262
49.2720	0.86	1.8479	222	91.5030	3.71	1.0754	930
49.5370	1.24	1.8386	331	92.2380	2.60	1.0687	10.0.0
50.8730	2.60	1.7935	132	92.8480	5.95	1.0633	842
51.0550	7.82	1.7875	601	94.0250	4.70	1.0530	171
52.2630	0.73	1.7490	512	95.4600	2.24	1.0410	752
53.1450	5.02	7.7220	241	96.4600	1.65	1.0328	660
54.2980	1.03	1.6881	332	96.9200	2.20	1.0291	10.2.0
54.5850	1.44	1.6799	203	98.3020	1.84	1.0183	10.2.2
55.1850	1.84	1.6631	003	100.8230	0.94	0.9996	172
55.5880	1.54	1.6520	113	101.5000	2.16	0.9947	244
56.6000	0.76	1.6248	531	103.5050	2.55	0.9808	11.1.1
57.8500	0.45	1.5926	313	104.5900	2.37	0.9736	154
58.9900	9.67	1.5645	113	105.3350	2.64	0.9688	644
59.6270	2.69	1.5493	440	105.7600	1.91	0.9661	425
60.1470	13.86	1.5372	223	108.3950	1.24	0.9498	605
60.3330	8.89	1.5329	422	109.1430	1.34	0.9453	752
61.1950	3.28	1.5134	042	110.1830	2.46	0.9393	335
63.4850	6.89	1.4642	621	111.5580	3.44	0.9316	932
63.9950	1.27	1.4537	151	111.9650	2.88	0.9293	534
65.0550	3.13	1.4326	151	113.4420	2.29	0.9214	625
66.0070	3.55	1.4142	242	114.7450	1.76	0.9146	173
66.3500	5.34	1.4077	133	115.6000	3.55	0.9103	315
68.3720	3.13	1.3709	333	116.7000	3.18	0.9049	11.3.2
69.4380	3.99	1.3525	133	117.8900	4.40	0.8992	10.0.4
70.3970	2.24	1.3364	800	118.4970	11.72	0.8963	480
71.2400	4.46	1.3226	351	119.4650	6.23	0.8919	481

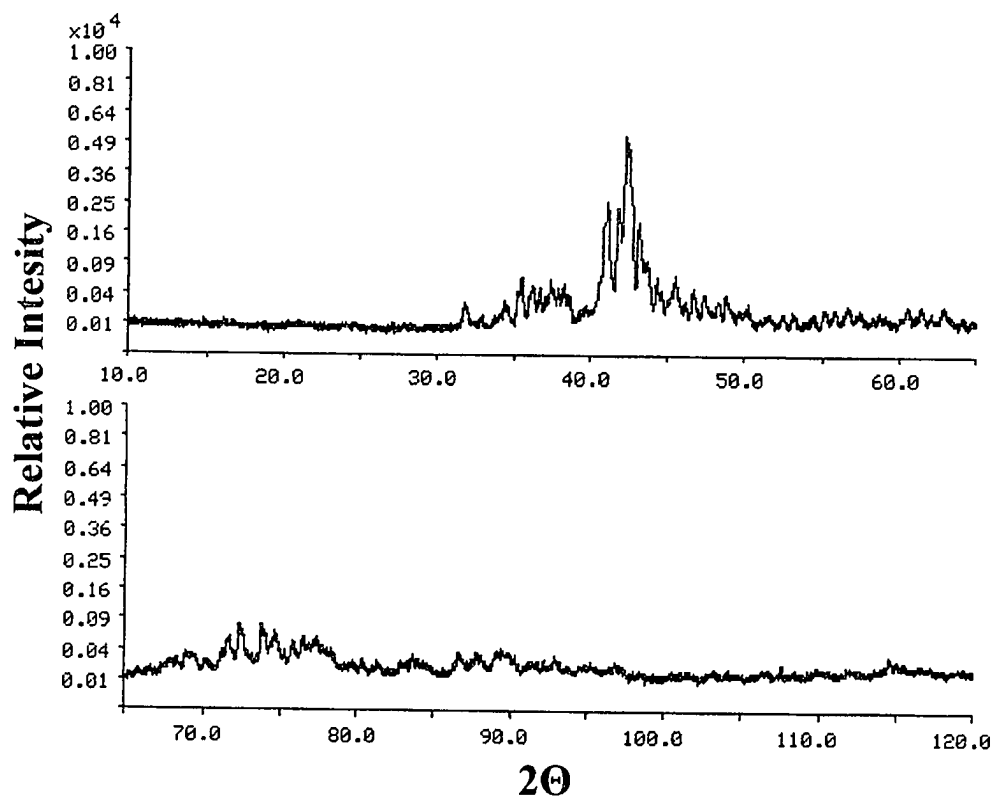


Figure 2.4. XRD spectrum of the δ sample FZ034F from 10° to 120° two-theta.

TABLE IX. XRD data for the δ sample FZ034F from 10° to 120° two-theta.

2Theta	I/I ₀	d (Å)	hkl	2Theta	I/I ₀	d (Å)	hkl
16.1075	0.67	5.4981	109, 201	58.6650	1.33	1.5724	704, 354
16.7225	0.58	5.2973	203, 116	59.0575	1.27	1.5629	706, 356
24.5475	0.58	3.6235	218, 303	59.5725	0.40	1.5506	6.0.20, 2.5.18
27.0600	0.62	3.2925	308	59.9900	1.03	1.5408	4.4.10
27.8050	0.67	3.2060	309	60.5450	2.95	1.5280	264
29.4450	0.20	3.0310	133, 226	61.3900	2.95	1.5090	267
31.7550	4.32	2.8156	2.1.15	62.0850	1.43	1.4938	269
32.8450	1.64	2.7246	404	62.8150	2.36	1.4782	7.0.14, 3.5.14
33.7275	1.50	2.6553	406	64.1125	0.71	1.4513	176
35.2125	6.64	2.5467	409, 321	64.6925	0.42	1.4397	178
35.4850	10.68	2.5277	232	65.8600	1.79	1.4170	451
35.5700	8.01	2.5219	323	66.5800	1.06	1.4034	456
36.0500	6.43	2.4894	3.0.17, 4.0.10	67.3175	1.83	1.3898	364
36.6625	7.70	2.4492	2.0.21, 4.0.11	67.9050	2.67	1.3792	804
37.0350	5.21	2.4254	327	68.2975	3.00	1.3722	806, 368
37.4125	9.69	2.4018	413, 328	68.8075	3.89	1.3633	369
37.6500	6.29	2.3872	414	69.2525	4.00	1.3556	809
37.8975	7.54	2.3722	415	69.4975	3.20	1.3515	272
38.2525	8.92	2.3510	4.0.13	70.1025	2.44	1.3413	276
38.6200	5.73	2.3294	1.0.24, 3.1.16	71.0925	3.89	1.3250	279
39.4000	2.76	2.2851	2.1.21, 2.3.11	71.5350	7.31	1.3179	2.7.10, 4.5.16
39.6900	3.20	2.2691	2.0.23, 3.0.20	72.3375	12.80	1.3052	1.7.20
40.8375	33.84	2.2079	502	74.0175	10.13	1.2797	552
41.0500	47.63	2.1970	2.0.24, 3.0.21	74.6625	10.13	1.2702	189, 461
41.6875	40.53	2.1649	3.2.14	74.9000	6.29	1.2668	464
42.2200	100.00	2.1388	507	75.2575	4.29	1.2617	466
42.6875	46.66	2.1164	508	76.4750	8.34	1.2446	373
43.0750	33.84	2.0983	509	77.1700	7.39	1.2351	8.0.21, 1.7.25
43.6350	17.26	2.0726	424	77.7025	6.14	1.2280	903, 378
43.7875	13.31	2.0658	3.0.23, 5.0.10	78.2700	5.02	1.2205	906
44.2775	10.77	2.0440	426, 338	79.7300	1.94	1.2018	285
44.9750	4.58	2.0140	428	81.3400	1.94	1.1820	1.8.20, 4.6.18
45.2025	6.64	2.0043	3.0.24, 4.1.16	82.8350	2.31	1.1644	9.0.16
45.4550	11.14	1.9938	511, 429	86.5775	3.78	1.1234	383
46.0950	4.29	1.9676	4.1.17, 4.2.10	87.7425	3.78	1.1115	388
46.5950	6.94	1.9476	516	89.0425	4.40	1.0986	10.0.7, 1.9.17
47.3425	5.87	1.9186	518	90.2725	3.40	1.0868	295
48.1925	4.23	1.8867	5.0.16, 3.1.24	91.3150	1.91	1.0771	299
48.2900	4.29	1.8832	5.0.16, 3.1.24	91.7750	1.61	1.0729	2.9.10, 3.8.16
48.7300	5.94	1.8672	4.2.14	92.1975	2.27	1.0691	10.0.14, 1.9.21
49.5575	2.53	1.8379	603	93.8800	1.27	1.0543	668
50.1450	3.30	1.8178	342	94.5150	1.43	1.0489	1.10.4, 6.6.10
50.9075	0.74	1.7923	346	94.8750	1.75	1.0458	483
51.4950	1.50	1.7732	609, 252	96.4775	1.40	1.0327	2.9.18, 3.8.22
52.3800	1.50	1.7453	256	96.8525	2.06	1.0297	4.8.10
53.1075	1.91	1.7231	5.0.21, 6.0.12	98.7025	0.26	1.0153	4.8.14
54.3625	1.33	1.6863	612	101.5500	0.81	0.9944	2.10.2, 2.10.3
55.1600	2.02	1.6638	166	103.2475	0.79	0.9826	672
55.7725	2.15	1.6469	168	104.4750	0.2	0.9744	583, 678
56.6175	2.90	1.6243	5.0.24, 3.4.16	106.3300	0.92	0.9624	1.10.24, 5.8.10
57.3800	2.49	1.6046	2.4.23, 3.4.17	114.5025	2.76	0.9159	3.10.14, 4.9.19
58.2425	0.86	1.5828	701, 351	114.9750	1.98	0.9135	772

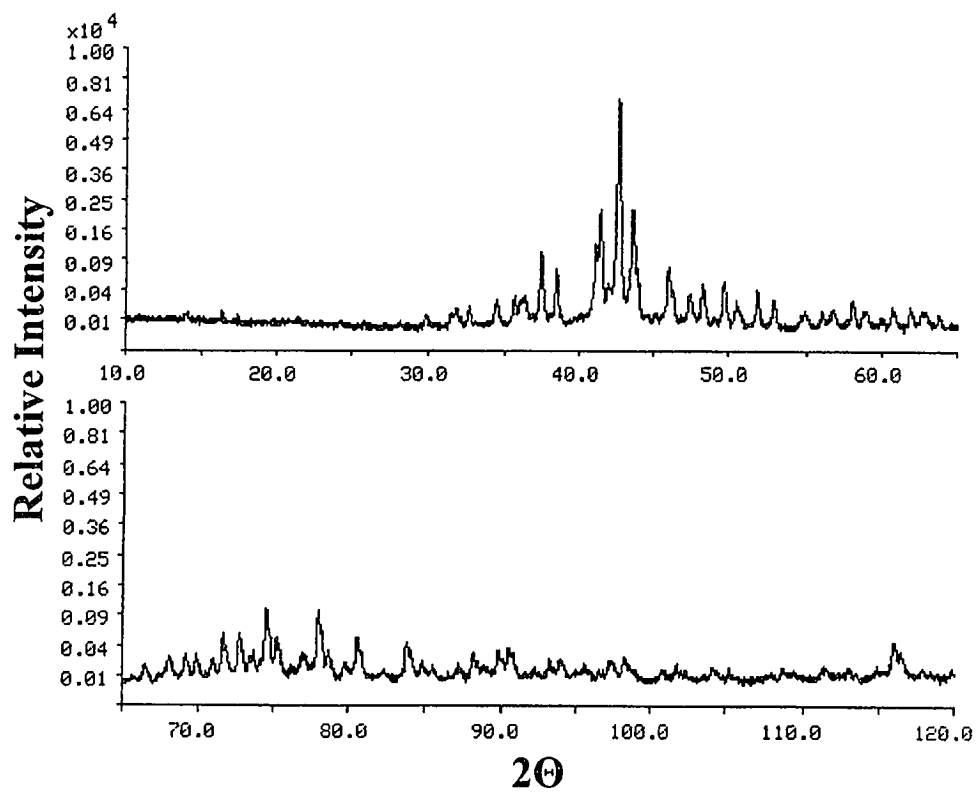


Figure 2.5. XRD spectrum of the Γ_1 sample FZ025G from 10° to 120° two-theta.

TABLE X. XRD data for the Γ_1 sample FZ025G from 10° to 120° two-theta.

2Theta	I/I ₀	d (Å)	hkl	2Theta	I/I ₀	d (Å)	hkl
14.0750	0.59	6.2872	220	69.9150	3.13	1.3444	977
16.3925	0.88	5.4032	311	71.0050	2.41	1.3264	12.6.2
21.3500	0.23	4.1584	331	71.6975	7.33	1.3153	995
24.2100	0.24	3.6733	422	72.7300	6.15	1.2991	888
28.0475	0.32	3.1788	440	73.6825	3.52	1.2847	12.6.4, 14.0.0
29.7900	1.02	2.9967	442, 600	74.5375	13.74	1.2721	10.10.0, 10.8.6
31.4575	1.17	2.8416	620	75.2000	6.09	1.2625	11.9.1, 13.5.3
32.6800	1.95	2.7380	533	76.9425	3.21	1.2382	997
34.5125	3.04	2.5967	444	77.9825	13.03	1.2242	10.10.4, 12.6.6
35.6750	3.62	2.5147	551, 711	78.6500	3.75	1.2155	11.7.7, 13.5.5
36.0250	2.84	2.4911	640	79.7400	1.85	1.2016	12.8.4
37.4375	14.28	2.4003	642	80.5800	6.69	1.1912	10.8.8, 14.4.4
38.4375	9.71	2.3401	553, 731	82.3025	0.97	1.1706	10.10.6, 14.6.2
40.1150	1.20	2.2460	800	83.7625	5.56	1.1539	999
41.0725	16.64	2.1958	733	84.7775	2.09	1.1426	12.10.2, 14.6.4
41.3875	29.32	2.1799	820, 644	85.4650	1.39	1.1352	11.9.7, 11.11.3
42.6375	100.00	2.1188	660, 822	87.1525	1.85	1.1175	13.9.3, 15.5.3
43.5725	30.24	2.0755	555, 751	88.1550	3.48	1.1073	10.10.8, 14.8.2
43.8850	9.27	2.0614	662	88.8250	1.45	1.1007	11.11.5, 13.7.7
45.0950	1.23	2.0089	840	89.8425	3.75	1.0909	12.8.8, 16.4.0
45.9225	8.62	1.9746	753, 911	90.5100	4.14	1.0846	13.9.5, 15.5.5
46.2975	4.59	1.9595	842	91.5575	0.69	1.0749	12.10.6
47.3525	3.80	1.9182	664	92.2275	1.28	1.0688	11.9.9, 15.7.3
48.2375	5.97	1.8851	931	93.2125	2.16	1.0601	12.12.0, 16.4.4
49.6125	6.33	1.8360	844	93.9150	2.34	1.0540	13.11.1, 11.11.7
50.4525	2.92	1.8074	755, 771	95.5700	1.69	1.0401	13.9.7, 13.11.3
51.7925	4.59	1.7637	862, 10.2.0	96.5400	0.86	1.0322	12.12.4
52.8450	2.92	1.7311	666, 10.2.2	97.2150	1.69	1.0268	15.9.1, 17.3.3
54.9150	1.31	1.6706	864, 10.4.0	97.4950	2.12	1.0246	12.10.8, 16.6.4
55.9500	1.33	1.6421	10.4.2	98.2925	2.80	1.0184	14.10.4
56.7175	1.82	1.6217	775, 11.1.1	100.8700	0.84	0.9992	12.12.6, 14.8.8
57.9400	2.68	1.5904	880	101.7225	1.63	0.9931	16.6.6, 18.2.0
58.7100	1.39	1.5713	955, 971	102.4650	1.15	0.9880	14.10.6, 13.9.9
58.9475	1.60	1.5656	882	104.1350	1.36	0.9766	13.11.7, 17.5.5
59.9025	0.79	1.5429	866	105.1650	0.81	0.9699	12.10.10
60.6375	1.88	1.5259	973	107.8875	0.73	0.9528	14.12.4, 16.8.6
61.8200	2.23	1.4995	884	108.6900	1.20	0.9480	14.10.8, 16.10.6
62.5525	1.25	1.4837	777	109.3925	0.97	0.9439	11.11.5, 17.7.5
62.9000	1.17	1.4764	12.2.0	111.3900	1.45	0.9325	16.10.4
63.7100	1.10	1.4595	10.6.4, 12.2.2	113.0025	1.33	0.9237	17.9.3, 19.3.3
65.6150	0.45	1.4217	12.4.0	114.8450	1.33	0.9141	15.9.9, 17.7.7
66.5175	1.66	1.4046	886	115.9925	5.56	0.9084	14.14.0, 16.10.6
68.0875	2.96	1.3760	993	117.8875	1.33	0.8992	16.12.0, 20.0.0
69.2350	3.17	1.3559	12.4.4	119.7675	1.12	0.8905	14.14.4, 20.2.2

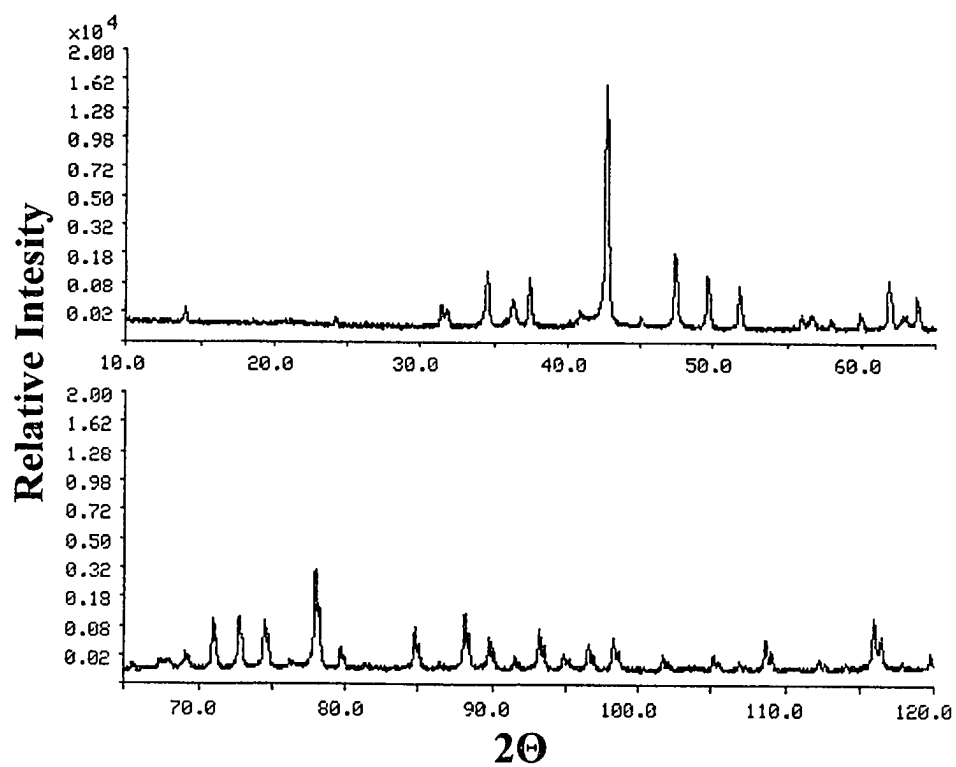


Figure 2.6. XRD spectrum of the Γ sample FZ035D from 10° to 120° two-theta.

TABLE XI. XRD data for the Γ sample FZ035D from 10° to 120° two-theta.

2Theta	I/I ₀	d (Å)	hkl	2Theta	I/I ₀	d (Å)	hkl
14.0250	1.10	6.3095	110	76.2450	0.56	1.2478	640
24.2150	0.36	3.6725	211	77.9550	19.75	1.2246	552, 633
26.7925	0.40	3.3248	220	79.6725	1.77	1.2025	642
31.4250	1.16	2.8444	310	81.3800	0.38	1.1815	730
34.5225	7.19	2.5960	222	84.7600	4.56	1.1428	651, 732
37.3725	6.02	2.4043	321	86.4475	0.42	1.1248	800
40.8300	0.14	2.2083	400	88.1375	7.27	1.1075	554, 741
42.5975	100.00	2.1207	330, 411	89.8225	3.08	1.0911	644, 820
45.0275	0.48	2.0117	420	91.4900	0.84	1.0755	653
47.3475	10.77	1.9184	332	93.1750	4.32	1.0604	660
49.5800	6.10	1.8371	422	94.8675	1.20	1.0459	743
51.7450	4.06	1.7652	431, 510	96.5725	2.26	1.0319	662
55.9075	0.81	1.6433	521	98.2500	3.02	1.0187	752
57.9200	0.47	1.5909	440	101.6425	1.15	0.9937	833
59.8625	0.95	1.5438	433, 530	105.1125	0.86	0.9702	655
61.7950	5.82	1.5001	442, 600	106.8950	0.37	0.9589	664
63.6750	2.94	1.4603	532, 611	108.6500	2.91	0.9483	754
65.5325	0.36	1.4233	620	112.2425	0.73	0.9278	763
67.3575	0.71	1.3891	541	114.1000	0.32	0.9180	844
69.1750	1.26	1.3570	622	115.9250	6.59	0.9087	770
70.9725	6.18	1.3269	631	117.8225	0.42	0.8995	860
72.7450	6.80	1.2989	444	119.7100	1.05	0.8908	772
74.4975	5.90	1.2726	543, 550				

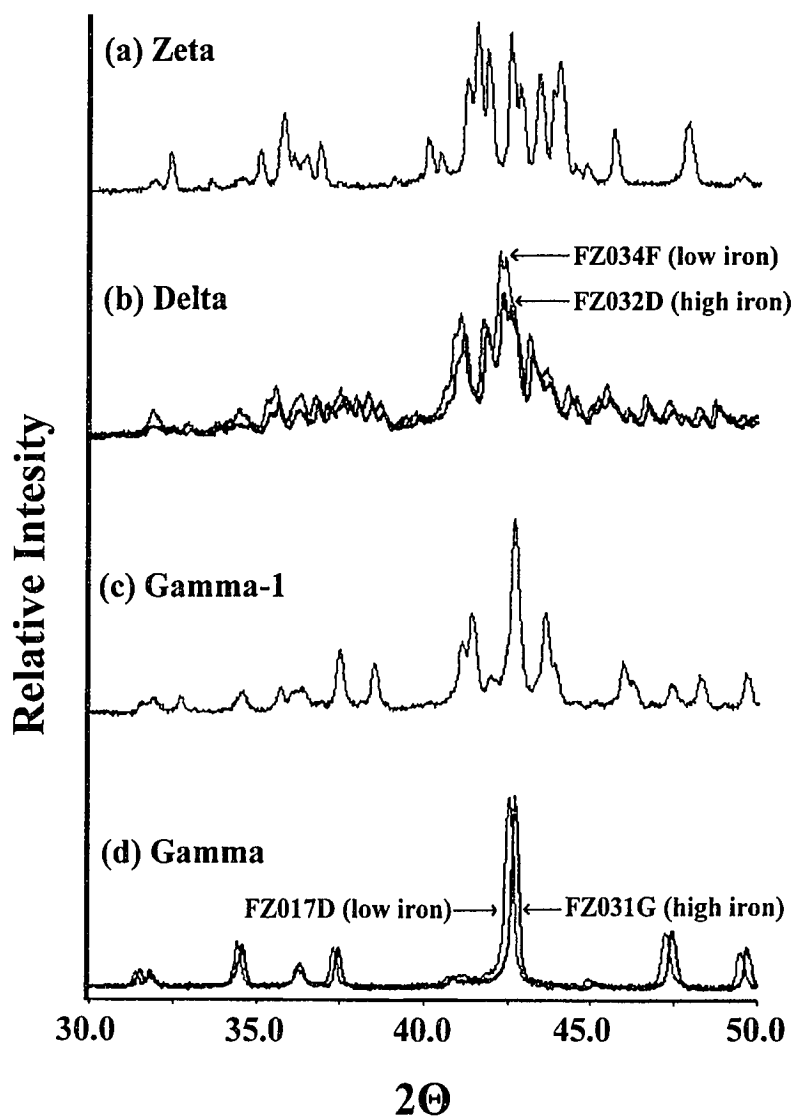


Figure 2.7. Typical XRD spectra of the four intermetallic binary alloys showing (a) Zeta, (b) Delta, (c) Gamma-1, and (d) Gamma, ranging from 30° to 50° two-theta.

Zeta Phase: As previously discussed, the Zeta phase spans a narrow iron concentration range between 5.9 at.% - 7.1 at.%, (5.1 wt.% - 6.1 wt.%) and crystallizes in the monoclinic structure, $a \neq b \neq c$, $\beta \neq 90^\circ$, with space group $C2/m$.² Three samples were prepared at two different iron concentrations within the ζ phase and analyzed using XRD and Mössbauer spectroscopy. Figures 2.3 and 2.7 (a) show the XRD spectrum for a typical sample within the ζ phase. The lattice parameters for the monoclinic structure were calculated from the recorded interplanar spacings, Table VIII, using the following equation:

$$\frac{1}{d_{hkl}^2} = \frac{1}{\sin^2\beta} \left(\frac{h^2}{a^2} + \frac{k^2 \sin^2\beta}{b^2} + \frac{l^2}{c^2} - \frac{2hlc \cos\beta}{ac} \right)$$

The lattice parameters for iron concentrations of 6.40 at.% and 7.04 at.% are plotted in Figure 2.8. Within experimental uncertainty, the parameters do not change as a function of iron concentration across the Zeta phase. This is perhaps expected since the range of homogeneity for the Zeta phase is very narrow. The mean values of $a = 10.880 \text{ \AA}$, $b = 7.611 \text{ \AA}$, $c = 5.079 \text{ \AA}$ and $\beta = 100.83^\circ$ are in agreement with those reported by Gellings et al.⁴ The unit cell volume is calculated to be about 413 \AA^3 . Samples FZ007C and FZ007F (see Figure 1.2) both have an iron concentration of 7.04 at.% and were prepared at 480°C and 450°C respectively. A comparison of their spectral line position show that there is no dependence of the lattice parameters on the sintering temperature.

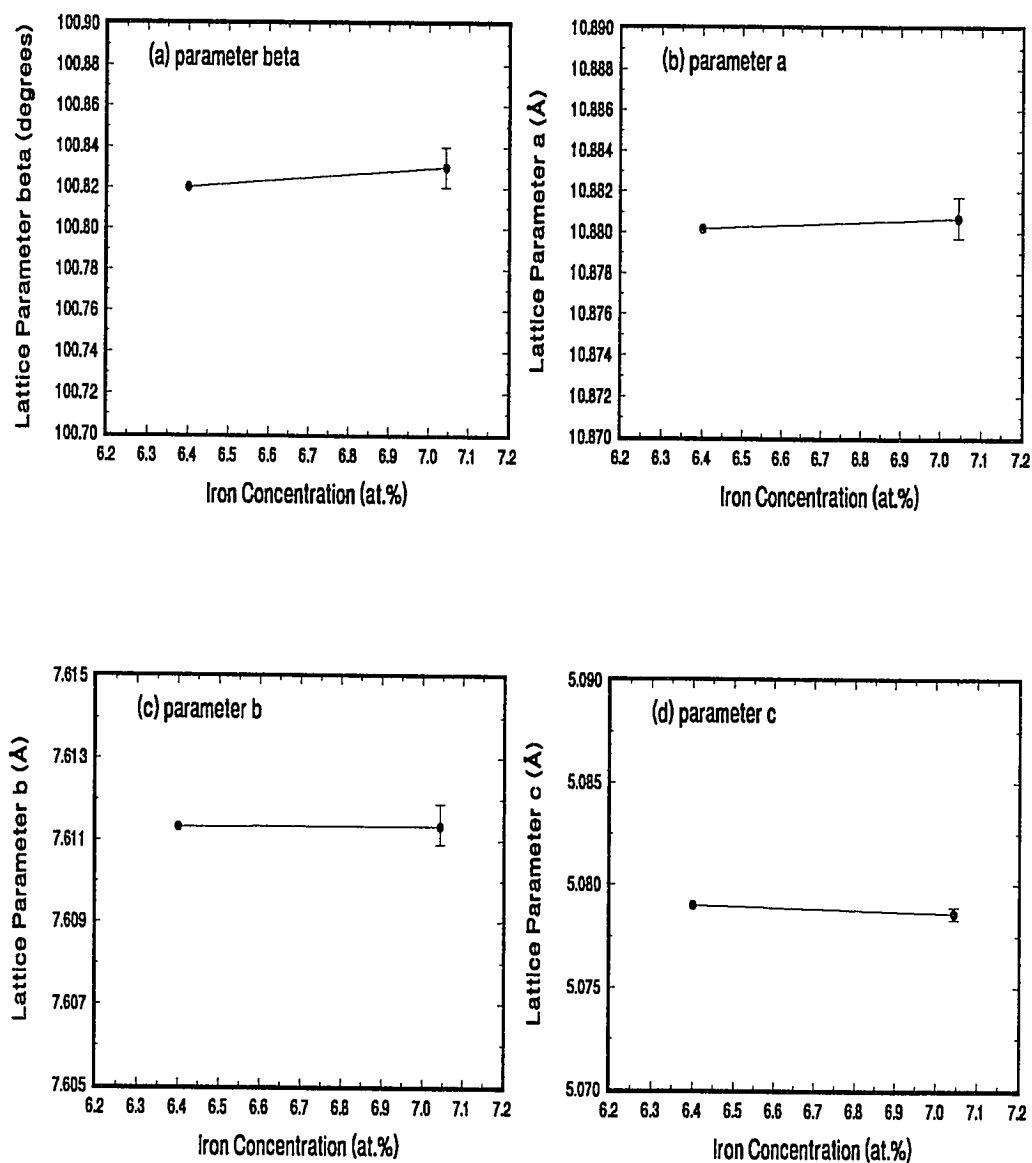


Figure 2.8. Zeta phase cell parameters (a) beta, (b) a spacing, (c) b spacing, and (d) c spacing as a function of iron concentration.

Delta Phase: A total of ten different samples were produced within the Delta phase. These samples spanned 6 different iron concentrations from 8.41 at.% to 13.01 at.% and were prepared at 3 different temperatures as shown in Figure 1.2. Figures 2.4 and 2.7 (b) show the typical XRD spectra of the Delta phase. It can be seen from the latter figure that the positions of the diffraction peaks change with iron concentration. As is observed by the large number of diffraction peaks, the Delta phase is perhaps the most complicated of the iron-zinc intermetallics. Therefore, careful analysis of these spectra was required in order to calculate the Miller indices for the peaks. The lattice parameters for the hexagonal phase were calculated using the following equation:

$$\frac{1}{d_{hkl}^2} = \frac{4}{3} \left(\frac{h^2 + hk + k^2}{a^2} \right) + \frac{l^2}{c^2}$$

The lattice parameters, a and c , as well as the Miller indices were treated as unknowns and were calculated from the recorded interplanar spacings. An iterative technique was used in order to index the peaks of the δ -phase spectra. The resultant Miller indices for a typical δ -phase XRD spectrum are shown in Table IX. The systematic absence of $h = k, l = \text{odd}$ reflections confirms the possible $P6_3mc$ or $P6_3/mmc$ space groups of the δ structure, as proposed by Bablik et al.⁷ Once indexed, the lattice parameters were calculated by least-squares fitting $\sin^2(\theta)/l^2$ versus $(h^2 + hk + k^2)/l^2$ and $\sin^2(\theta)/(h^2 + hk + k^2)$ versus $l^2/(h^2 + hk + k^2)$ as a means of minimizing error due to the determination of peak positions, and eliminating angle dependence from the calculation. In other words, if only a few select peaks were used

in calculating the lattice parameters, the uncertainty in the calculation would be much greater than by using a least-squares fitting technique. Figure 2.9 shows the observed relationships between the lattice parameters and the iron concentration, as well as the ratio, c/a , and the unit cell volume dependence on the iron concentration. The lattice parameters a and c both appear to decrease linearly and continuously with increasing iron content. This finding does not concur with Bastin et al.⁹ who reported a non-linear relationship between the lattice parameters and the iron concentration. Also, we report no change in the lattice parameters for samples having the same iron concentration but prepared at different temperatures.

It can be noted from Figure 2.9 (c) that the ratio of c/a is independent of iron concentration indicating that the contraction of the unit cell with increasing iron content is isotropic. That is, the unit cell at a particular iron concentration is the same shape as at any other iron concentration; hence, no distortion of the unit cell is observed. As a result, the cell volume decreases with increasing iron content.

Several publications have suggested the presence of two different Delta morphologies, compact (δ_k) and palisade (δ_p).^{24,27} Through careful analysis of the data, no discontinuity in the lattice parameters or cell volume across the phase is observed. Moreover, no change in crystal structure is apparent. In conclusion, the data agrees with the findings of Johansson et al.,²⁵ and Brandon et al.,²⁶ who determined the Delta phase to be a single morphology between the extreme iron limits. We find no crystallographic evidence of two separate phases, δ_k and δ_p , as has been reported.^{24,27}

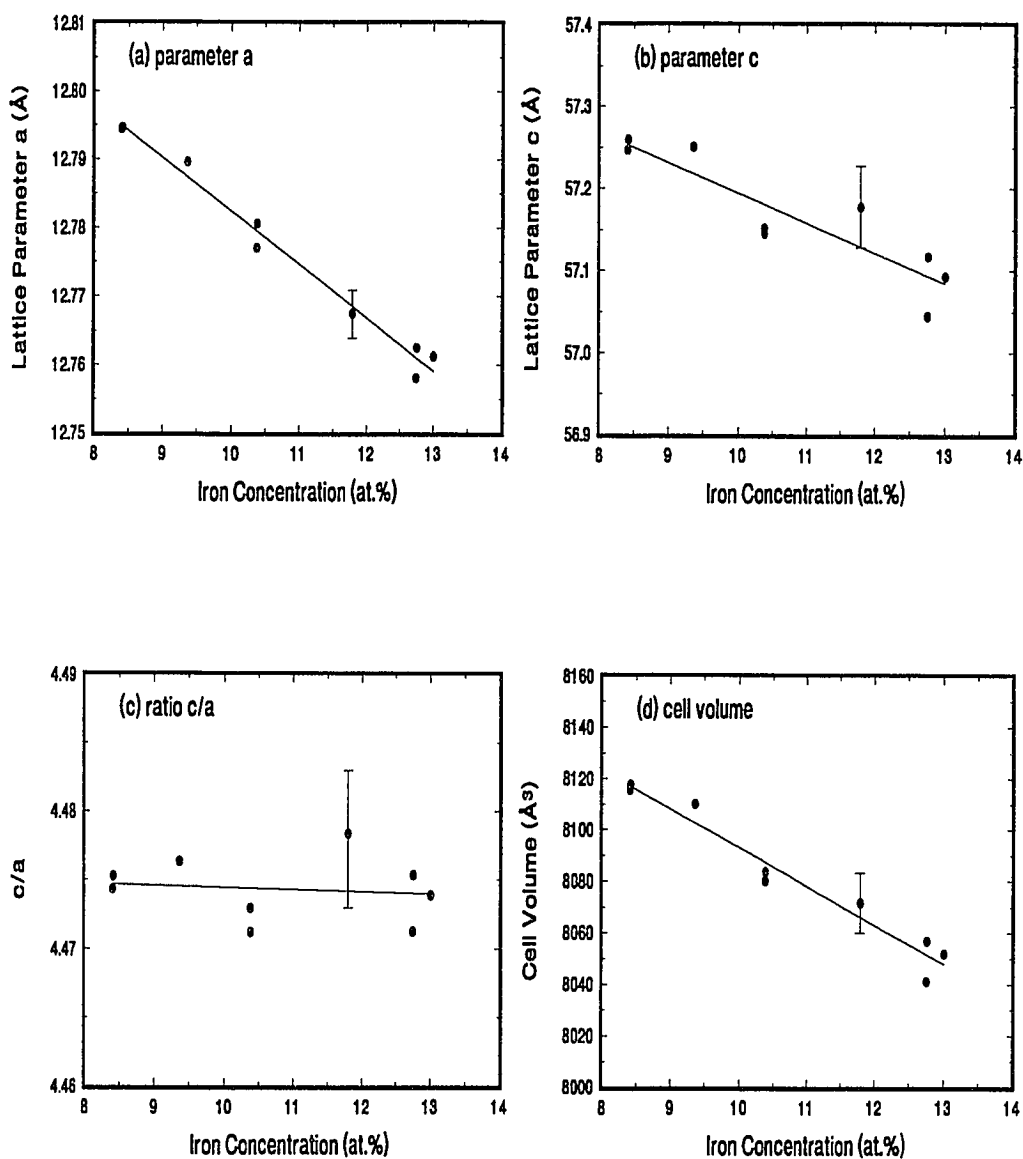


Figure 2.9. The change in the δ phase lattice parameters, (a) a spacing and (b) c spacing, as a function of iron concentration. (c) The ratio of the lattice parameters and (d) the volume of the unit cell. Solid lines are least squares fits to the data.

One sample in particular, FZ032G, did not form as expected. Although it was produced within the upper corner of the δ phase, as indicated on the phase diagram, Figure 1.2, it appears to have formed outside that region. The spectrum had peaks present which corresponded to the existence of the Γ phase in addition to the δ phase; i.e., the sample formed in the Γ - δ mixed phase region. Perhaps this indicates that pure phase formation near the phase boundary is difficult or that the phase diagram of Kubaschewski is not accurate in this region. Nonetheless, the sample produced a different XRD spectrum than expected, and therefore, was not used in determining the reported trends in the lattice parameters.

Gamma-1 Phase: Four samples having three different iron concentrations of 19.35 at.%, 20.44 at.% and 21.54 at.% were studied within the Γ_1 phase. Figures 2.5 and 2.7 (c) show the typical spectrum of the Γ_1 phase. The lattice parameter and Miller indices were calculated using the well known equation for the cubic structure:

$$\frac{1}{d_{hkl}^2} = \frac{h^2 + k^2 + l^2}{a^2}$$

The Miller indices were determined using the method of $\sin^2 \theta$ ratios.²⁸ Using Figure 2.5, it was possible to index more than 100 peaks ranging from 10° to 120° two-theta. These are documented in Table X. No systematic absence of reflections were observed, which supports the $F\bar{4}3m$ space group proposed by Koster and Schoone.¹¹ Although there appears to be a marginal increase in the lattice parameter as a function of iron concentration (Figure 2.10),

consideration of the error bars makes this observation questionable. In any event, there does not appear to be any significant changes in the lattice parameter across the Γ_1 phase. The phase has an fcc crystal structure with a lattice parameter of approximately 17.977 Å.

An attempt was made to investigate the uppermost corner of Γ_1 phase by producing sample FZ024J, (as shown in Figure 1.2). The chemical analysis confirmed the expected iron concentration for this sample. However, the XRD analysis of this sample showed the sample formed in a region outside the Γ_1 phase and contained a mixture of the δ and Γ_1 phases. Again, this may reflect the difficulty in producing samples close to the phase boundary or indicate an error in the phase diagram. Therefore, this sample was not used in determining the trends in the lattice parameter mentioned above.

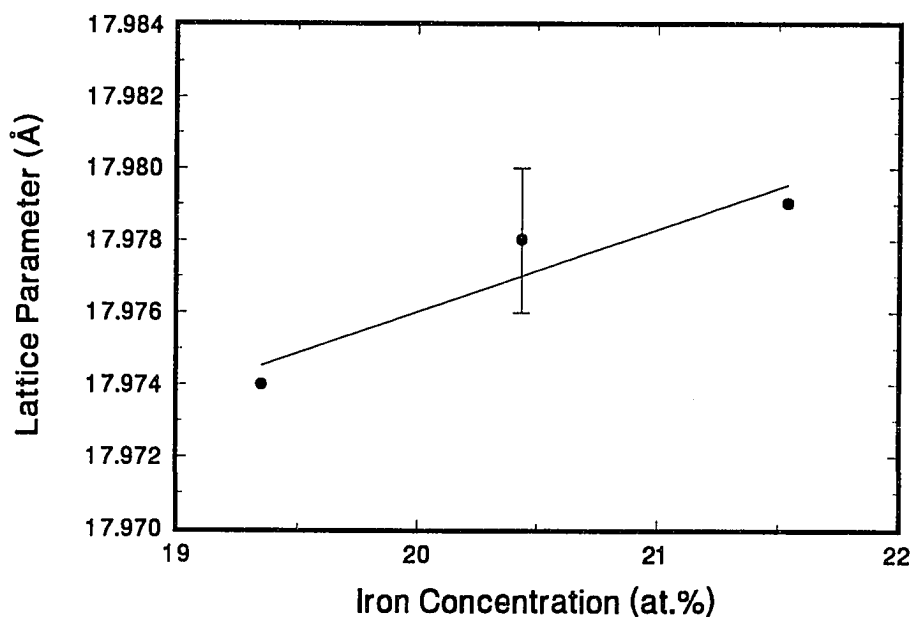


Figure 2.10. Lattice parameter of the Γ_1 structure as a function of the atomic percent iron. The solid line is a least-squares fit of the data.

Gamma Phase: The Gamma phase forms between the iron concentrations of 18 at.% - 31 at.%, (15.8 wt.% - 27.8 wt.%). Figures 2.6 and 2.7 (d) show the typical XRD spectra of the Gamma phase. As can be seen from Figure 2.7 (d), the diffraction lines shift to higher angles as the iron concentration increases from 21.77 at.% for sample FZ017D to 29.33 at.% for sample FZ031G. The Gamma phase has the largest iron concentration range of the four phases. Fourteen different samples were prepared covering 9 different iron concentrations and 3 different temperatures. The iron concentration ranged from 18.04 at.% to 30.24 at.% for samples sintered at 650 °C, thereby covering the full iron concentration possible for this phase. Furthermore, since part of the Gamma phase overlaps the Gamma-1 phase in iron concentration (see Figure 1.2), it was possible to produce Gamma samples with the same iron concentration as the Gamma-1 phase but at a different sintering temperature. The XRD spectra were analyzed using the same method as for the Γ_1 phase. Over 70 peaks were indexed from the angles 10° to 120° two-theta. The Miller indices, which are listed in Table XI, confirm that the phase is bcc. Figure 2.11 shows the lattice parameter as a function of iron concentration. It ranges from approximately 8.97 Å to 9.03 Å as the iron concentration decreases. The lattice parameter appears to vary linearly with iron content from 30.24 at.% down to 26.00 at.%. However, as the low iron concentration end of the Γ phase is approached, the lattice parameter converges toward a constant value of 9.024 Å. It should be noted, that the value of 9.024 Å for the lattice parameter is nearly half the lattice spacing of the Gamma-1 phase. This concurs with the structural information for the Gamma-1 phase described in section 2.1.2. That is, if eight cells of the Gamma structure were stacked together and the lattice spacing doubled, then a large Gamma-1 cell would be formed. The

resulting X-ray diffraction peaks from the Gamma phase directly align with peaks from the Gamma-1 spectrum.

Samples were prepared at the sintering temperatures of 450 °C, 650 °C, 665 °C, and 770 °C in order to investigate a possible temperature dependence of the crystal structure. As illustrated in Figure 2.12, there is no apparent difference in the crystal structures of samples formed at different temperatures within the Γ phase. The lattice parameter of the three samples were nearly identical, thereby demonstrating that the lattice parameters are independent of sintering temperature. One sample produced at the uppermost point of the phase, FZ035J, was pure Γ phase, indicative of a well defined region within the phase diagram.

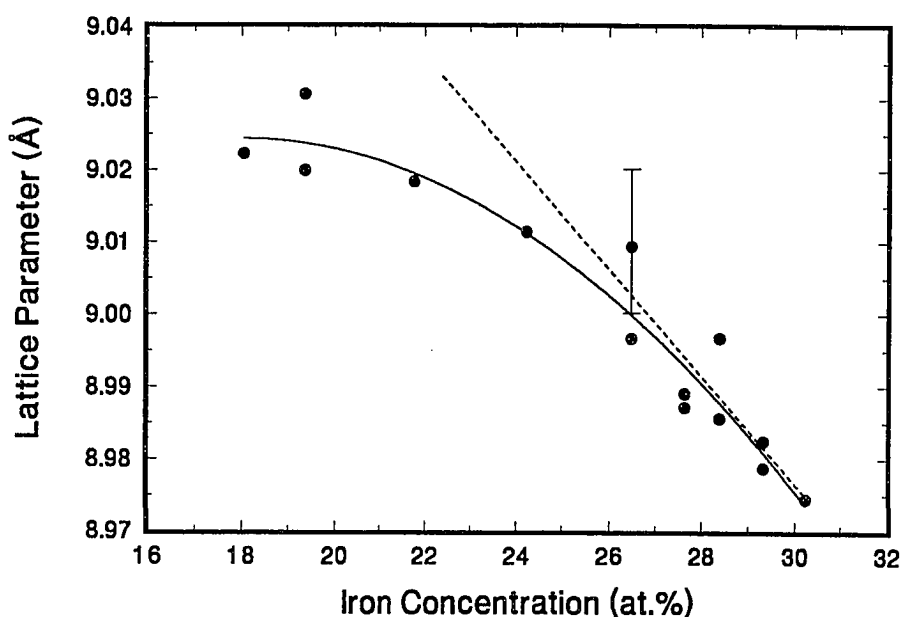


Figure 2.11. Lattice parameter of the Γ structure as a function of the atomic percent iron. The solid line is a 2nd-order least-squares fit to the data. The dotted line indicates the linearity of the data at high iron concentrations.

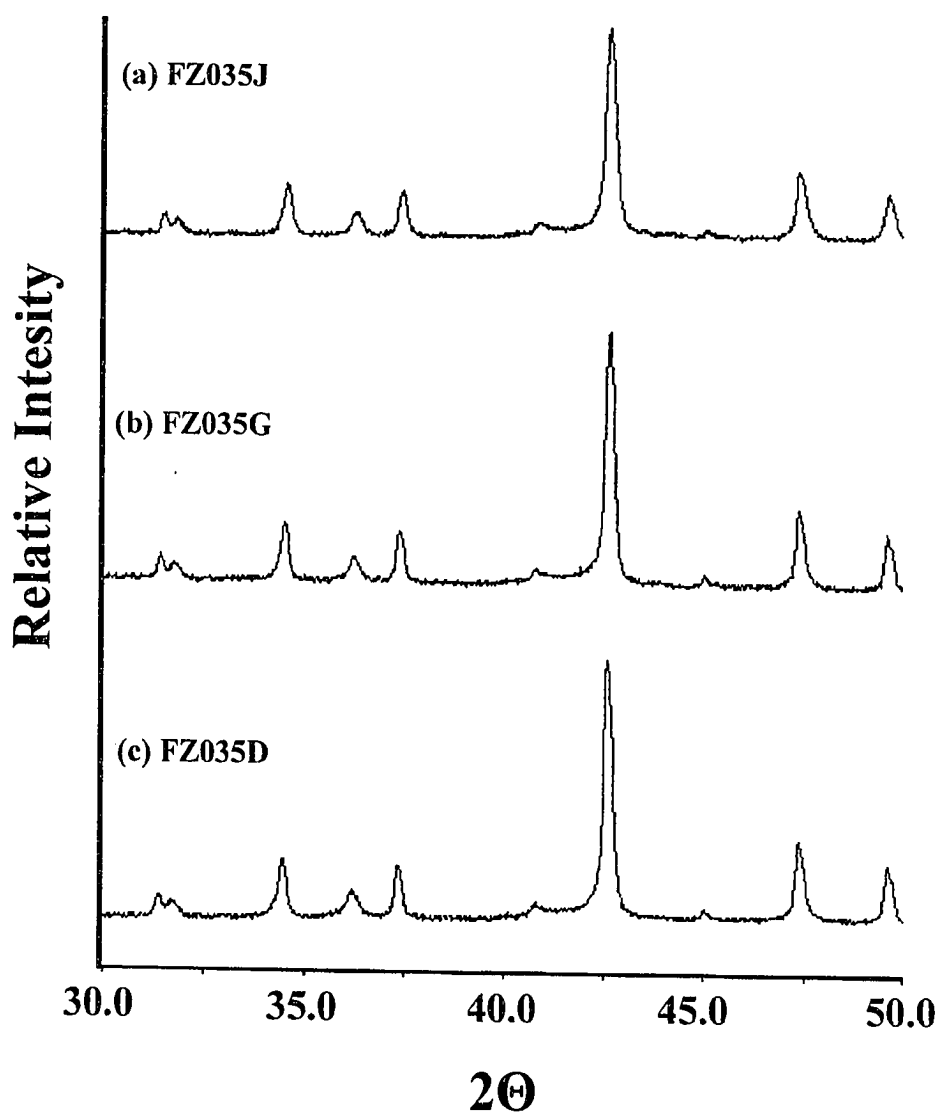


Figure 2.12. XRD spectra of three Γ samples, (a) FZ035J, (b) FZ035G and (c) FZ035D. All three contain 7.63 at.% Fe, but were sintered at 770°C, 650°C and 450°C respectively.

2.1.4 Analysis of Mixed Phase Regions

Several samples were prepared between the main iron-zinc phases in mixed phase regions of the phase diagram. This was performed in order to determine their characteristics so that their possible presence in commercial galvanneal coatings could be identified. Five samples, FZ017F, FZ016N, FZ028K, FZ027K, and FZ026K as listed in Figure 1.2, were produced in the Γ - δ region of the phase diagram. Figure 2.13 shows the XRD spectra of samples FZ017F, FZ016N and FZ027K between the angles of 40° and 45° two-theta. It is evident that sample FZ017F is predominantly Γ and as the iron concentration decreases, the percentage of δ present in the sample increases.

Sample FZ018I was prepared at 450 °C in the Γ - Γ_1 region of the phase diagram. The XRD analysis indicates the presence of the Γ_1 phase. As discussed earlier, since the fcc crystal structure of the Gamma-1 phase is nearly twice that of the bcc structure of the Gamma phase, all of the Γ peaks are also present in the Γ_1 spectrum. Hence, it is impossible to tell whether or not Γ exists in sample FZ018I purely on the basis of XRD peak positions. It may be possible to compare the relative peak intensities of a purely Γ_1 reflection to those of a Γ_1 + Γ reflection. Also, it is possible to investigate this region using the Mössbauer effect as will be discussed in a later section.

Samples produced in the Γ_1 - δ region of the phase diagram provided some interesting results. Three samples, FZ028H, FZ027H and FZ026H, ranging in iron concentration from 18.04 at.% to 13.52 at.% were produced in this mixed region at 450 °C. Until now, one problem has been to distinguish between the Γ_1 and δ phases using XRD. As demonstrated in the previous section, it is possible to examine the XRD spectra from 40° to

45° two-theta and differentiate between the Γ_1 and δ phases. Figure 2.14 compares the XRD spectra of the three samples. The change in the peak intensity at approximately 41.2°, demonstrates that the relative concentrations of each phase change proportionally as one moves from the Γ_1 to the δ phase. Recall, the spectral peak positions of the Delta phase change as a function of iron concentration (see section 2.1.3). Therefore, by comparing the positions of the Delta peaks in these mixed phase samples with those of the pure Delta samples, it is evident that the stoichiometry nearest this mixed phase domain is present in these samples. That is, the peak positions of the Delta phase found in these mixed phase samples is a high iron concentration Delta as indicated by the positions of the diffraction peaks.

2.1.5 Summary of XRD Analysis

An important outcome of this research is the development of a method which permits identification of the Γ_1 and δ phases through the use of XRD techniques. The ζ and Γ phases are easily identified because they produce distinctive XRD spectra which contain well resolved diffraction peaks. However, at the present time no report has been published discussing the difference between the δ and Γ_1 structures using XRD spectroscopy. Nevertheless, there are differences in the spectra which may prove useful for phase identification within galvanneal coatings. Figure 2.15 shows overlapped XRD spectra of the Delta and Gamma-1 phases plotted over the narrow range of 40° - 45° two-theta. The peak located at approximately 41.4° is unique to the Γ_1 spectrum while the peak located at approximately 43.1° is unique to the δ spectrum. Through analysis of the XRD spectra of

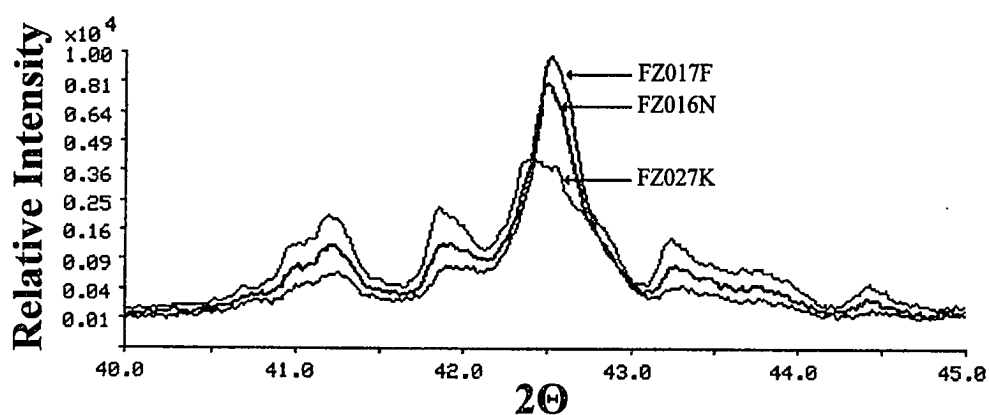


Figure 2.13. Overlap of the XRD spectra for samples prepared in the Γ - δ mixed phase region of the phase diagram. Sample FZ017F, FZ016N, and FZ027K have 21.77 at.% Fe, 19.36 at.% Fe, and 15.01 at.% Fe, respectively.

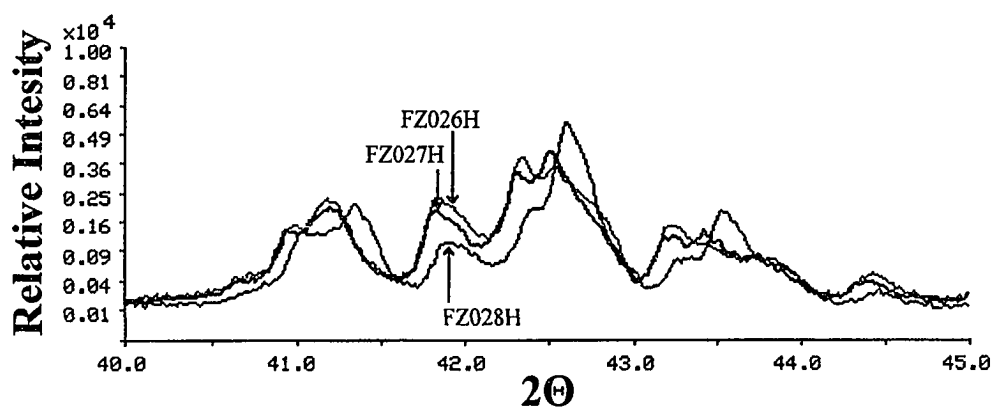


Figure 2.14. Overlap of the XRD spectra for samples prepared in the Γ_1 - δ mixed phase region of the phase diagram. Sample FZ028H, FZ027H, and FZ026H have 18.04 at.% Fe, 15.01 at.% Fe, and 13.52 at.% Fe, respectively.

galvanneal coatings in these specific regions, it is possible to identify the presence of these two phases. It should be noted that the existence of the Γ and ζ phases in the coatings would further complicate the spectra and make phase identification difficult.

Another point of interest is the ability of XRD spectroscopy to monitor the growth of the δ phase and the disappearance of the ζ phase as a function of sintering time. Figure 2.16 shows the XRD spectra of the same pressed powder sample at various times in the annealing process. The peak located at 41.5° two-theta denotes the existence of ζ in the sample. As the annealing process continues, the intensity of this peak decreases until the spectra shows that a pure δ phase has been reached. Such capability of monitoring the evolution of phase formation may lead to a better understanding and control of the phases formed in steel coatings.

Another difficulty in phase identification arises when both the Γ and Γ_1 phases are present in a sample. As is shown in Figure 2.17, all of the Γ peaks overlap with Γ_1 peaks. This is simply due to the fact that the same lattice spacings are produced in a fcc structure by doubling the lattice parameter and Miller indices of a bcc structure, as illustrated in the following equation:

$$\frac{(2h)^2 + (2k)^2 + (2l)^2}{(2a)^2} = \frac{1}{d_{h'k'l'}^2} = \frac{1}{d_{hkl}^2} = \frac{h^2 + k^2 + l^2}{a^2}$$

$$\text{where: } h' = 2h, k' = 2k, l' = 2l$$

The condition for allowed reflections from a fcc structure is satisfied, $h, k, l = \text{all odd or all even}$

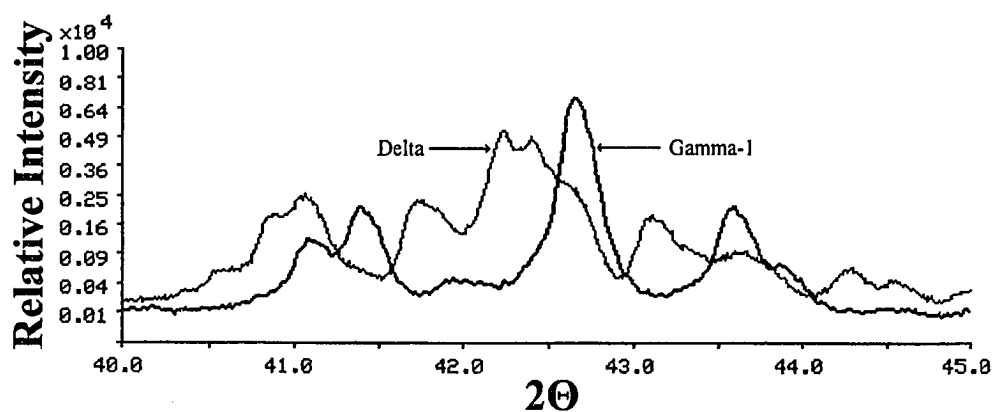


Figure 2.15. Overlap of the XRD spectra of samples FZ034F, (δ), and FZ025G, (Γ_1), between 40° and 45° two-theta, illustrating the differences in peak positions.

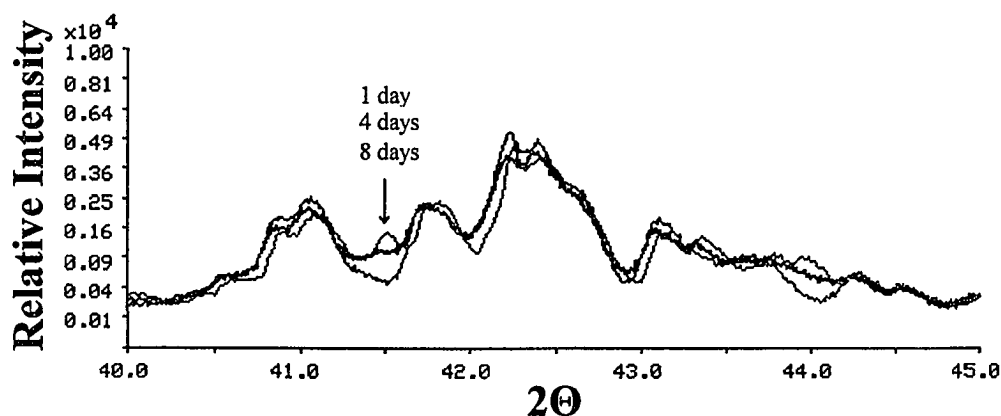


Figure 2.16. Overlap of the XRD spectra of a samples FZ034F, (δ), at different times during the sintering process. The disappearance of the peak at 41.5° indicates the suppression of the ζ phase and the formation of the δ phase.

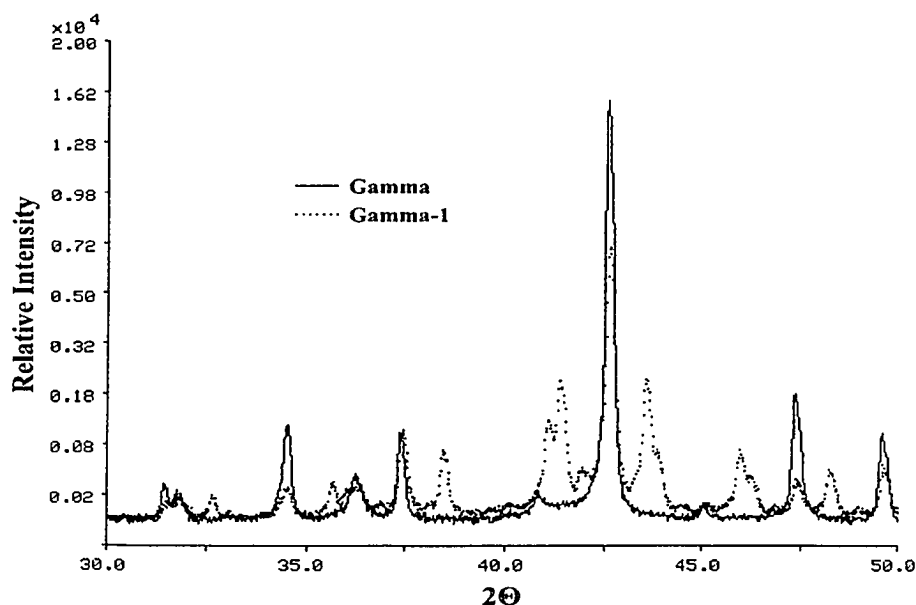


Figure 2.17. Overlap of the XRD spectra of a samples FZ035D, (Γ), and FZ025G, (Γ_1), between 10° and 120° two-theta, showing the overlap of the peak positions.

even by doubling the Miller indices of a bcc structure. Therefore, it is not possible to identify the presence of Γ in a sample containing both Γ and Γ_1 , based solely on peak location. It is unfortunate that for samples prepared within the Γ and Γ_1 phases, the experimentally measured lattice parameter for the Γ_1 phase almost double that for the Γ phase. Therefore, separate identification of the two phases present in the same coating or sample must be made by comparing the relative intensities of Γ_1 peaks to $\Gamma_1 + \Gamma$ peaks. Thus it is possible to determine the relative concentrations of each phase present within a sample.

Finally, samples produced in the "corners" of the Delta and Gamma-1 phases were analyzed; we found that these samples were not pure but contained mixtures of more than one phase. It is possible that the phase boundaries specified by Kubaschewski¹ are not as accurately defined as believed. A recently published update to the iron-zinc phase diagram²⁹

shows that several of the boundaries have been repositioned slightly. This could possibly place the samples closer to the mixed phase regions and explain the observed mixed phase.

2.2 Mössbauer Effect Analysis

Research performed over the past several years has involved the Mössbauer Effect study of commercially produced galvanneal coatings and the four iron-zinc intermetallics. Although Mössbauer spectroscopy can uniquely identify the four main iron-zinc phases, it was recognized that a more detailed study of the pure phases was needed to study commercially produced galvanneal coatings using Mössbauer spectroscopy. The results of this analysis are now presented. In several cases the conclusions of this analysis are slightly different from the previous study of the four iron-zinc phases.¹⁴ This deviation can be explained by the higher quality of the samples prepared for this research, as well as better resolved spectra than previously reported.

2.2.1 Experimental Technique

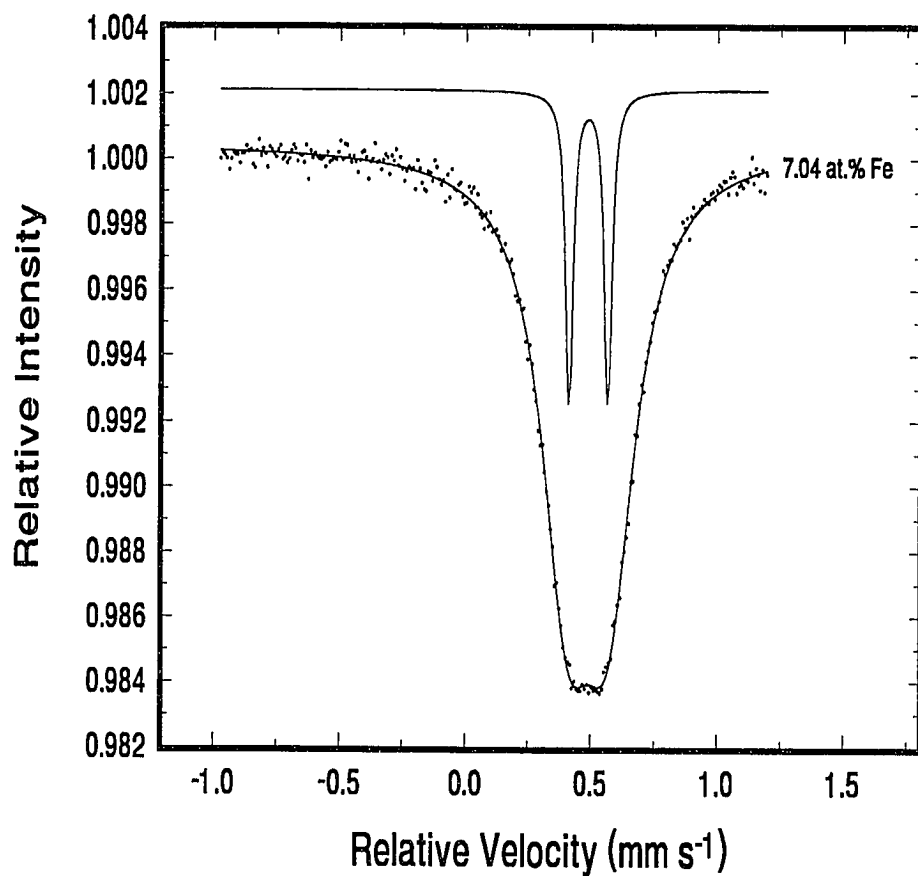
The Mössbauer spectra of the iron-zinc intermetallics (listed in Figure 1.2) were recorded at 300 K using standard Mössbauer equipment. Transmission geometry was employed to study the powders obtained through crushing and annealing of the alloyed pellets. Thirty to fifty milligrams of a sample was mixed with approximately 5mg of boron nitride and pressed into a thin wafer 1cm in diameter. This was then loaded into a standard holder and installed into the Mössbauer apparatus. A 50 mCi, ⁵⁷Co in a rhodium matrix,

source was used for all experiments. Most spectra were recorded over a velocity range of $\pm 1.2 \text{ mm s}^{-1}$. Data collection times ranged from two days to two weeks depending on the iron concentration of the sample and the desired spectral resolution. The spectra were analyzed using an IBM3090 computer with fitting routines written by Dr. Desmond C. Cook.³⁰ All isomer shifts are referenced to $\alpha\text{-Fe}$ at 300 K.

2.2.2 Mössbauer Parameters of the Four Phases

Zeta Phase: The Mössbauer spectrum of a general Zeta phase intermetallic is shown in Figure 2.18. It has a very small quadrupole split doublet, indicating that the iron is present in only one environment which crystallographically is nearly cubic. The fit parameters, shown listed with Figure 2.18, are identical to those found in earlier studies.¹⁴ As was reported earlier, we still observe a narrow linewidth for the spectrum of the Zeta phase. It remains unclear as to the reason for this phenomenon which is unusual for alloys. It is possibly related to the fact that the Zeta phase exists only over a very narrow range of iron concentration, and therefore, the samples are extremely pure and homogeneous.

Samples were produced at two different iron concentrations, 6.40 at.% and 7.04 at.%, within the Zeta phase. Their Mössbauer spectra are shown in Figure 2.19. As was the case for the XRD spectra, both Mössbauer spectra are identical, probably due to the limited iron concentration range for this phase. Also, the Mössbauer spectra for samples FZ007C and FZ007F, produced with an iron concentration of 7.04 at.% and at temperatures of 480 °C and 450 °C respectively, were identical indicating that there is no dependence of the ζ structure on sample annealing temperature over this small range.



Isomer Shift (mm s ⁻¹)	Quadrupole Splitting (mm s ⁻¹)	Linewidth (mm s ⁻¹)	Relative Area (%)
0.489	0.153	0.244	100.0

Figure 2.18. Mössbauer spectrum and corresponding parameters of the ζ sample FZ007F.

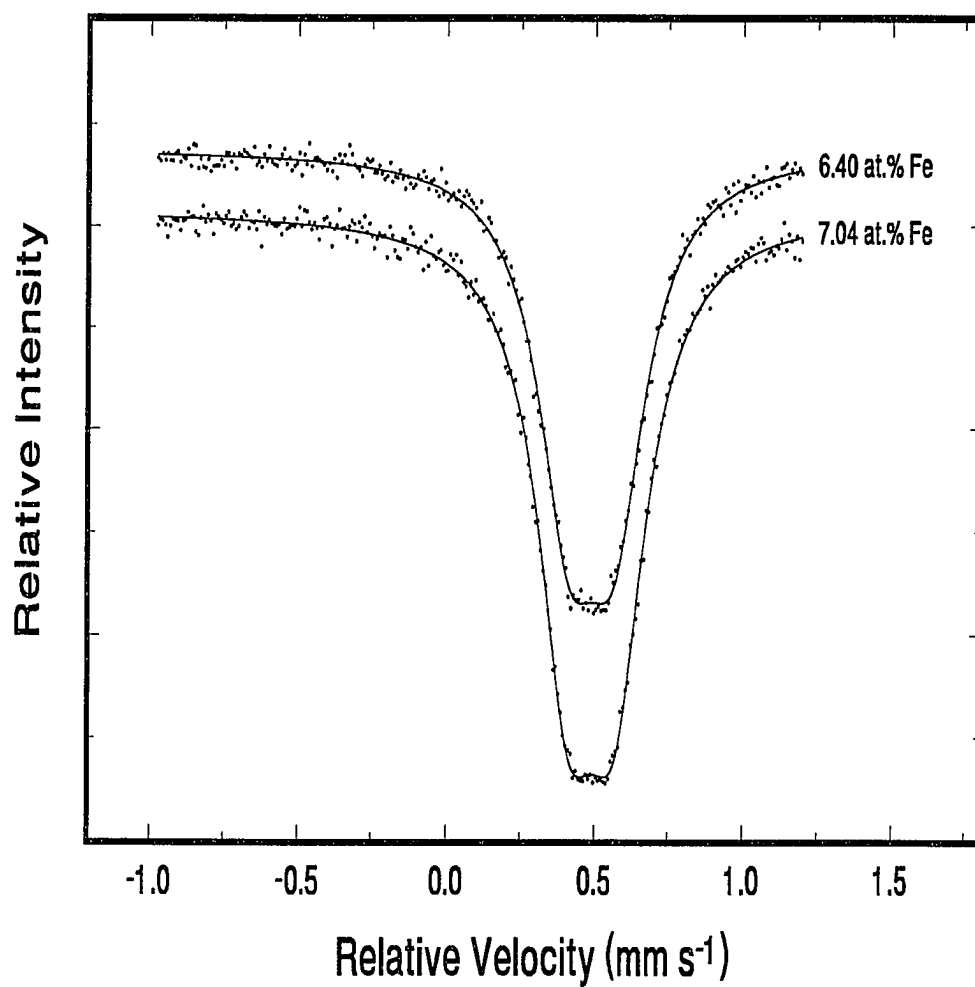
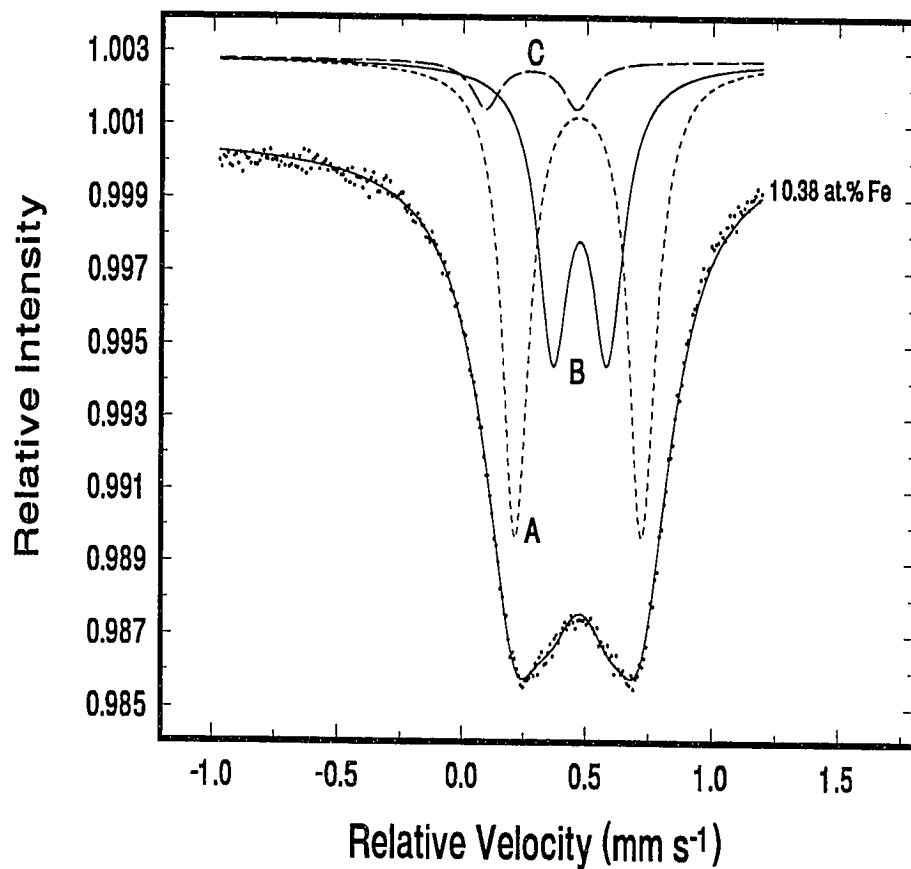


Figure 2.19. Overlap of the Mössbauer spectra for different samples produced within the ζ phase. No changes in the spectra as a function of iron concentration are observed.

Delta Phase: A total of nine samples at six different iron concentrations were analyzed within the Delta phase. By fitting the spectra in a consistent manner, we were able to determine there were three distinct iron sites, A, B, and C. The Mössbauer spectrum of a typical Delta phase is shown in Figure 2.20 along with the general fit parameters. This differs from the previous findings for both coatings and "standard" phases in which only one,¹² or two^{14,31} iron sites were reported. Each iron site is purely quadrupole split.

The Mössbauer spectra of the 6 samples produced within the δ phase at varying iron concentrations, between 8.41 at.% and 13.01 at.%, are shown in Figure 2.21. Clearly, there are significant changes in the spectra as the iron concentration is varied. Analysis of the Mössbauer spectra indicates the presence of three iron sites in all samples although one site is only marginally populated with iron at the lower concentrations. These spectra are very similar to the many galvanneal coatings which were reported in an earlier study.³¹ Figures 2.22 (a), (b), and (c) show the variation in isomer shift, quadrupole splitting, and relative area of the three sites as a function of total iron concentration. As indicated, the isomer shifts of all three sites decrease gradually, but continuously, with increasing iron content.

The isomer shifts of the A and B sites are nearly identical. Furthermore, the quadrupole splittings of the A and B sites increase only marginally, in contrast with the rapid rise at site C as iron concentration increases. This indicates that the crystal symmetry of the A and B sites remains relatively constant across the Delta phase, but that of site C changes continuously. This is supported by the XRD data which indicates a uniform expansion of the hexagonal lattice with decreasing iron concentration. Of particular interest is the change in relative area of the three subspectra. Assuming the recoilless fraction of each iron site is the



	Isomer Shift (mm s ⁻¹)	Quadrupole Splitting (mm s ⁻¹)	Linewidth (mm s ⁻¹)	Relative Area (%)
Site A	0.468	0.508	0.275	57.7
Site B	0.474	0.216	0.295	37.6
Site C	0.275	0.372	0.285	5.7

Figure 2.20. Mössbauer spectrum and corresponding parameters of the δ sample FZ033D.

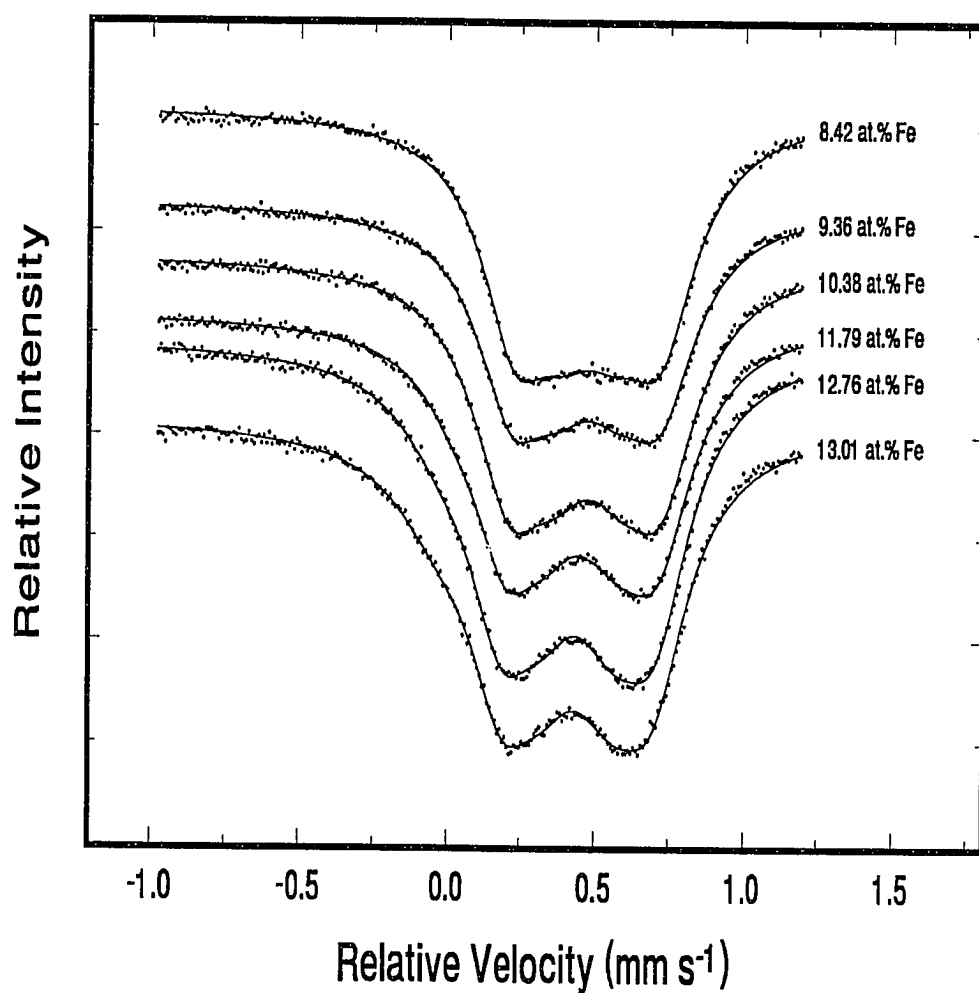


Figure 2.21. Overlap of the Mössbauer spectra for different samples produced within the δ phase. Note the significant changes in the spectra as a function of iron concentration.

same, the subspectral relative areas are direct measures of the site occupation by iron. Therefore, it would appear that the occupancies by iron of the two main sites, A and B, decrease while the occupancy of the C site increases with an increase in iron concentration. However, as indicated in Figure 2.22 (d), the ratio of the site occupancies of the two most populated iron sites (RA_A/RA_B =relative areas of A/B), remains constant at approximately 6:4. This indicates that as one moves from the low iron concentration end to the high iron concentration end of the δ phase, the iron preferentially enters the C site. Thus, sites A and B remain close to their initial occupancies. Perhaps the constant 6:4 ratio is suggestive of the octahedral and tetrahedral symmetries observed in the Γ structure, as will be discussed later in this section.

It should be noted that in the previous studies of the Delta phase, and of galvanneal coatings which contained a significant amount of the Delta phase, performed at Old Dominion University^{14,31} it was believed that only two sites were present and that only their relative population by iron was changing not the Mössbauer parameters. It is now apparent that the observed changes in the Delta phase of different galvanneal coatings is due to the population of a third iron site at high iron concentration, as well as changes in the Mössbauer parameters. This explains why it was believed that some of the Gamma-1 phase was present in several of the coatings even though the detected radiation has since been determined not to have probed to this layer of the coating³². What was originally believed to be Gamma-1 phase in some of the coatings could very well have been the third Delta site.

Analysis of the Mössbauer spectra of the Delta phase has not revealed any information concerning the formation of the compact (δ_c) and palisade (δ_p) morphologies,

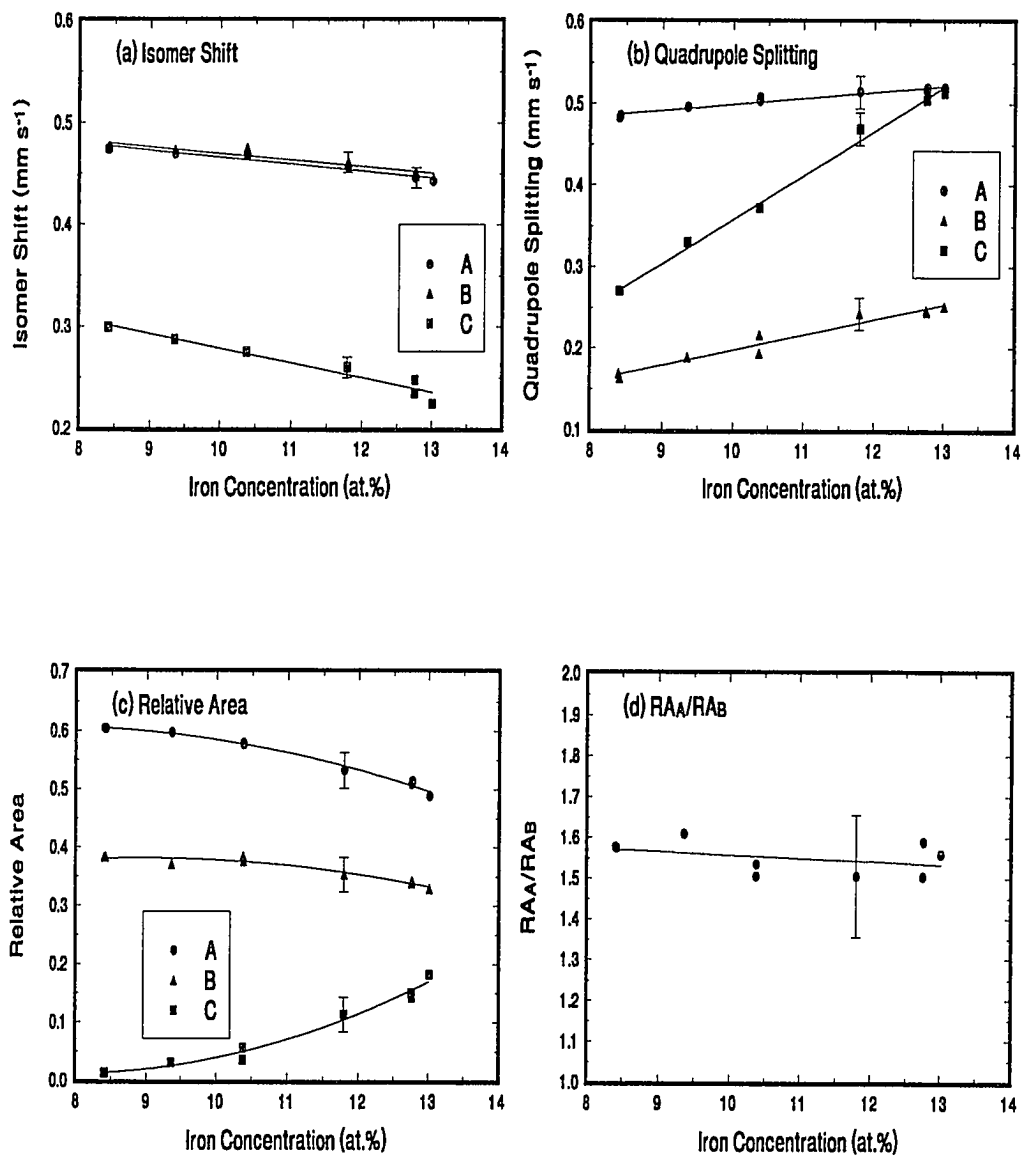
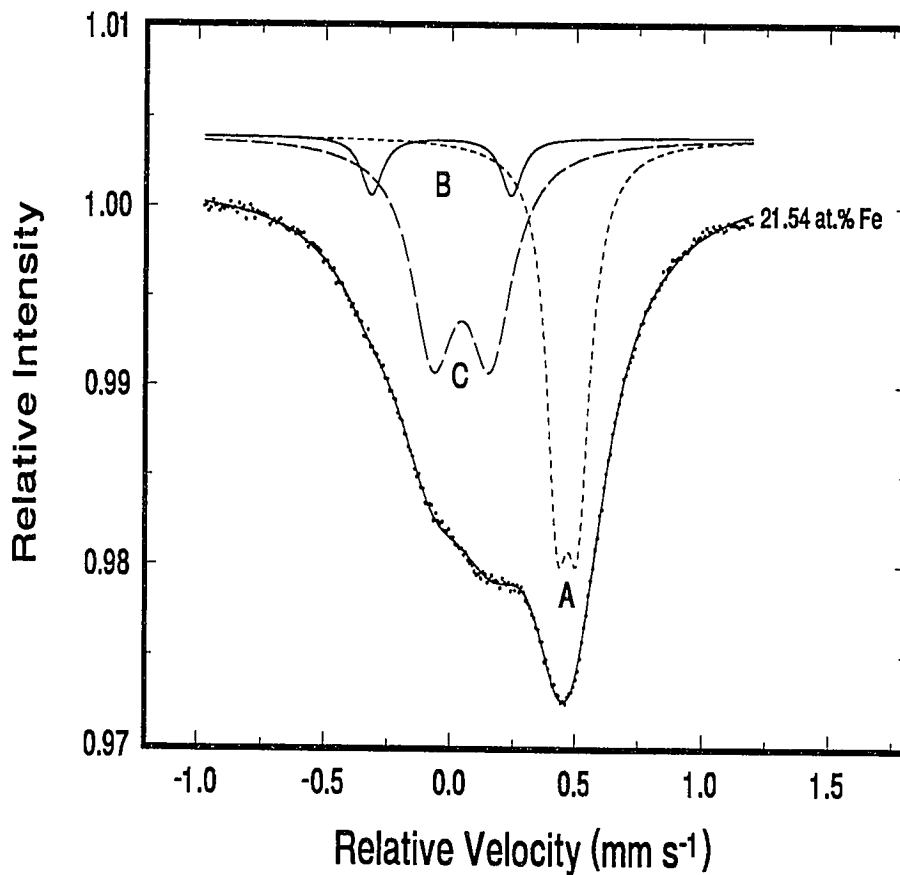


Figure 2.22. Mössbauer parameters for the δ phase showing (a) isomer shift, (b) quadrupole splitting, (c) relative area, and (d) the relative area ratio for the A and B sites, RA_A/RA_B , as a function of iron concentration.

as has been previously reported.^{33,34} As observed with the lattice parameters, no discontinuous changes in the Mössbauer parameters are observed as iron concentration is varied.

Gamma-1 Phase: Figure 2.23 shows the Mössbauer spectrum of a typical sample within the Γ_1 phase. The spectrum is slightly different to those we¹⁴ and others¹² previously reported, due primarily to the fact that this sample does not contain mixtures of the δ and Γ phases. Spectral analysis still shows the presence of three iron sites, A, B and C. The general fit parameters for these three sites are listed with Figure 2.23. The isomer shift and quadrupole splitting are significantly different for each site, indicative of very different electronic and crystalline environments. The Mössbauer spectra of three samples produced within the Γ_1 phase between iron concentrations of 19.35 and 21.54 at.% are shown in Figure 2.24. The spectra only show moderate changes with iron concentration. This is in accordance with the XRD spectra in which there is only a very small change in lattice parameter with iron concentration. The variations of the Mössbauer parameters for the Γ_1 phase are shown in Figure 2.25. The quadrupole splittings and isomer shifts of the three iron sites remain nearly constant while their populations vary continuously over a small range across the phase as iron concentration increases. This is not unexpected since the atomic concentration in the fcc unit cell of this phase is significantly less than in the other phases. That is, the substitution of iron into the three sites does not change the crystal, and therefore, electronic symmetry to any measurable amount due to the fact that the nearest neighbor atomic distances are large.



	Isomer Shift (mm s ⁻¹)	Quadrupole Splitting (mm s ⁻¹)	Linewidth (mm s ⁻¹)	Relative Area (%)
Site A	0.470	0.079	0.298	46.0
Site B	-0.042	0.555	0.294	6.2
Site C	0.042	0.224	0.394	47.8

Figure 2.23. Mössbauer spectrum and corresponding parameters of the Γ_1 sample FZ025G.

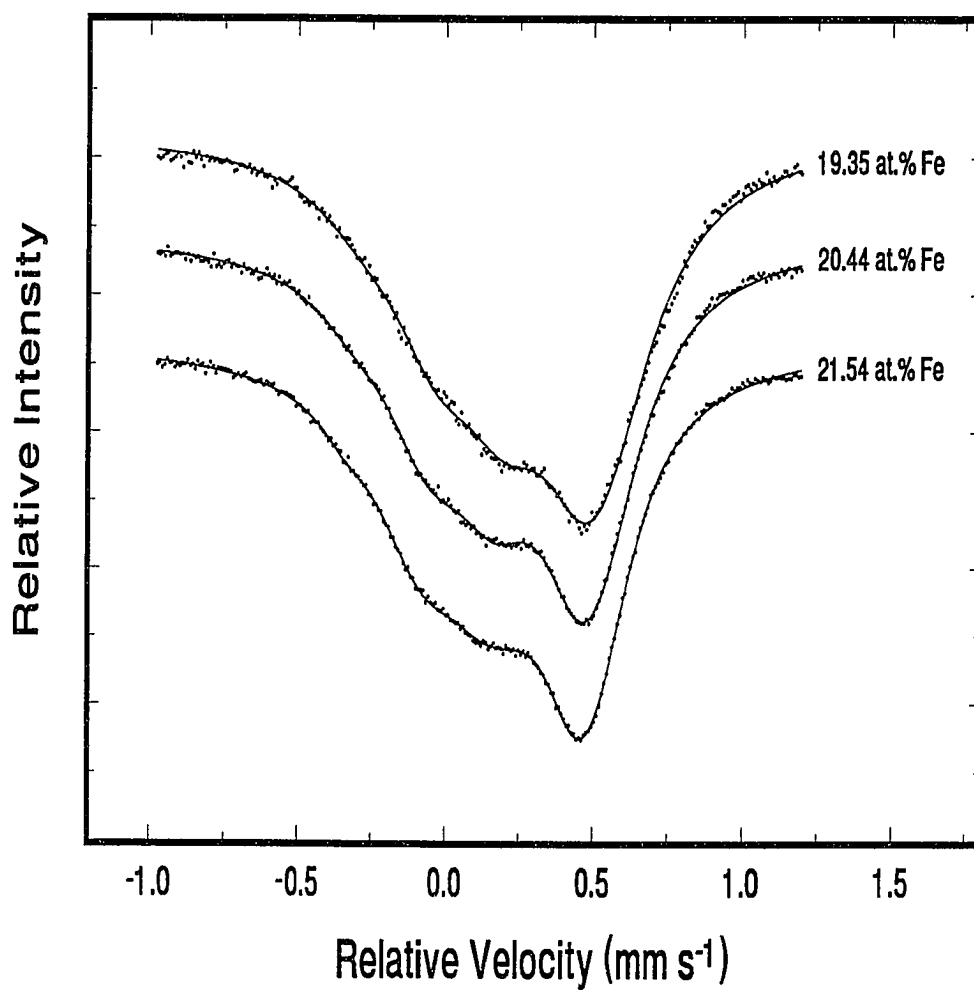


Figure 2.24. Overlap of the Mössbauer spectra for different samples produced within the Γ_1 phase. Note the marginal changes in the spectra as a function of iron concentration.

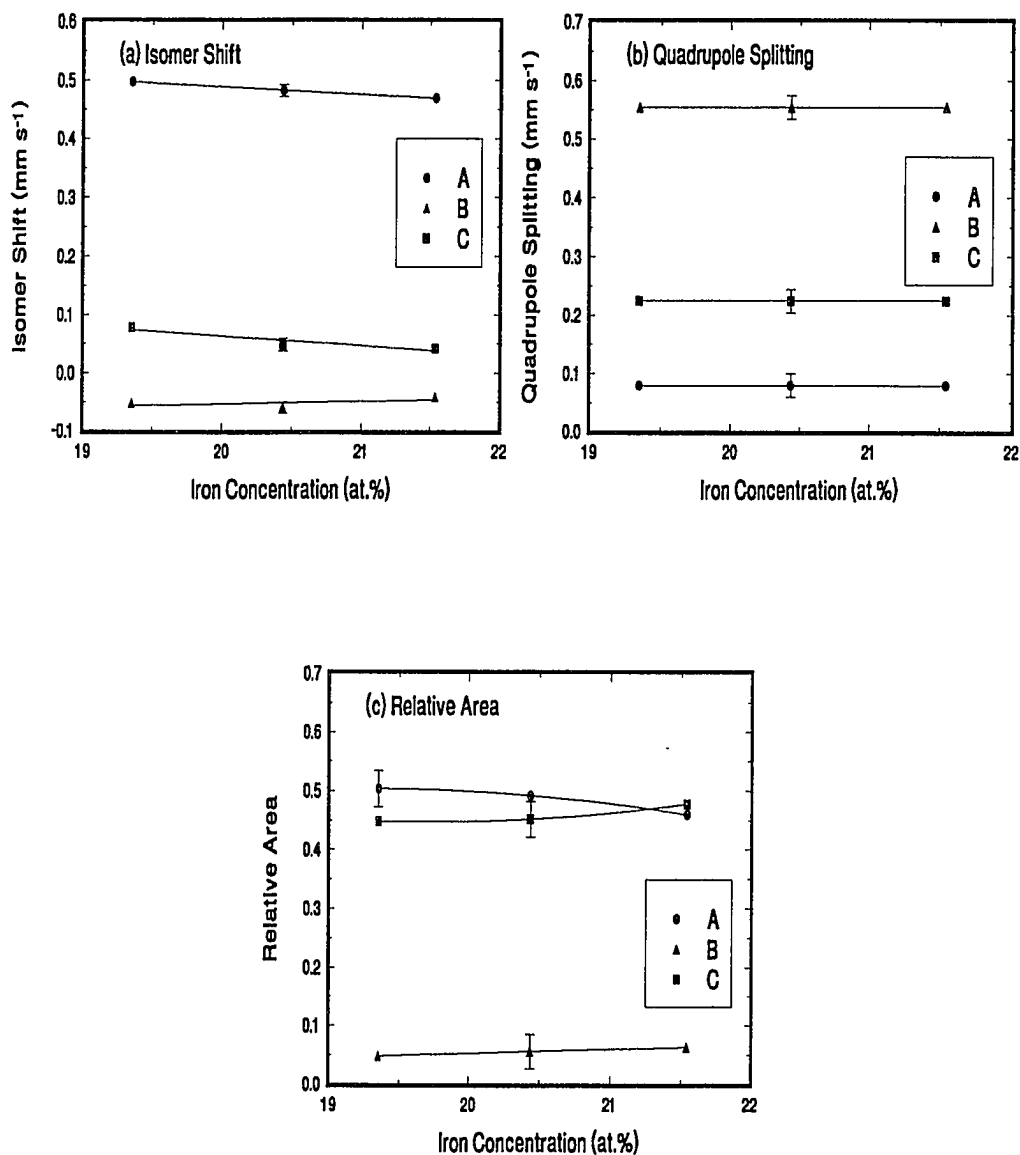
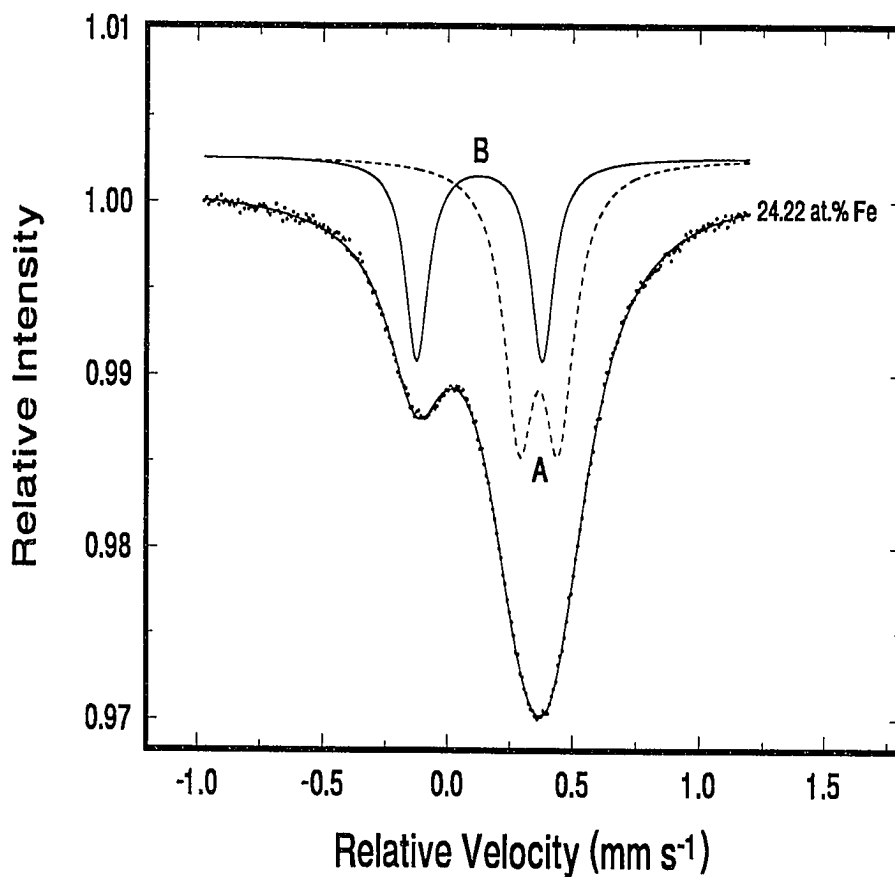


Figure 2.25. Mössbauer parameters, (a) isomer shift, (b) quadrupole splitting, and (c) relative area as a function of iron concentration for the Γ_1 phase. Solid lines are least-squares fits to the data.

Gamma Phase: A great deal of our initial research was performed on the Gamma phase since it contains the highest and spans the largest range, of iron concentration. Figure 2.26 shows a typical Mössbauer spectrum of the Gamma phase. The crystal structure described earlier in section 2.2.2 indicates four possible atomic sites which iron could potentially occupy. However, we have now established from the Mössbauer analysis that only two of these four sites, A and B, are occupied by iron atoms. The Mössbauer parameters are listed with Figure 2.26. The observation of only two iron sites and the values obtained for the fit parameters concurs with our previous studies.¹⁴

Eight Mössbauer spectra were recorded between the iron concentrations of 19.36 at.% and 30.24 at.%. These are shown in Figure 2.27. There are significant changes in the spectra as a function of iron concentration. Specifically, the main peak shifts left as the iron concentration increases. This shift is illustrated by comparing the main peak position relative to the vertical dotted line in Figure 2.27. Figures 2.28 (a), (b), and (c) show the changes in the Mössbauer parameters as a function of iron concentration for the two iron sites. The quadrupole splitting of site A exhibits a small decrease with increasing iron concentration indicating a marginal improvement in the cubic symmetry at the iron sites. The isomer shifts of both sites decrease continuously with increasing iron concentration. This represents an increase in the conduction electron concentration as iron concentration increases. Significant changes can also be observed in the relative areas of the two iron sites as iron content is varied. A 6:4 ratio of the relative areas, and thus the site occupancies, is found as one approaches the high iron concentration end of the Γ phase.



	Isomer Shift (mm s ⁻¹)	Quadrupole Splitting (mm s ⁻¹)	Linewidth (mm s ⁻¹)	Relative Area (%)
Site A	0.365	0.140	0.285	65.4
Site B	0.129	0.506	0.285	34.6

Figure 2.26. Mössbauer spectrum and corresponding parameters of the Γ sample FZ018D.

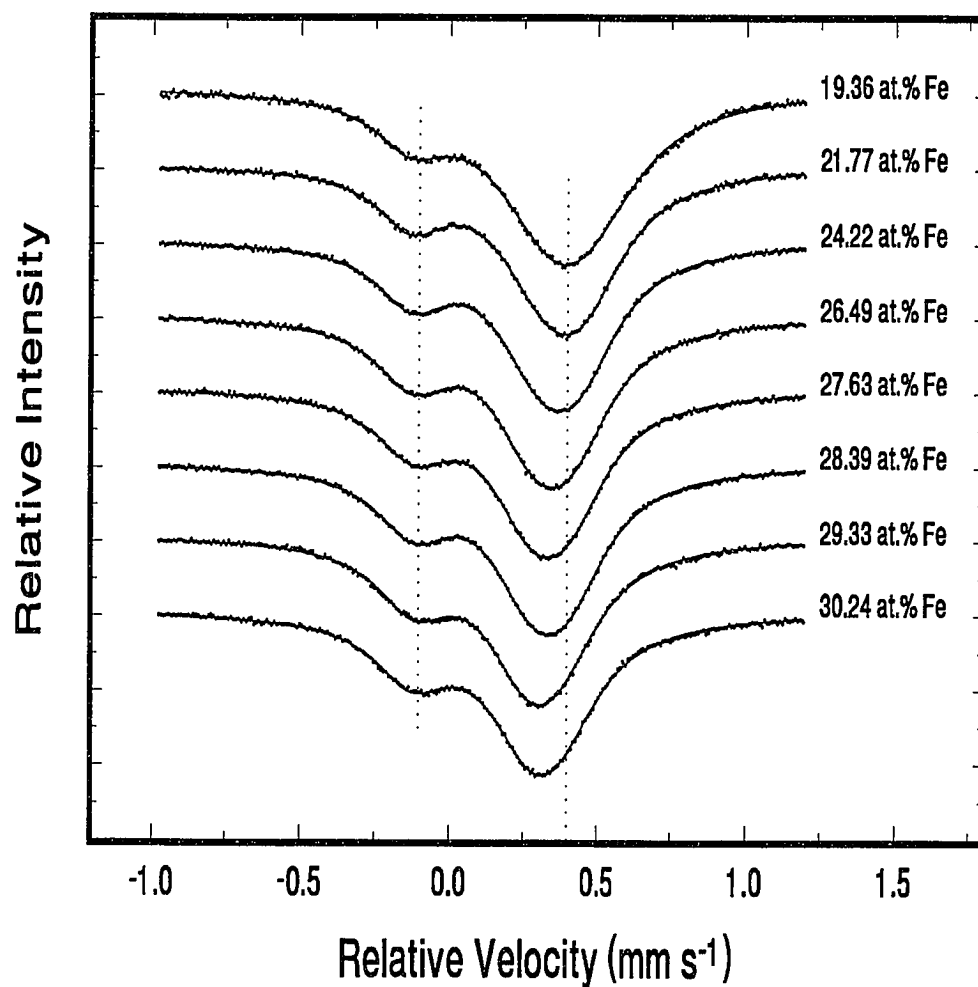


Figure 2.27. Overlap of the Mössbauer spectra for different samples produced within the Γ phase. Note the positional changes in the spectra as a function of iron concentration.

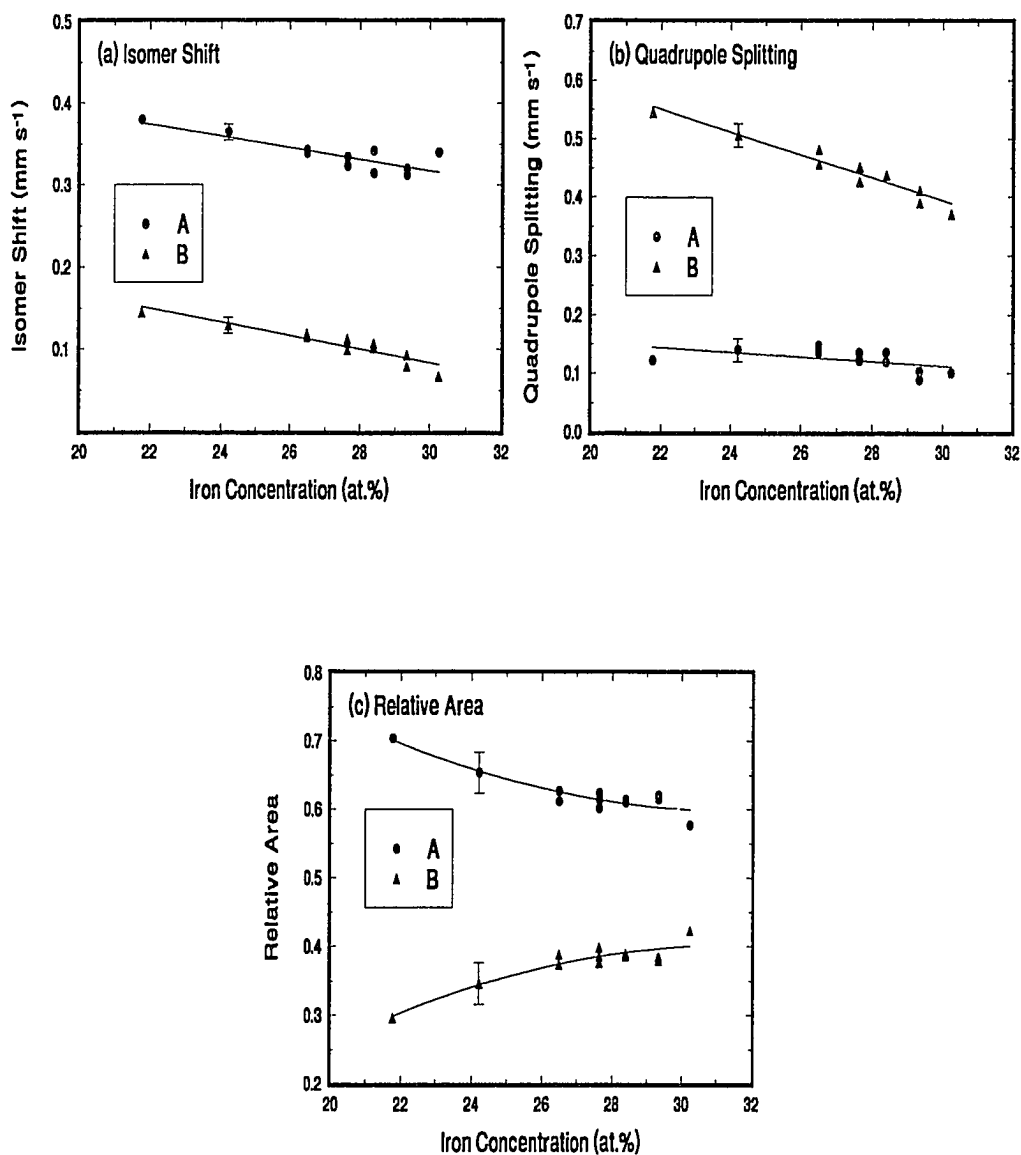


Figure 2.28. Mössbauer parameters, (a) isomer shift, (b) quadrupole splitting, and (c) relative area as a function of iron concentration for the Γ phase. Solid lines are least squares fits to the data.

The continuous changes in Mössbauer parameters across the Γ phase are significant, and answer a longstanding question concerning the location of the iron atoms. Recall from section 2.2.2 that there are four possible atomic sites which iron may occupy, the inner tetrahedral (IT), outer tetrahedral (OT), octahedral (OH), and cubo-octahedral (CO). Furthermore, we discussed that Brandon et al.²⁶ produced a sample in the low iron end of the Γ phase and determined that the iron occupied only the inner tetrahedral and outer tetrahedral sites. On the other hand, Johansson et al.²⁵ produced a sample in the high iron concentration region of the Γ phase and proposed that the iron occupied the inner tetrahedral and octahedral sites. Since our Mössbauer analysis shows that the site location of the iron remains unchanged across the entire Γ phase, only one of these configurations can be correct. That is, we observe no discontinuity in the Mössbauer parameters as iron concentration is varied. Therefore, the iron must continuously occupy the same two atomic sites. The relative areas of the two sites approach the limit of 6:4 indicating that the iron is occupying the inner tetrahedral and octahedral sites, consistent with Johansson et al.

Of interest is the similarity between the electronic environments of the two sites in the Γ phase and the two main sites in the Γ_1 phase. Comparing Figures 2.28 (a) and (b) with Figures 2.25 (a) and (b) in the region of 21 at.% Fe, it is shown that site A in the Γ_1 phase has a large isomer shift and a small quadrupole splitting, similar to site A in the Γ phase. Furthermore, site B in the Γ_1 phase has a small isomer shift and a large quadrupole splitting similar to site B in the Γ phase. Perhaps the same octahedral and tetrahedral configurations that are present in the Γ phase are responsible for this similarity.

2.2.3 Analysis of Mixed Phase Regions

Mössbauer spectroscopy was used to study three samples, FZ017F, FZ016N, and FZ027K within the Γ - δ mixed phase region of the phase diagram. Figure 2.29 compares the spectra of these samples. Consistent with XRD analysis, the percentage of the δ phase present in the samples decreases as the iron concentration is increased. Spectral analysis shows that these samples are indeed a mixture of the pure phases bordering the mixed phase region; i.e., a proportional mixture of a low iron concentration Γ and a high iron concentration δ is formed.

Mössbauer effect analysis of sample FZ018I (see Figure 1.2), formed in the Γ - Γ_1 region, shows the existence of both the bordering phases. The broadening of the main peak confirms the existence of Γ_1 in the sample (Figure 2.30). The similarity between this spectrum and that produced by FZ015S indicates that the Γ formed in this sample has the stoichiometry of approximately 26.5 at.% Fe. This is the maximum fraction of iron present in a sample of this phase sintered at 650 °C.

Finally, Figure 2.31 compares the Mössbauer spectra of samples FZ028H, FZ027H, and FZ026H, all included in the Γ_1 - δ mixed phase region. These spectra verify the presence of both the Γ_1 and δ phases. By comparing these spectra to the pure phase Γ_1 and δ spectra discussed earlier, it appears that the stoichiometries of the pure phases nearest this mixed region, are formed. This implies that mixed phase samples contain proportions of the two phases bordering the mixed region. Furthermore, the iron concentration in each of the phases is the same as that found in the pure phase whose boundary is closest to the mixed phase region at the sintering temperature of the mixed sample.

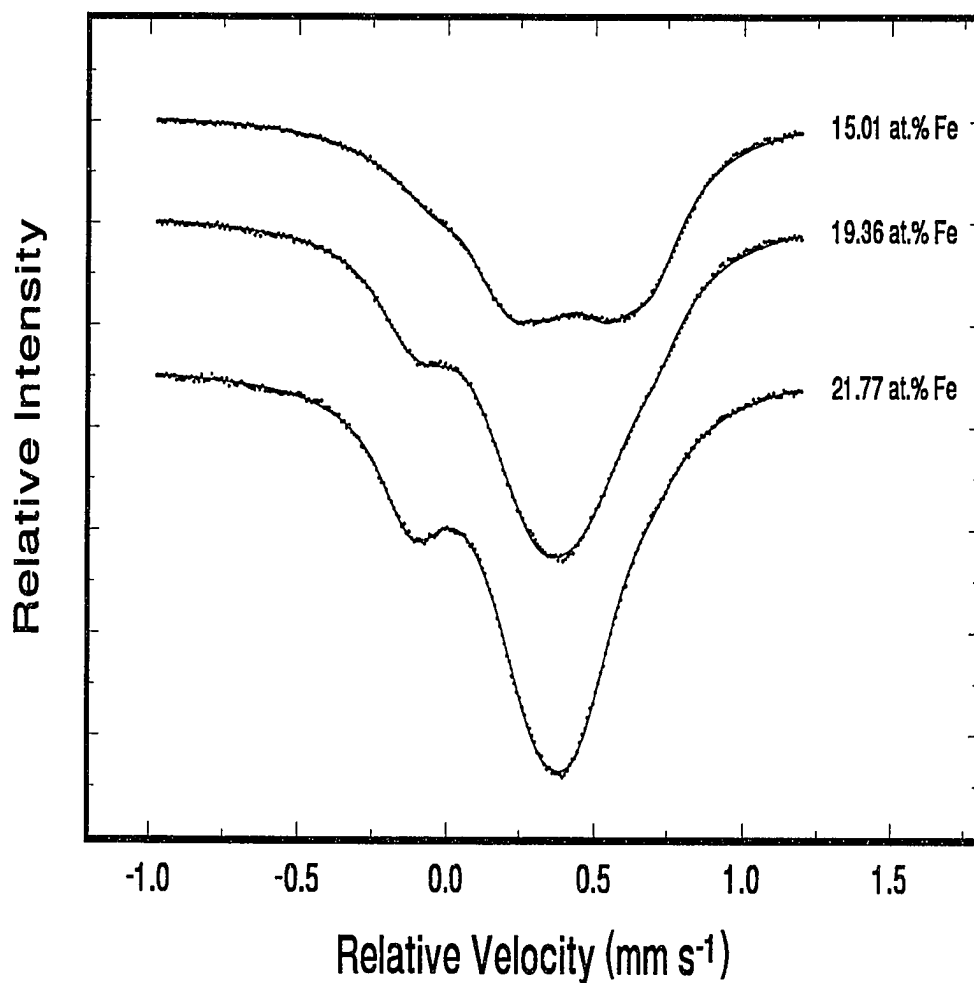


Figure 2.29. Overlap of the Mössbauer spectra for samples, FZ017F, FZ016N and FZ027K, all within the Γ - δ mixed phase region. Note the change in the percentage of each phase present as one moves across this region.

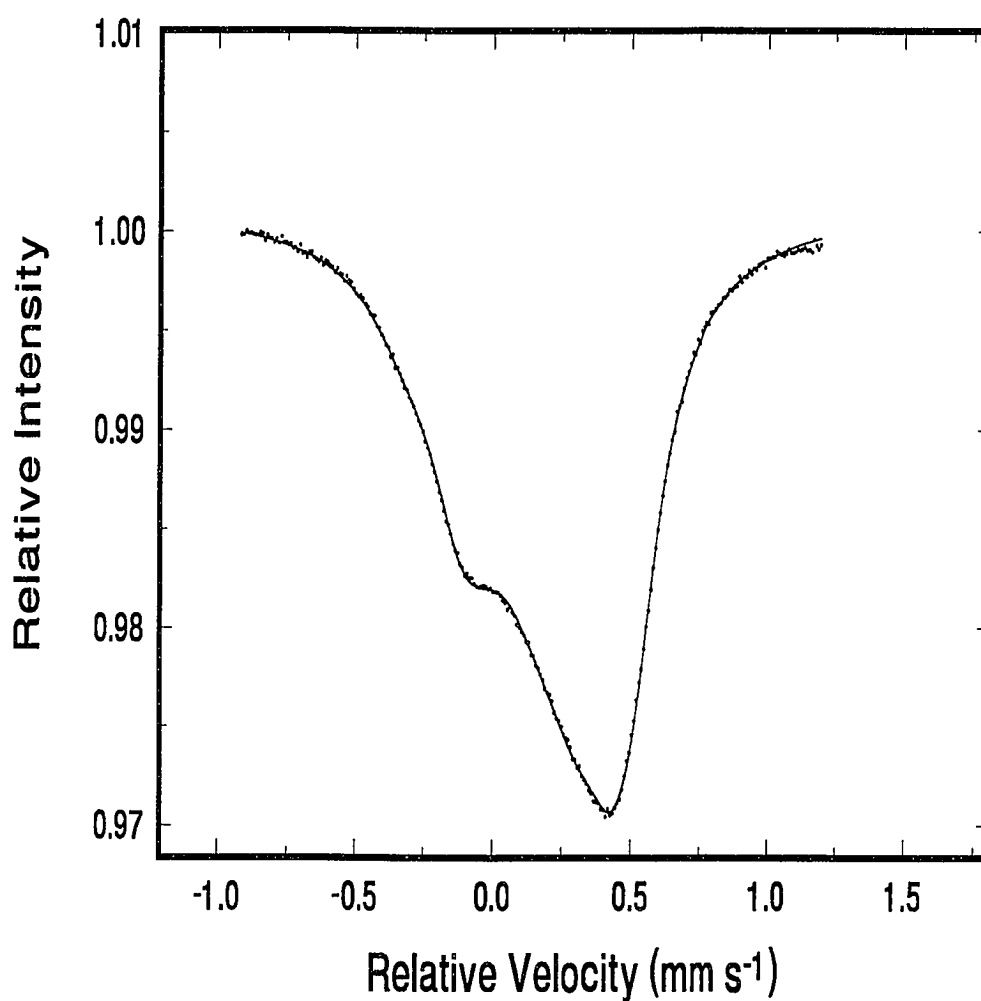


Figure 2.30. Mössbauer spectrum of sample FZ018I, formed in the Γ - Γ_1 mixed phase region. The broadening of the main peak indicates the presence of Γ_1 in the sample.

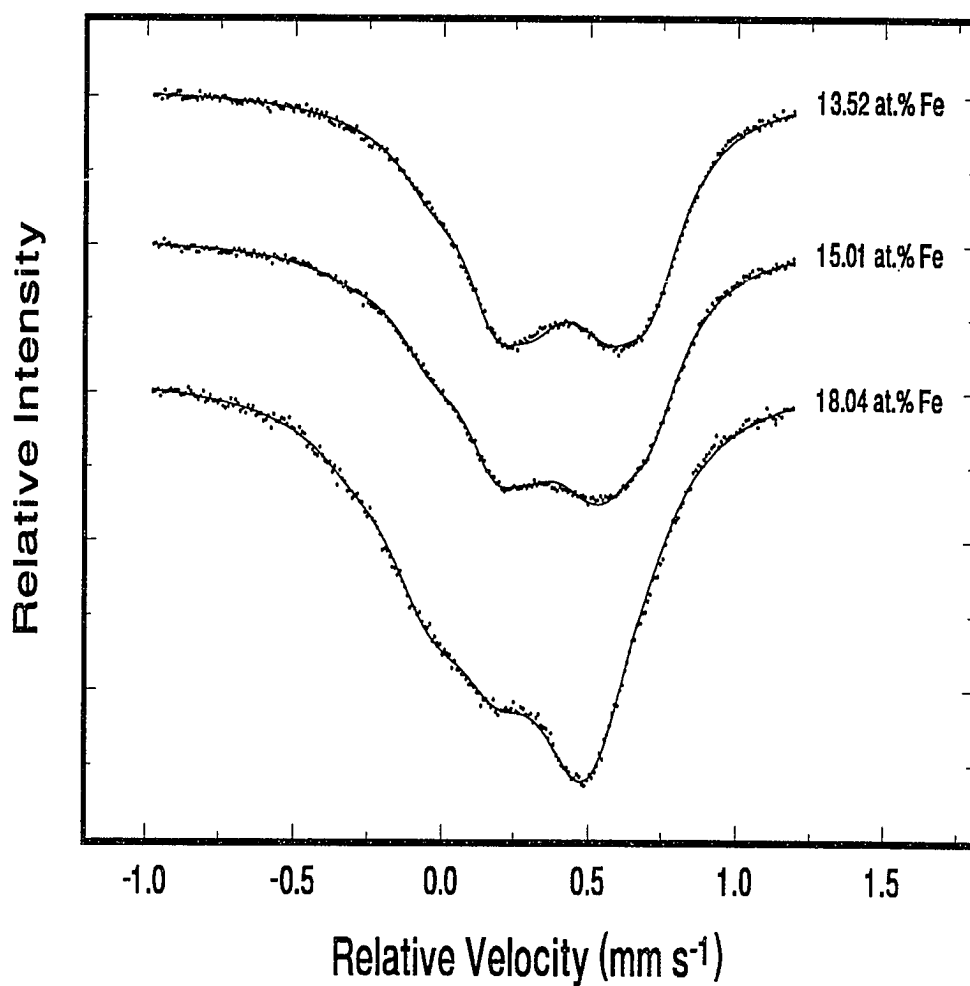


Figure 2.31. Overlap of the Mössbauer spectra for samples, FZ028H, FZ027H and FZ026H, all within the Γ_1 - δ mixed phase region. Note the change in the percentage of each phase present as one moves across this region.

2.2.4 Summary of Mössbauer Effect Analysis

Mössbauer spectroscopy provides a better fundamental understanding of the pure phase and the mixed phase regions of the iron-zinc phase diagram. Significant points, as discussed previously, will now be summarized. Firstly, the ζ phase has been found to possess a single iron site whose isomer shift and quadrupole splitting is independent of iron concentration. The small variance in iron concentration across the ζ phase is thought to be responsible for this constancy.

The δ phase was found to contain three iron sites in contrast with our previous findings of two iron sites. The isomer shifts of all three sites decrease continuously with increasing iron content. However, only the quadrupole splitting and site occupation of the third, least occupied, site changes appreciably across the phase. In addition, the ratio of the relative areas of the two most populated iron sites remains a constant 6:4 across the δ phase. This ratio is similar to that approached in the high iron concentration end of the Γ phase.

Analysis of the three samples produced in the Γ_1 phase indicate the existence of three iron sites. However, only the site occupancies change as a function of iron concentration. As previously discussed, the two most occupied sites have similar electronic environments to those observed in the Γ phase.

Production and analysis of many samples within the Γ phase produced some interesting results. Two iron sites are found within the Γ structure, whose populations change dramatically and continuously with iron content. The ratio of the site occupancies approaches the value of 6:4 at the high iron end of the phase. This indicates that the iron is populating the inner tetrahedral and octahedral positions in the bcc structure. The isomer

shifts of the two sites were found to decrease continuously across the phase, whereas only the quadrupole splitting of the tetrahedral site (site B) was found to decrease continuously with increasing atomic percent iron. The consistency of the Mössbauer parameters indicates that iron is only occupying these two sites and therefore only one configuration is possible; i.e. the iron only occupies the inner tetrahedral and octahedral sites of the 26 atom cluster previously described. Mixed phase studies show that the bordering pure phases form in the different proportions within these regions. Furthermore, the stoichiometry of the phases present in a mixed phase region are those of the pure phase nearest the pure-mixed phase boundary.

In turn, Mössbauer effect analysis of the iron-zinc intermetallics has shown that it is uniquely capable of separately identifying the four phases. Furthermore, Mössbauer spectroscopy can distinguish between the Gamma-1 and Gamma phases. However, X-ray diffraction fails to make this distinction in samples which are produced in the Γ_1 - Γ mixed phase region.

Finally, the production and characterization of high purity iron-zinc alloys will serve as calibration standards for the industrial XRD and Mössbauer analysis of commercially produced galvaneal coatings. The compiled database of the crystallographic and hyperfine parameters of the iron-zinc intermetallics will facilitate the identification of the iron-zinc alloys in galvaneal coatings. The application of these results will be described in the next section of this dissertation entitled, Galvaneal Steel Coatings.

GALVANNEAL STEEL COATINGS

Part 2: Galvanneal Steel Coatings

Once the characterization of the microstructural properties of iron-zinc intermetallics was complete, an investigation of these intermetallics in commercial galvanneal coatings could proceed. The second part of this dissertation, covering Chapters 3-5, deals with the identification of the iron-zinc phases in commercially produced galvanneal steel. Chapter 3 discusses the processing and general properties of galvanneal steel in comparison to galvanized and uncoated sheet steel as background and motivation for coating analysis. The corrosion resistance, formability, paintability, and weldability of galvanneal steel are examined with particular emphasis on the affect of coating composition on these metallurgical properties. In Chapter 4, the development and testing of a toroidal scattering Mössbauer detector is discussed. This detector was developed to study galvanneal coatings in-situ; i.e., without removing the coatings from the steel substrate. Testing of the detector was performed using a bilayered foil of stainless steel and α -Fe, as well as using three commercially produced galvanneal coatings. Chapter 5 presents the detailed analysis of several commercially produced galvanneal coatings in order to identify the phases present in the coatings and compare the results with the metallurgical properties provided by the galvanneal producers. Coatings are analyzed with the new detector, using the database of the microstructural parameters developed in the first part of this dissertation. General conclusions are drawn in the sixth and final chapter. Finally, a description of the present research performed on galvanneal steel at Old Dominion University is followed by some recommendations for further study in the area of galvanneal research.

CHAPTER THREE

Galvanneal Steel

The corrosion resistance of steel sheet is of economic and environmental importance, in particular, to the automotive industry. Consequently, processes for successful application of zinc and zinc alloy coatings to steel sheet have been the recent focus of industrial research efforts. Hot-dip galvanized and galvanneal sheet steel are two products whose popularity has grown over the past several years. Both methods are an economic way to apply the zinc, and the continuous coating lines of the day permit the production of materials having well controlled coating thickness and uniformity. Galvanneal steel differs from galvanized steel in that it results from the post annealing of the zinc-coated steel sheet. This allows the interdiffusion of the iron and zinc and the formation of an iron-zinc alloy coating. The following chapter discusses the processing and properties of galvanneal steel and the problems facing galvanneal producers.

3.1 Processing of Galvanneal Steel Coatings

Prior to the galvannealing process, steel sheet is produced through various hot and cold rolling techniques. The resulting coils of sheet steel range from 0.5 to 2.5 mm thick. The coils are thoroughly cleaned, usually by acid pickling, in order to remove any oxide layer which may have formed in the milling process.³⁵ Figure 3.1 is a schematic of a typical continuous coating galvannealing line. As indicated, once the sheet leaves the payoff coil it undergoes an extensive cleaning which may involve chemical as well as heat treatment. It is then passed through a pre-annealing, high temperature furnace which is typically operated at 600 °C or more.³⁶ A protective atmosphere, typically consisting of hydrogen and nitrogen, is maintained in the furnace to prevent the steel sheet from oxidizing. Pre-annealing allows the steel to regain the ductility lost during the rolling process. Once annealed, the steel sheet enters the molten metal pot and upon emergence passes through gas knives (wipers) where excess coating metal is wiped away. For galvanized and galvannealed coatings, the bath consists of zinc, iron and small amounts of a variety of other elements added to enhance or suppress specific phase formation. Next, the coated steel sheet passes through the galvannealing furnace where it is heated for up to 10 seconds at temperatures ranging from 500 °C to 570 °C. This allows the interdiffusion of the iron and zinc and forms an alloy coating typically 6 to 11 microns thick.³⁶ Following the galvannealing furnace, the sheet is cooled and post treated before being coiled at the end of the process. Critical parameters are the annealing temperature and time which can affect the coating thickness, coating iron content, and quantities of the phases formed.

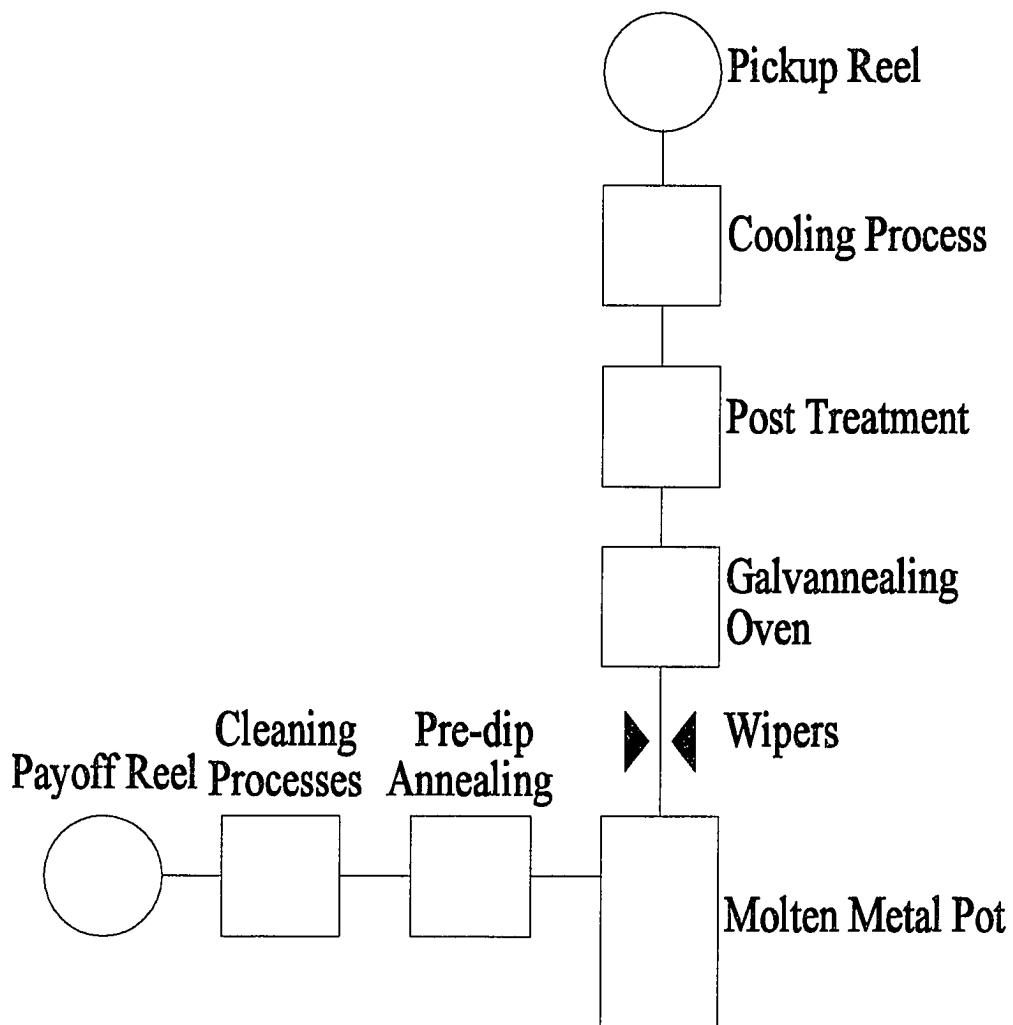


Figure 3.1. Schematic of a continuous hot-dip galvannealing line.

3.2 Properties of Galvanneal Steel Coatings

Annealing of the zinc coated sheet allows the formation of up to four iron-zinc intermetallics. Shown in Figure 3.2 is a typical cross sectional micrograph of a galvanneal coating. The four iron-zinc intermetallics form layers within the coating; the Gamma phase is present at the base of the coating next to the steel substrate followed by the Gamma-1, Delta, and Zeta phases. The presence of each phase in the coating controls the performance of the material in different ways. The Gamma phase is generally a hard thin layer with high iron content. It is easier to weld but more difficult to form than the other phases. The high iron content also results in the poor corrosion resistance of the Gamma phase. Increasing the thickness of the Gamma phase leads to a harder coating but promotes cracking of the entire coating which can lead to further reduced resistance to corrosion. The formability and corrosion resistance improve for the phases containing more zinc. However, this improvement compromises the weldability. The Delta phase is generally believed to be the most ductile and corrosion resistant of the four phases. The following sections summarize the general characteristics of zinc and zinc-alloy coated steel sheet and discuss the metallurgical properties which are of most concern to the automotive industry. Generally, these metallurgical properties are controlled by the phases present and their relative abundances. However, the primary problems presently facing steel producers involve not only controlling the phase formation but also identifying the phases present within a coating.

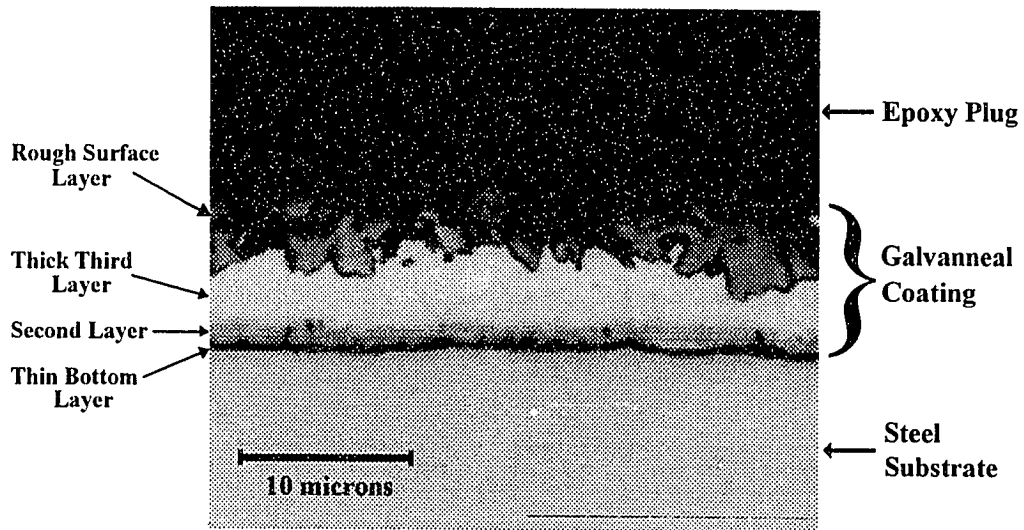


Figure 3.2. Cross sectional micrograph of a typical galvanneal coating. Note the layering of the iron-zinc intermetallic phases within the galvanneal coating. The black region is the epoxy plug used to mount and polish the sample and the light region below the coating is the steel substrate.

3.2.1 Corrosion

The major advantage of galvanneal coatings is their superior resistance to corrosion when used in automotive environments. This is particularly evident if the coatings are painted. Salt spray testing as well as atmospheric exposure tests have shown that galvanneal steel coatings have a greater resistance to corrosion than do galvanized coatings.³⁷ Several factors contribute to the exceptional corrosion resistance of galvanneal coatings. First of all, the presence of a coating produces a barrier between the corrosive environment and the reactive steel surface. The larger the coating weight or thickness, then the larger the protective barrier. This is also true for galvanized steel surfaces. Secondly, protection through the galvanic or sacrificial mechanism is observed in both galvanized and galvanneal products. However, it has been shown that the iron-zinc alloys in galvanneal coatings are less electrochemically active than the pure zinc coating in galvanized steel.³⁸ These factors have contributed to the dramatic increase in the use of galvanneal coatings in recent years.

3.2.2 Formability

During the production of automobile body panels, sheet steel is subjected to various deformations which may stretch the steel and increase its surface area. In the case of coated sheet steel the problem is further complicated. The coating must also stretch and conform to the bends of the steel base if product quality is to be maintained. Generally, the steel composition, coating process, coating thickness, and phases present can all affect the formability of galvanneal steel sheet. The adhesion between the coating and the steel substrate is perhaps the most important concern. During the deformation of galvanneal

coatings the coating can powder, i.e., the coating can crumble or disintegrate into a fine powder producing a region where the substrate is exposed to the atmosphere. This may reduce the corrosion resistance of the coating and inhibit the paintability of the final product. However, by keeping coating thicknesses and iron contents low, the powdering loss is minimized.³⁹ Another parameter affecting the formability is the frictional coefficient between the sheet and the tool surfaces. The frictional coefficient can vary from coating to coating; nevertheless, problems due to friction can be controlled through the proper lubrication and operation of the fabricating tools. Finally, the ductility of a galvaneal coating is an important factor influencing its formability. Coatings containing high amounts of the Gamma phase are generally more brittle and more likely to crack. In contrast, galvanized coatings, primarily containing pure zinc, are more ductile.

3.2.3 Paintability

When coated steel sheet is used for exterior automotive body panels, paintability is an aesthetic concern. The cathodic electrophoretic process is the most common technique used in the automotive industry for the application of the primer coat of paint. During this process craters in the paint film may appear. Craters are small defects in the otherwise smooth surface. In general, galvaneal coatings are less resistant to cratering than galvanized coatings. However, galvaneal coatings have a smoother surface yet are more microscopically rough and porous than galvanized coatings. This leads to better paint adhesion and a smoother, more desired appearance.

3.2.4 Weldability

Spot welding is the primary method for joining together pieces of steel sheet within the automotive industry. This involves the overlapped sheets being pressed between two copper electrodes and an electrical current passed through them fusing the two sheets together. However, this procedure is affected by the presence of a zinc or zinc-iron coating on the steel surface. The pure zinc surfaces of galvanized coatings tend to alloy with the copper electrodes reducing the life span of the electrodes. Furthermore, spot weld currents must be increased in order to sufficiently fuse galvanized steel sheets. On the other hand, galvanneal coatings are generally easier to weld than galvanized steel. This is primarily because the iron-zinc phases have a higher electrical resistivity than pure zinc.³⁸ Therefore, sufficient resistance heating and fusion of the steel sheets can be achieved at lower currents than in the case of galvanized steel.³⁸ In turn, this extends the life span of the copper weld tips.

3.2 Summary

Galvanneal steel results from the post annealing of zinc coated steel sheet. This process alloys the iron and zinc to interdiffuse and form a layered alloy coating. Up to four phases can form in the coating, the composition of which controls the microscopic and macroscopic properties of the coating. The weldability, formability, paintability, and corrosion resistance of galvanneal coatings are generally better than galvanized coatings. Specifically, the corrosion resistance after painting of galvanneal coatings is far superior to

galvanized steel. Successful application of galvanneal coatings has provided a means by which steel companies can economically meet the environmental demand to improve the corrosion resistance of steel sheet. In order to tailor the properties of galvanneal coatings to specific applications, it is necessary to understand and control the phase formation during the galvannealing process. Positive identification of each phase and the fraction present in a galvanneal coating is difficult. As presented in Chapters 1, and 2, Mössbauer spectroscopy and X-ray diffraction are now able to separately identify the iron-zinc phases. However, when analyzing galvanneal coatings, separate phase identification using XRD is difficult. Furthermore, the presence of the thick steel substrate prevents the use of conventional transmission Mössbauer techniques. Nevertheless, scattering Mössbauer spectroscopy has demonstrated the ability to separately identify the iron-zinc phases without having to remove them from the steel substrate. The existing scattering Mössbauer detectors are limited in efficiency and require long analysis times to achieve sufficient subspectral resolution. Hence, a new toroidal detector was constructed to alleviate these problems, the details of which are discussed in the next chapter.

CHAPTER FOUR

Mössbauer Detector for Characterization of Galvanneal Steel Coatings

Once an adequate database of the microstructural properties of the iron-zinc intermetallics was obtained, it became feasible to study galvanneal coatings in greater detail than was previously possible. However, we needed a detector capable of accurately monitoring the fraction of the four iron-zinc phases present in a galvanneal coating. Therefore, a Mössbauer detector specifically designed for coating analysis was constructed. The new detector was used to study several commercial coatings to ascertain its ability to accurately detect and monitor the iron-zinc phases present. It was concluded that this new detector is capable of identifying the presence and fraction of each phase in a galvanneal coating in-situ; that is, without the need to remove the coating from the steel substrate. In probing the whole coating, the detector collects the emitted radiation from within the entire thickness of the coating down to the steel substrate. The detector design, construction, and testing is the focus of this chapter.

4.1 Toroidal Detector

4.1.1 Mössbauer Spectroscopy and Detector Theory

Mössbauer spectroscopy is a versatile research technique used for analyzing some of the microscopic properties of materials. It is uniquely able to characterize and fingerprint every iron containing compound. The Mössbauer effect involves the resonant absorption of gamma radiation by the iron in materials, and as such is able to identify different phases which may have similar crystal structures. This is possible because Mössbauer spectroscopy is sensitive to the local magnetic and electric environments of the iron nuclei. As a result, Mössbauer spectroscopy is often able to differentiate between materials whose X-ray diffraction spectra are nearly identical. Also, it is able to identify multiple iron sites within the one crystal structure, as was observed in three of the four pure iron-zinc intermetallic phases.

Two common experimental geometries are used, transmission and scattering. Transmission Mössbauer Spectroscopy (TMS) was used to study the pure iron-zinc intermetallic powders discussed in the first section. TMS can measure samples up to about 50 μm thick by passing the γ -rays through the entire sample. Furthermore, it is possible to study galvanneal coatings once removed from the steel substrate since galvanneal coatings range from 6 - 11 μm thick. TMS is generally used as an analytical tool for bulk samples and has long been used for metallurgical studies of lattice defects, phase identification, corrosion phenomena, and oxidation. In scattering geometry, the re-emitted radiation is detected following the absorption of a γ -ray. This emitted radiation can be either another γ -ray or

through a process called internal conversion, one of several different electrons called conversion electrons which are emitted from the K, L and M electronic shells. In addition, following the emission of a conversion electron, a characteristic X-ray will also be emitted from the sample. Figure 4.1 shows a schematic of the decay modes of ^{57}Fe nuclei following the resonant absorption of a γ -ray. Table XII summarizes the energy and relative numbers of each type of particle emitted. Since the emitted radiation is less than 15 keV, scattering Mössbauer spectroscopy is ideal for studying coatings and surface phenomena. Most importantly, it is a non-destructive probe, i.e., its use is warranted for in-situ investigations where the removal of the coating from the substrate is either difficult or detrimental to its microstructure.

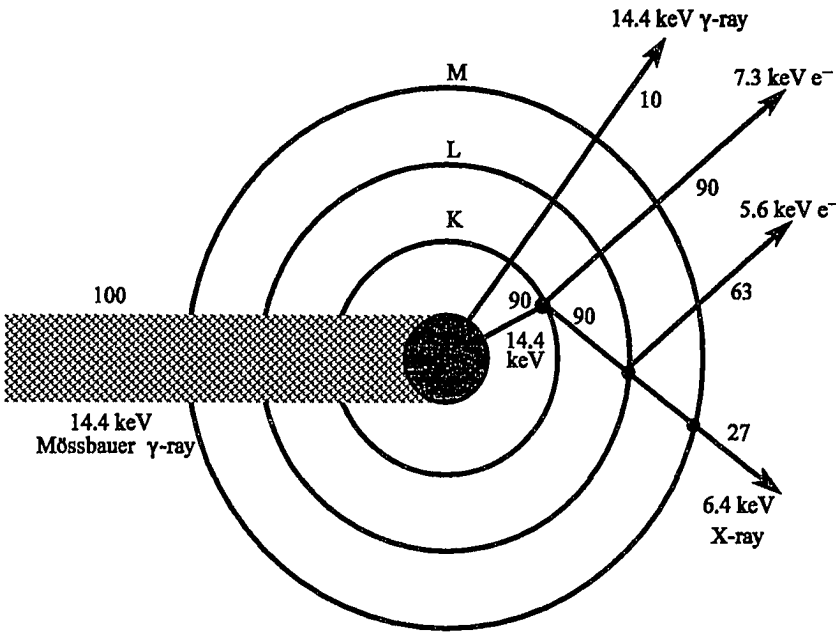


Figure 4.1. Schematic view of the Conversion Electron, X-ray and γ -ray emission processes following the resonant absorption of a 14.4 keV γ -ray by an ^{57}Fe nucleus.

TABLE XII. Summary of the major emissions during the decay of the first excited state of ^{57}Fe .

Emitted Particle	Energy (keV)	# of Events	Approximate Range
γ -rays	14.4	10	50 μm
K X-rays	6.4	27	50 μm
K conversion electrons	7.3	90	0.5 μm
L conversion electrons	13.6	9	1 μm
M conversion electrons	14.3	1	1 μm
KLL Auger electrons	5.6	63	0.5 μm
LMM Auger electrons	0.5		

The γ -rays, X-rays and conversion electrons have very different attenuation in materials. Therefore, detecting the three types of radiation in scattering geometry provides depth-dependent information on the coating. This is particularly important in galvanneal coatings where the different iron-zinc phases are layered parallel to the steel substrate. Furthermore, by detecting the conversion electrons, one is able to study the surface regions of the coatings to a depth of about 1 μm . This allows near surface phases such as Zeta and Delta to be studied in addition to the entire coating analysis. Therefore, a detector capable of monitoring the three types of radiation simultaneously is necessitated. Figure 4.2 shows the geometries and instrumentation required for transmission and scattering Mössbauer spectroscopy.

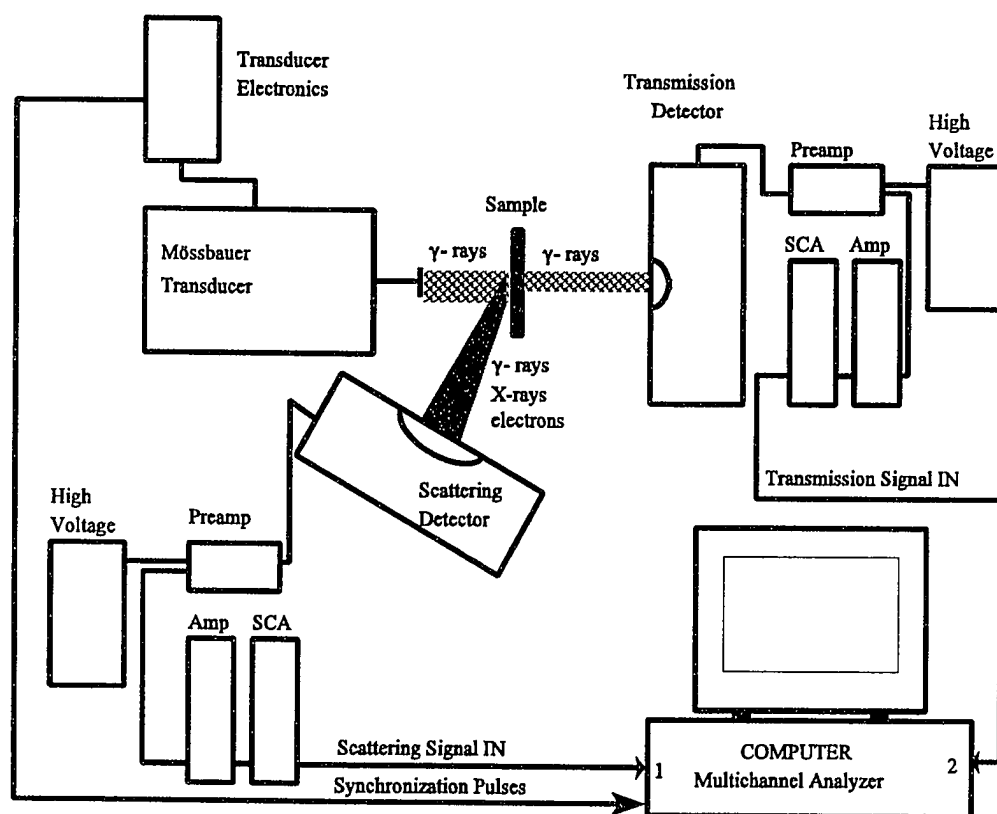
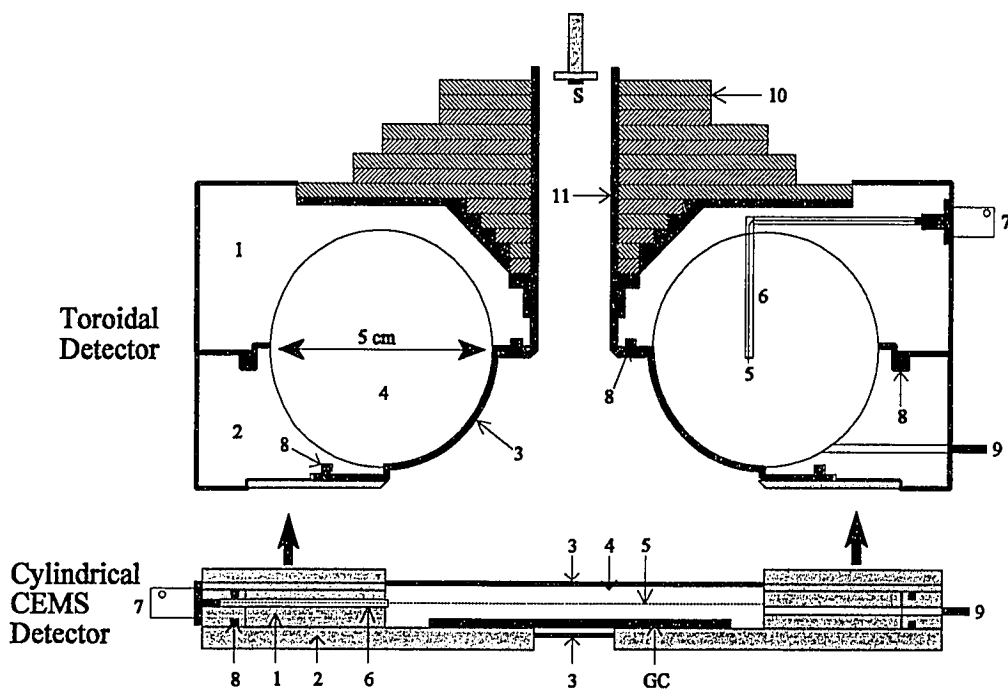


Figure 4.2. Geometries and Instrumentation for Transmission and Scattering Mössbauer Spectroscopy.

4.1.2 Detector Design

In the early investigations of galvanneal coatings^{21,22,31} a gas-filled detector with cylindrical geometry was designed and manufactured. However, the geometrical design resulted in detection of the direct radiation from the source in addition to the scattered radiation from the coating. This prevented its use for the study of coatings using scattered γ -rays. Furthermore, when scattered X-rays were detected, the signal to noise was very poor due to the direct X-rays coming from the source. The cylindrical detector did prove useful for detecting the conversion electrons but this limited the cylindrical detector to analyzing the uppermost 1 μm of the coating. In order to monitor the phases present in commercial galvanneal coatings using scattering Mössbauer spectroscopy, either the emitted 14.4 keV γ -rays or 6.4 keV X-rays must be detected. These techniques are referred to as GMS (γ -ray Mössbauer Spectroscopy) and XMS (X-ray Mössbauer Spectroscopy). Therefore, the cylindrical geometry was set aside in exchange for a new toroidal geometry.³⁹⁻⁴² Toroidal geometry enables the detection of both the scattered γ -rays and X-rays and provides excellent efficiency and resolution since the detection region is well shielded from the direct source of radiation. Furthermore, toroidal geometry offers a large acceptance window to allow a significant fraction of the scattered radiation to be detected. Also, the toroidal detector allows one to attach a second gas-filled proportional counter with cylindrical geometry to detect the conversion electrons emitted from the coating. Figure 4.3 shows a cross sectional drawing of the two detectors.



Item	Toroidal Detector	Cylindrical CEMS Detector
1	Upper half of chassis	Annular chassis
2	Lower quarter of chassis	Detector end plate
3	Detector window	Detector window
4	Detection volume	Detection volume
5	Tungsten anode wire	Tungsten anode wire
6	Insulating anode support	Insulating anode support
7	High voltage connector	High voltage connector
8	Viton O-ring	Viton O-ring
9	Gas inlet/outlet tube	Gas inlet/outlet tube
10	Alternating lead/tungsten shielding	--
11	Shielding support tube	--
S	⁵⁷ Co source	--
GC	Galvanneal coating	--

Figure 4.3. Cross sectional view of the toroidal and CEMS proportional detectors.

4.1.3 Construction

The toroidal detector is constructed of high purity, iron free aluminum. It has a window made of Delrin approximately 0.5 mm thick. Delrin is transparent to γ -rays and X-rays yet is gas tight making it ideal for use in proportional counters. The main body of the detector is divided into two sections. Both sections are circular in cross section, but the upper section consists of a half toroid [1] and the lower section a quarter toroid [2]. The Delrin window [3] makes up the final quarter of the toroid. Each section was produced using a computer controlled milling machine.⁴³ The two aluminum sections were highly polished on the inside using "wet or dry", 600 grit, corundum paper. Following this, 3 μm and then 0.3 μm alumina powder were used to polish the aluminum sections. Finally, a dry piece of standard photocopy paper was carefully rubbed over the highly polished surfaces. The sections were then rinsed with ethanol before the detector was assembled. A circular anode [5] of 20 μm diameter, gold coated tungsten wire, runs around the center of the toroid. The anode was mounted inside the detector body using 6 insulating Lucite rods [6] and is supplied the high voltage via a connector mounted in the larger aluminum section [7]. The two aluminum sections and the Delrin window are bolted together, and Viton O-rings [8] form gas tight seals between each section. Gas inlet and outlet connectors [9] are recessed into the smaller aluminum section [2]. The shielding consists of alternating disks of lead and tungsten [10] which are mounted on a brass support tube [11]. For GMS and XMS Mössbauer studies the galvanneal coating can be attached to the bottom plate of the detector.

The cylindrical Conversion Electron Mössbauer spectroscopy (CEMS) proportional counter, may be attached directly to the bottom of the toroidal proportional counter if near

surface studies are desired. The design and operation of the CEMS detector has been previously reported.^{44,45} As illustrated in Figure 4.3, combining the two detectors allows the simultaneous detection of the γ -rays, X-rays and conversion electrons being emitted from a galvanneal coating. This provides some depth profiling information of the phases in the coating.

Figure 4.4 shows four photographs of the toroidal detector. Figure 4.4 (a) shows the assembled detector with the white Delrin window in the center facing upwards. Samples may be mounted directly on the top plate for GMS and XMS studies. For CEMS operation, the CEMS detector is mounted to the top plate. The inlet gas flow is controlled by the needle valve shown to the right of the aluminum chassis. The outlet pipe is to the left of the chassis and the high voltage connector is to the bottom right of the chassis. Figure 4.4 (b) shows the assembled detector from the top view. The alternating lead and tungsten disks can be seen stacked at the top. Figure 4.4 (c) shows the inside of the two aluminum chassis sections of the disassembled toroidal detector. On the right is the half toroid chassis section in which the 6 Lucite anode support rods are visible. To the left is the quarter toroid chassis section which contains the gas inlet and outlet connectors. Also discernible is the inside of the curved Delrin window and the Viton O-rings. Figure 4.4 (d) shows the parts of the disassembled detector. The two chassis sections are seen at the bottom. To the top left are the lead and tungsten shielding discs and the screws for joining the chassis sections. To the top right are the brass plate and tube used to support the shielding disks.

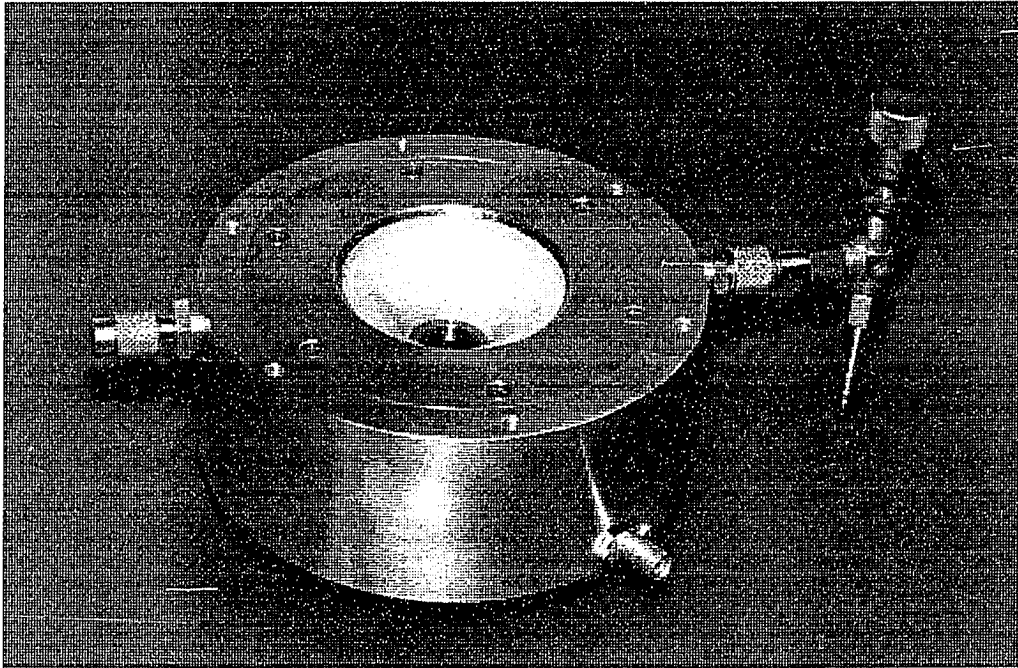


Figure 4.4 (a). Toroidal detector: Sample end.

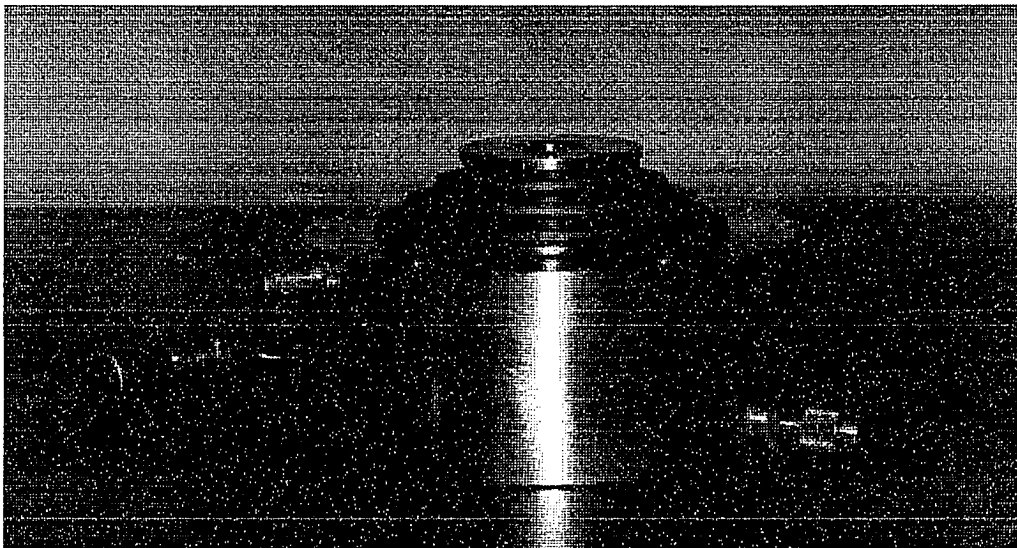


Figure 4.4 (b). Toroidal detector: Shielding end.



Figure 4.4 (c). Two chassis sections of toroidal detector.

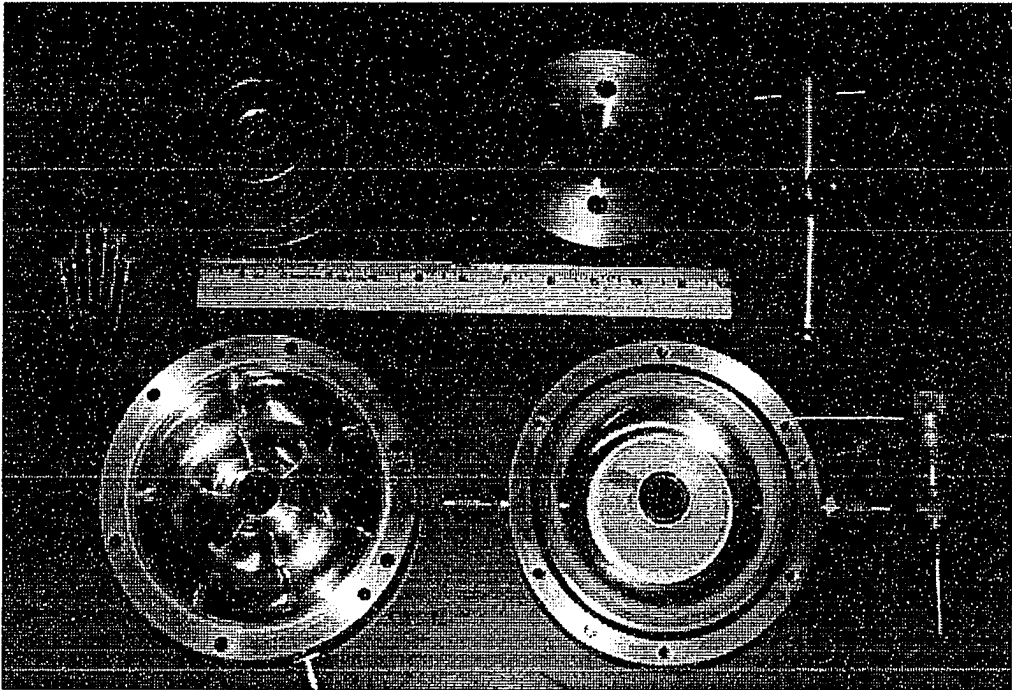


Figure 4.4 (d). Completely disassembled toroidal detector.

4.1.4 General Operation

Proportional counters are able to detect low energy γ -rays, X-rays, and electrons depending on the gas used in the detector and its absorption characteristics. The most commonly used gases are high purity xenon, krypton, or argon. The selection of gas is based on the energies of the photons being detected and the efficiency and spectral resolution of the gas at those energies. Shown in Figure 4.5 are the gas absorption characteristics of argon and krypton for energies up to 100 keV.⁴⁶ These figures apply to the gases at one atmosphere pressure and for a photon path length of approximately 5 cm. Argon has an absorption K-edge at 3.2 keV, thus it is highly efficient for detecting the 6.4 keV X-rays produced in iron Mössbauer spectroscopy. Figure 4.5 (a) shows that argon has an absorption of 90% for the 6.4 keV X-rays but only 20% for the 14.4 keV γ -rays. Krypton has an absorption K-edge at 14.3 keV which makes it sensitive for detecting the 14.4 keV γ -rays. Figure 4.5 (b) shows that krypton has an absorption of about 90% for both the X-rays and γ -rays.

The efficiency, gain and resolution of the gas filled toroidal detector is governed by many factors. The symmetry of the electric field lines surrounding the anode is perhaps the most important factor for optimizing the resolution. Therefore, it is common to design cylindrical proportional counters having a coaxial anode-cathode geometry. However, a toroidal shape also meets these requirements, and is preferred, since it can eliminate the detection of direct source radiation. The type of gas, voltage supplied across the anode and cathode, and gas flow rate also effect the overall performance of the detector. These parameters control the efficiency and gain of the detector and need to be optimized to enable high quality Mössbauer spectra to be recorded. This new toroidal detector is capable of

operating with the detection chamber permanently filled with gas or in a gas-flow mode. However, previous experience with the conversion electron detectors has shown us that more stable operation is attained using a flowing gas. This is due to the improved ability to suppress charge build up near the anode when the gas is continuously refreshed. Gas mixtures are commonly used in proportional counters in order to increase the detection efficiency and stabilize the gain. The main detection gas is usually mixed with a small amount of inert quench gas consisting of either methane, ethane, or carbon dioxide. This prevents charge build up in the detector and inhibits the onset of continuous discharge.

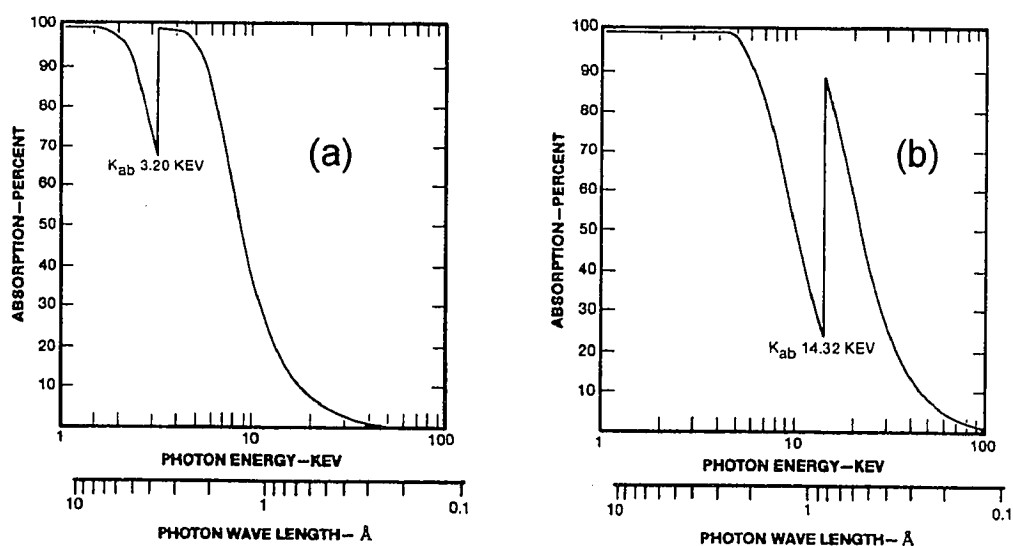


Figure 4.5. Gas absorption characteristics for X-rays in (a) argon and (b) krypton.⁴⁶

Three gas mixtures were used to test the efficiency and resolution of the toroidal detector, 90% argon with 10% methane, 90% krypton with 10% methane, and 45% krypton and 45% argon with 10% methane. A gas mixture of 90% helium with 10% methane was used for surface analysis using the CEMS detector since helium has nearly zero absorption for the γ -rays and X-rays but is ideal for detecting the 7.3 keV conversion electrons.

The gas flow through each detector is controlled by a low pressure regulator (0-30 psig) coupled to a high pressure regulator (0-400 psig) which is attached to the gas cylinder. The flow rate is controlled using a needle valve. Flow rates from 0-10 cm³ min⁻¹ are monitored with a gas flow transducer. Stable gas flow rates are important in order to maintain a constant detector gain. Gas flows were stabilized at around 5.0 ± 0.2 cm³ min⁻¹ prior to the high voltage being applied. The voltage was slowly increased until the appropriate pulse-height spectra was observed. Generally voltages of 1500 V for the toroidal detector and 1000 V for the CEMS detector were used. In each detector the chassis forms the cathode which is maintained at ground potential.

The initial tests used a mixture of 90% Kr + 10% CH₄. As discussed above, krypton has an absorption K-edge at 14.3 keV which makes it sensitive for detecting the 14.4 keV γ -rays and the 6.4 keV X-rays. Investigation of the effects the various gases have on the detector efficiency and resolution necessitated, first of all, calibration of the pulse height analyzer to be certain of the energy of the various peaks observed. This was performed by collecting the pulse height spectrum of a 12 μ Ci ⁵⁷Co source and comparing it with the pulse height spectrum of an ⁷³As source. ⁷³As decays to ⁷³Ge through the conversion electron process producing a characteristic 9.9 keV X-ray. This peak is expected to lie between the

6.4 keV and 14.4 keV peaks from the ^{57}Co source. Figure 4.6 (a) shows the pulse height spectrum recorded using both sources simultaneously. The 9.9 keV X-ray peak from ^{73}As falls between two peaks from the ^{57}Co source. The position of the three peaks enabled the energy scale of the PHA spectrum to be calibrated from which it was concluded that the two ^{57}Co peaks corresponded to 6.4 keV and 14.4 keV. The additional peak at 1.8 keV corresponds to the escape peak of krypton. The energy of the incident γ -ray is primarily deposited in the detector through the K-shell ionization of the krypton atoms. However, if the krypton ion de-excites and the characteristic 12.6 keV X-ray escapes the detector, then only 1.8 keV will be deposited in the detector giving rise to the observed escape peak. Figure 4.6 (b) shows the pulse height spectrum obtained from only the ^{57}Co source.

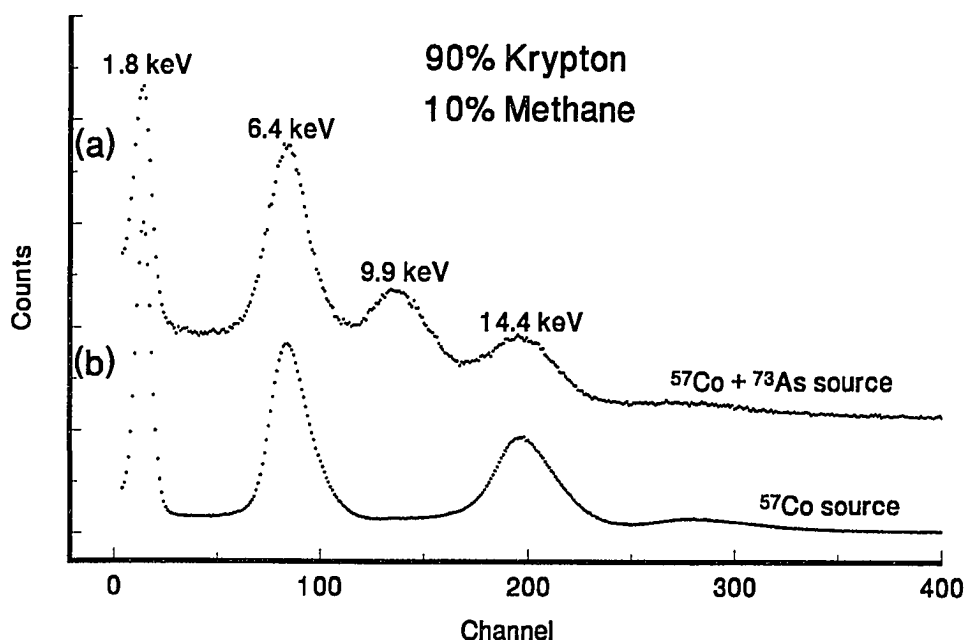


Figure 4.6. Comparison of PHA spectra of (a) $^{57}\text{Co} + ^{73}\text{As}$ sources with (b) just a ^{57}Co source in order to calibrate the radiation energy.

Following the identification of the 6.4 keV and 14.4 keV peaks, it was possible to investigate the influence of the various gases on the performance of the detector. Figure 4.7 shows the pulse height spectra of the ^{57}Co in Rh source using the three different gas mixtures. For each gas, the flow rate was maintained at $5 \text{ cm}^3 \text{ min}^{-1}$. For the 90% Ar with 10% CH_4 gas mixture, as seen in Figure 4.7 (a), detection of the 6.4 keV Fe X-ray is more efficient than the 14.4 keV Fe γ -ray. This is due to the argon absorption K-edge at 3.2 keV. The small peak to the left of the main 6.4 keV peak is the argon escape peak. Inset into Figure 4.7 (a) is a table showing the relative peak areas which have been background corrected for the detected radiation.

Further testing was performed using a gas mixture of 45% Kr and 45% Ar with 10% CH_4 . The combination of both krypton and argon is expected to provide good efficiency for detecting both the 14.4 keV γ -rays and the 6.4 keV X-rays. Figure 4.7 (b) shows the pulse height spectrum of the same ^{57}Co in Rh source using this gas mixture. Again the 6.4 keV and the 14.4 keV peaks are well resolved. The 14.4 keV γ -ray peak is more efficiently counted when compared with the argon-methane mixture. The 1.8 keV escape peak due to the krypton is well resolved. The inset table on this PHA spectrum shows the relative area under each peak. Figure 4.7 (c) shows the pulse height spectrum using the 90% Kr with 10% CH_4 gas mixture. This is the same pulse height as was shown in Figure 4.6 (b) now plotted with the energy scale. The inset table indicates that both gas mixtures containing krypton give similar relative efficiencies in counting the X-rays and γ -rays. However, each of the three PHA spectra of Figure 4.7 were recorded for the same time period. Therefore, a slightly higher count rate is observed for the krypton-methane gas mixture. The detector efficiency

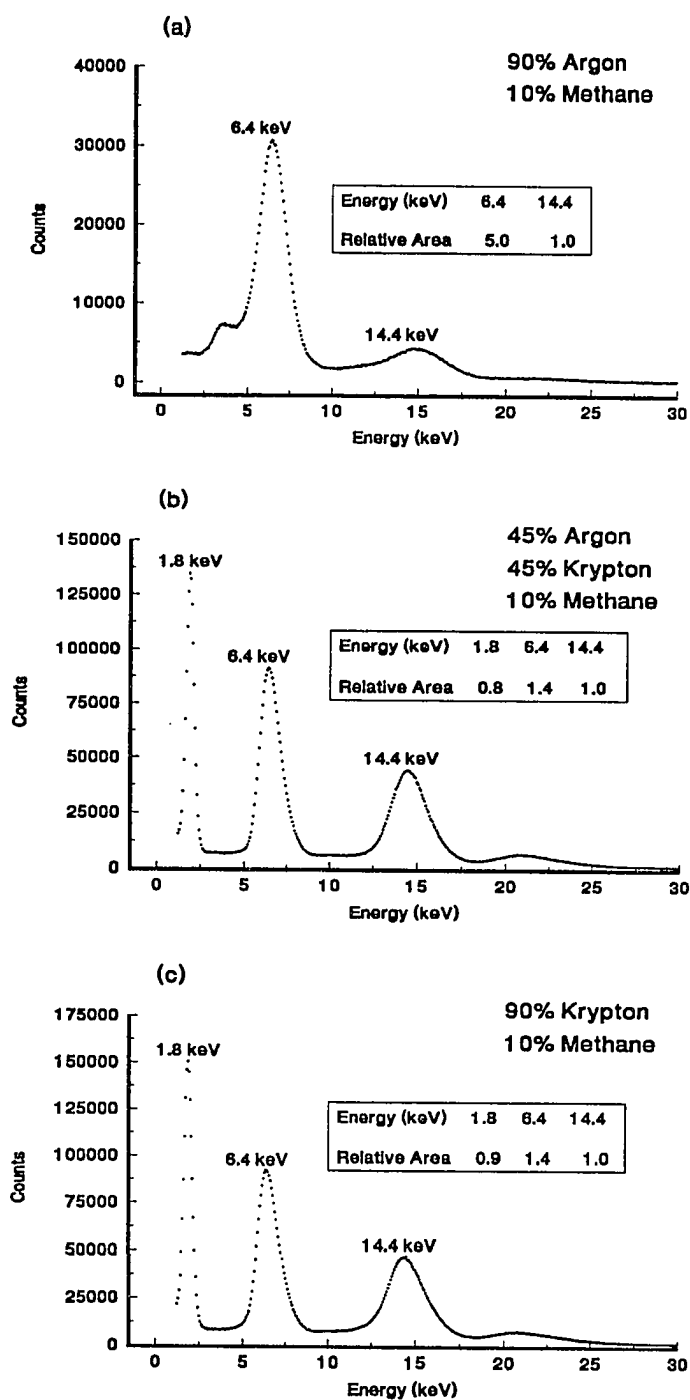


Figure 4.7. Pulse height spectra of a 12 μCi ^{57}Co in Rh source using three different gas mixtures.

for detecting the γ -rays and X-rays improved by about 4% and approximately 12% for the escape peak.

The resolution of the detector was calculated using the pulse height spectra data shown in Figure 4.7. Detector resolution is measured from the full-width at half the peak maximum, (FWHM), and is expressed as a percentage of the peak position. The lower the number, the better the detector resolution. Values for the three different gas mixtures are given in Table XIII. The detector resolution at 6.4 keV and 14.4 keV is close to the same for both the 90% Kr + 10% CH₄ and the 45% Kr + 45% Ar + 10% CH₄ gas mixtures.

The resolution of the new toroidal detector appears to be very good and can be compared with the commercially produced, gas-filled proportional counters used for transmission Mössbauer experiments. Table XIII shows the reported resolution for a 97% krypton gas X-ray proportional counter commonly used for TMS studies.⁴⁶

TABLE XIII. Detector resolution for the three gas mixtures.

Gas Mixture	Detector Resolution (FWHM as % of peak position)		
	1.8 keV peak	6.4 keV peak	14.4 keV peak
90% Ar + 10% CH ₄	---	29	18
45% Ar + 45% Kr + 10 % CH ₄	57	24	15
90% Kr + 10% CH ₄	60	25	16
Proportional Counter used for TMS containing 97% Kr + 3% CO ₂	52	19	12

Next, the toroidal detector was tested with the detection gas in non-flow mode; i.e., the detector was filled with gas and the inlet and outlet valves were closed. Its operation was studied over a period of time. The detector was first evacuated to 5×10^{-5} Torr prior to filling to 0.1 MPa (1 atmosphere) with a 90% Ar+10% CH₄ mixture of gas. In Figure 4.8, the pulse height spectra of a 25 mCi ⁵⁷Co source scattered from a pure iron powder sample is shown. These pulse height spectra are plotted as a function of time. The continual drift of the peak to the left indicates a reduction in the gain of the detector, and therefore, an inherent instability which would decrease the quality of the Mössbauer spectra. This change in gain may be due to either the out-gassing within the detector contaminating the gas mixture, or the consumption of the methane quench gas which could lead to charge build up inside the detector. Further pumping on the detector for a longer period of time may help alleviate this problem.

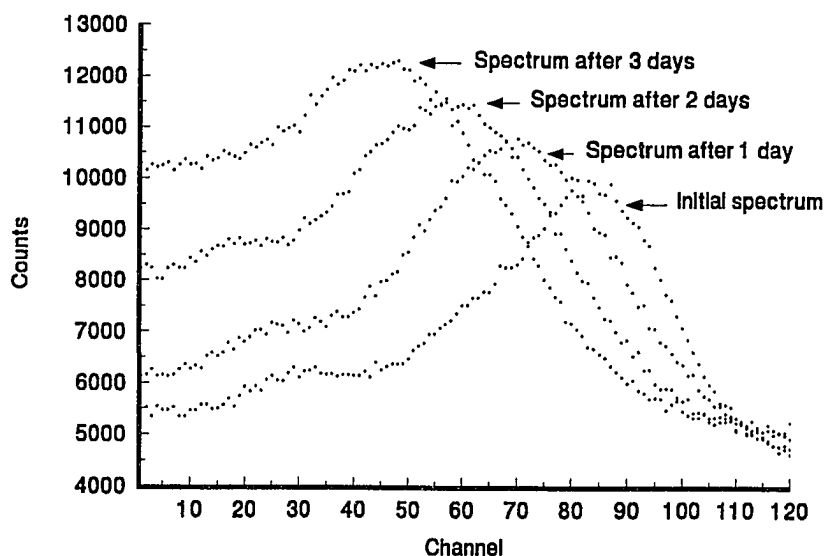


Figure 4.8. Pulse height spectra of a ⁵⁷Co in Rh source as a function of time. The gradual shift of the peak indicates a decrease in the gain of the detector.

In summarizing the PHA tests with the three mixtures, it was shown, that both krypton gases detect X-rays and γ -rays with about the same relative efficiency. Moreover, detector resolution for the three gas mixtures is very good allowing each peak to be used for recording Mössbauer spectra. However, the slightly increased counting efficiency of the 90% Kr + 10% CH₄ mixture makes it the logical choice for either GMS or XMS studies. The cost of the krypton is higher than argon but does not exclude its use. It is important to note that the 1.8 keV escape peak from krypton is coincident with the resonant γ -rays emitted from the coating surface. Therefore, this peak can also be used to record the GMS spectra.

Since galvanneal coatings contain a minimum of 65 at.% zinc, it was important to investigate the effect of zinc on the pulse height characteristics. If zinc in a coating significantly adds to the noise in the detector, then detector resolution and efficiency would be affected. In order to study this, four pulse height spectra were recorded under identical conditions using the 90% Kr + 10% CH₄ gas mixture flowing at 2 cm³ min⁻¹. The pulse height spectra were recorded in scattering geometry using a 25 mCi ⁵⁷Co in Rh source; i.e., the source was placed in its regular well shielded position so that no direct radiation was detected (see Figure 4.3). Different metal powders were placed in the normal sample position in order to detect the non-resonant, scattered radiation that resulted from the interaction with the X-rays and γ -rays from the source. Each sample was a high purity powder sandwiched between sheets of tissue paper and mounted to a sheet of cardboard using double sided tape. The first sample was the pure iron powder used to produce the iron-zinc intermetallics previously discussed in Chapter 1. The second was a mixed powder of 13 at.% Fe and 87 at.% Zn. The third was the iron zinc intermetallic sample, FZ030G containing 13 at.% Fe,

discussed in Chapter 2. Finally a pure zinc sample was used.

Figure 4.9 shows a comparison of the four pulse height spectra all recorded under the same conditions. Peak intensities can be directly compared in order to evaluate the effect of zinc. The lower spectrum of the pure iron powder (curve (d)) is virtually identical to the PHA spectrum recorded earlier using the same gas mixture (Figure 4.7 (c)). The 6.4 keV and 14.4 keV peaks are well resolved. For pure zinc (curve (a)) the intense peak at 8.6 keV corresponds to its principal X-ray emission line. Comparing the iron spectrum with the zinc spectrum it is evident that the zinc X-ray line closely overlaps the 6.4 keV X-ray line of iron. Both the iron-zinc mixture and iron-zinc intermetallic spectra also produce a large zinc peak as would be expected from the large fraction of zinc in each sample. Consequently, the influence of zinc on the pulse height spectrum is to produce a large amount of non-resonant background counts to the resonant iron X-rays used in the Mössbauer analysis. This in turn complicates the setting of the single channel analyzer window around the iron 6.4 keV X-ray peak, resulting in a reduction in the signal-to-noise ratio of the Mössbauer spectra.

Following the testing of the new toroidal detector, it was concluded that the detector operates best in gas flow mode with a flow rate of about $5 \text{ cm}^3 \text{ min}^{-1}$. For detection of γ -rays and X-rays, the highest counting efficiency was obtained using the 90% Kr with 10% CH_4 gas mixture. Three scattering Mössbauer spectra can be recorded simultaneously using the above criteria. For the CEMS analysis, the single channel analyzer is set to count only the electrons with energy between 2 keV and 7 keV. Most of the low energy non-resonant electrons from the detector chassis are filtered out using this setting. From the toroidal detector, pulses from the 6.4 keV X-rays are counted separately by setting the single channel

analyzer window between 4 keV and 7 keV. This setting partially filters out the 8.6 keV X-rays from the zinc. Two single channel analyzers are used to count the γ -rays. One is set to count the pulses from the 14.4 keV radiation using a window between 11.5 keV and 18 keV. The other SCA acceptance window is set between 0.8 keV and 2.5 keV to count the pulses from the 1.8 keV escape peak of krypton. As mentioned earlier in this section, the 1.8 keV escape peak originates from the resonant 14.4 keV γ -rays. Therefore, these pulses can be used to collect a GMS Mössbauer spectrum. In order to accumulate a GMS spectrum, both the 14.4 keV and the 1.8 keV pulses, which are selected using separate single channel analyzers, are simultaneously collected on the same multichannel analyzer board.

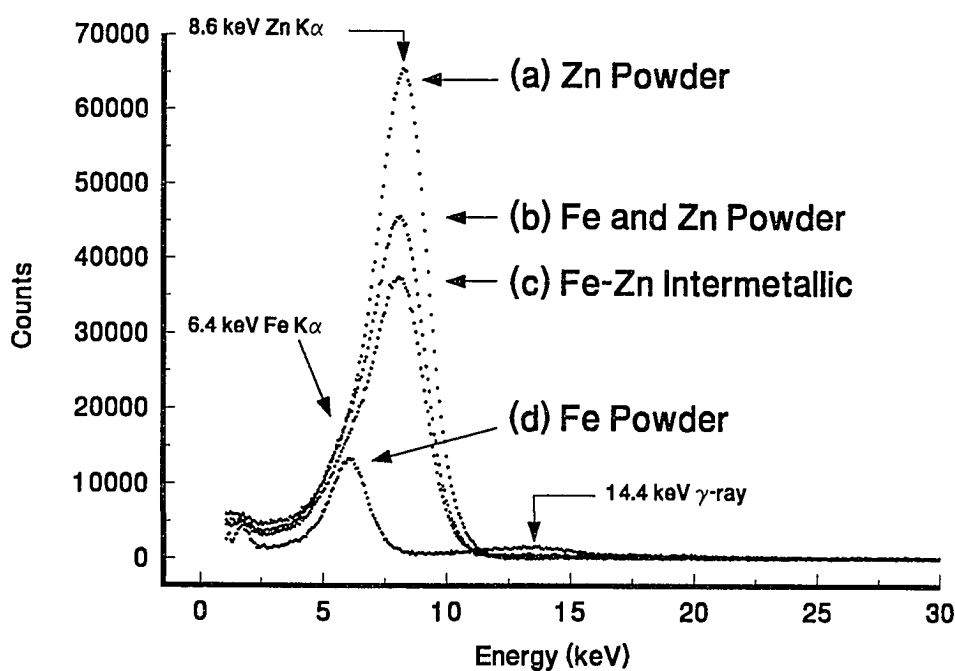


Figure 4.9. Comparison of pulse height spectra of four different samples: Pure iron powder, pure zinc powder, iron-zinc mixture, and an iron-zinc intermetallic.

4.2 Evaluation of the Mössbauer Detector

The evaluation of the detector began by analyzing standard Mössbauer foils. This was performed in order to measure the signal-to-noise ratio and to study the depth profiling characteristics of the detector. Finally, three commercially produced galvaneal coatings were studied to establish that the detector was capable of identifying the different components present in the samples and to determine the relative fraction of each phase present. The scattering spectra were compared with transmission spectra recorded for the same samples.

4.2.1 Mössbauer Analysis of Standard Foils

Mössbauer spectra were recorded using two standard Mössbauer foils which were stacked together to form a bilayered sample. These foils were a 5.1 μm thick stainless steel (Type 310) and a 12.7 μm thick iron foil. At room temperature, stainless steel (fcc γ -Fe) is paramagnetic, and the Mössbauer spectrum is a single absorption peak. The standard iron foil (bcc α -Fe) is ferromagnetic at room temperature, and the Mössbauer spectrum is a sextet. The superimposed contribution of each foil to a Mössbauer spectrum is easily separated. The foils were stacked in two ways. Bilayer SSFE had the foils stacked with the stainless steel on top of the iron foil and toward the incident γ -radiation. This geometry is shown in Figure 4.10. The FESS bilayer reversed the order placing the iron foil closer to the radioactive source. Four spectra were recorded with each of the two bilayer samples. One spectrum was recorded using transmission geometry and three spectra were recorded in

scattering geometry using the new detector. The reversed bilayer sample was studied in order to evaluate the effect of radiation attenuation in the 17.8 μm thick samples.

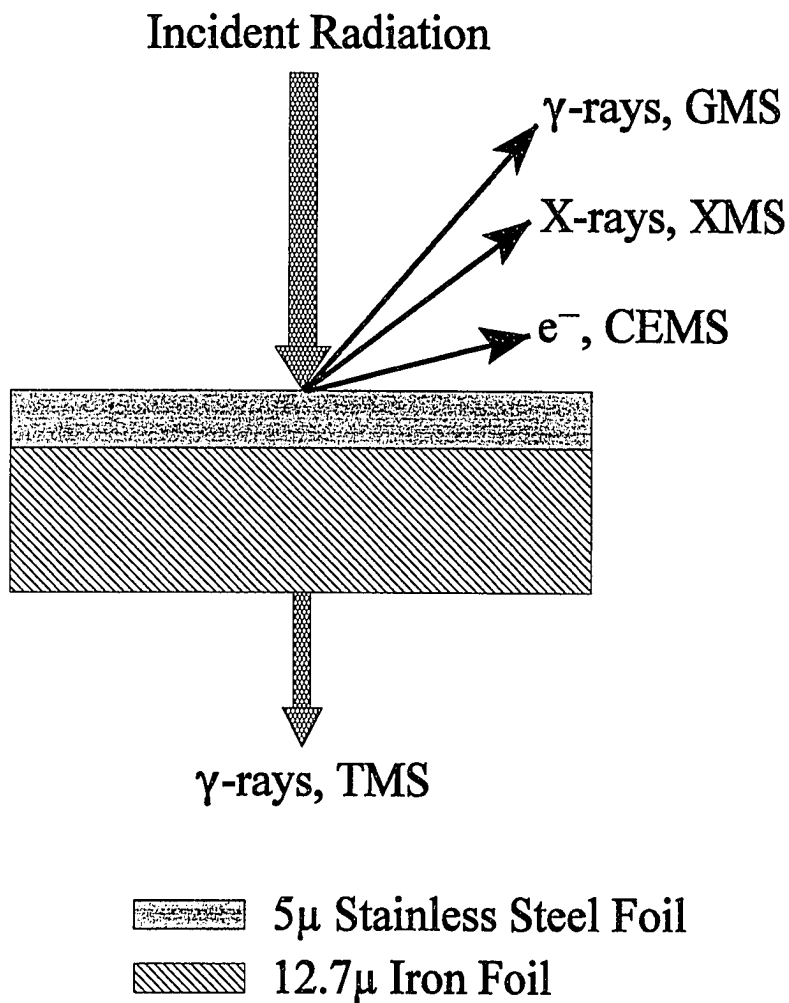
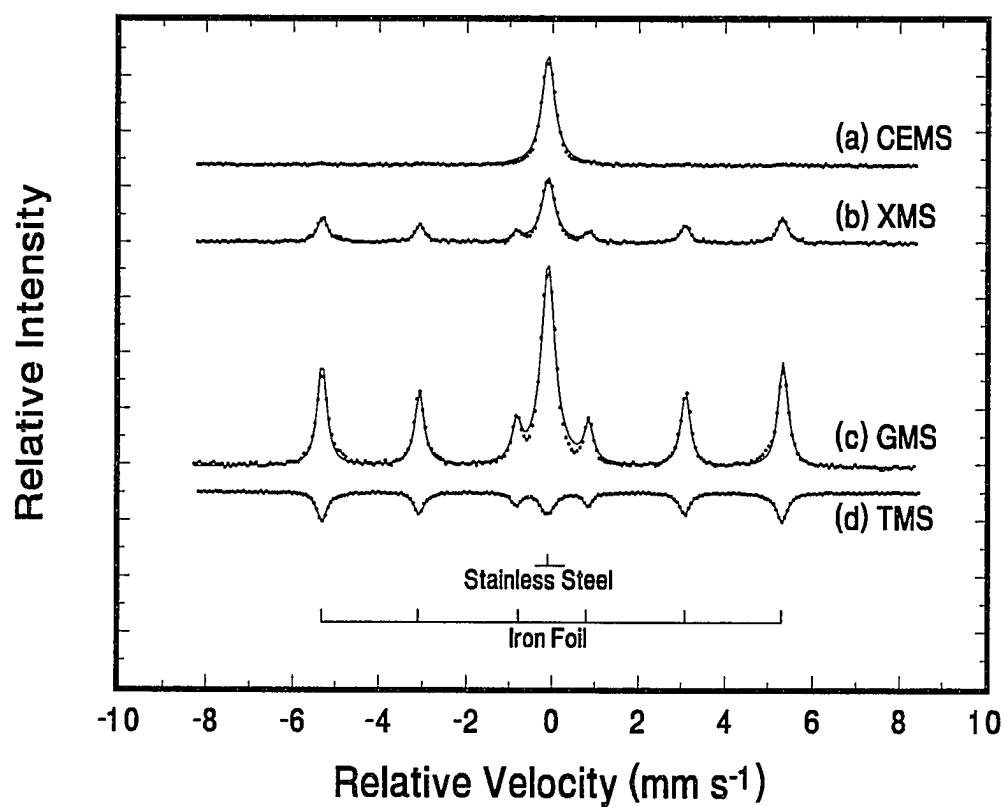


Figure 4.10. Schematic showing the two layered foils used to test the detector. Spectra were recorded simultaneously using GMS, XMS, CEMS and TMS.

Figures 4.11 (a-d) show the four spectra recorded of the bilayer SSFE using CEMS, XMS, GMS and TMS, respectively. The conversion electron spectrum (Figure 4.11 (a)) shows the presence of only the single line of the stainless steel foil. This is expected due to the attenuation of the electrons which restricts the probe depth to less than 0.5 μm . The XMS, GMS and TMS spectra, shown in Figures 4.11 (b), (c) and (d), identify the presence of two subspectra. The singlet spectrum is from the stainless steel foil and is superimposed on the sextet spectrum from the iron foil. The spectra were fitted using standard computer techniques and the relative area of each subspectrum is included with Figure 4.11. These areas are nearly proportional to the number of iron atoms being probed through the Mössbauer effect. The Mössbauer fit parameters correspond with those of the two individual foils. The XMS spectrum shows a slightly lower fraction of the α -Fe sextet than the GMS spectrum due to the higher attenuation of the lower energy X-rays. The relative subspectral areas in the XMS and GMS spectra show small attenuation of the γ -rays and X-rays from the Fe foil since these photons must travel through the stainless steel foil before being detected. The actual path length for some of this radiation can be as large as 36 μm , i.e., twice the bilayer thickness. The TMS spectrum shows that a larger fraction of the α -Fe sextet is present. If there was no attenuation of the γ -radiation through the 17.8 μm thick bilayer, then the theoretical subspectral area due to the α -Fe is about 83%. Also shown are the corrected experimental relative subspectral areas for each geometry and radiation energy. The correction has been made using the attenuation coefficients of the two foils. The details of these calculations are shown in Appendix A. Since these values are closer to the relative



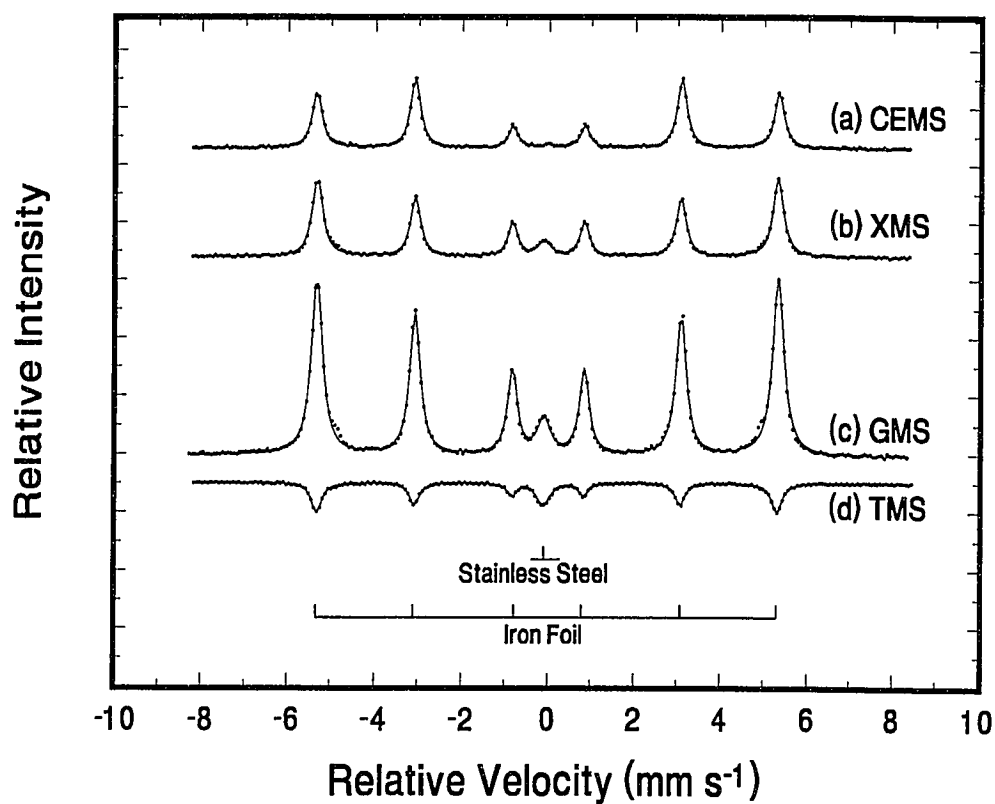
	Relative Areas		Corrected Relative Areas	
	Iron Foil	Stainless Steel	Iron Foil	Stainless Steel
(a) CEMS	3.30	96.70	--	--
(b) XMS	51.26	48.74	70.4	29.6
(c) GMS	55.93	44.07	73.8	26.2
(d) TMS	82.07	17.94	82.3	17.7
Theory	--	--	82.6	17.4

Figure 4.11. Comparison of the Mössbauer spectra: **(a)** CEMS, **(b)** XMS, **(c)** GMS, and **(d)** TMS for the SSFE bilayer configuration.

number of iron atoms actually present, this data can be used to estimate the actual thickness of each foil from the measured subspectral areas.

Figures 4.12 (a-d) show the CEMS, XMS, GMS and TMS spectra of the reversed bilayer sample, FESS, along with the relative subspectral areas. Figure 4.12 (a), shows only the sextet of the iron foil which is closer to the source. Once again, this shows the surface sensitivity of the CEMS geometry. Comparing the XMS and TMS spectra of Figures 4.12 (b) and (c), a similar fraction of the α -Fe and stainless steel foils is being probed with the γ -rays and X-rays. However, when comparing these figures with Figures 4.11 (b) and (c), it is evident that much more of the thicker α -Fe foil is being probed due to the effect of radiation attenuation in the bilayer. The TMS spectrum (Figure 4.12 (d)) is nearly identical to that for the other bilayer geometry shown in Figure 4.11 (d). This is expected since the γ -radiation traverses through 17.8 μm of sample independent of the order of layering of the two foils. The corrected relative areas are in accordance with those in Figure 4.11 and are close to the theoretical values.

In summary, the toroidal detector is able to separately identify the two components in the bilayer foils. The Mössbauer parameters are identical to those expected for the standard calibration foils. When using the scattering geometry, radiation attenuation must be taken into account since the radiation path lengths can be longer than the sample thickness. This will be discussed in the next section with respect to studying galvanneal samples. Although, by application of known attenuation coefficients for each phase, the individual phase thicknesses can be estimated.



	Relative Areas		Corrected Relative Areas	
	Iron Foil	Stainless Steel	Iron Foil	Stainless Steel
(a) CEMS	98.92	1.08	--	--
(b) XMS	95.47	4.53	84.5	15.5
(c) GMS	95.90	4.10	85.4	14.6
(d) TMS	82.00	18.00	83.6	16.4
Theory	--	--	82.6	17.4

Figure 4.12. Comparison of the Mössbauer spectra: (a) CEMS, (b) XMS, (c) GMS, and (d) TMS for the FESS bilayer configuration.

4.2.2 Test on Galvanneal Steel Coatings

Once the detector was found to be operating satisfactorily using the standard Mössbauer calibration foils, three different commercially produced galvanneal coatings were selected to evaluate the detectors performance. The principle aim was to determine the detectors ability to identify the iron-zinc phases present in the coatings as well as their relative abundances.

Analysis of the three coatings was performed solely to test the effectiveness of the new detector in identifying which phases and how much of each phase was present in the coatings. Furthermore, the spectra were analyzed using the parameters compiled in the pure iron-zinc phase database previously discussed in Chapters 1 and 2. It was not the focus of this work to investigate the correlation between the different coatings' metallurgical properties and their compositions. This analysis will be discussed in Chapter 5. The three commercial galvanneal coatings were selected on the basis of their X-ray diffraction spectra. All the XRD patterns were recorded using the same Philips model APD3720 automated powder diffractometer and using the same technique which was discussed in section 2.1.1. The first coating was determined to have a high fraction of the Zeta phase on its surface. The second coating had no Zeta phase but a large amount of a low iron concentration Delta phase on its surface. Finally, the third coating was chosen because it had a large fraction of the high iron concentration end of the Delta phase on its surface. Figure 4.13 shows an overlap of the three XRD spectra from 40° to 45° two-theta. The XRD spectra were compared with the iron-zinc standards discussed in Chapters 1 and 2 in order to identify the phases present in the coatings. Sample A shows a large amount of the Zeta phase on its surface. This is

evident by observing the prominent peaks at approximately 40.1° , 41.5° , and 44.0° two-theta. Samples B and C do not show the presence of the Zeta phase; however, both coatings show the existence of the Delta phase. Specifically, the double peak between 40.5° and 41.0° two-theta, as well as, the most intense peak at approximately 42.2° two-theta are due to Delta peaks, (ref. section 2.1.3). The difference in the peak positions of Sample B and C indicate that Sample B primarily consists of a low iron concentration Delta; whereas, Sample C consists of a high iron concentration Delta.

After the coatings were chosen based on their XRD spectra, a portion of each was stripped from its substrate to further study the coatings and determine if the new detector was probing the entire coating depth. Small strips of each sample, approximately 1 cm wide and 5 cm long, were cut for fracturing. These were then joined to a piece of stainless steel sheet, with an overlap of approximately 1 cm, using PPG Industries, Inc., HC5099 epoxy. The samples were baked at 177°C for 30 minutes to cure the epoxy, removed from the oven and allowed to cool to room temperature. Once cool, the coatings were scored to the substrate with a razor blade and pulled apart as illustrated in Figure 4.14. The coatings were easily stripped from the substrate leaving little or no intermetallic on the steel. With the coating and epoxy still fixed to the stainless steel, the strip could be bent popping off the epoxy and coating. The epoxy was then thinned to 0.5 mm with 600 grit sandpaper making sure not to damage the attached coating. The intact portions of the coatings were analyzed with CEMS and XMS and the fractured samples were analyzed with TMS through the fractured coating, and CEMS on the exposed underside of the coating.

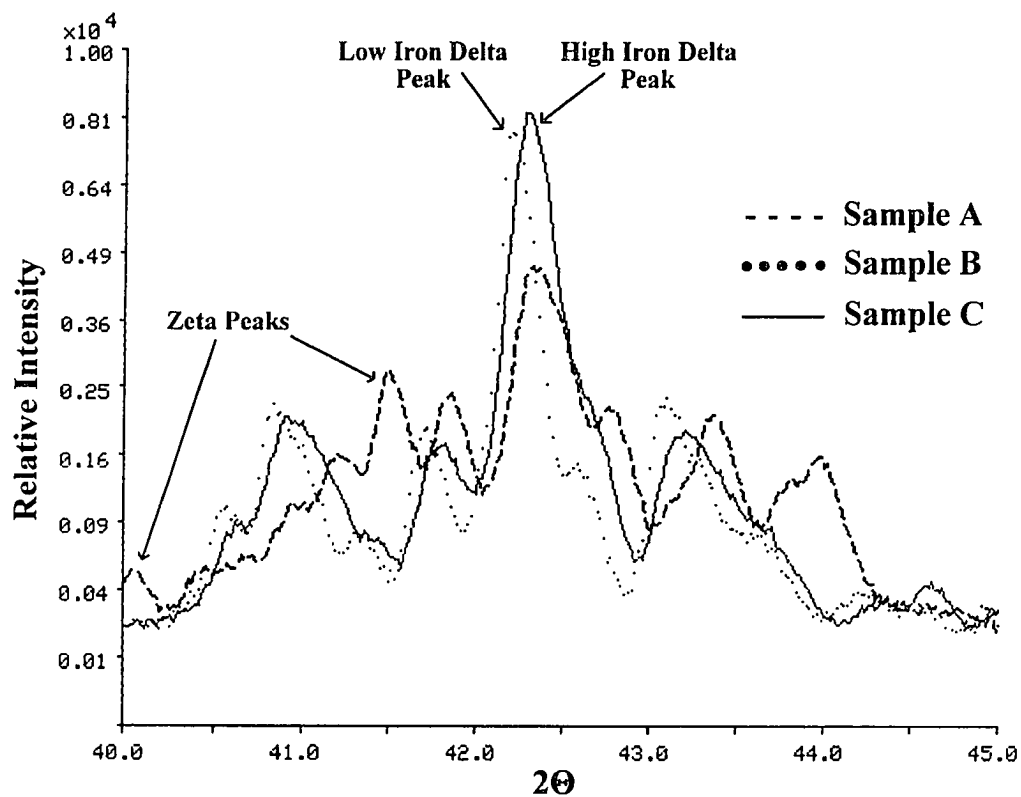


Figure 4.13. Overlap of the XRD spectra of the three coatings from 40° to 45° two-theta. Sample A shows a large amount of the Zeta phase present. Sample B shows the presence of a low iron concentration Delta phase. Sample C shows the presence of a high iron concentration Delta phase.

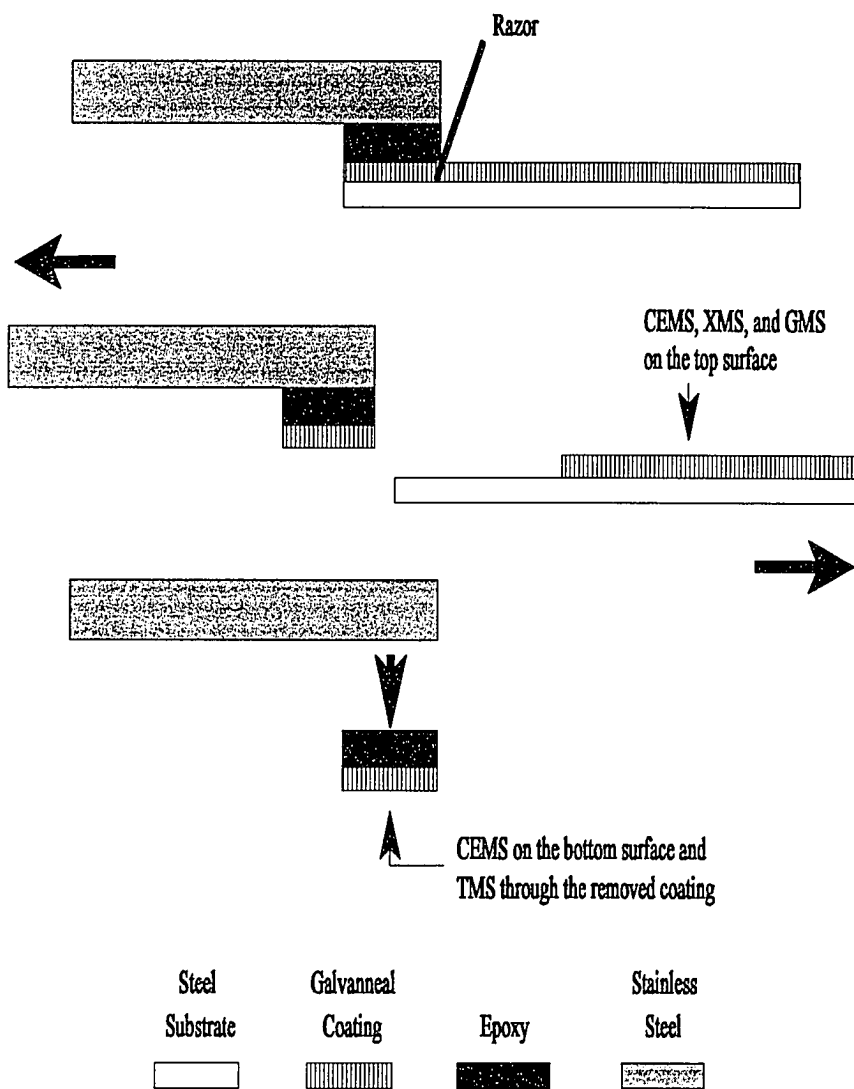


Figure 4.14. Schematic diagram of the fracturing technique used to strip the coatings cleanly off the steel substrate. Also shown are the experiments performed on the intact and fractured coatings.

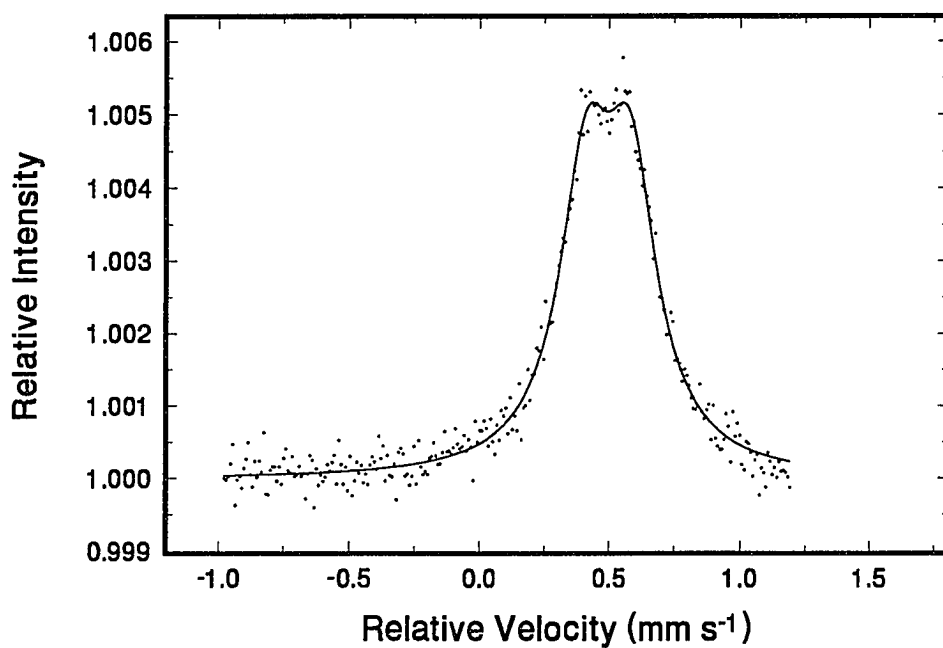
Sample A

Figure 4.15 shows the CEMS spectrum of the intact coating of Sample A. The results show that pure Zeta is present on the surface of the coating. This corresponds with the XRD data which also identified pure Zeta on the coating surface. CEMS on the underside of the fractured coating, as shown in Figure 4.16, shows that a mixture of the Gamma and Gamma-1 phases are located at the bottom of the coating, nearest the steel substrate. The spectrum is comprised of 97% of the Gamma phase and only 3% of the Gamma-1 phase. This could imply that the two phases are not uniformly layered exposing both phases at the surface of the fractured sample. Alternatively, the Gamma phase may be very thin, hence the detection of conversion electrons from the underlying Gamma-1 layer. Furthermore, a small amount of the steel substrate signal is present in the spectrum of this removed coating. These results concur with previous findings that the coatings fracture cleanly from the steel substrate exposing the Gamma phase.³² Recall from Chapter 2 that the Mössbauer parameters of this Gamma phase correspond to the high iron concentration end of the phase.

The TMS analysis of the fractured coating indicates that the coating consists of all four phases, as shown in Figure 4.17. The Delta phase makes up over 50% of the coating composition while the Gamma phase constitutes less than 1% of the coating. The remainder of the coating is comprised of equal amounts of the Zeta and Gamma-1 phases. From this spectrum it is evident that this coating only has a very thin layer of the Gamma phase present. Therefore, the Gamma-1 component observed in the CEMS spectrum of the coating underside is clearly due to the electrons from the Gamma-1 phase penetrating through the very thin Gamma phase and being detected. The XMS analysis of the intact coating of

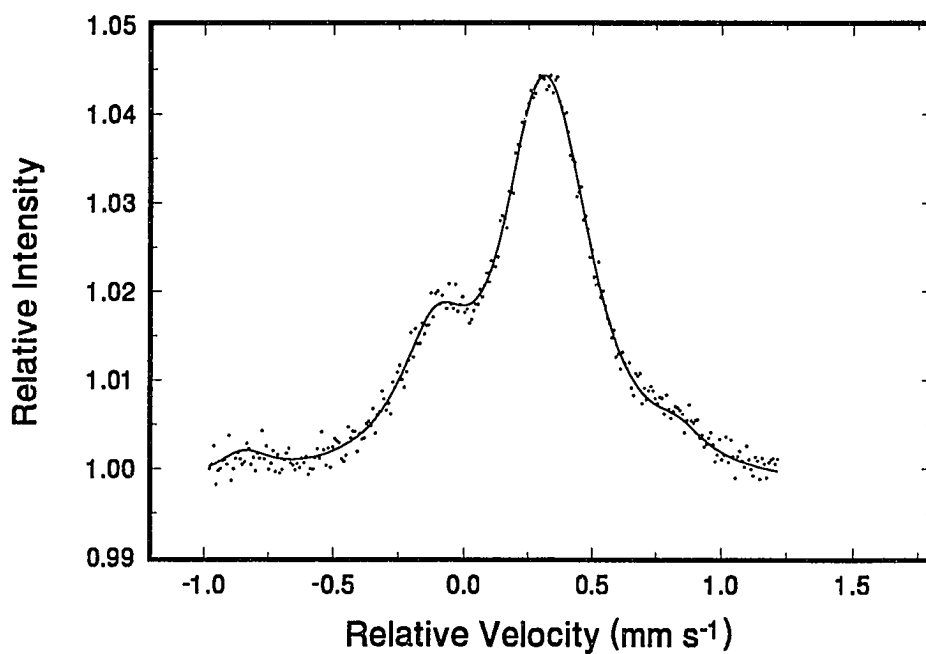
Sample A is shown in Figure 4.18. The strong signal from the steel substrate, as indicated by the peaks at approximately $\pm 0.8 \text{ mm s}^{-1}$, shows that the detector is able to easily probe through the entire coating and into the substrate. Since the Mössbauer parameters of the steel substrate are well known, its spectrum can be easily subtracted away leaving only the spectrum of the coating. This subtraction spectrum is shown in Figure 4.19 and then compared with the TMS spectrum in Figure 4.20.

The fit parameters of these spectra and the fit parameters of the pure iron-zinc standard phases (ref. section 2.2.2) are quite comparable. As indicated in the table of fit parameters in Figure 4.19, the relative fraction of each phase appear to be different than in the TMS spectrum. This difference is due to the attenuation of the γ -rays and X-rays through the coating, as discussed in section 4.2.1, and can be accounted for in order to determine the actual coating composition. The attenuation coefficients for each of the four iron-zinc phases have been calculated and are listed in Appendix B.



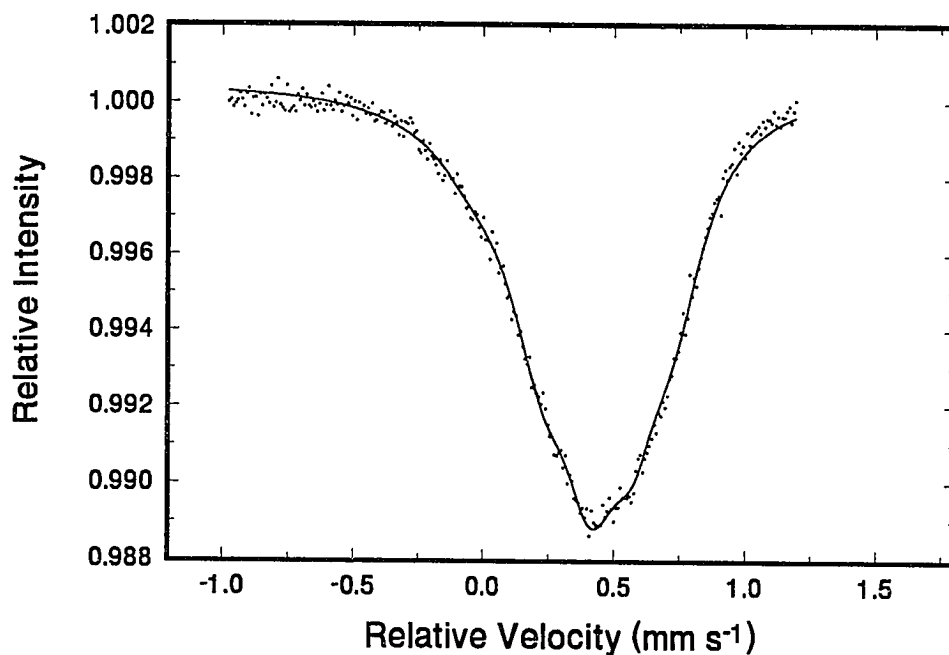
	Isomer Shift (mm s ⁻¹)	Quadrupole Splitting (mm s ⁻¹)	Linewidth (mm s ⁻¹)	Relative Area (%)	Phase Fraction (%)
Zeta	0.489	0.153	0.224	100.0	100.0
Delta A	--	--	--	0.0	0.0
B	--	--	--	0.0	
C	--	--	--	0.0	
Gamma-1 A	--	--	--	0.0	0.0
B	--	--	--	0.0	
C	--	--	--	0.0	
Gamma A	--	--	--	0.0	0.0
B	--	--	--	0.0	
Iron Base	--	--	--	0.0	

Figure 4.15. Mössbauer spectrum of the surface of Sample A recorded at 300 K using CEMS. The coating has pure Zeta on the surface.



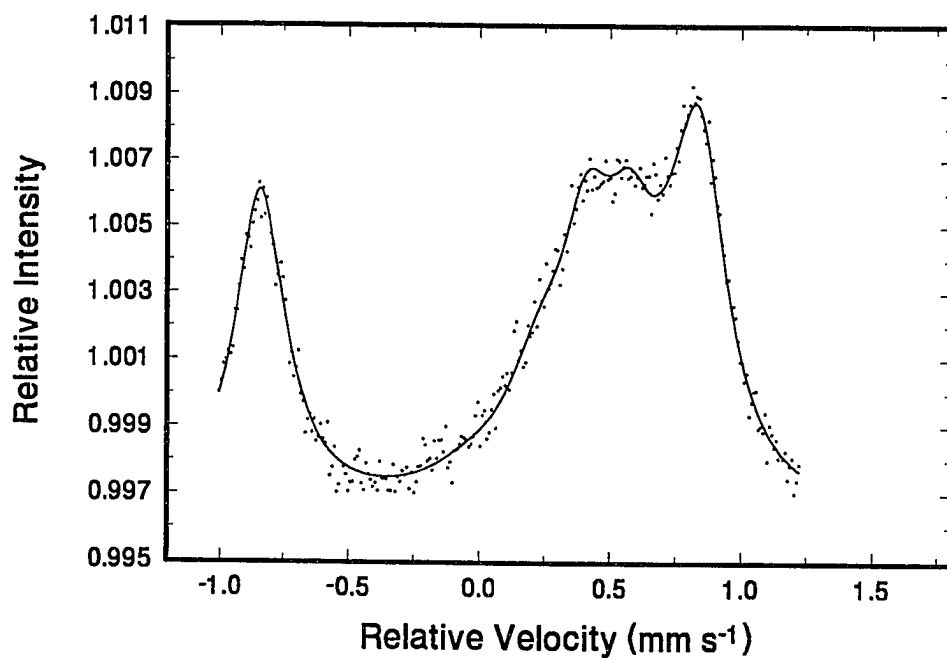
	Isomer Shift (mm s ⁻¹)	Quadrupole Splitting (mm s ⁻¹)	Linewidth (mm s ⁻¹)	Relative Area (%)	Phase Fraction (%)
Zeta	--	--	--	0.0	0.00
Delta A	--	--	--	0.0	0.00
B	--	--	--	0.0	
C	--	--	--	0.0	
Gamma-1 A	0.470	0.079	0.298	1.4	3.2 ± 10%
B	-0.042	0.555	0.294	0.2	
C	0.042	0.224	0.394	1.4	
Gamma A	0.322	0.120	0.285	53.7	96.8 ± 5%
B	0.105	0.380	0.288	36.7	
Iron Base	-0.036	0.000	0.265	6.7	

Figure 4.16. Mössbauer spectrum of the underside of Sample A recorded using CEMS. The spectrum shows Γ with a small amount of the Γ_1 phase.



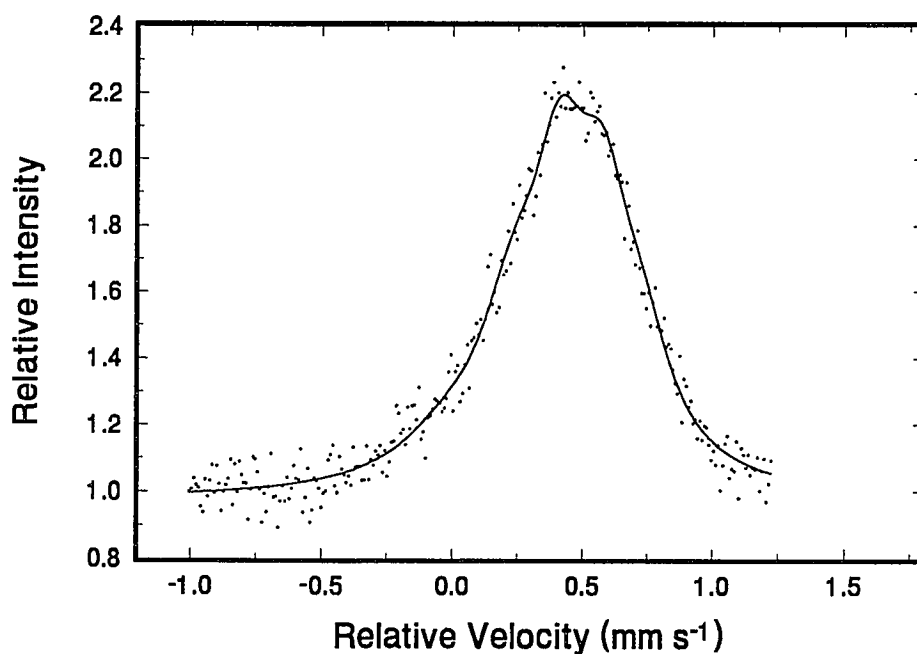
	Isomer Shift (mm s ⁻¹)	Quadrupole Splitting (mm s ⁻¹)	Linewidth (mm s ⁻¹)	Relative Area (%)	Phase Fraction (%)
Zeta	0.494	0.153	0.244	25.5	25.5 ± 7%
Delta A	0.474	0.486	0.275	28.8	44.0 ± 5%
B	0.476	0.162	0.292	14.0	
C	0.299	0.270	0.285	1.2	
Gamma-1 A	0.470	0.079	0.298	11.4	24.7 ± 7%
B	-0.042	0.555	0.294	1.6	
C	0.042	0.224	0.394	11.7	
Gamma A	0.322	0.120	0.285	3.4	5.8 ± 10%
B	0.105	0.380	0.288	2.4	
Iron Base	--	--	--	0.00	

Figure 4.17. Mössbauer spectrum of Sample A recorded at 300 K using TMS. The spectrum shows the presence of all four phases.



	Isomer Shift (mm s ⁻¹)	Quadrupole Splitting (mm s ⁻¹)	Linewidth (mm s ⁻¹)	Relative Area (%)	Phase Fraction (%)
Zeta	0.494	0.153	0.244	17.4	37.0 ± 5%
Delta A	0.474	0.486	0.275	12.3	43.4 ± 5%
B	0.476	0.162	0.292	7.8	
C	0.299	0.270	0.285	0.4	
Gamma-1 A	0.470	0.079	0.298	3.5	15.9 ± 10%
B	-0.042	0.555	0.294	0.5	
C	0.042	0.224	0.394	3.6	
Gamma A	0.322	0.120	0.285	1.0	3.7 ± 10%
B	0.105	0.380	0.288	0.7	
Iron Base	0.000	0.000	0.255	52.8	

Figure 4.18. Mössbauer spectrum of Sample A recorded at 300 K using XMS.



	Isomer Shift (mm s ⁻¹)	Quadrupole Splitting (mm s ⁻¹)	Linewidth (mm s ⁻¹)	Relative Area (%)	Phase Fraction (%)
Zeta	0.494	0.153	0.244	36.8	36.8 ± 5%
Delta A	0.474	0.486	0.275	26.0	43.4 ± 5%
B	0.476	0.162	0.292	16.6	
C	0.299	0.270	0.285	0.8	
Gamma-1 A	0.470	0.079	0.298	7.4	15.9 ± 10%
B	-0.042	0.555	0.294	1.0	
C	0.042	0.224	0.394	7.6	
Gamma A	0.322	0.120	0.285	2.2	3.7 ± 10%
B	0.105	0.380	0.288	1.5	
Iron Base	--	--	--	0.0	

Figure 4.19. Mössbauer spectrum of Sample A recorded at 300 K using XMS with the iron base signal subtracted away.

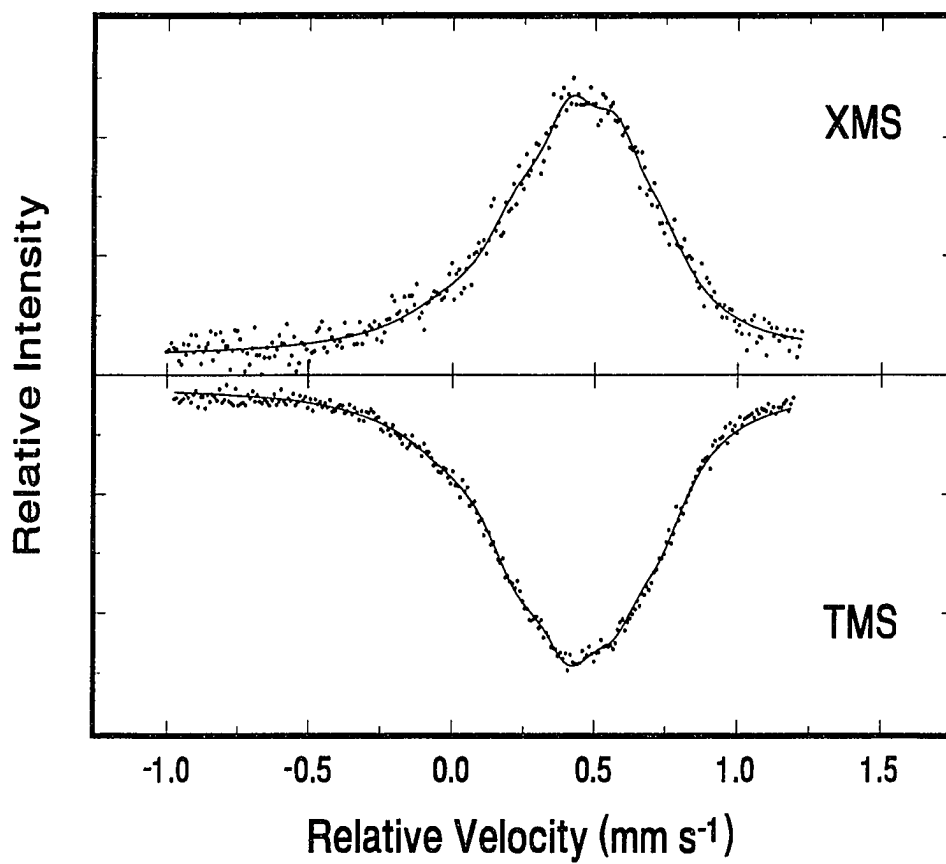
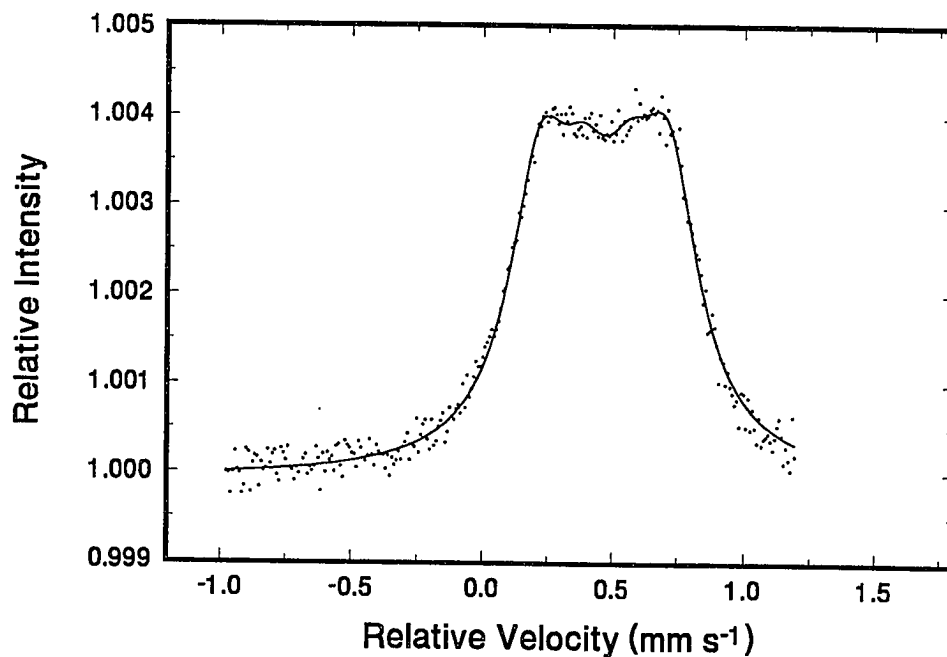


Figure 4.20. Comparison of the XMS and TMS Mössbauer spectra of Sample A.

Sample B

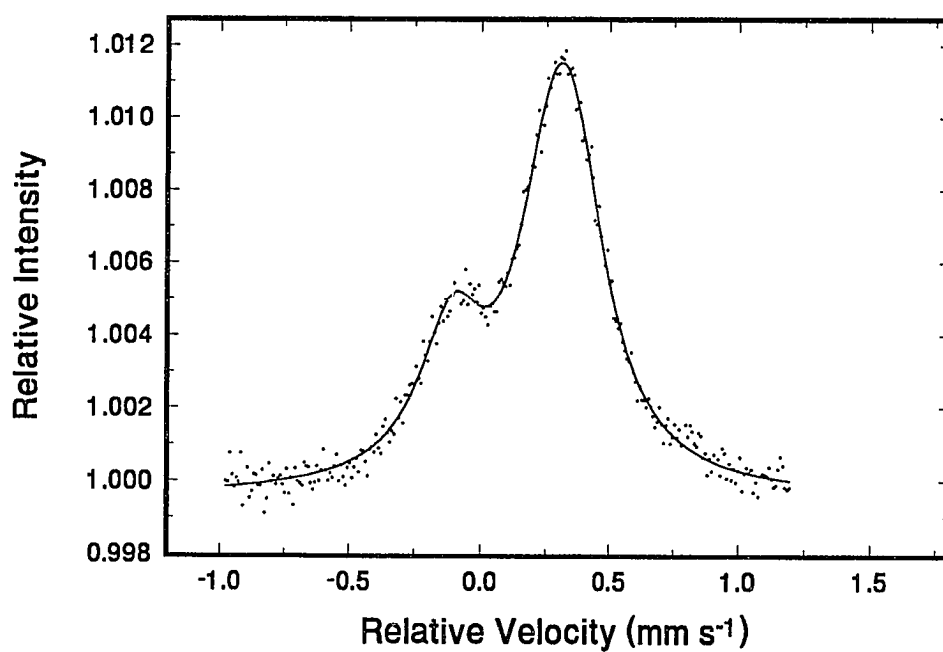
The CEMS spectrum of the intact coating of Sample B is shown in Figure 4.21. The results show that pure low iron concentration Delta is present on the surface of the coating. This is consistent with the XRD data, shown in Figure 4.13. Neither the XRD spectrum nor the CEMS spectrum indicate the presence of the Zeta phase in this coating. The CEMS spectrum from the underside of the fractured coating is shown in Figure 4.22. This spectrum shows that pure high iron concentration Gamma is located on the coating underside at the coating-substrate interface, in support of previously reported results.³² Comparing this spectrum with Sample A, one concludes that this sample must contain a larger amount of the Gamma phase since no Gamma-1 is observed.

The TMS analysis of Sample B is shown in Figure 4.23. Analysis of this spectrum shows that the Delta phase makes up approximately 71% of the coating composition while the Gamma-1 and Gamma phases constitute 15% and 14%, respectively. This amount of the Gamma phase confirms the conclusion from the CEMS spectrum of the fractured surface which identified a much thicker Gamma phase than in Sample A. XMS analysis of the intact coating of Sample B is shown in Figure 4.24. The XMS spectrum minus the steel substrate signal is shown in Figure 4.25; then compared with the TMS spectrum in Figure 4.26. Again, the relative fraction of each phase appears different from the TMS spectrum due to the attenuation of the γ -rays and X-rays through coating. As was demonstrated in the last section, this attenuation can be accounted for in order to obtain the same coating composition observed using TMS. Significantly, the fitted Mössbauer parameters once again strongly agree with those of the standard phases.



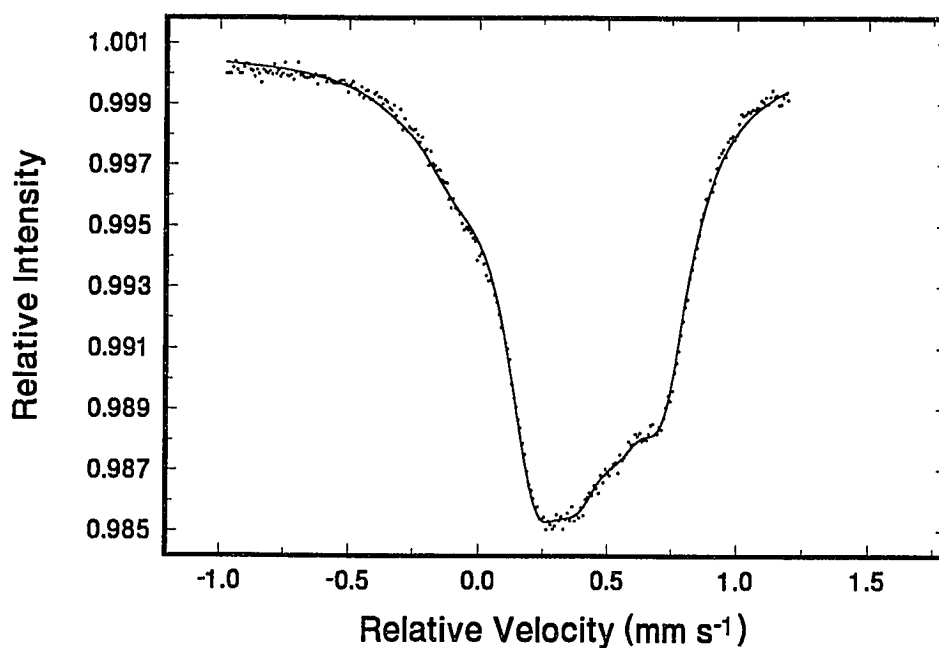
	Isomer Shift (mm s ⁻¹)	Quadrupole Splitting (mm s ⁻¹)	Linewidth (mm s ⁻¹)	Relative Area (%)	Phase Fraction (%)
Zeta	--	--	--	--	0.0
Delta A	0.465	0.500	0.254	59.8	100.0
B	0.473	0.175	0.273	38.3	
C	0.297	0.270	0.269	1.9	
Gamma-1 A	--	--	--	--	0.0
B	--	--	--	--	
C	--	--	--	--	
Gamma A	--	--	--	--	0.0
B	--	--	--	--	
Iron Base	--	--	--	--	

Figure 4.21. Mössbauer spectrum of the surface of Sample B recorded at 300 K using CEMS. The coating has a pure low at.% Fe Delta phase on the surface.



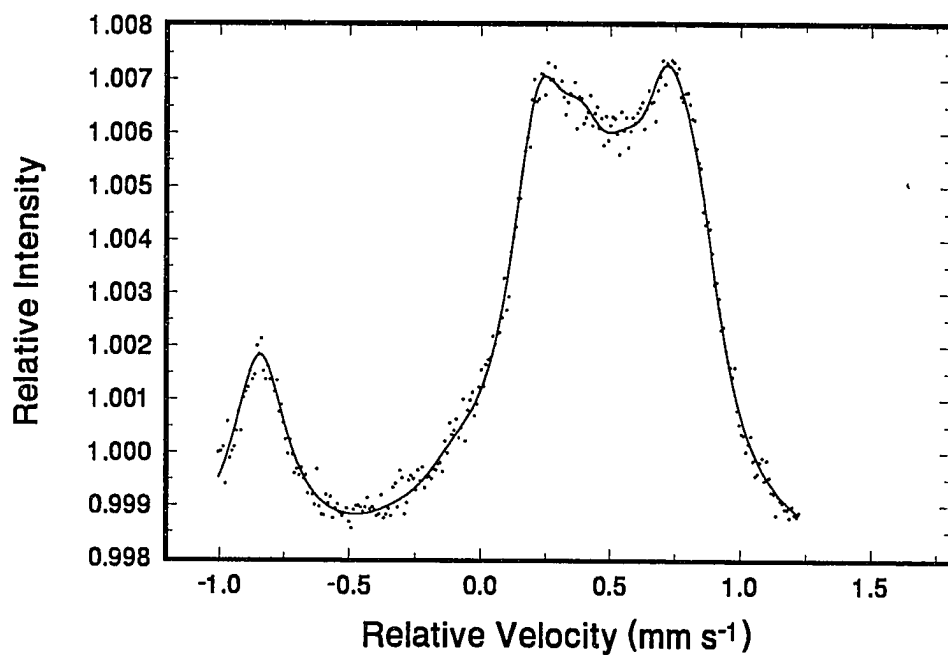
	Isomer Shift (mm s ⁻¹)	Quadrupole Splitting (mm s ⁻¹)	Linewidth (mm s ⁻¹)	Relative Area (%)	Phase Fraction (%)
Zeta	--	--	--	--	0.0
Delta A	--	--	--	--	0.0
B	--	--	--	--	
C	--	--	--	--	
Gamma-1 A	--	--	--	--	0.0
B	--	--	--	--	
C	--	--	--	--	
Gamma A	0.292	0.056	0.285	58.8	100.0
B	0.133	0.484	0.288	41.2	
Iron Base	--	--	--	--	

Figure 4.22. Mössbauer spectrum of the underside of Sample B recorded at 300 K using CEMS. The spectrum shows the presence of a high at.% Fe Gamma phase.



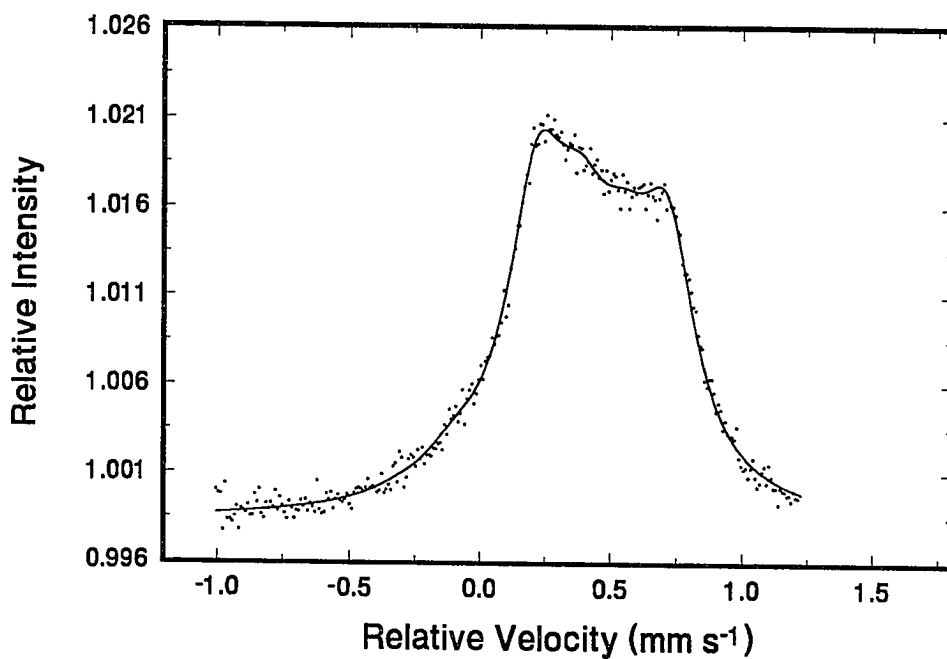
	Isomer Shift (mm s ⁻¹)	Quadrupole Splitting (mm s ⁻¹)	Linewidth (mm s ⁻¹)	Relative Area (%)	Phase Fraction (%)
Zeta	--	--	--	--	0.00
Delta A	0.465	0.500	0.254	42.2	70.5 ± 5%
B	0.473	0.175	0.273	26.9	
C	0.297	0.270	0.269	1.4	
Gamma-1 A	0.467	0.079	0.280	7.0	15.4 ± 10%
B	-0.462	0.546	0.282	1.5	
C	0.043	0.225	0.365	6.9	
Gamma A	0.292	0.056	0.285	8.3	14.1 ± 10%
B	0.133	0.484	0.288	5.8	
Iron Base	--	--	--	--	

Figure 4.23. Mössbauer spectrum of Sample B recorded at 300 K using TMS. The spectrum shows the presence of the Delta, Gamma-1, and Gamma phase.



	Isomer Shift (mm s ⁻¹)	Quadrupole Splitting (mm s ⁻¹)	Linewidth (mm s ⁻¹)	Relative Area (%)	Phase Fraction (%)
Zeta	--	--	--	--	0.0
Delta A	0.465	0.500	0.254	34.8	78.2 ± 5%
B	0.473	0.175	0.273	19.7	
C	0.297	0.270	0.269	1.5	
Gamma-1 A	0.467	0.079	0.280	3.7	11.4 ± 10%
B	-0.462	0.546	0.282	0.8	
C	0.043	0.225	0.365	3.7	
Gamma A	0.292	0.056	0.285	4.4	10.4 ± 10%
B	0.133	0.484	0.288	3.1	
Iron Base	-0.007	0.000	0.260	28.3	

Figure 4.24. Mössbauer spectrum of Sample B recorded at 300 K using XMS.



	Isomer Shift (mm s ⁻¹)	Quadrupole Splitting (mm s ⁻¹)	Linewidth (mm s ⁻¹)	Relative Area (%)	Phase Fraction (%)
Zeta	--	--	--	--	0.0
Delta A	0.465	0.500	0.254	48.7	78.3 ± 5%
B	0.473	0.175	0.273	27.5	
C	0.297	0.270	0.269	2.1	
Gamma-1 A	0.467	0.079	0.280	5.2	11.4 ± 10%
B	-0.462	0.546	0.282	1.1	
C	0.043	0.225	0.365	5.1	
Gamma A	0.292	0.056	0.285	6.1	10.3 ± 10%
B	0.133	0.484	0.288	4.2	
Iron Base	--	--	--	--	

Figure 4.25. Mössbauer spectrum of Sample B recorded at 300 K using XMS with the iron base signal subtracted away.

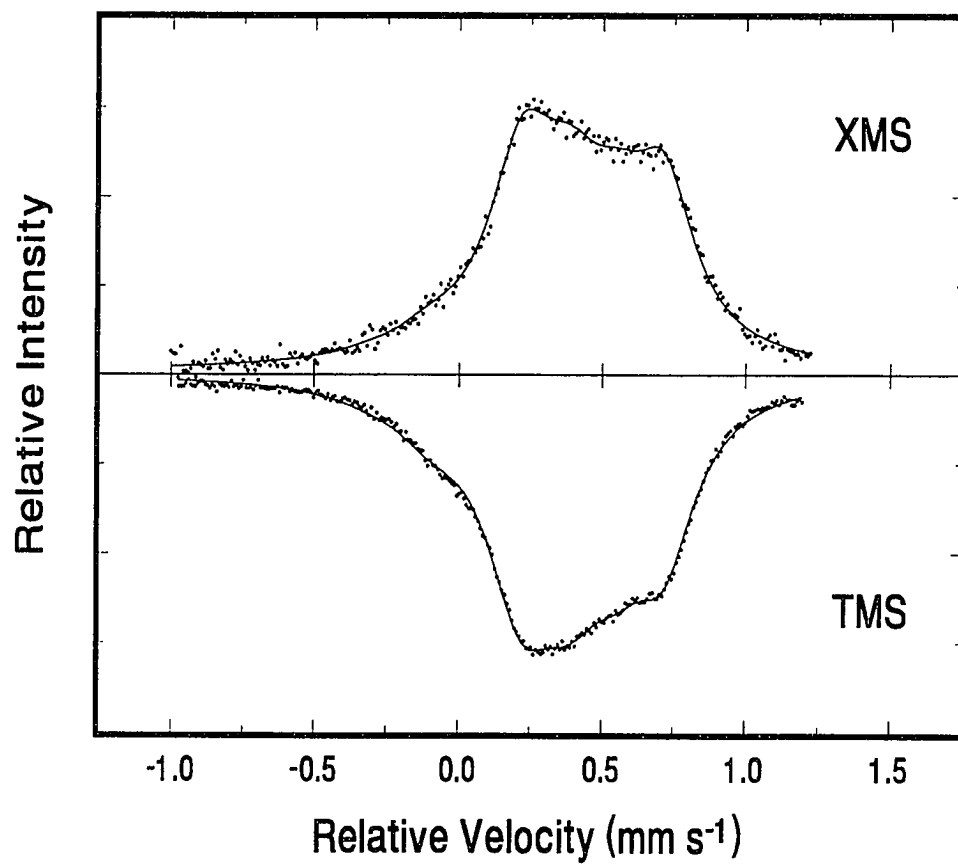
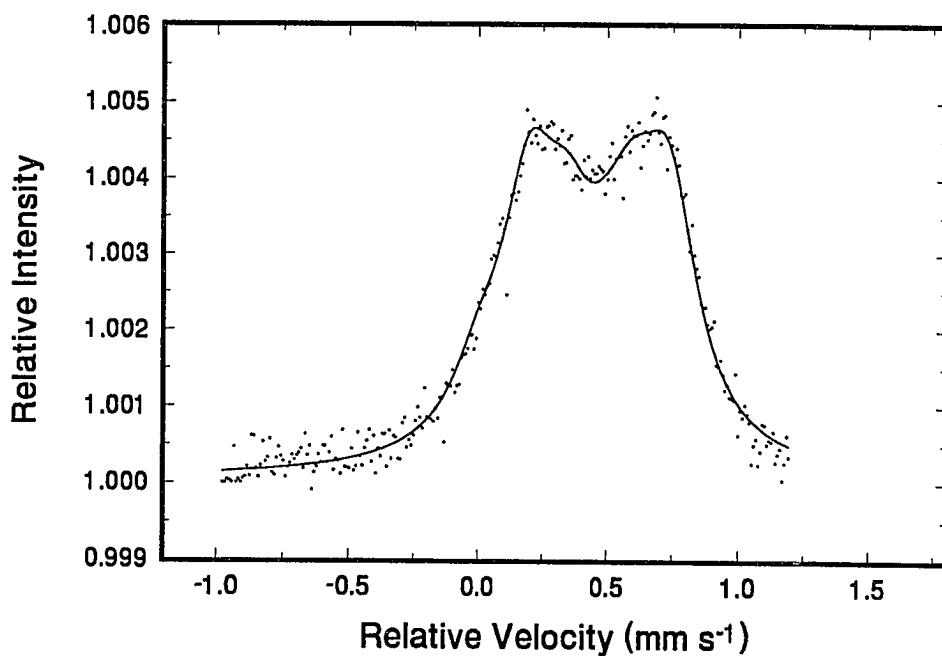


Figure 4.26. Comparison of the XMS and TMS Mössbauer spectra of Sample B.

Sample C

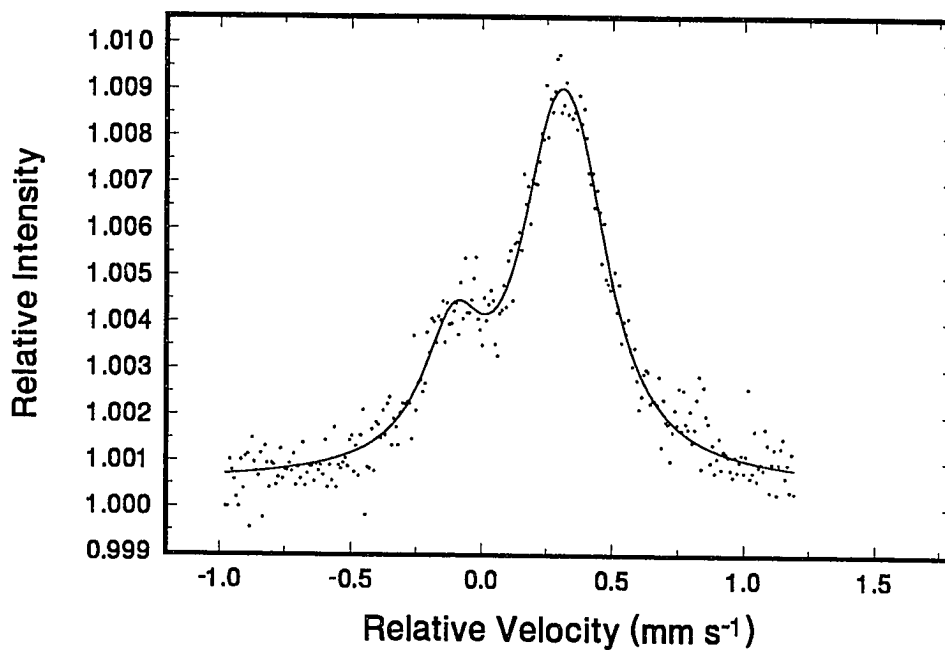
Figure 4.27 shows the CEMS spectrum of the intact coating of Sample C. The results show that a high iron concentration Delta is present on the surface of the coating with no Zeta phase present. This was also observed in the XRD analysis. CEMS on the underside of the fractured coating, shown in Figure 4.28, again isolates pure high iron concentration Gamma on the underside of the coating in contact with the steel substrate.

The TMS analysis of the fractured coating indicates that the coating is composed of the Delta, Gamma-1, and Gamma phases, as shown in Figure 4.29. The Delta phase constitutes approximately 55% of the coating composition, while the Gamma-1 phase approximately 20%, and the Gamma phase approximately 25%. XMS analysis of Sample C, shown in Figure 4.30, once again demonstrates that the detector successfully probed the entire coating reaching the steel substrate. After subtracting away the steel substrate spectrum, as shown in Figures 4.31 and 4.32, we compare the remaining coating spectrum with the TMS results. As previously observed, the XMS phase fractions are different than the TMS fractions due to the attenuation of the γ -rays and X-rays. Nevertheless, this difference can be accounted for, as was previously shown in section 4.2.1. Once again the Mössbauer parameters agree with those of the pure standards.



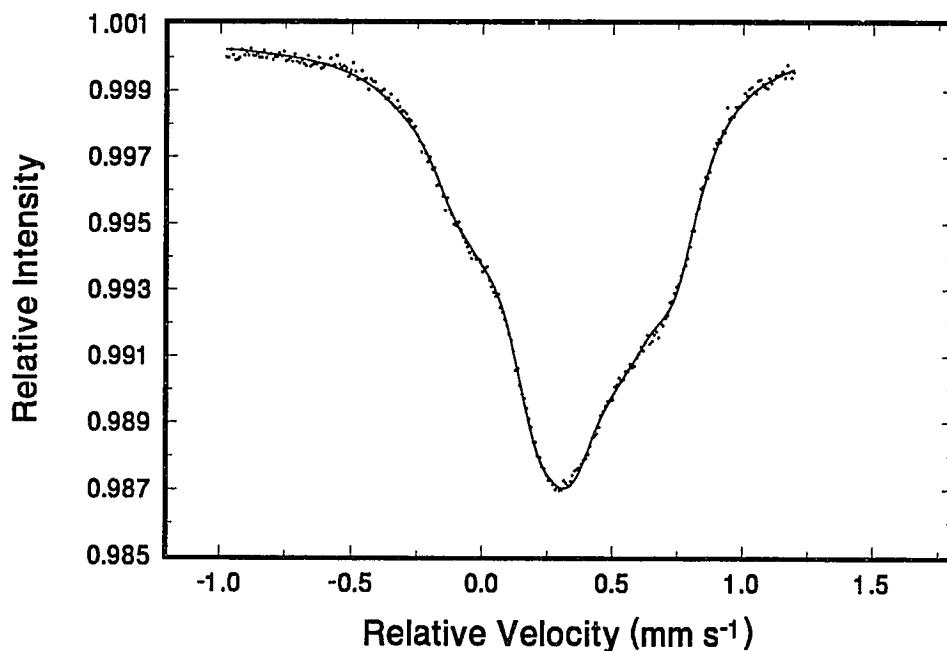
	Isomer Shift (mm s ⁻¹)	Quadrupole Splitting (mm s ⁻¹)	Linewidth (mm s ⁻¹)	Relative Area (%)	Phase Fraction (%)
Zeta	--	--	--	--	0.0
Delta A	0.465	0.540	0.261	51.2	100.0
B	0.470	0.253	0.260	33.6	
C	0.251	0.492	0.268	15.2	
Gamma-1 A	--	--	--	--	0.0
B	--	--	--	--	
C	--	--	--	--	
Gamma A	--	--	--	--	0.0
B	--	--	--	--	
Iron Base	--	--	--	--	

Figure 4.27. Mössbauer spectrum of the surface of Sample C recorded at 300 K using CEMS. The coating has a pure high at.% Fe Delta phase on the surface.



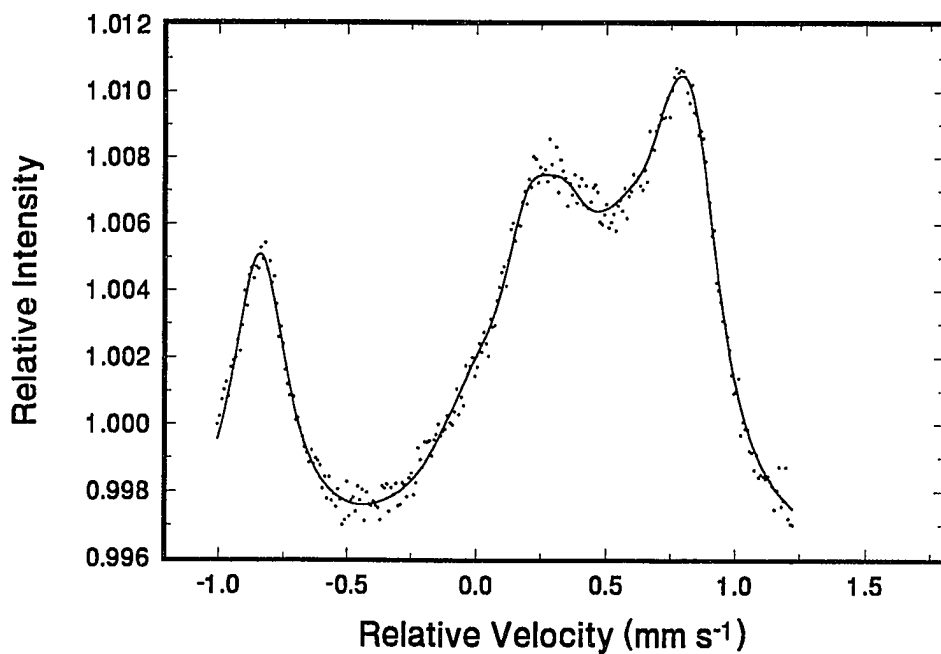
	Isomer Shift (mm s ⁻¹)	Quadrupole Splitting (mm s ⁻¹)	Linewidth (mm s ⁻¹)	Relative Area (%)	Phase Fraction (%)
Zeta	--	--	--	--	0.0
Delta A	--	--	--	--	0.0
B	--	--	--	--	
C	--	--	--	--	
Gamma-1 A	--	--	--	--	0.0
B	--	--	--	--	
C	--	--	--	--	
Gamma A	0.292	0.061	0.275	62.3	100.0
B	0.140	0.498	0.275	37.7	
Iron Base	--	--	--	--	

Figure 4.28. Mössbauer spectrum of the underside of Sample C recorded at 300 K using CEMS. The spectrum shows the presence of a high at.% Fe Gamma phase.



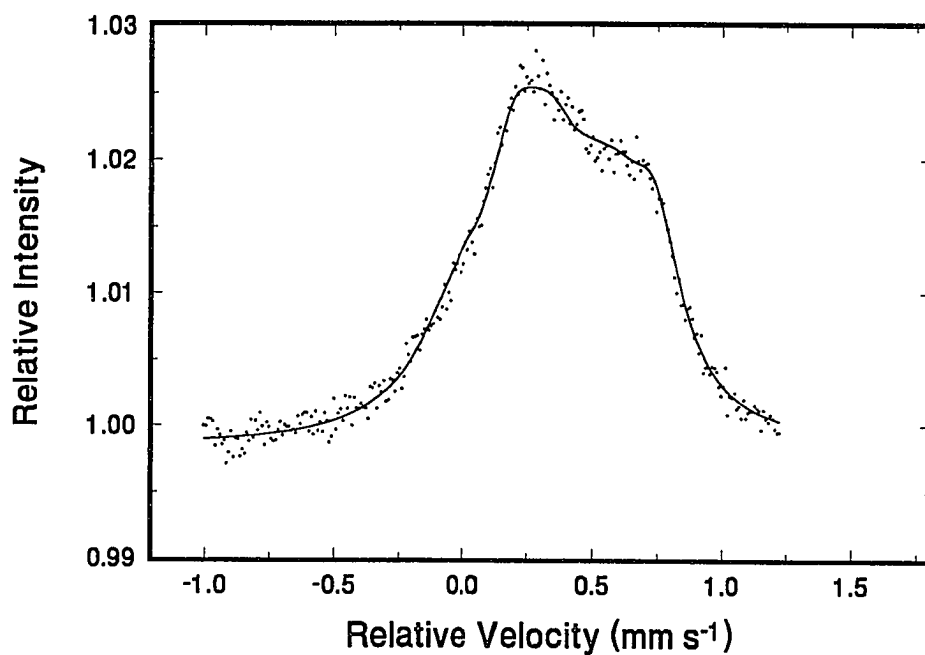
	Isomer Shift (mm s ⁻¹)	Quadrupole Splitting (mm s ⁻¹)	Linewidth (mm s ⁻¹)	Relative Area (%)	Phase Fraction (%)
Zeta	--	--	--	--	0.0
Delta A	0.465	0.540	0.261	29.0	55.5 ± 5%
B	0.470	0.253	0.260	18.2	
C	0.251	0.492	0.268	8.3	
Gamma-1 A	0.470	0.079	0.280	9.0	19.6 ± 10%
B	-0.043	0.546	0.282	1.9	
C	0.042	0.225	0.365	8.7	
Gamma A	0.292	0.061	0.275	14.5	24.9 ± 7%
B	0.140	0.498	0.275	10.4	
Iron Base	--	--	--	--	

Figure 4.29. Mössbauer spectrum of Sample C recorded at 300 K using TMS. The spectrum shows the presence of the Delta, Gamma-1, and Gamma phase.



	Isomer Shift (mm s ⁻¹)	Quadrupole Splitting (mm s ⁻¹)	Linewidth (mm s ⁻¹)	Relative Area (%)	Phase Fraction (%)
Zeta	--	--	--	--	0.0
Delta A	0.465	0.540	0.261	23.2	75.1 ± 5%
B	0.470	0.253	0.260	12.6	
C	0.251	0.492	0.268	7.9	
Gamma-1 A	0.470	0.079	0.280	3.0	11.0 ± 10%
B	-0.043	0.546	0.282	0.6	
C	0.042	0.225	0.365	2.8	
Gamma A	0.292	0.061	0.275	4.7	13.9 ± 10%
B	0.140	0.498	0.275	3.4	
Iron Base	-0.002	0.000	0.260	41.8	

Figure 4.30. Mössbauer spectrum of Sample C recorded at 300 K using XMS.



	Isomer Shift (mm s ⁻¹)	Quadrupole Splitting (mm s ⁻¹)	Linewidth (mm s ⁻¹)	Relative Area (%)	Phase Fraction (%)
Zeta	--	--	--	--	0.0
Delta A	0.465	0.540	0.261	38.8	75.0 ± 5%
B	0.470	0.253	0.260	21.4	
C	0.251	0.492	0.268	14.9	
Gamma-1 A	0.470	0.079	0.280	5.1	11.0 ± 10%
B	-0.043	0.546	0.282	1.1	
C	0.042	0.225	0.365	4.9	
Gamma A	0.292	0.061	0.275	8.2	14.0 ± 10%
B	0.140	0.498	0.275	5.8	
Iron Base	--	--	--	--	

Figure 4.31. Mössbauer spectrum of Sample C recorded at 300 K using XMS with the iron base signal subtracted away.

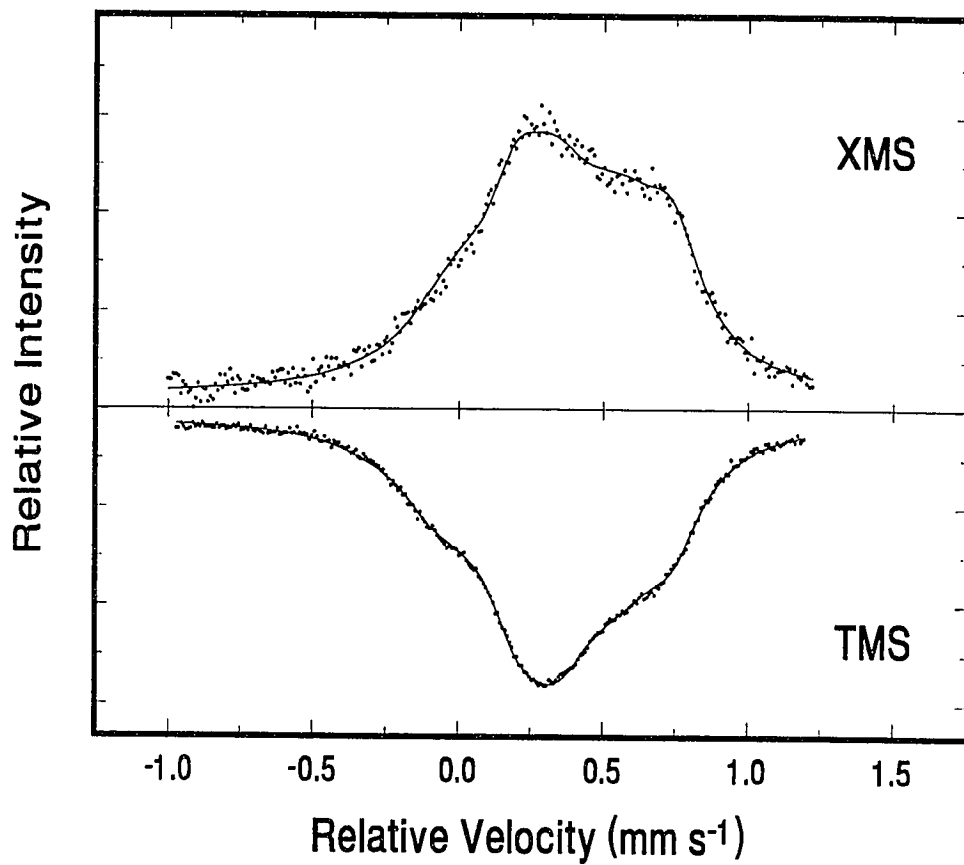


Figure 4.32. Comparison of the XMS and TMS Mössbauer spectra of Sample C.

4.3 Summary

The newly constructed and tested Mössbauer detector effectively analyzed galvanneal coatings in-situ. Tests showed that in selecting a detector geometry which was toroidal, it was possible to eliminate the detection of the direct radiation from the source. This allowed the spectra to be recorded with a higher signal-to-noise ratio and resulted in better resolved spectra with lower counting times. The detector was able to collect X-rays and γ -rays simultaneously when operated with krypton gas. This resulted in a significant improvement in the count rate since both radiations provide information about the coating microstructure. Addition of a CEMS detector to the main detector permits probing the near surface region of the coating.

Mössbauer analysis of bilayer foils showed that the detector could accurately identify each component present. The studies of the three commercial galvanneal coatings demonstrated that the detector system is able to identify the phases present in galvanneal coatings and that the Mössbauer parameters strongly agree with the pure iron-zinc standards discussed in Chapters 1 and 2. Furthermore, the detector can differentiate between a high and a low iron concentration Delta formed in a galvanneal coating. Finally, with the development and testing of this new detector, it is now possible to study commercially produced galvanneal coatings in-situ, in order to investigate their properties. This is the focus of the next chapter in which several commercially produced coatings are studied with XRD, CEMS, and GMS, and the results compared with the metallurgical properties.

CHAPTER FIVE

Galvanneal Steel Coating Analysis

Producing galvanneal coatings for specific applications requires the ability to identify the phases formed during the galvannealing process. An understanding of the microstructural properties of the phases is required to control their formation as well. Until recently, the lack of detailed information on the microstructural properties of the phases has made phase identification difficult, inhibiting the advancement of coating quality control. Through the careful preparation and analysis of high purity iron-zinc alloys (described in Chapters 1 and 2), we have compiled a data-base of the crystallographic and other microstructural properties for each of the main iron-zinc phases which will aid in the study of galvanneal coatings.

Another complicating factor in coating analysis has been the inability of standard cylindrical scattering Mössbauer detectors to provide adequate spectral resolution to confidently determine coating composition. This resulted from the direct source radiation decreasing the signal to noise ratio of the detector. As described in Chapter 4, a newly developed toroidal detector overcame this problem providing the tool necessary for efficient

analysis of commercially produced galvanneal coatings. With this detector and the compiled database, several commercially produced galvanneal coatings have been analyzed in an attempt to identify the phases present in the coatings. The amount of each phase and the relative iron concentration of each phase were determined and compared with the metallographic results supplied to us by the galvanneal producers. Coatings were analyzed using XRD, CEMS, and GMS Mössbauer spectroscopy. The coatings were then stripped from their steel substrates and analyzed with transmission Mössbauer spectroscopy as was described in section 4.2.2. Studying the coatings using TMS, CEMS, and GMS provided a complete picture of the coating composition; however, only the CEMS and the GMS spectra of the intact coatings are required to determine the coating compositions. The GMS spectra will be described in detail in this chapter and compared with the metallurgical results. Specifically, coating compositions are compared with the cross sectional micrographs to investigate the possible correlation between the thickness of the layers and the phase abundances determined by the data. Cross sectional micrographs are scanning electron microscope, SEM, photographs of the cross section of galvanneal coatings. They provide a visual means by which the layers in a coating can be compared with the Mössbauer spectroscopic results. As will be described, there is definite agreement between the layer thicknesses in the micrographs and the relative phase fractions determined by Mössbauer spectroscopy. In addition to the composition information obtained through GMS analysis of the coatings, it is possible to determine the weight of iron in the coating by comparing the spectral area of the coating with that of the substrate. Relative spectral areas were compared with the metallographic cross sections to illustrate their correspondence, the results of which

will be discussed. Furthermore, the effect of aluminum impurity in the galvanneal bath will be discussed by comparing two coatings produced under identical processes. However, one of the iron saturated zinc baths was free of aluminum while the other bath contained 0.13% aluminum. In section 4.3, the dramatic differences in the two coatings are described; the results of which may prove effective in controlling phase formation during galvanneal production.

5.1 Sample Preparation and Experimental Procedure

Many samples of galvanneal steel produced using the hot-dip process were supplied by four different commercial galvanneal producers or users. The coatings were prepared under different conditions which represent a range of possible processing conditions. Six samples were chosen for comparison in this chapter based on their differences and well characterized metallographic properties. Prior to analysis, each sample was rinsed with acetone to remove any dirt or oil from the coating surface. Sections of each sample which were free from scratches or obvious defects were selected for analysis. Each sample was analyzed on its surface using XRD spectroscopy since this technique permits identification of the Zeta and Delta phases. Furthermore, X-ray diffraction analysis is able to determine the relative iron concentration of the Delta phase present in the coatings. Next, the coating was fractured in order to remove part of it from the steel substrate using the technique described in Chapter 4, and transmission Mössbauer spectroscopy was performed on the removed coating. CEMS spectra were recorded from the underside of the fractured coatings.

Finally, GMS and CEMS spectra were recorded in-situ with the coating still attached to the steel substrate. XRD spectra were recorded using the same Philips model APD3720 automated powder diffractometer and technique discussed in section 2.1.1. Small strips of the galvanneal sheet could be mounted directly into the X-ray diffractometer without the need for the standard holder used for powder samples. The Mössbauer spectra were recorded at 300 K using a 50 mCi ^{57}Co in Rh source. The GMS spectra were recorded using the newly developed toroidal detector using a gas mixture of 90% Kr + 10% CH_4 and a flow rate of approximately $2 \text{ cm}^3 \text{ min}^{-1}$ (see Chapter 4). The 1.8 keV and 14.4 keV pulses were simultaneously recorded to improve the count rate and reduce collection time. CEMS spectra were recorded using a 90% He + 10% CH_4 gas mixture flowing at $8.5 \text{ cm}^3 \text{ min}^{-1}$. Spectra were analyzed on an IBM3090 mainframe computer using our standard fitting routines.³⁰ During the analysis, many spectral fits showed that the Mössbauer parameters of the phases in the coatings agreed well with those of the pure phases described in section 2.2.2. As fitting proceeded, we found we could constrain the parameters to those found in the pure phases and allow only the relative fraction of each phase and the iron concentration of the Gamma and Delta phases to vary.

5.2 Comparison of Mössbauer Findings with the Metallographic Properties

Following the evaluation of the six galvanneal coatings using X-ray diffraction and Mössbauer spectroscopy, the relative phase fractions were compared with the thickness of each layer measured from the corresponding cross sectional SEM micrograph. The average

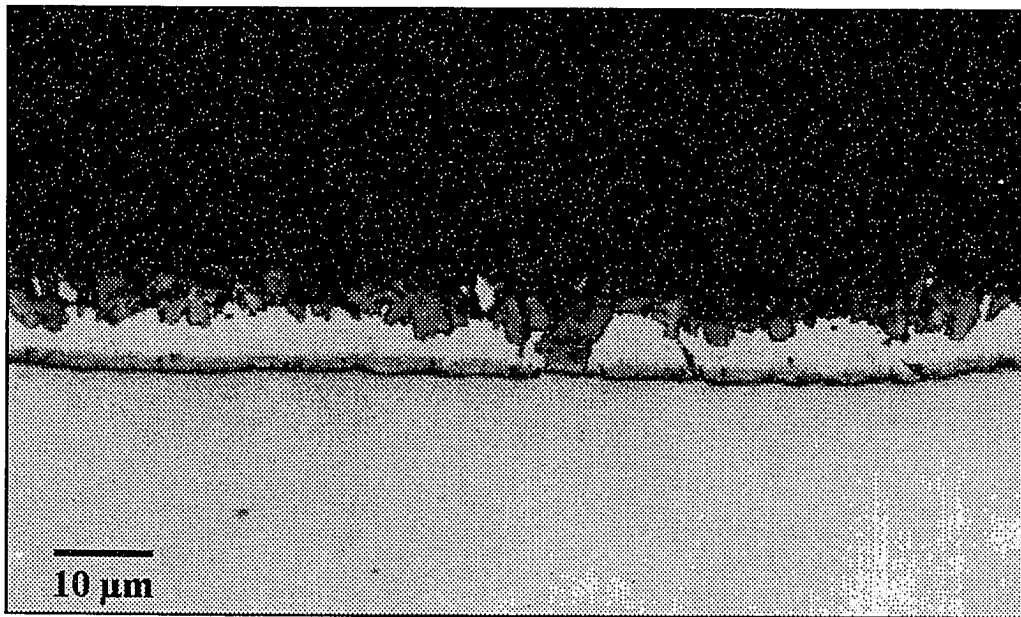
thickness of the coatings and the layers within the coatings were determined by measuring each layer at ten points across the SEM micrograph using a Vernier caliper. The errors correspond to the standard deviations in these measurements. Coating weight and iron content were determined by the individual corporations who provided the coatings. The coating weights were measured by the weigh-strip-weigh method. In this technique, a standard disc of a galvanized coating sample was weighed. Next the coating was stripped from the substrate using a solution of hydrochloric acid and an organic inhibitor. The remaining substrate was once again weighed and the coating weight calculated. The acid solution containing the dissolved coating was analyzed for iron content using atomic absorption spectroscopy.

The GMS technique probes through the entire galvanized coating and into the steel substrate (see Chapter 4). This results in the superposition of the α -Fe base signal with the coating spectrum. However, to facilitate the analysis, the base signal may be subtracted away leaving only the GMS spectrum of the galvanized coating. In the following chapter, the GMS spectra following the subtraction of the steel substrate signal are shown for each sample. Furthermore, the XRD and CEMS analysis of the coating surfaces are shown to illustrate the ability of these techniques to identify the Zeta and Delta phases. Also included are plots of the CEMS spectra from the underside of the fractured coatings. These spectra identify the presence of a relatively high iron concentration Gamma layer next to the steel substrate. Included with these spectra, are tables showing the GMS spectral fit parameters. Cross reference between these parameters and those of the pure iron-zinc phases described in section 2.2, will allow the reader to confirm the findings described within the chapter.

In the following section, the bottom layer in a coating refers to the layer closest to the steel substrate. The second, third, and possible fourth layers refer to layers as they progress further from the steel substrate (see Figure 3.2). Previous XRD and CEMS analysis of fractured coatings has provided us with some information on the identification of the layers within coatings.³² Specifically, the Gamma phase generally forms as a thin bottom layer next to the steel substrate. Also, the Zeta phase forms as a rough jagged layer on the surface of the coating. The Gamma-1 phase has never been clearly identified within a coating; although, it is believed to form next to the Gamma phases as the second layer in the coating. The Delta phase generally constitutes the bulk of the coating. One of the aims of this work has been to clearly identify the layers observed in the cross sectional micrographs of galvaneal coatings and correlate the relative thicknesses of the layers with the phase fractions determined by Mössbauer spectroscopy. The following research was performed under contract and has not been published; therefore, the names of the commercial galvaneal producers have been withheld and the samples are labeled one through six.

The metallographic cross section for Sample #1 is shown in Figure 5.1. The bottom layer is a very thin dark layer next to the steel substrate. The average thickness of the bottom layer is 0.6 μm having approximately 6% of the total coating thickness. This layer is followed by a lighter layer with an average thickness of 1.2 μm making up nearly 12% of the coating. A very light layer having 40% of the coating thickness is next followed by the dark top layer which forms a rough jagged layer on the surface on the coating. The XRD analysis of the coating surface is shown in Figure 5.2 (a) and compared with (b) a low iron Delta and (c) a Zeta XRD spectrum. As indicated, the Zeta phase in the coating is clearly

identified by the peaks at approximately 40.1° , 41.5° , and 44.0° two-theta. Furthermore, comparison of the coating spectrum with that of the low iron Delta shows reasonably agreement. Figure 5.3 (a) shows the CEMS analysis of the coating surface. Consistent with the XRD findings, spectral analysis identifies the Zeta phase on the coating surface. The CEMS analysis of the underside of the fractured coating, illustrated in Figure 5.3 (b), shows a high iron concentration Gamma phase as well as a small amount of the Gamma-1 phase. This indicates that the Gamma phase must be very thin in order for the Gamma-1 signal to be detected with CEMS. The GMS spectrum of this coating following the subtraction of the substrate signal is shown in Figure 5.2 (c). Spectral analysis shows the coating is comprised of 36.8% Zeta, 43.4% Delta, 16.0% Gamma-1, and 3.7% Gamma. A comparison of these values with those observed in Figure 5.1 identifies that the Gamma, Gamma-1, Delta, and Zeta phases form respectively from the substrate to the coating surface. As was observed in all the coatings we have studied thus far, the Mössbauer parameters of the Gamma phase correspond to the high iron concentration end of the phase. The Mössbauer parameters of the Delta phase correspond to the low iron concentration end of that phase. This is expected in coatings containing large amounts of the Zeta phase since the total iron content in these coatings is generally low.



	Full Coating	Bottom Layer	Second Layer	Third Layer	Fourth Layer
Average Thickness (μm)	9.8 ± 1.1	0.6 ± 0.1	1.2 ± 0.5	3.9 ± 1.7	4.1 ± 2.0
Percentage of Full Coating	100	6	12	40	42

Coating Weight (g m ⁻²)	Coating Iron Content (%)
66.7	8.0

Figure 5.1. Cross sectional micrograph and metallurgical properties of Sample #1.

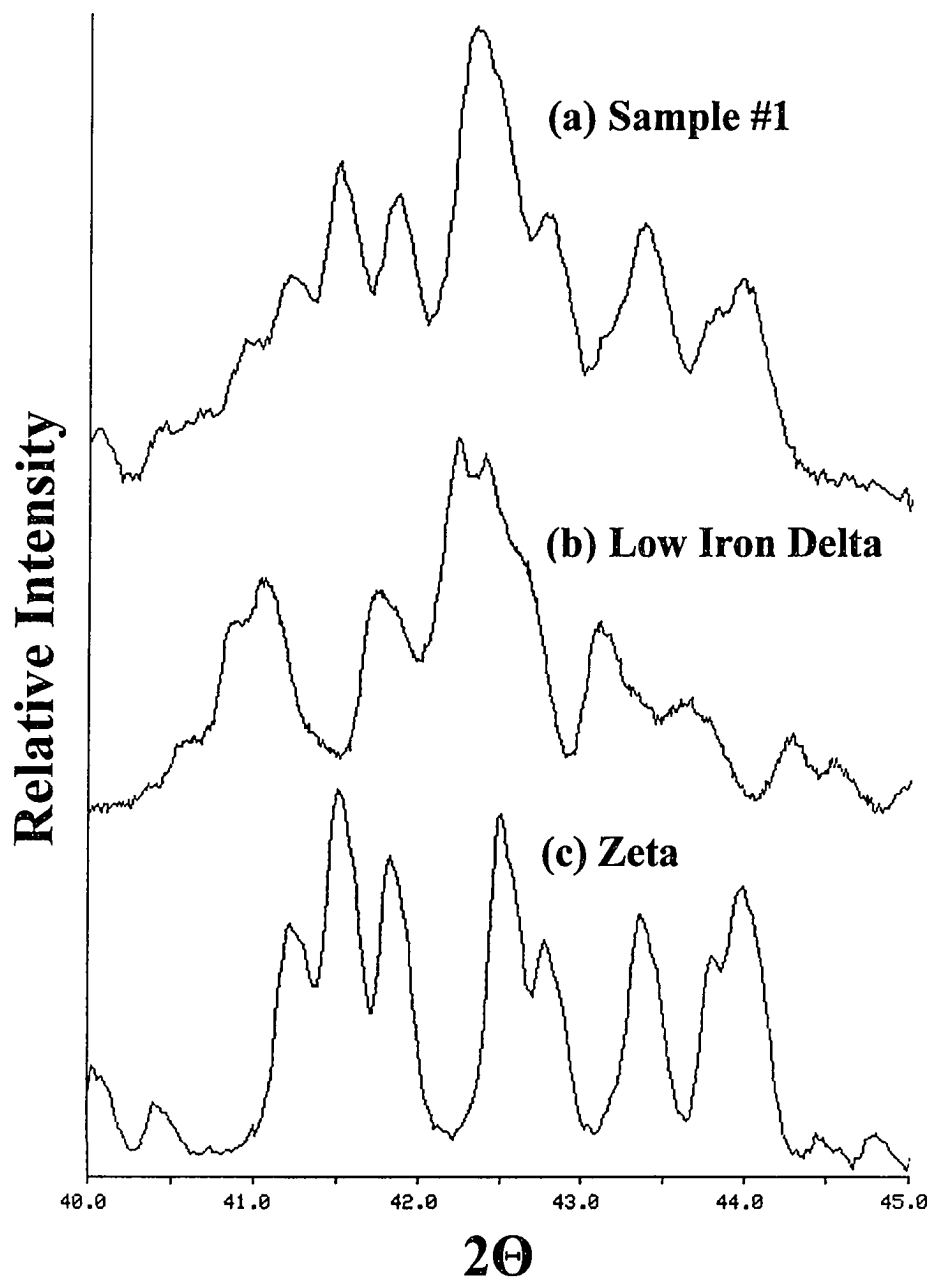
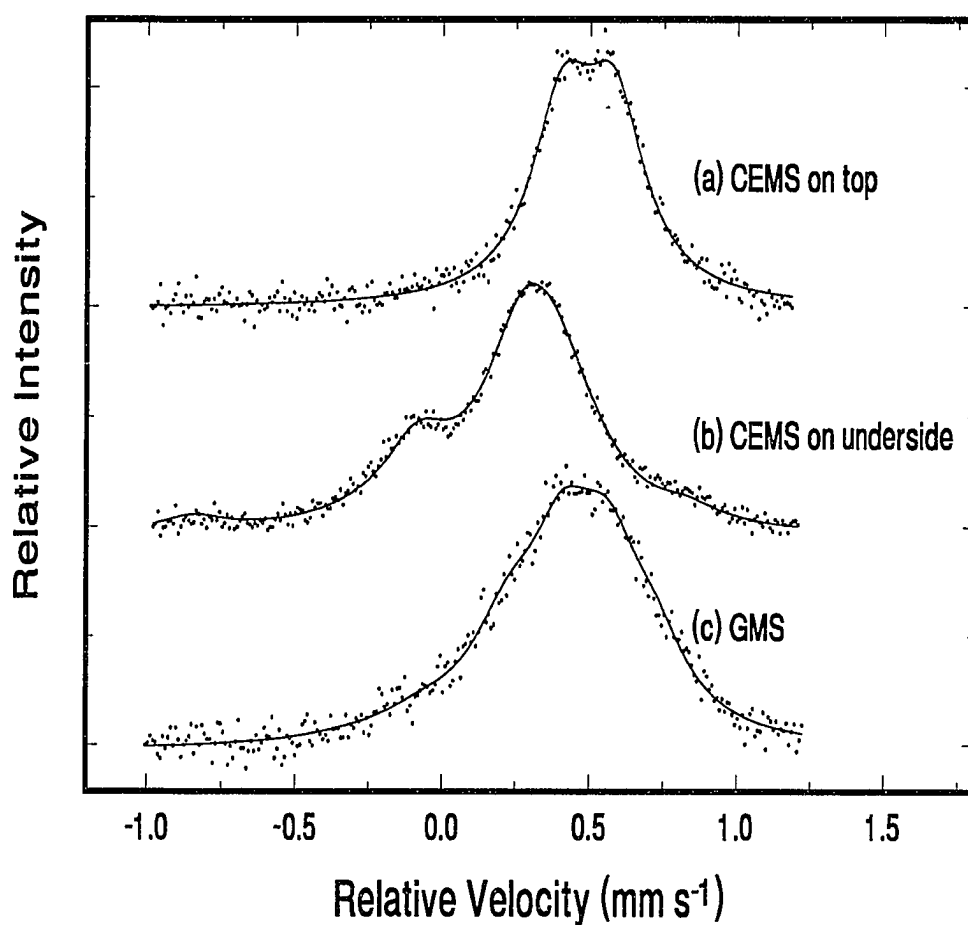


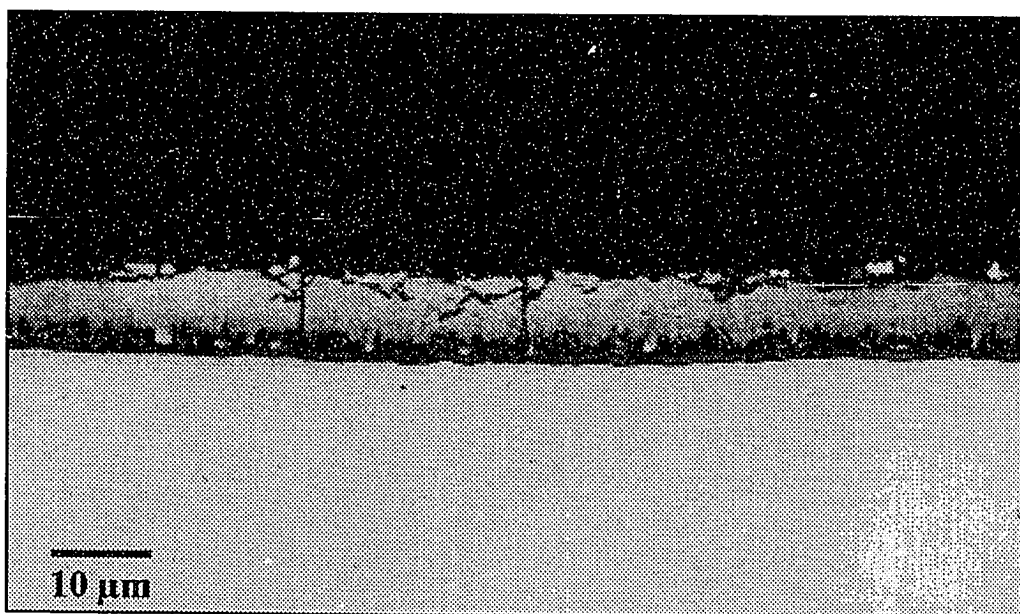
Figure 5.2. Comparison of the XRD spectra of **(a)** Sample #1, **(b)** low iron concentration Delta, and **(c)** Zeta from 40°-45° two-theta.



	Isomer Shift (mm s ⁻¹)	Quadrupole Splitting (mm s ⁻¹)	Linewidth (mm s ⁻¹)	Relative Area (%)	Phase Fraction (%)
Zeta	0.489	0.153	0.244	36.8	36.8 ± 5%
Delta A	0.474	0.486	0.275	26.0	43.4 ± 5%
B	0.476	0.162	0.292	16.6	
C	0.299	0.270	0.285	0.8	
Gamma-1 A	0.470	0.079	0.298	7.4	16.0 ± 10%
B	-0.042	0.555	0.294	1.0	
C	0.042	0.224	0.394	7.6	
Gamma A	0.322	0.120	0.285	2.2	3.7 ± 10%
B	0.105	0.380	0.288	1.5	

Figure 5.3. Mössbauer spectra of Sample #1 recorded at 300 K using (a) CEMS on the surface, (b) CEMS on the underside, and (c) GMS on the surface of the coating.

The metallographic cross section of Sample #2 is shown in Figure 5.3. The bottom layer is a much thicker layer than in Sample #1, averaging 1.2 μm thick and 14% of the total coating thickness. This layer is followed by another dark layer of vertically oriented crystals having an average thickness of 1.4 μm . A very thick, light layer is the third and final layer in this coating. No fourth layer is observed on the coating surface. The X-ray diffraction analysis of the coating surface is shown in Figure 5.5 (a), and compared with the high iron concentration Delta and Zeta phases in Figures 5.5 (b) and (c), respectively. The absence of peaks at 40.1° , 41.5° , and 44.0° two-theta in the spectrum shows that no Zeta is on the coating surface. Furthermore, the XRD and CEMS (Figure 5.6 (a)) analysis of the coating shows the presence of a high iron concentration Delta in the coating. No Zeta phase is observed in accordance with the metallurgical findings. As found with cross sectional analysis, the CEMS analysis of the underside of the fractured coating (Figure 5.6 (b)) shows a high iron concentration Gamma phase indicating that the Gamma phase is much thicker than in the previous sample. The GMS spectrum of this coating is shown in Figure 5.6 (c). Spectral analysis shows the coating composition to be 81.0% Delta, 11.0% Gamma-1, and 8.0% Gamma. Comparing these values with those observed in Figure 5.4, the layers from the substrate to the coating surface are once again the Gamma, Gamma-1, and finally the Delta phase. The Mössbauer parameters of the Delta phase correspond to the medium-high iron concentration end of that phase as was observed in the CEMS analysis. This may be expected in coatings with relatively thick Gamma-1 and Gamma layers; i.e. a relatively high iron concentration, Delta layer results from the iron-zinc diffusion necessary to form thick Gamma-1 and Gamma layers.



	Full Coating	Bottom Layer	Second Layer	Third Layer	Fourth Layer
Average Thickness (μm)	8.8 ± 0.7	1.2 ± 0.2	1.4 ± 0.6	6.2 ± 0.8	0.0
Percentage of Full Coating	100	14	16	70	0
Coating Weight (g m ⁻²)			Coating Iron Content (%)		
71.7			12.0		

Figure 5.4. Cross sectional micrograph and metallurgical properties of Sample #2.

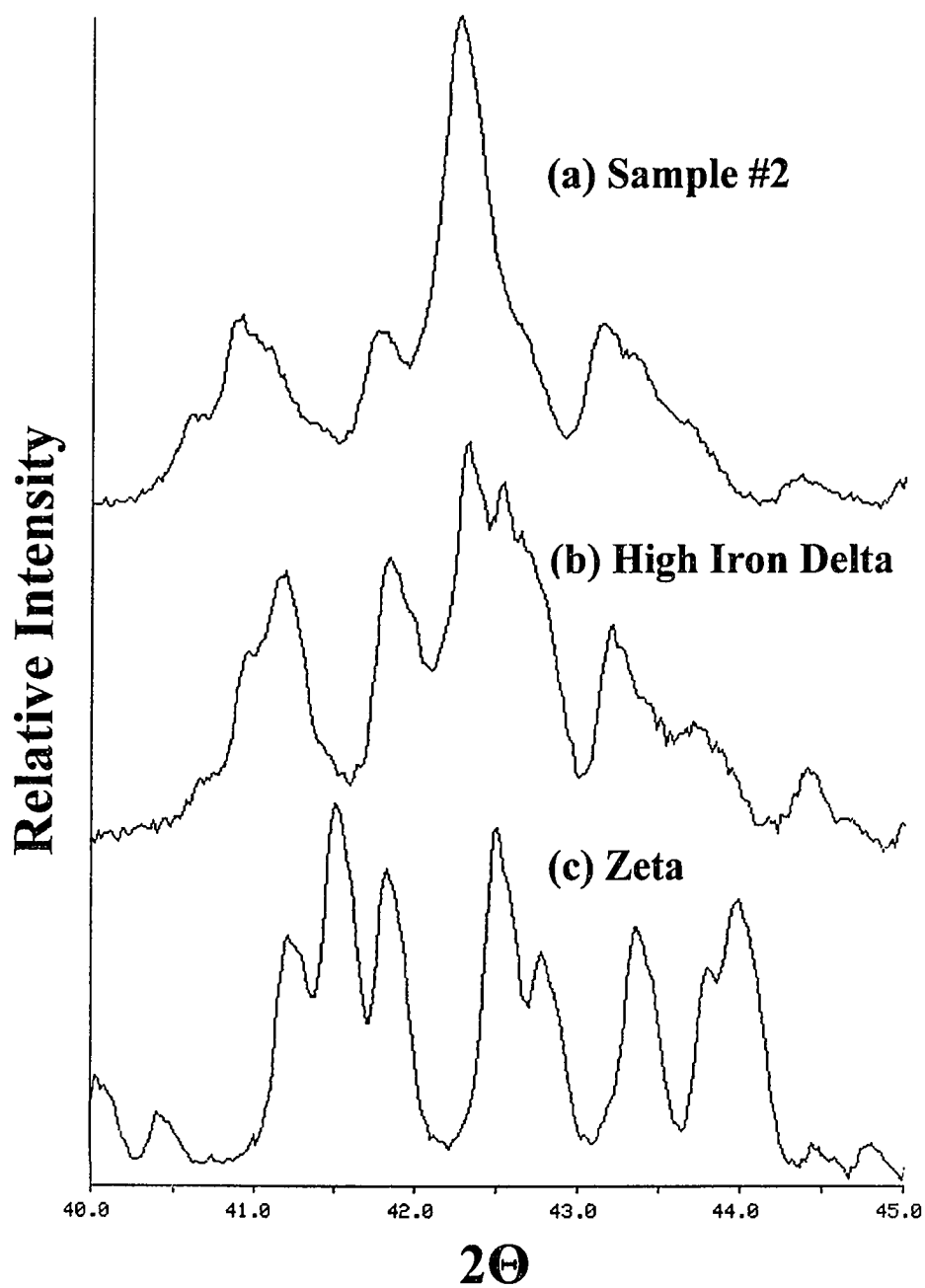
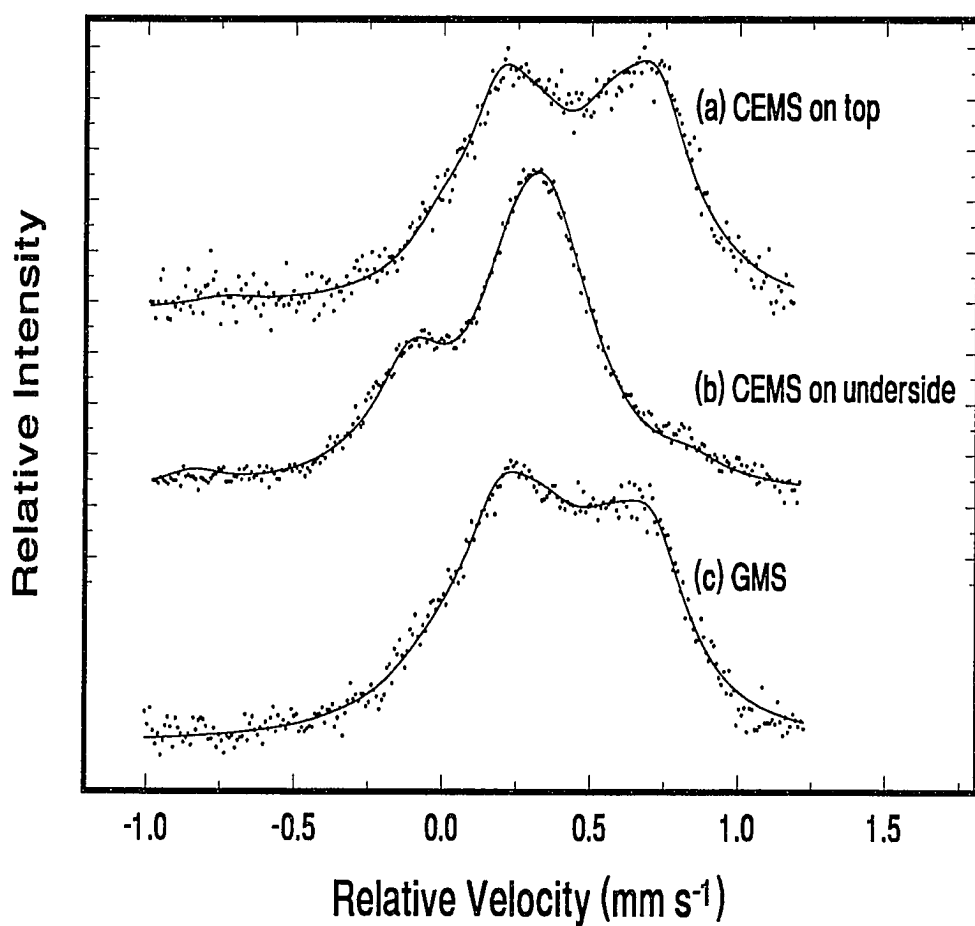


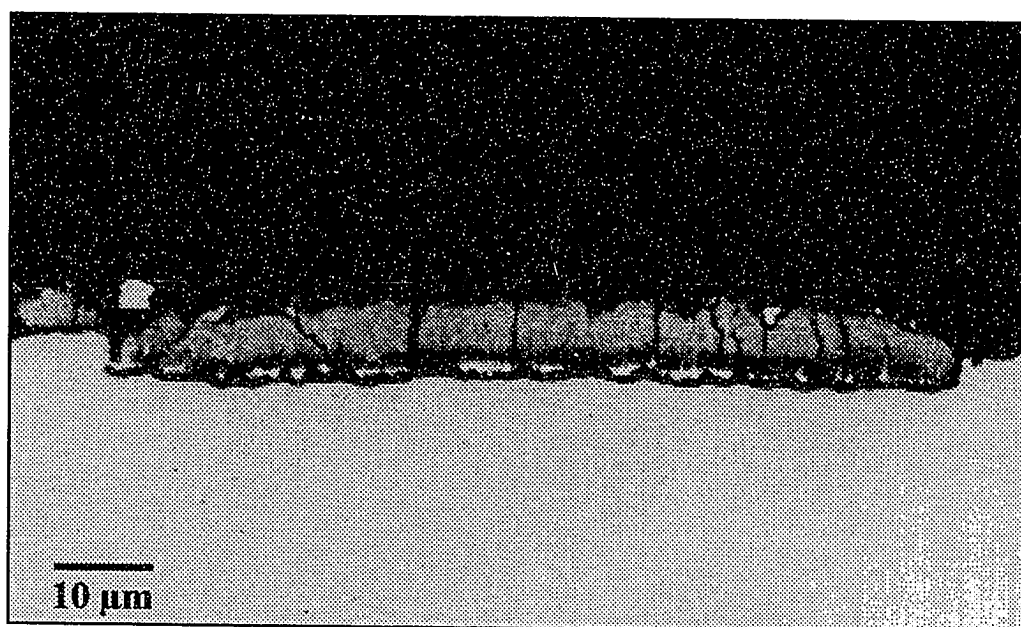
Figure 5.5. Comparison of the XRD spectra of (a) Sample #2, (b) high iron concentration Delta, and (c) Zeta from 40°-45° two-theta.



	Isomer Shift (mm s ⁻¹)	Quadrupole Splitting (mm s ⁻¹)	Linewidth (mm s ⁻¹)	Relative Area (%)	Phase Fraction (%)
Zeta	--	--	--	0.0	0.0
Delta A	0.451	0.520	0.275	46.3	81.0 ± 5%
B	0.459	0.246	0.292	25.7	
C	0.256	0.452	0.285	9.0	
Gamma-I A	0.470	0.079	0.298	5.1	11.0 ± 10%
B	-0.042	0.555	0.294	0.7	
C	0.042	0.224	0.394	5.2	
Gamma A	0.322	0.120	0.285	4.5	8.0 ± 10%
B	0.105	0.380	0.288	3.5	

Figure 5.6. Mössbauer spectra of Sample #2 recorded at 300 K using (a) CEMS on the surface, (b) CEMS on the underside, and (c) GMS on the surface of the coating.

The metallographic cross section of Sample #3 is shown in Figure 5.5. The bottom layer has an average thickness of 0.7 μm making up approximately 9% of the total coating thickness. As was observed in Sample #2, this layer is followed by another dark layer of vertically oriented crystals with an average thickness of 1.2 μm and comprising more than 16% of the total coating thickness. A light layer having over 75% of the coating thickness is the third and final layer in this coating. Overall, this coating has similar cross sectional properties as Sample #2; however, its average thickness is more than 1 μm less than Sample #2. The XRD spectrum of this coating is shown in Figure 5.8 (a) and compared with (b) a medium iron concentration Delta and (c) Zeta phase. Clearly, no Zeta peaks are present in the coating spectra. However, there is excellent agreement between the coating and the medium iron concentration Delta spectra. CEMS analysis of the coating confirms the presence of a medium-high iron concentration Delta phase (see Figure 5.9 (a)). The absence of the Zeta phase concurs with the metallurgical findings. The CEMS analysis of the underside of the fractured coating (Figure 5.9 (b)) shows only the presence of a high iron concentration Gamma phase indicating that the Gamma phase is at least 0.5 μm thick. The GMS spectrum of this coating is shown in Figure 5.9 (c). Spectral analysis shows the coating is comprised of 74.6% Delta, 14.7% Gamma-1, and 10.7% Gamma. Again, these values agree with the micrograph results (Figure 5.7). The Mössbauer parameters of the Delta phase correspond to the medium-high iron concentration end of that phase as was observed in the CEMS analysis. This coincides with the results of Sample #2 in that coatings containing a relatively thick layer of Gamma-1 and Gamma also contain a medium-high iron concentration Delta phase.



	Full Coating	Bottom Layer	Second Layer	Third Layer	Fourth Layer
Average Thickness (μm)	7.5 ± 1.6	0.7 ± 0.2	1.2 ± 0.7	5.6 ± 1.1	0.0
Percentage of Full Coating	100	9	16	75	0

Coating Weight (g m ⁻²)	Coating Iron Content (%)
55.9	11.8

Figure 5.7. Cross sectional micrograph and metallurgical properties of Sample #3.

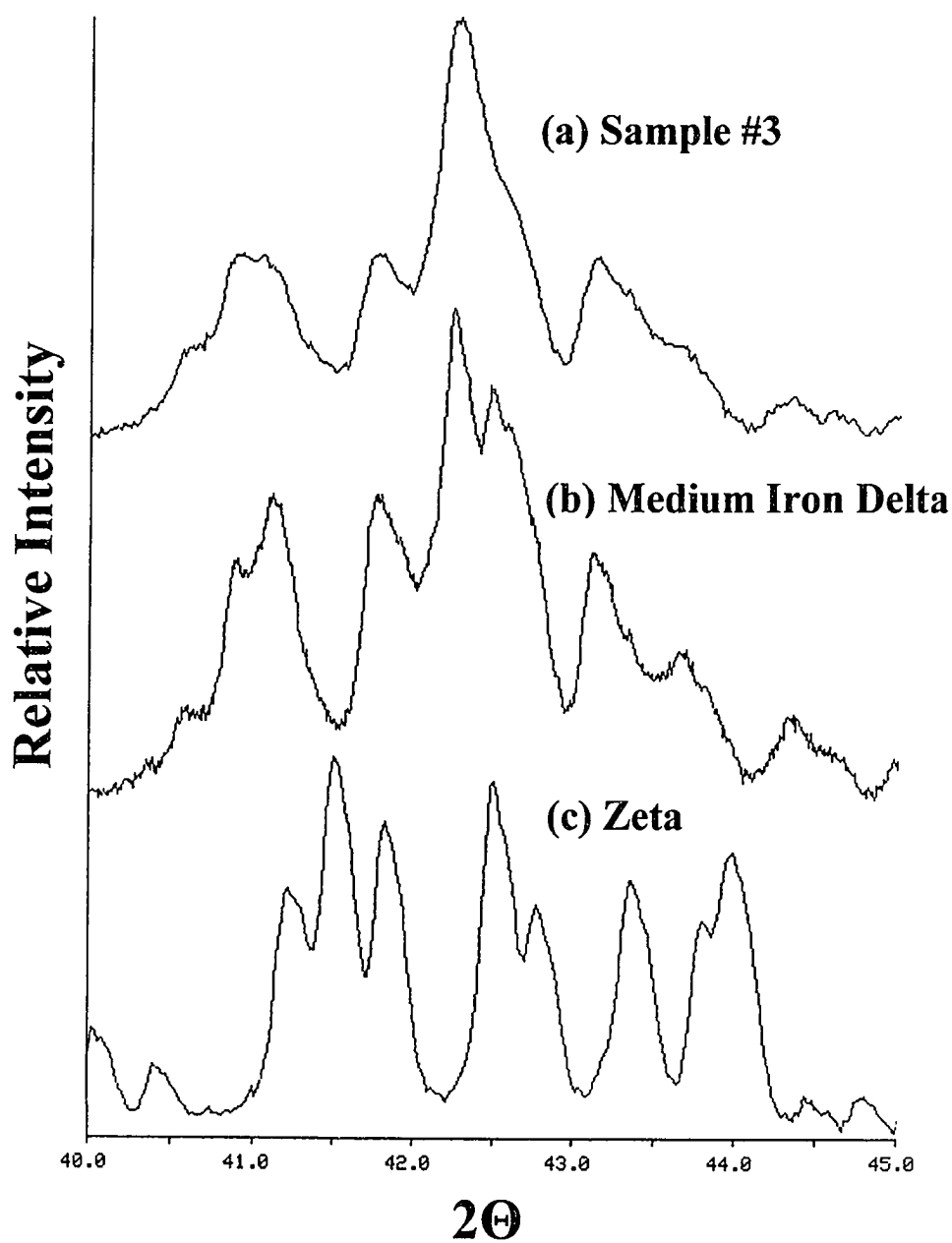
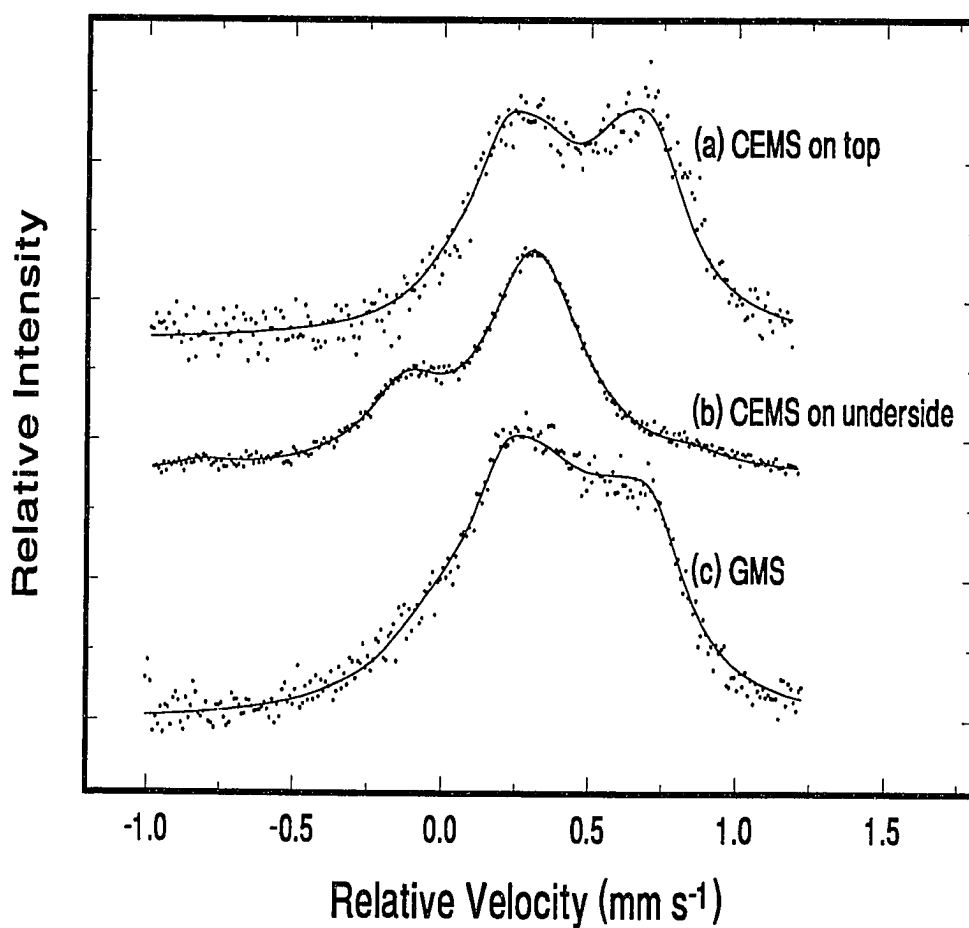


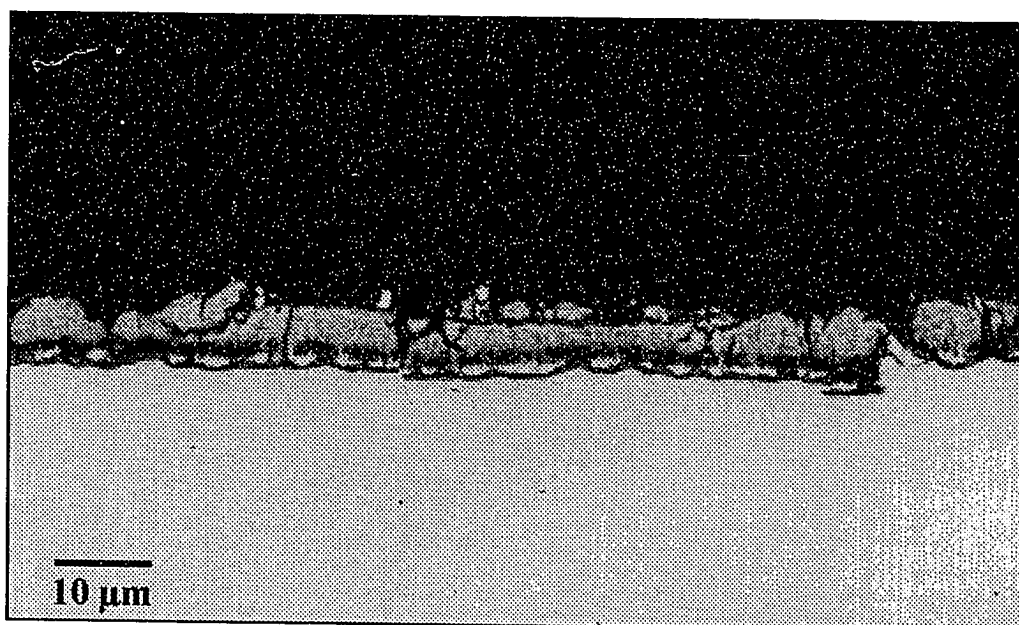
Figure 5.8. Comparison of the XRD spectra of (a) Sample #3, (b) medium iron concentration Delta, and (c) Zeta from 40°-45° two-theta.



	Isomer Shift (mm s ⁻¹)	Quadrupole Splitting (mm s ⁻¹)	Linewidth (mm s ⁻¹)	Relative Area (%)	Phase Fraction (%)
Zeta	--	--	--	0.0	0.0
Delta A	0.462	0.510	0.275	41.8	74.6 ± 5%
B	0.470	0.244	0.292	23.9	
C	0.256	0.453	0.285	8.9	
Gamma-1 A	0.470	0.079	0.298	6.8	14.7 ± 10%
B	-0.042	0.555	0.294	0.9	
C	0.042	0.224	0.394	6.9	
Gamma A	0.322	0.120	0.285	6.0	10.7 ± 10%
B	0.105	0.380	0.288	4.7	

Figure 5.9. Mössbauer spectra of Sample #3 recorded at 300 K using (a) CEMS on the surface, (b) CEMS on the underside, and (c) GMS on the surface of the coating.

The metallographic cross section of Sample #4 is shown in Figure 5.10. The bottom layer has an average thickness of 0.5 μm making up approximately 7% of the total coating thickness. As in previous samples, this layer is followed by another dark layer of vertically oriented crystals comprising over 13% of the total coating thickness. A light layer having over 80% of the coating thickness is the third layer in this coating. Again, no fourth layer is observed. Comparing this sample with the previous coating (Figure 5.7), similarity between coatings is detected except for a slight reduction in overall coating thickness in this sample. Therefore, we should expect similar results from the XRD and Mössbauer analysis. Figure 5.11 compares the XRD spectra of (a) Sample #4, (b) a medium iron Delta, and (c) the Zeta phase. As indicated, no Zeta is present in this coating. This is confirmed by the CEMS analysis of the coating surface (shown in Figure 5.12 (a)), which identified a medium iron concentration Delta phase on the coating surface. Again, there is no identification of a Zeta phase on the coating surface concurrent with the metallurgical findings. The CEMS analysis of the underside of the fractured coating (Figure 5.12 (b)) shows a high iron concentration Gamma phase as well as a small amount of the Gamma-1 phase concurring with the micrograph observation of a thin bottom layer. The GMS spectrum of this coating is shown in Figure 5.12 (c). Spectral analysis reveals a coating composition of 73.4% Delta, 14.8% Gamma-1, and 11.8% Gamma correspondent to the micrograph results, and very similar to the results of Sample #3 (Figure 5.9). The Mössbauer parameters of the Delta phase correspond to a medium iron concentration region of that phase also observed in the CEMS analysis.



	Full Coating	Bottom Layer	Second Layer	Third Layer	Fourth Layer
Average Thickness (μm)	6.9 ± 1.3	0.5 ± 0.1	0.9 ± 0.6	5.5 ± 1.2	0.0
Percentage of Full Coating	100	7	13	80	0

Coating Weight (g m ⁻²)	Coating Iron Content (%)
59.7	10.8

Figure 5.10. Cross sectional micrograph and metallurgical properties of Sample #4.

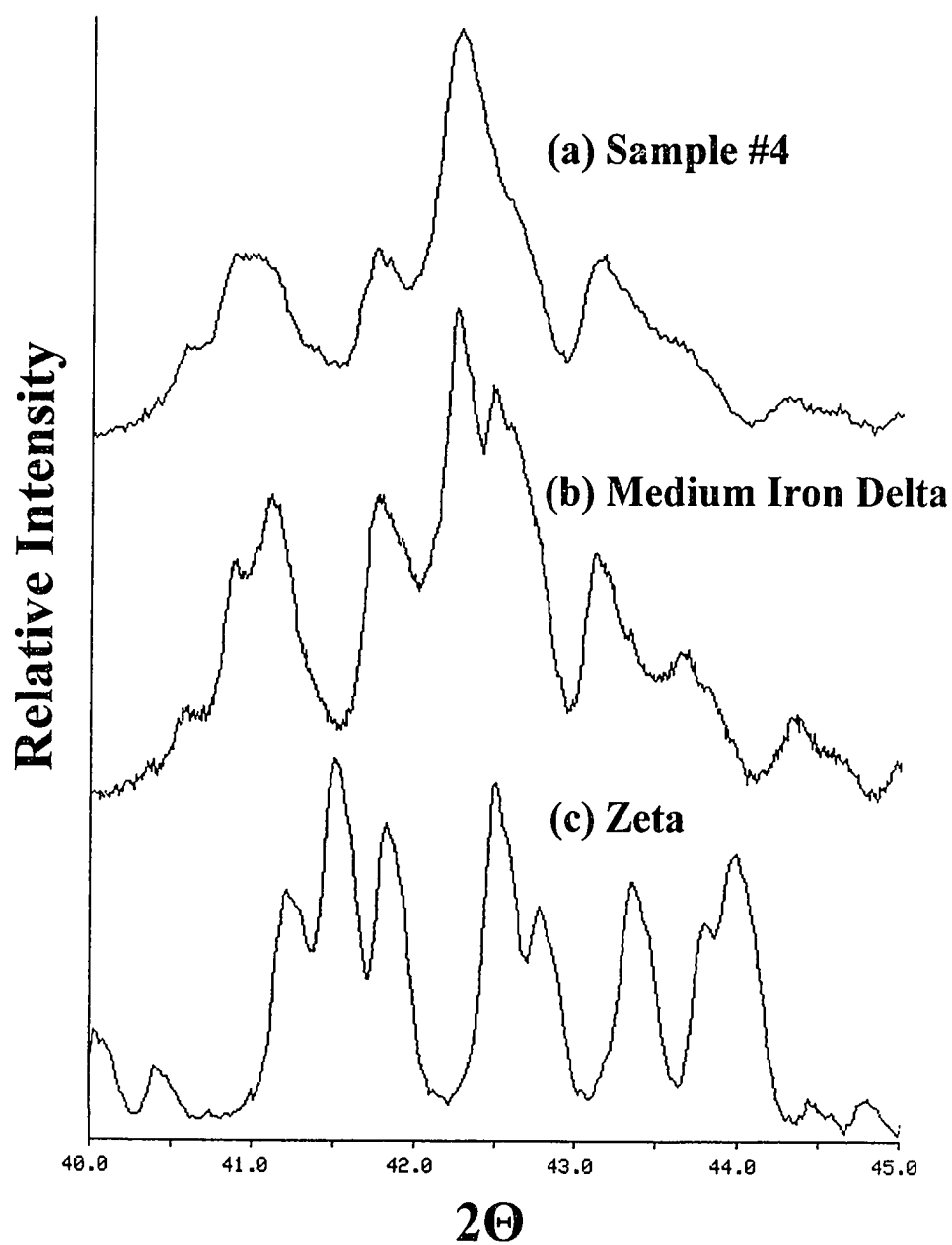
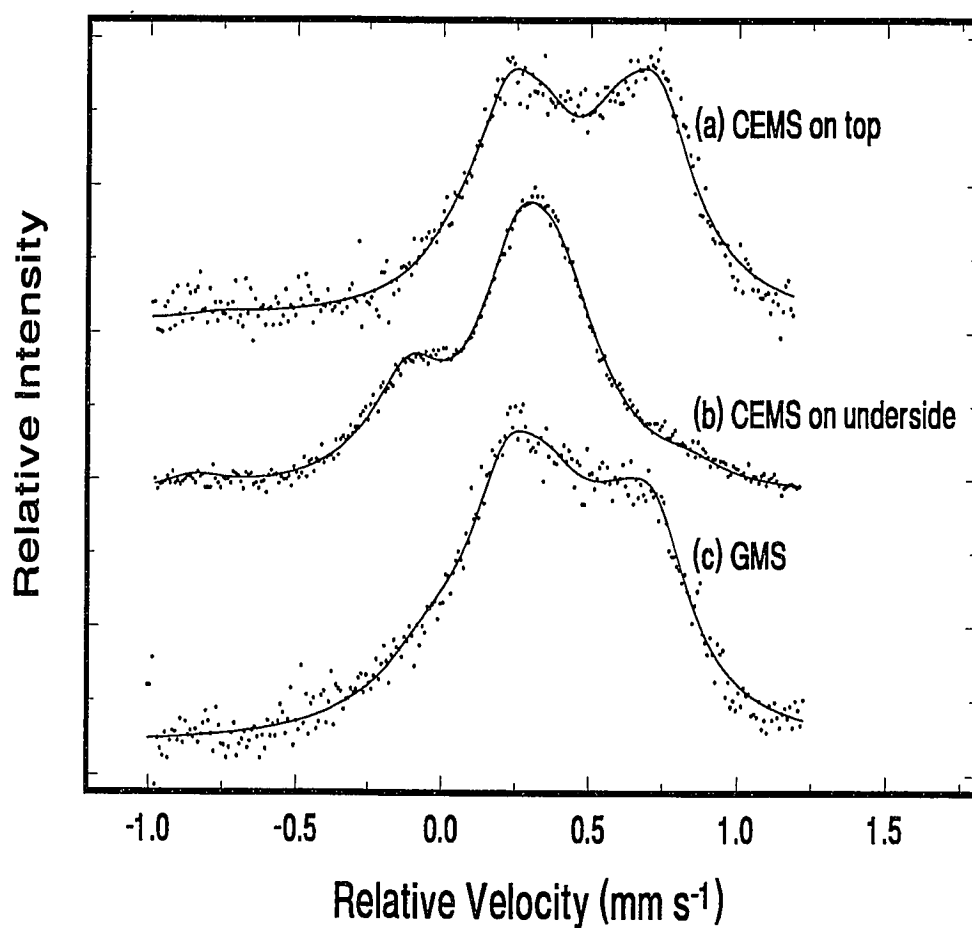


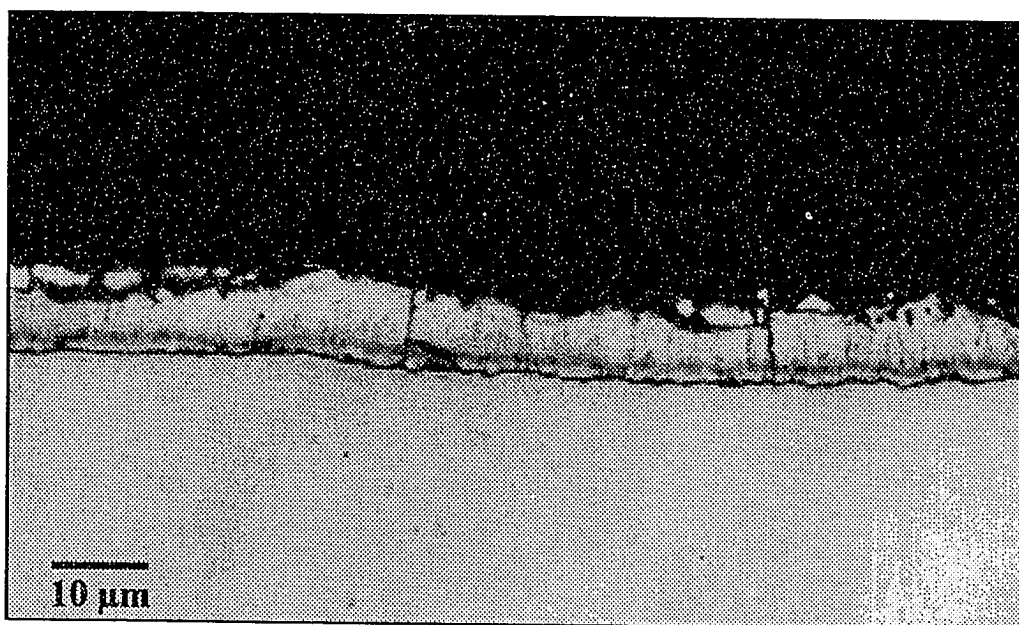
Figure 5.11. Comparison of the XRD spectra of (a) Sample #4, (b) medium iron concentration Delta, and (c) Zeta from 40°-45° two-theta.



	Isomer Shift (mm s ⁻¹)	Quadrupole Splitting (mm s ⁻¹)	Linewidth (mm s ⁻¹)	Relative Area (%)	Phase Fraction (%)
Zeta	--	--	--	0.0	0.0
Delta A	0.468	0.512	0.275	42.1	73.4 ± 5%
B	0.480	0.254	0.292	24.0	
C	0.266	0.472	0.285	7.3	
Gamma-1 A	0.470	0.079	0.298	6.9	14.8 ± 10%
B	-0.042	0.555	0.294	0.9	
C	0.042	0.224	0.394	7.0	
Gamma A	0.322	0.120	0.285	7.1	11.8 ± 10%
B	0.105	0.380	0.288	4.7	

Figure 5.12. Mössbauer spectra of Sample #4 recorded at 300 K using (a) CEMS on the surface, (b) CEMS on the underside, and (c) GMS on the surface of the coating.

Sample #5 is significantly different than the previously studied coatings. The metallographic cross section is shown in Figure 5.13. Note however the similarities to Sample #1. First of all, the bottom layer is a very thin, dark layer next to the steel substrate. Secondly, this layer is followed by a lighter layer, unlike the dark crystalline layer observed in Samples #2-#4. It has an average thickness of 0.90 μm making up about 11% of the coating thickness. A very light layer follows this layer making up the bulk of the coating. However, this coating differs from Sample #1 in that no rough, jagged fourth layer is observed on the coating surface. Based on these results one would expect the XRD and Mössbauer analysis to detect a low iron concentration Delta phase in this coating similar to Sample #1. Indeed, the XRD and CEMS analysis of the coating surface, shown in Figures 5.14 (a) and 5.15 (a), respectively, indicate the presence of a low iron concentration Delta phase with no evidence of the Zeta phase. The CEMS analysis of the underside of the fractured coating shows a high purity Gamma phase as well as a small amount of the Gamma-1 phase (Figure 5.15 (b)). Hence, the Gamma layer must be very thin for detection of the Gamma-1 signal with CEMS. The GMS spectrum of this coating is shown in Figure 5.15 (c). Spectral analysis shows the coating is comprised of 75.2% low iron concentration Delta, 19.1% Gamma-1, and 5.7% Gamma. Comparatively, these values reasonably concur with those observed in Figure 5.13. As was expected from the metallurgical results, this sample is very similar to Sample #1 except for the absence of Zeta in this sample.



	Full Coating	Bottom Layer	Second Layer	Third Layer	Fourth Layer
Average Thickness (μm)	8.1 ± 0.9	0.3 ± 0.1	0.9 ± 0.2	6.9 ± 0.9	0.0
Percentage of Full Coating	100	4	11	85	0

Coating Weight (g m ⁻²)	Coating Iron Content (%)
59.5	8.7

Figure 5.13. Cross sectional micrograph and metallurgical properties of Sample #5.

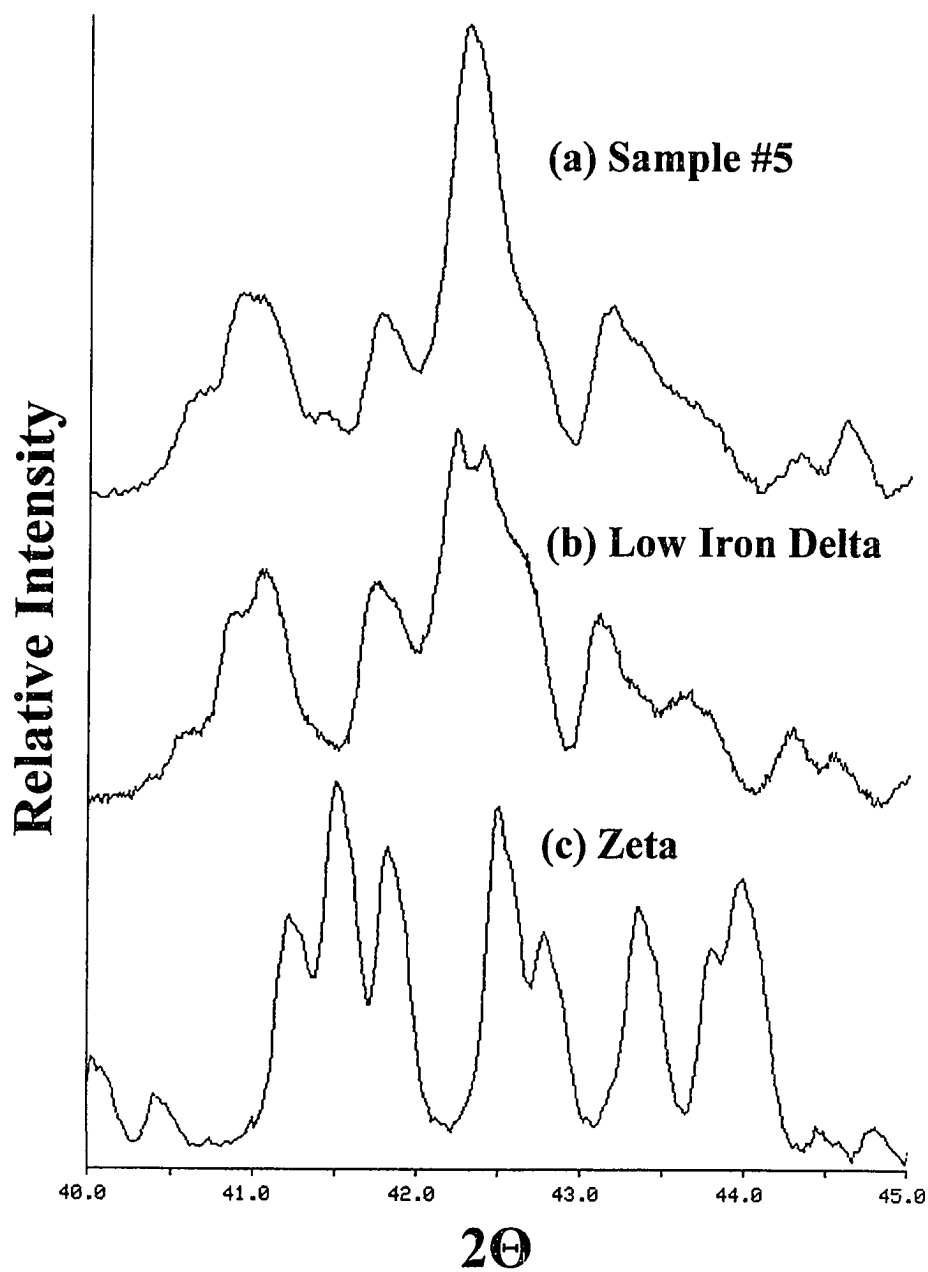
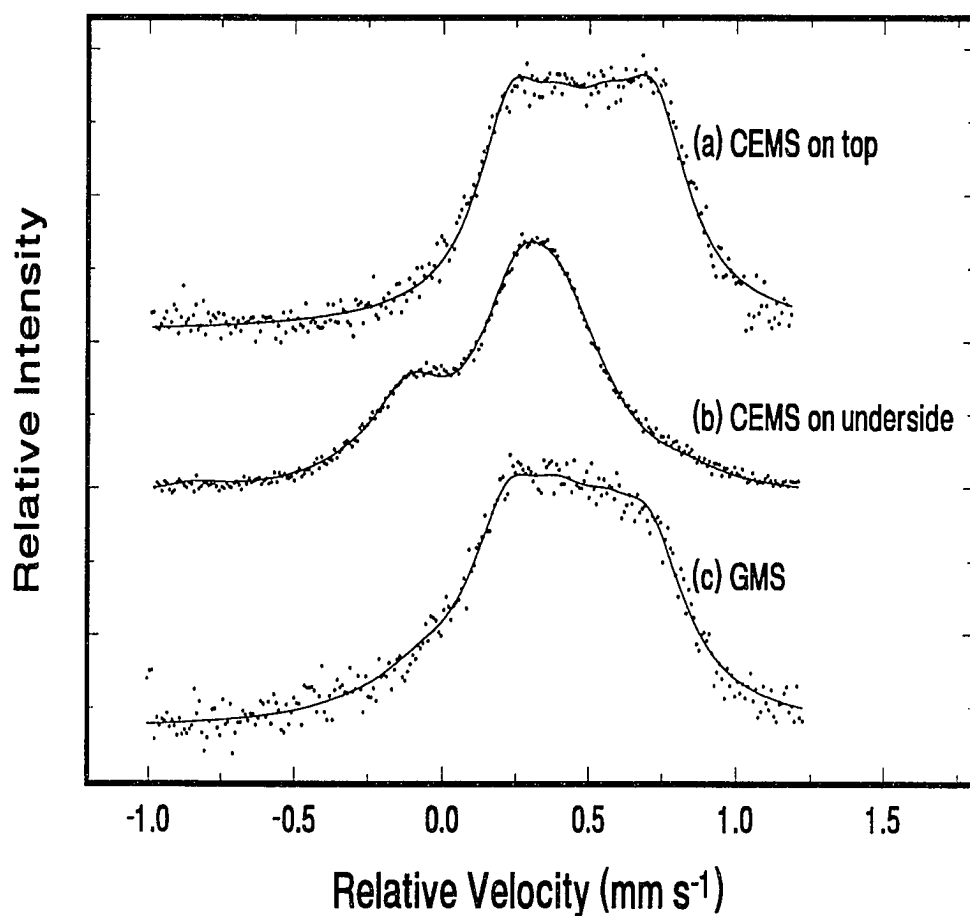


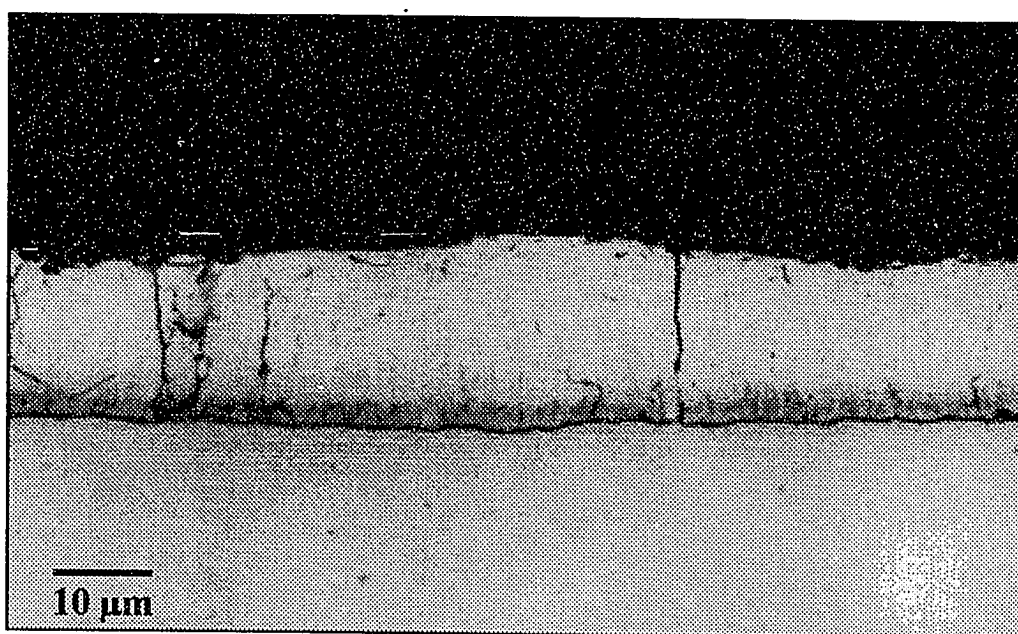
Figure 5.14. Comparison of the XRD spectra of (a) Sample #5, (b) low iron concentration Delta, and (c) Zeta from 40°-45° two-theta.



	Isomer Shift (mm s ⁻¹)	Quadrupole Splitting (mm s ⁻¹)	Linewidth (mm s ⁻¹)	Relative Area (%)	Phase Fraction (%)
Zeta	--	--	--	0.0	0.0
Delta A	0.465	0.492	0.275	45.6	75.2 ± 5%
B	0.476	0.182	0.292	29.5	
C	0.299	0.290	0.285	0.1	
Gamma-l A	0.470	0.079	0.298	8.6	19.1 ± 10%
B	-0.042	0.555	0.294	1.0	
C	0.042	0.224	0.394	9.5	
Gamma A	0.322	0.120	0.285	3.4	5.7 ± 10%
B	0.105	0.380	0.288	2.3	

Figure 5.15. Mössbauer spectra of Sample #5 recorded at 300 K using (a) CEMS on the surface, (b) CEMS on the underside, and (c) GMS on the surface of the coating.

The metallographic cross section for the sixth and final sample is shown in Figure 5.11. This coating is much thicker than the previously studied coatings. Again the bottom layer is a very thin dark layer next to the steel substrate as was observed in Samples #1 and #5. Furthermore, this layer is followed by a much thicker second layer than previously observed in Samples #1 and #5. Again, a very light layer follows this layer making up the remaining coating thickness. In contrast to Samples #1 and #5, the XRD and CEMS analysis of the coating surface, shown in Figures 5.17 (a) and 5.18 (a), respectively, indicate the presence of a medium iron concentration Delta phase; Samples #1 and #5 possessed a low iron concentration Delta layer. The CEMS analysis of the underside of the fractured coating (Figure 5.18 (b)) shows a high iron concentration Gamma phase as well as a small amount of the Gamma-1 phase indicating the thinness of the Gamma layer. The GMS analysis (shown in Figure 5.18 (c)) reveals the coating is comprised of 83.8% medium-high iron concentration Delta, 14.2% Gamma-1, and 2.0% Gamma. When compared with the metallographic results (Figure 5.16), we see a high degree of consistency between corresponding values. It is important to note that even though the coating thickness is over 17 μm thick, the GMS technique is able to detect the presence of the Gamma-1 and Gamma layers which are deep within the coating.



	Full Coating	Bottom Layer	Second Layer	Third Layer	Fourth Layer
Average Thickness (μm)	17.5 ± 1.3	0.3 ± 0.1	1.9 ± 0.2	15.3 ± 1.3	0.0
Percentage of Full Coating	100	2	11	87	0

Coating Weight (g m ⁻²)	Coating Iron Content (%)
123.6	9.3

Figure 5.16. Cross sectional micrograph and metallurgical properties of Sample #6.

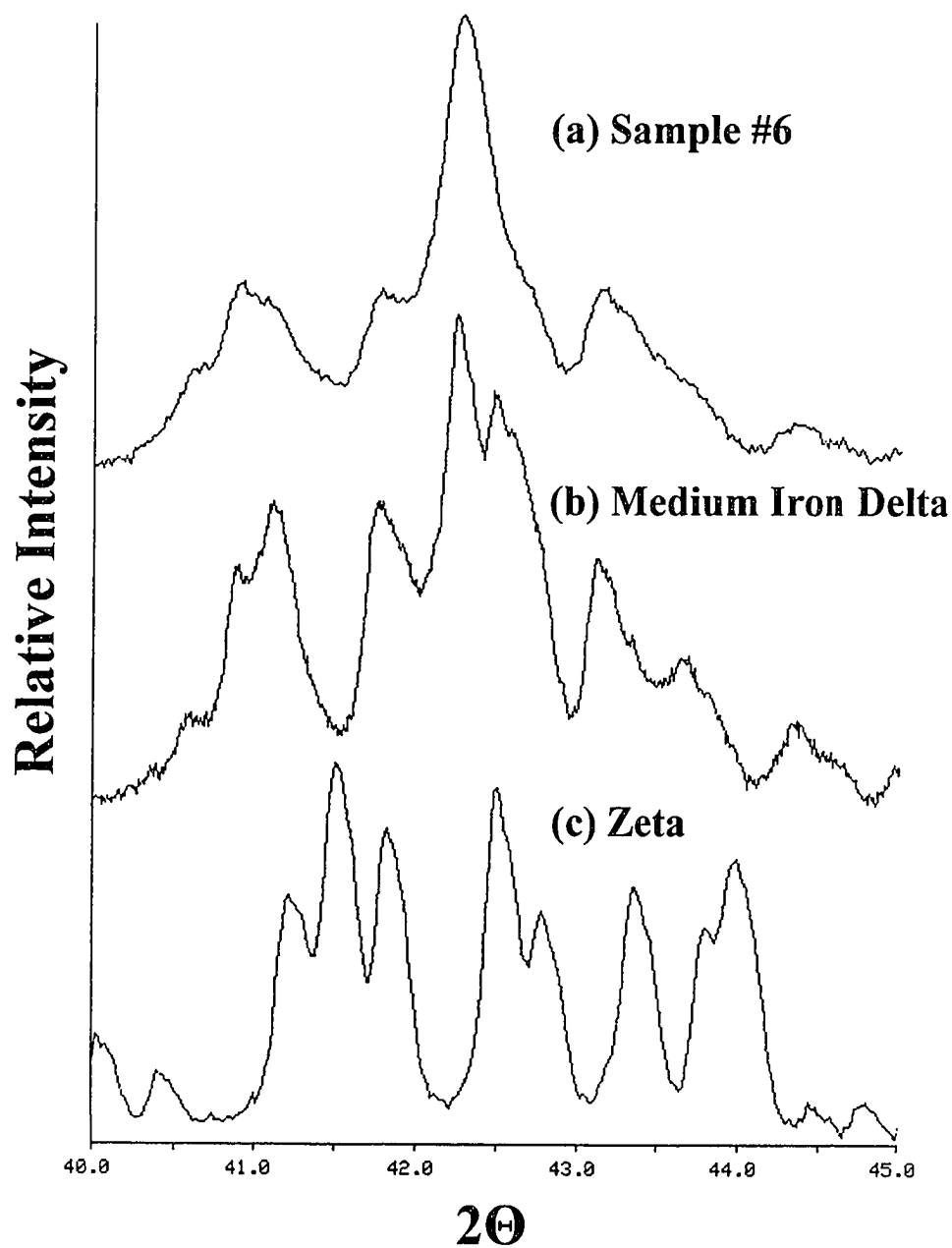
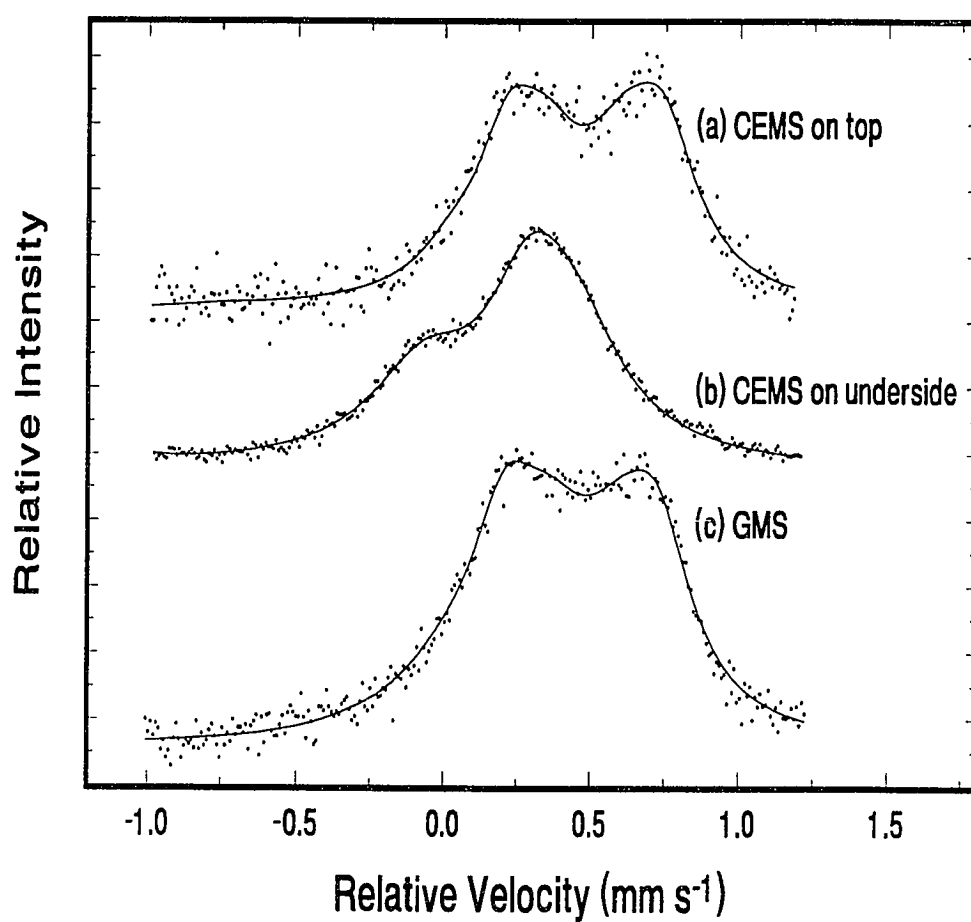


Figure 5.17. Comparison of the XRD spectra of **(a)** Sample #6, **(b)** medium iron concentration Delta, and **(c)** Zeta from 40°-45° two-theta.



	Isomer Shift (mm s ⁻¹)	Quadrupole Splitting (mm s ⁻¹)	Linewidth (mm s ⁻¹)	Relative Area (%)	Phase Fraction (%)
Zeta	--	--	--	0.0	0.0
Delta A	0.468	0.513	0.275	48.4	83.8 ± 5%
B	0.483	0.252	0.292	30.0	
C	0.265	0.472	0.285	5.4	
Gamma-1 A	0.470	0.079	0.298	6.6	14.2 ± 10%
B	-0.042	0.555	0.294	0.9	
C	0.042	0.224	0.394	6.7	
Gamma A	0.322	0.120	0.285	1.1	2.0 ± 10%
B	0.105	0.380	0.288	0.9	

Figure 5.18. Mössbauer spectra of Sample #6 recorded at 300 K using (a) CEMS on the surface, (b) CEMS on the underside, and (c) GMS on the surface of the coating.

Some general observations are in order. The CEMS analysis of the underside of fractured coatings consistently detects the presence of a relatively high iron concentration Gamma phase at the bottom of the coating next to the steel substrate. This concurs with our previously reported findings.³² Therefore, the dark bottom layer observed in the metallographic cross sections is clearly the Gamma phase. Even in coatings containing only a small amount of the Gamma phase, there is observed a thin dark layer next to the steel substrate. In coatings with a rough, jagged layer on the coating surface, XRD and CEMS analysis finds a large amount of the Zeta phase on the coating surface. This indicates that the Zeta phase forms on the coating surface in a porous, non-uniform layer. Additionally, coatings that contain a large amount of Zeta also have a low iron concentration Delta layer. The correspondence between the layer thickness observed in the cross sectional micrographs and the phase abundances determined by Mössbauer spectroscopy shows that the Gamma-1 phase forms next to the Gamma phase in either a light layer or in dark vertical crystals. Furthermore, a light Gamma-1 layer forms in coatings containing less than 10% iron; i.e., it is found when the Gamma phase is very thin and possibly when the Zeta phase is present on the coating surface. For samples with greater than 10% iron, a thick Gamma layer is found followed by very dark vertical crystals of Gamma-1. These samples containing a thick layer of the Gamma phase also possess a medium-high iron concentration Delta layer. Finally, coatings that were found to contain large amounts of the Zeta phase or a low iron concentration Delta layer on the surface always possess only a thin layer of Gamma at the coating-steel interface.

5.3 Coating Iron Weight Compared with Coating Spectral Area

A comparison has been made between the coating spectral areas of eleven samples (five samples in addition to the previously discussed six) and the weight of iron in the coatings. The GMS spectra shown in the previous section were modified to facilitate the analysis and comparison with the cross sectional micrographs. Since the GMS technique probes the entire coating, including the underlying steel substrate, the signal from the substrate is superimposed on the coating signal to produce the unmodified GMS spectra shown in Figure 5.19. The substrate is α -Fe and has well documented Mössbauer parameters; therefore, its subspectrum is easily subtracted away leaving the coating subspectra. However, by comparing the total area under the coating spectra with the area under the substrate subspectra (see Figure 5.19), a measure of the iron content in the coating is obtained. To illustrate this, the coating spectral areas were determined for each of the eleven samples and compared with the weight of iron in the coatings. Specifically, metallurgical analysis determined the weight of iron in a coating to be the product of the total coating weight and the coating iron content. Figure 5.20 illustrates the comparison. As expected, a linear correlation between the coating spectral area and the weight of iron in the coating exists indicating that the Mössbauer analysis can accurately determine the weight of iron in a galvanneal coating.

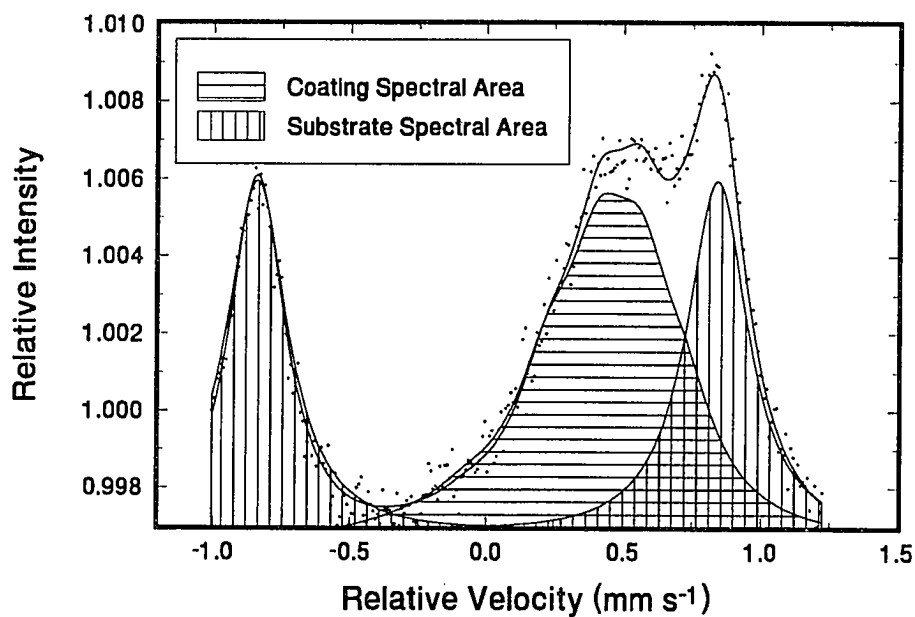


Figure 5.19. A typical GMS spectrum of a galvaneal coating illustrating the spectral area from the coating and the spectral area from the underlying steel substrate.

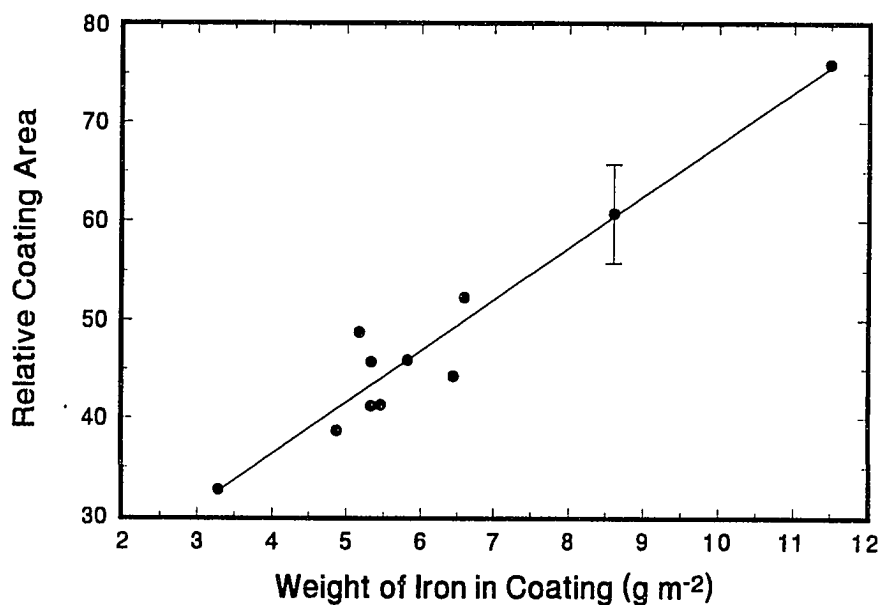


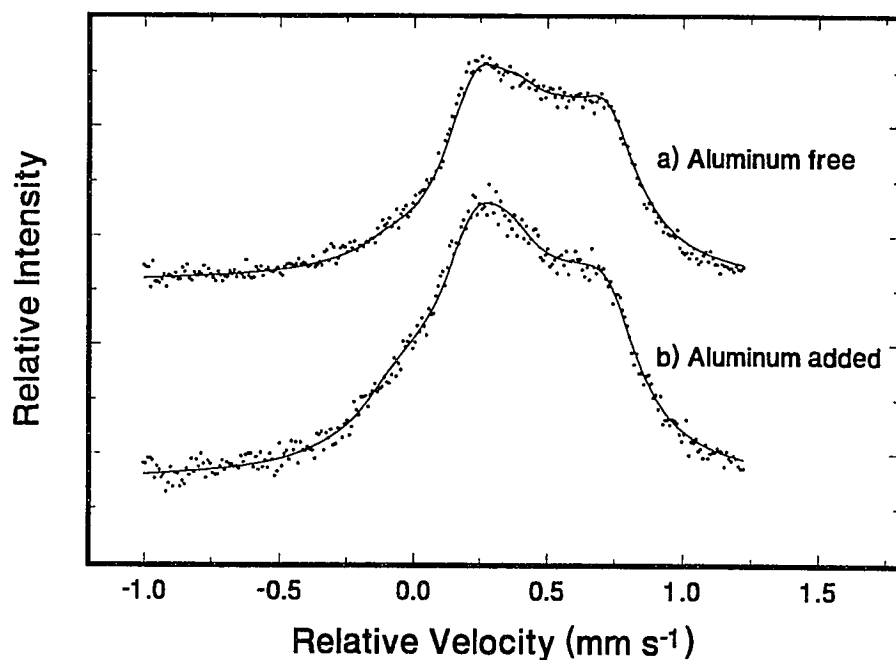
Figure 5.20. Comparison of the coating spectral area with the weight of iron in the coating. The weight of iron in the coating is the product of the coating weight and the coating iron content.

5.4 Effect of Aluminum in the Galvannealing Bath

Aluminum is commonly added to hot-dip batch galvanizing zinc baths to improve the luster of the coating and reduce the atmospheric oxidation of the bath.⁴⁷ Although there has been some work on the effect small additions of aluminum to the zinc bath has on the phase formation^{47,48} the results vary from one study to another. It is suggested that upon the initial submergence of the steel sheet into an aluminum containing zinc bath, an aluminum-iron layer forms which inhibits the interdiffusion of the iron and zinc. The kinetics of this inhibition layer are not well understood. Furthermore, little work has been performed on the effect this layer has on alloy formation during the annealing process. It would seem that since the inhibition layer serves to delay the iron-zinc alloy formation, then the resultant galvanneal coating would form in the low iron concentration end of the phase diagram; i.e., less Γ -1 and Γ would be formed than in an aluminum free coating. This of course assumes that the thickness of the coatings were the same.

In order to investigate the effect aluminum has on the phase formation, two coatings were analyzed with X-ray diffraction and Mössbauer spectroscopy and their compositions compared. The two samples were prepared under the identical preparation conditions except for the addition of 0.13% aluminum to one of the iron saturated zinc baths. The steel was degreased with acetone before being annealed at 750 °C for 2 minutes in a 5% H_2 - N_2 atmosphere. Following the annealing, the steel sheet was submerged in an iron saturated zinc bath for 6 seconds. The molten metal bath was maintained at 465 °C. The coated steel was then annealed for 10 seconds at 530 °C, furnace cooled for 20 second and finally quench

cooled. Upon receipt, the samples were rinsed with acetone and analyzed by XRD and Mössbauer spectroscopy. The XRD spectrum of the aluminum free sample showed that no Zeta phase was present on the coating surface. Analysis of this spectrum showed a low iron concentration Delta phase on the coating surface. CEMS of this sample concurred with the XRD findings and identified only a low iron concentration Delta on the coating surface. The XRD spectrum of the aluminum containing sample again indicated that no Zeta phase had formed on the coating surface. However, a high iron concentration Delta was identified; the CEMS spectra agreed with these findings. The GMS spectra of both samples are compared in Figure 5.21. The aluminum free sample (a) was found to contain 85.0% low iron concentration Delta, 2.4% Gamma-1, and 12.6% Gamma. In contrast, the aluminum added sample (b) was found to contain 67.5% high iron concentration Delta, 13.1% Gamma-1, and 19.4% Gamma. A small addition of aluminum to the zinc bath resulted in an increase in the percentage of iron in the coating. That is, the aluminum added sample was found to contain a greater relative amount of the Gamma-1 and Gamma phases in addition to the increase in the iron content of the Delta phase. This would seem to be in contrast to the expected results. The aluminum-iron inhibition layer is thought to delay the iron-zinc alloy formation. However, comparing the relative coating spectral areas from the uncorrected GMS spectra with Figure 5.20, we find that the aluminum free coating contains approximately 11 g m^{-2} of Fe and the aluminum containing coating approximately 8 g m^{-2} of Fe. Hence, less alloying has resulted from the addition of aluminum to the zinc bath, consistent with the expected results. Clearly, more research on the effect of bath composition on phase formation is warranted and is the focus of present research at Old Dominion University.



		Isomer Shift (mm s ⁻¹)	Quadrupole Splitting (mm s ⁻¹)	Linewidth (mm s ⁻¹)	Relative Area (%)	Phase Fraction (%)
(a)	Zeta	--	--	--	0.0	0.0
	Delta A	0.474	0.483	0.254	52.9	85.0 ± 5%
	B	0.476	0.162	0.273	29.9	
	C	0.299	0.270	0.269	2.3	
	Gamma-1 A	0.470	0.079	0.280	1.1	2.4 ± 10%
	B	-0.042	0.555	0.282	0.2	
	C	0.042	0.224	0.365	1.1	
	Gamma A	0.322	0.120	0.285	7.6	12.6 ± 10%
	B	0.105	0.380	0.288	5.0	
(b)	Zeta	--	--	--	0.0	0.0
	Delta A	0.468	0.512	0.254	37.2	67.5 ± 5%
	B	0.479	0.254	0.273	21.2	
	C	0.266	0.473	0.269	9.1	
	Gamma-1 A	0.470	0.079	0.280	6.0	13.1 ± 10%
	B	-0.042	0.555	0.282	0.8	
	C	0.042	0.224	0.365	6.2	
	Gamma A	0.322	0.120	0.285	11.7	19.4 ± 10%
	B	0.105	0.380	0.288	7.8	

Figure 5.21. Comparison of the GMS spectra, with the substrate signal removed, of two samples produced under identical processing conditions except for the addition of 0.13% Al to one of the galvannealing baths.

5.5 Summary

Six different commercially produced galvanneal coatings were analyzed using X-ray diffraction, CEMS, and GMS spectroscopy using the newly developed toroidal detector. The study was performed in an attempt to identify the phases present in a coating as well as their relative abundances. The amount of each phase and the relative iron concentration of each phase were determined by Mössbauer spectroscopy and compared with the metallographic results supplied to us by the galvanneal producers. Agreement between the layer thicknesses in the SEM micrographs and the relative phase fractions determined by GMS was very good, demonstrating the unique ability of Mössbauer spectroscopy to identify the phases formed in galvanneal coatings. A relatively high iron concentration Gamma was always found to form at the bottom of the coating next to the steel substrate. The Gamma phase generally formed a uniformly thick layer ranging from 0.3-1.2 μm thick among the coatings. Even in coatings containing only a small amount of the Gamma phase, a thin dark layer next to the steel substrate was observed in the cross sectional micrographs. Next to the Gamma layer, either a light layer or a layer of dark, vertical crystals was present in the micrographs. This layer was identified to be the Gamma-1 phase. Furthermore, in coatings containing less than 10% total iron content, the Gamma-1 phase was formed as a light layer and Gamma formed a very thin layer. In samples containing greater than 10% iron, a much thicker Gamma layer was found next to the steel substrate followed by very dark, vertical crystals of Gamma-1; a medium-high concentration Delta layer was also observed in these coatings. Those samples which contained a rough, jagged layer on the coating surface were determined to contain a

large amount of the Zeta phase on the coating surface. This indicates that the Zeta phase forms on the coating surface in a porous, non-uniform layer. Furthermore, if a large amount of Zeta was indicated, then a low iron concentration Delta layer was also observed. Coatings found to have a Delta layer in the medium to high iron concentration range, generally showed thicker Gamma and Gamma-1 layers.

The GMS spectra prior to subtracting the substrate signal were analyzed and compared with the metallographic properties of each coating. The coating spectral areas, relative to the total spectral areas, were compared to the weight of iron in the coatings. This comparison showed a linear relationship, thus demonstrating the ability of Mössbauer spectroscopy to determine the weight of iron in galvanized coatings in-situ. This relationship is expected since Mössbauer spectroscopy probes only the iron in the coatings and spectral areas are proportional to the number of iron atoms.

Finally, the effect of aluminum impurity in the galvanneal bath on phase formation was investigated. Two coatings were analyzed whose preparation conditions were identical except for the addition of 0.13% aluminum to one of the iron saturated zinc baths. XRD and Mössbauer spectroscopy showed that the addition of aluminum seems to suppress the iron-zinc alloying resulting in a coating with less total weight of iron. This was observed even though the percentage of iron in the aluminum containing coating was greater. More research in the area of the effects of bath composition on coating phase formation was indicated.

The tailoring of galvanneal coatings for specific applications requires the ability to identify the phases and their relative quantities which form during the galvannealing process. With the compilation of the microstructural properties of the iron-zinc phase and the

development of a new Mössbauer detector, we have demonstrated the ability to identify the layers observed in cross sectional micrographs of galvanneal coatings and determine the relative abundances of the phases present in-situ. Also, the iron concentration of the Delta and Gamma phases can be determined. This will enable galvanneal producers to investigate the effect the various production parameters have on the phase formation within the galvanneal coatings. Furthermore, they will be able to correlate the metallurgical properties, such as the formability, weldability, paintability, and corrosion resistance of their product with the coating composition.

CHAPTER SIX

Conclusions and Recommendations for Further Study

The goal of my work was to develop a technique for the identification of the iron-zinc phases formed in commercially produced galvanneal steel coatings. Henceforth, the research focussed on two distinct projects. The first section involved the production and characterization of high purity iron-zinc alloys. The aim was to compile a database of the microstructural parameters of the iron-zinc phases in order to aid in the identification of the phases in commercial galvanneal coatings. The second section of this research entailed the development and testing of a toroidal scattering Mössbauer detector specifically for the study of galvanneal coatings. Primarily, use of the detector involved a study of several commercially produced galvanneal coatings with the subsequent correlation of the results with the metallurgical properties of each sample.

In the alloy production and characterization part of this dissertation, a method was developed by which high purity, homogeneous iron-zinc alloys could be produced. More

than forty samples were prepared within the four main iron-zinc phases and mixed phase regions of the phase diagram. The bulk iron concentrations of the prepared alloys were measured with induction coupled plasma spectroscopy (ICP) and wet chemical titration. Analysis indicated that we were capable of determining the iron content of our alloys to within 0.5 at.%. This allowed us to prepare samples at specific points in the iron-zinc phase diagram in order to study their microstructural properties. Comparisons of the two analytical techniques showed that the ICP method consistently underestimated the iron and overestimated the zinc content in our samples. On the other hand, the wet chemical titration results proved capable of determining the iron content to the required accuracy. Furthermore, sample homogeneity of greater than 93% was measured with an electron microprobe and a scanning transmission electron microscope.

Once the production of high quality iron-zinc intermetallics was demonstrated, it was possible to proceed with microstructural characterization. Hence, samples were prepared at varying iron concentrations within each phase in order to monitor the crystallographic and other microstructural properties of the phases as a function of iron concentration across each phase. Specifically, X-ray diffraction and transmission Mössbauer spectroscopy were employed to determine the crystallographic and hyperfine parameters of the prepared alloys. XRD analysis demonstrated that the lattice parameters remain constant across the ζ and Γ_1 phases, whereas, they vary continuously as a function of iron concentration across the δ and Γ phases. Furthermore, separate identification of the ζ , δ , and Γ_1 phases is now possible using XRD. These findings are significant since they now permit the identification of the phases in galvanneal coatings, as well as the relative iron concentrations of the δ and Γ

phases, to be determined. Additionally, Mössbauer spectroscopy provided a better fundamental understanding of the pure phase and the mixed phase regions of the iron-zinc phase diagram.

The ζ phase was found to possess a single iron site whose isomer shift and quadrupole splitting is independent of iron concentration. The small variance in iron concentration across the ζ phase is thought to be responsible for this constancy. The δ phase was found to contain three iron sites in contrast with our previous findings of two iron sites. The isomer shifts of all three sites decrease continuously with increasing iron content; however, only the quadrupole splitting and site occupation of the third, less occupied site changes appreciably across the phase. Moreover, the ratio of the relative areas of the two most populated iron sites, remains a constant 6:4 across the δ phase. Three iron sites are also present in the Γ_1 phase. However, only the site occupancies and not the hyperfine and lattice parameters change as a function of iron concentration. Production and analysis of many samples within the Γ phase identified two iron sites whose populations change dramatically and continuously with iron content. The ratio of the site occupancies approaches the value of 6:4 at the high iron end of the phase indicating that the iron is populating the inner tetrahedral and octahedral positions in the bcc structure. The isomer shifts and quadrupole splittings of the two iron sites were found to decrease continuously as iron concentration increased. Mixed phase studies show that these samples contained proportional amounts of the bordering phases. Thus, Mössbauer effect analysis of the iron-zinc intermetallics has shown that it is uniquely capable of separately identifying the four phases. All the more, Mössbauer spectroscopy can distinguish between the Γ_1 and Γ phases. The production and

characterization of high purity iron-zinc alloys will serve as calibration standards for the industrial XRD and Mössbauer analysis of commercially produced galvanized coatings. The compiled database of the crystallographic and hyperfine parameters of the iron-zinc intermetallics will facilitate the identification of the iron-zinc alloys in galvanized coatings.

The second part of this dissertation dealt with the identification of the iron-zinc phases in commercially produced galvanized steel. The research proceeded with the construction and testing of a toroidal scattering Mössbauer detector. This detector was essentially developed to study galvanized coatings in-situ; i.e., without removing them from the steel substrate. The detector is able to collect X-rays and γ -rays simultaneously resulting in a significant improvement in count rate over previous detectors. Furthermore, the addition of a CEMS detector to the main detector permits probing the near surface region of the coating thereby providing us with pertinent coating profile information. Application of the detector to commercial galvanized coatings demonstrated the detector's ability to identify the phases present. Several commercially produced galvanized coatings were then studied in order to identify the phases present in the coatings and compare the results with the metallurgical properties. The studies revealed that the Mössbauer parameters of the phases in galvanized coatings strongly agree with those of the pure iron-zinc standards. Likewise, the detector can differentiate between a high and a low iron concentration δ formed in a galvanized coating. On comparing the Mössbauer analysis of commercial galvanized steel with the metallographic cross sections, the phases were identified as layers within the coatings. The Γ phase was found to form as a thin layer next to the steel substrate. Followed by the Γ_1 phase forming in a thicker layer or as vertically oriented crystals. The δ phase

generally constituted the bulk of the coatings and the ζ phase was observed as a rough layer on the coating surface. Furthermore, the coating spectral areas were compared to the weight of iron in the coatings. The comparison demonstrated a linear relationship supporting the assessment that Mössbauer spectroscopy is a valuable tool in determining the weight of iron in galvanneal coatings in-situ.

Finally, the effect of aluminum impurity in the galvanneal bath on phase formation was investigated by comparing the Mössbauer spectra of two coatings. The preparation conditions of the coatings differed by the addition of aluminum to one of the iron saturated zinc baths. Analysis suggested that the aluminum suppressed the iron-zinc alloying process.

With the compilation of the microstructural properties of the iron-zinc phase and the development of a new Mössbauer detector, we have clearly demonstrated the ability to identify the layers observed in cross sectional micrographs of galvanneal coatings and determine the relative abundances of the phases present in-situ. The iron concentration of the δ and Γ phases can be determined as well. This will enable galvanneal producers to investigate the effect the various production parameters have on the phase formation within the galvanneal coatings. Furthermore, they will be able to correlate the metallurgical properties, such as the formability, weldability, paintability, and corrosion resistance of their product, with the coating composition.

With the completion of this work, the XRD and Mössbauer data will serve as a basic background to enable studies to be made on coatings which have been produced with interstitial and substitutional elements added to the zinc bath. Also, the influence of the steel substrate composition and carbon content on phase formation may be investigated. However,

several more standard samples will have to be produced with interstitial elements added in order to monitor the change in crystalline structure as a result of the additions. At present, the research at Old Dominion University focuses on the microstructural study of aluminum and other substituted iron-zinc binary alloys. Samples containing varying amounts of aluminum have been prepared within each of the four iron-zinc phases. Mössbauer and X-ray diffraction analysis have been performed on these samples to characterize these alloys in order to identify the iron sites and monitor the location of the added impurity. It is expected that through an investigation of the effect that these elements have on the pure iron-zinc phase formation, an understanding of the effect of bath composition on phase formation will be achieved. Also, the influence of annealing times and temperatures on phase formation is a concern. Henceforth, commercially produced galvaneal coatings prepared at different annealing times and temperatures are presently being analyzed to investigate the effect that these parameters have on phase formation. This coating analysis is being performed with the aid of the new toroidal detector and compiled database.

Ultimately, phase formation must be controlled if coatings are to be tailored for specific environmental and industrial applications. Furthermore, problems such as powdering loss, cracking, flaking, and chipping of galvaneal coatings need to be addressed. We have found in the galvaneal coating analysis described in Chapters 4 and 5, that through shear stress, galvaneal coatings always fracture cleanly at the interface of gamma layer and the steel substrate. The reasons for this phenomenon are not known, hence further research is warranted. The research compiled within this dissertation forms the background knowledge and tools necessary to proceed with investigations into these problems.

REFERENCES

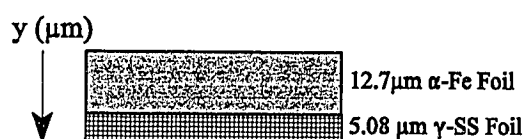
- ¹ O. Kubaschewski, Iron-Binary Phase Diagrams, (Springer-Verlag, 1982), pp. 86-87.
- ² P.J. Brown, *Acta Cryst.* **15**, 608-612 (1962).
- ³ P.J. Gellings, E.W. deBree and G. Gierman, *Z. Metallkde.* **70**, 312-314 (1979).
- ⁴ P.J. Gellings, E.W. deBree and G. Gierman, *Z. Metallkde.* **70**, 315-317 (1979).
- ⁵ P.J. Gellings, G. Gierman, D. Koster and J. Kuit, *Z. Metallkde.* **71**, 70-75 (1980).
- ⁶ A. Osawa and Y. Ogawa, *Z. Kristallogr.* **68**, 177-188 (1928).
- ⁷ H. Bablik, F. Götzl and F. Halla, *Z. Metallkde.* **30**, 248-252 (1938).
- ⁸ G.F. Bastin, F.J. van Loo and G.D. Rieck, *Z. Metallkde.* **67**, 694-698 (1976).
- ⁹ G.F. Bastin, F.J. van Loo and G.D. Rieck, *Z. Metallkde.* **68**, 359-361 (1977).
- ¹⁰ G.F. Bastin, F.J. van Loo and G.D. Rieck, *Z. Metallkde.* **65**, 656-660 (1974).
- ¹¹ A.S. Koster and J.C. Schoone, *Acta Crystallogr.* **37B**, 1905-1907 (1981).
- ¹² M. Gu, M.R. Notis and A.R. Marder, *Metallurgical Transactions* **21A**, 273-277 (1990).
- ¹³ M. Ghafari, M. Saito, Y. Hirose and Y. Nakamura, *Hyperfine Int.* **69**, 447-450 (1991).
- ¹⁴ D.C. Cook, Mössbauer Effect Study of Four Metal Powder Galvanneal Standards, Final Technical Report #ODUDCC0191, 1991 (unpublished).
- ¹⁵ ICP standards: Inorganic Ventures Inc., Lakewood, NJ, U.S.A.
- ¹⁶ W.E Harris and B. Kratochvil, Chemical Separations and Measurement, (Saunders Publishing Co., 1974).
- ¹⁷ R.B. Fischer and D.G. Peters, Basic Theory and Practice of Quantitative Chemical Analysis, (Saunders Publishing Co., 1968).
- ¹⁸ Joseph Goldstein, Practical scanning electron microscopy: electron and ion microprobe, (Plenum Press, New York, 1975).
- ¹⁹ ETEC Corporation, 3392 Investment Blvd., Hayward CA 94545 (no longer in business).
- ²⁰ W.A. Furdanowicz and K.E. Downey, *Journal of Microscopy* **174**, 66 (1994).
- ²¹ D.C. Cook, R.S. Tuszynski and H.E. Townsend, *Hyperfine Int.* **54**, 781-785 (1990).
- ²² D.C. Cook, Mössbauer Analysis of the Zinc-Iron Phases on Galvannealed Steel, Final Technical Report #ODUDCC0289, 1989 (unpublished).
- ²³ I.C.D.D., International Center for Diffraction Data, publishers of the Powder Diffraction File, Newtown Square, PA, U.S.A..
- ²⁴ M. Ghoniem and K. Löhberg, *Z. Metallkde.* **26**, 1026 (1972).
- ²⁵ A. Johansson, H. Ljung and S. Westman, *Acta Chem. Scand.* **22(9)**, 2743-2753 (1968).

- ²⁶ J.K. Brandon, R.Y. Brizard, P.C. Chieh, P.K. Millan and W.B. Pearson, *Acta Crystallogr.* **30B**, 1412-1417 (1974).
- ²⁷ A. Jena and K. Löhberg, *Z. Metallkde.* **73(8)**, 517-521 (1982).
- ²⁸ H.P. Klug and L.E. Alexander, X-Ray Diffraction Procedures for Polycrystalline and Amorphous Materials, (Wiley and Sons Publishing Co., 1954).
- ²⁹ B.P. Burton and P. Perrot, Phase Diagrams in Binary Iron Alloys, A.S.M. Binary Alloy Monograph Series, No. 9, 459-466 (1993).
- ³⁰ D.C. Cook and J.D. Cashion, *Hyperfine Interactions* **5**, 479-486 (1978).
- ³¹ D.C. Cook, Mössbauer Analysis of the Zinc-Iron Phases on Galvannealed Steel: Phase II, Final Technical Report #ODUDCC0291, 1991 (unpublished).
- ³² D.C. Cook, Mössbauer Effect Study of Galvanneal Steel Coating Fracture Surfaces, Final Technical Report #ODUDCC0192, 1992 (unpublished).
- ³³ R.D. Jones and S.G. Denner, *Scripta Metal.* **8(3)**, 175-180 (1974).
- ³⁴ M.J. Graham, P.E. Beaubien and G.I. Sproule, *J. Mater. Sci.* **5**, 626-630 (1980).
- ³⁵ H.E. Townsend, L. Allegra, R.J. Dutton, and S.A. Kriner, *Materials Performance* **25**, No.8, 36-46 (1986).
- ³⁶ H.E. Townsend, The NACE Annual Conference and Corrosion Show, paper #416 (1991).
- ³⁷ F.W. Salt, J.F. Stanners, and K.O. Watkins, *Brit. Corrosion J.* **1**, No.1, 5 (1965).
- ³⁸ C.A. Drewien, Review of Structure and Properties of Galvanneal and Electrogalvanized Iron-Zinc Coatings on Steel Sheet, Lehigh University, 1989 (unpublished).
- ³⁹ B. Fultz, United States Patent No. 4,393,306 (12 July 1983).
- ⁴⁰ L. Blaes, H.G. Wagner, U. Gonser, J. Welsch, and J. Sutor, *Hyperfine Int.* **29**, 1571-1574 (1986).
- ⁴¹ P. Schaaf, L. Blaes, J. Welsch, H. Jacoby, F. Aubertin, and U. Gonser, *Hyperfine Int.* **58** 2541-2546 (1990).
- ⁴² U. Gonser, P. Schaaf, and F. Aubertin, *Hyperfine Int.* **66**, 95-100 (1991).
- ⁴³ Bethlehem Steel Corporation, Bethlehem, PA. 18016, U.S.A.
- ⁴⁴ D.C. Cook and E. Agyekum, *Nuc. Instr. and Methods* **B12**, 515-520 (1985).
- ⁴⁵ D.C. Cook, *Hyperfine Int.* **29**, 1463-1466 (1986).
- ⁴⁶ X-Ray Proportional Counters Performance & Specification Guide, Reuter-Stokes Engineering Data Bulletin 3.00, March 1978.
- ⁴⁷ A.R.P. Ghuman and J. Goldstein, *Met Trans.* **2A**, 2903 (1971).
- ⁴⁸ H. Smith and W. Batz, *J. of the Iron and Steel Inst. of Japan*, 895 (1972).

APPENDIX A

Corrected areas in the bilayer foil experiment used to test the toroidal detector.

In this appendix we describe the calculation used to correct the relative subspectral areas of the bilayer foil experiment discussed in section 4.2.1. The calculations are shown for the FESS bilayer configuration, although the method was similar for the SSFE arrangement. We have calculated the relative areas based on the average values of three points within each foil; although, a more precise calculation involves integrating over the foil thickness.



The γ -SS foil has 2.12 mg cm² of iron.

The α -Fe foil has 10.00 mg cm² of iron.

Ideal Relative Areas: 17.5% SS and 82.5% Fe.

From the Mössbauer spectrum we have a total of 4% resonant absorption by γ -SS.

Therefore, we have 19% resonant absorption by α -Fe.

			α -Fe Foil			SS Foil		
y(μ m)	TF	nr	r ₀	r _{rms}	r ₁	r ₁	r _{rms}	r ₂
0.00	1.00	100	81					
8.98	0.68	68.0		55.08				
12.70	0.53	53.2			43.09	51.07		
16.29	0.45	44.5					42.72	
17.78	0.41	41.4						39.74
TMS			0.41	0.65	0.78	0.78	0.93	1.00
		TF	33.53	35.58	33.48	39.68	39.69	39.74
		T _{Corr}						
		$\langle T_{Corr} \rangle$		34.20			39.70	
		Absorption		7.20			1.70	
		Relative Area		81.00			19.00	
		Expt. Relative Area		82.00			18.00	
		Corrected Relative Area		83.63			16.37	
GMS			19.00	12.92	10.11	2.13	1.78	1.66
		EM						
		TF	1.00	0.68	0.53	0.53	0.45	0.41
		EM _{Corr}	19.00	8.79	5.38	1.13	0.79	0.69
		$\langle EM_{Corr} \rangle$		11.06			0.87	
		Relative Area		92.71			7.29	
		Expt. Relative Area		95.90			4.10	
		Corrected Relative Area		85.45			14.55	
XMS			19.00	12.92	10.11	2.13	1.78	1.66
		EM						
		TF	1.00	0.58	0.47	0.41	0.38	0.35
		EM _{Corr}	19.00	7.55	4.73	1.00	0.67	0.57
		$\langle EM_{Corr} \rangle$		10.43			0.75	
		Relative Area		93.29			6.71	
		Expt. Relative Area		95.47			4.53	
		Corrected Relative Area		84.53			15.47	

nr = # of non resonant photons transmitted.

r_i = # of resonant photons transmitted after absorption through depth y.

TF = transmission factor = attenuation fraction (I/I_0).

T_{corr} = TF · r_i

EM = nr · TF

EM_{Corr} = TF · EM

APPENDIX B

Attenuation coefficients for the four main iron-zinc phases.

Attenuation follows the exponential law:

$$I = I_0 e^{-(\mu/\rho)\rho x}$$

where: I = intensity at a depth x
 I_0 = intensity at surface
 (μ/ρ) = mass attenuation coefficient
 ρ = density

The mass attenuation coefficients are dependent on the material and the energy of the incident photons. In order to calculate the attenuation of γ -rays and X-rays through the iron zinc phases, the total attenuation cross section must be known for each phase. The following calculations determine the total attenuation cross section for each of the four iron-zinc intermetallics.

$$\begin{aligned}
 (\mu/\rho)_{\text{Fe}} &= 63.1 \text{ cm}^2/\text{g}, \text{ at } 14.4 \text{ keV} \\
 &= 76.0 \text{ cm}^2/\text{g}, \text{ at } 6.40 \text{ keV} \\
 (\mu/\rho)_{\text{Zn}} &= 96.0 \text{ cm}^2/\text{g}, \text{ at } 14.4 \text{ keV} \\
 &= 108.3 \text{ cm}^2/\text{g}, \text{ at } 6.40 \text{ keV}
 \end{aligned}$$

Zeta:

FeZn₁₃

28 atoms / unit cell

Cell volume = 412 Å³

$$\mu_{\zeta} = (\mu/\rho)_{\text{Zn}} \rho_{\text{Zn in } \zeta} + (\mu/\rho)_{\text{Fe}} \rho_{\text{Fe in } \zeta}$$

$$\rho_{\text{Zn in } \zeta} = \frac{(\# \text{ of Zinc atoms/unit cell})(\text{atomic mass of Zinc})}{(V_{\text{cell}})(N_A)} = 6.85 \text{ g cm}^{-3}$$

$$\rho_{\text{Fe in } \zeta} = \frac{(\# \text{ of Iron atoms/unit cell})(\text{atomic mass of Iron})}{(V_{\text{cell}})(N_A)} = 0.45 \text{ g cm}^{-3}$$

$$\begin{aligned}
 \text{Therefore: } \mu_{\zeta} &= 686.14 \text{ cm}^{-1}, \text{ at } 14.4 \text{ keV} \\
 \mu_{\zeta} &= 775.32 \text{ cm}^{-1}, \text{ at } 6.4 \text{ keV}
 \end{aligned}$$

Delta:

FeZn₁₀

555 atoms / unit cell

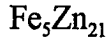
Cell volume = 8228 Å³

$$\mu_{\delta} = (\mu/\rho)_{\text{Zn}} \rho_{\text{Zn in } \delta} + (\mu/\rho)_{\text{Fe}} \rho_{\text{Fe in } \delta}$$

$$\rho_{\text{Zn in } \delta} = \frac{(\# \text{ of Zinc atoms/unit cell})(\text{atomic mass of Zinc})}{(V_{\text{cell}})(N_A)} = 6.66 \text{ g cm}^{-3}$$

$$\rho_{\text{Fe in } \delta} = \frac{(\# \text{ of Iron atoms/unit cell})(\text{atomic mass of Iron})}{(V_{\text{cell}})(N_A)} = 0.57 \text{ g cm}^{-3}$$

$$\begin{aligned}
 \text{Therefore: } \mu_{\delta} &= 675.01 \text{ cm}^{-1}, \text{ at } 14.4 \text{ keV} \\
 \mu_{\delta} &= 763.09 \text{ cm}^{-1}, \text{ at } 6.4 \text{ keV}
 \end{aligned}$$

Gamma-1:

408 atoms / unit cell

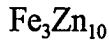
Cell volume = 5813 Å³

$$\mu_{\Gamma-1} = (\mu/\rho)_{\text{Zn}} \rho_{\text{Zn in } \Gamma-1} + (\mu/\rho)_{\text{Fe}} \rho_{\text{Fe in } \Gamma-1}$$

$$\rho_{\text{Zn in } \Gamma-1} = \frac{(\# \text{ of Zinc atoms/unit cell})(\text{atomic mass of Zinc})}{(V_{\text{cell}})(N_A)} = 6.15 \text{ g cm}^{-3}$$

$$\rho_{\text{Fe in } \Gamma-1} = \frac{(\# \text{ of Iron atoms/unit cell})(\text{atomic mass of Iron})}{(V_{\text{cell}})(N_A)} = 1.25 \text{ g cm}^{-3}$$

$$\begin{aligned} \text{Therefore: } \mu_{\Gamma-1} &= 669.84 \text{ cm}^{-1}, \text{ at } 14.4 \text{ keV} \\ \mu_{\Gamma-1} &= 759.18 \text{ cm}^{-1}, \text{ at } 6.4 \text{ keV} \end{aligned}$$

Gamma:

52 atoms / unit cell

Cell volume = 724 Å³

$$\mu_{\Gamma} = (\mu/\rho)_{\text{Zn}} \rho_{\text{Zn in } \Gamma} + (\mu/\rho)_{\text{Fe}} \rho_{\text{Fe in } \Gamma}$$

$$\rho_{\text{Zn in } \Gamma} = \frac{(\# \text{ of Zinc atoms/unit cell})(\text{atomic mass of Zinc})}{(V_{\text{cell}})(N_A)} = 6.00 \text{ g cm}^{-3}$$

$$\rho_{\text{Fe in } \Gamma} = \frac{(\# \text{ of Iron atoms/unit cell})(\text{atomic mass of Iron})}{(V_{\text{cell}})(N_A)} = 1.54 \text{ g cm}^{-3}$$

$$\begin{aligned} \text{Therefore: } \mu_{\Gamma} &= 672.83 \text{ cm}^{-1}, \text{ at } 14.4 \text{ keV} \\ \mu_{\Gamma} &= 763.35 \text{ cm}^{-1}, \text{ at } 6.4 \text{ keV} \end{aligned}$$

AUTOBIOGRAPHICAL STATEMENT

PERSONAL DATA:

Date of birth: June 23, 1965
Place of birth: Oakville, Ontario, Canada
Marital status: Married
Residential status: Permanent U.S. resident

EDUCATION:

B.Sc.: November 1988, University of Toronto, Ontario, Canada
Major: Physics
Minor: Mathematics

M.S.: June 1990, Florida Institute of Technology, Melbourne, Florida
Major: Physics
Thesis: "Theory, Design, and Application of a Photocombustion Reactor."

M.S.: May 1992, Old Dominion University, Norfolk, Virginia
Major: Applied Physics

PROFESSIONAL EXPERIENCE:

RESEARCH ASSISTANT

Condensed Matter and Materials Physics Laboratory
Department of Physics
Old Dominion University, Norfolk, Virginia
September 1990 to May 1995

TEACHING ASSISTANT

Department of Physics
Old Dominion University, Norfolk, Virginia
Summer 1993, September 1990 to May 1991

TUTOR

Department of Student Services
Old Dominion University, Norfolk, Virginia
January 1991 to May 1991

STUDENT INTERN

Physics Division
Continuous Electron Beam Accelerator Facility (CEBAF)
May 1991 to August 1991

RESEARCH ASSISTANT

Department of Physics, Florida Institute of Technology in conjunction with
Photokinetics Corporation, Melbourne, Florida
September 1989 to June 1990

PUBLISHED PAPERS:

1. "Mössbauer Effect and XRD Studies of Iron-Zinc Binary Alloys."
R.G. Grant and D.C. Cook
Hyperfine Interactions, Vol. 94, pp. 2309-2316 (1994).
2. "Raman Spectroscopy of the Zeta Phase Zinc-Iron Intermetallic Compound."
H.E. Townsend, G.L. Johnson, R.G. Grant and D.C. Cook.
Scripta Metallurgica et Materialia, Vol. 31, No. 11, pp. 1445-1447 (1994).
3. "Preparation and Chemical Analysis of High Purity Iron-Zinc Alloys."
R.G. Grant, P.S. Cook, and D.C. Cook.
Submitted for publication to Journal of Materials Science in January 1995.

PAPERS IN PREPARATION:

1. "Characterization of Four Iron-Zinc Alloy Phases by Mössbauer Spectroscopy and X-Ray Diffraction."
R.G. Grant and D.C. Cook.
To be submitted for publication to Journal of Materials Science in June 1995.
2. "Identification and Characterization of the Iron-Zinc Intermetallics in Commercial Galvanneal Steel Coatings."
D.C. Cook and R.G. Grant.
Mössbauer Spectroscopy Applied to Magnetism and Material Science, Ed. G.J. Long and F. Grandjean, Plenum Press, NY. Vol. 2, Ch 10. To be published 1996.

**PUBLISHED ABSTRACTS and RESEARCH PAPERS PRESENTED
AT PROFESSIONAL MEETINGS:**

1. "Mössbauer Effect Study of Four Metal Powder Galvanneal Standards."
D.C. Cook and R.G. Grant.
Proceedings of the March Meeting of the American Physical Society.
Indianapolis, IN, March 16-20 1992, #S28-6.
Bulletin of the APS, vol. 37, No. 1, p. 799.
2. "A Study of Iron-Zinc Intermetallics in Galvanneal Steel Coatings."
R.G. Grant and D.C. Cook.
Proceedings of the 70th Annual Meeting of the Virginia Academy of Science.
University of Richmond, Richmond, VA, May 19-22 1992.
Virginia Journal of Science, vol. 43, No. 2, p. 80.
3. "Microstructural Properties of the Four Iron-Zinc Metal Powder Galvanneal Standards."
R.G. Grant and D.C. Cook.
Proceedings of the March Meeting of the American Physical Society.
Seattle, WA, March 22-26 1993, #C16-5.
Bulletin of the APS, vol. 38, No. 1, p. 161.
4. "Mössbauer Effect Study of Galvanneal Steel Coating Fracture Surfaces."
D.C. Cook, R.G. Grant and H.E. Townsend.
Proceedings of the March Meeting of the American Physical Society.
Seattle, WA, March 22-26 1993, #C16-6.
Bulletin of the APS, vol. 38, No. 1, p. 162.
5. "Studies of Iron-Zinc Binary Alloys Utilizing XRD and Mössbauer Spectroscopy."
R.G. Grant. Invited Seminar presented at Bethlehem Steel Corporation,
Bethlehem, PA, May 5 1993.
6. "Microstructural Properties of the Four Iron-Zinc Galvanneal Standards."
R.G. Grant and D.C. Cook.
Proceedings of the 71st Annual Meeting of the Virginia Academy of Science.
Old Dominion University, VA, May 18-21 1993.
Virginia Journal of Science, vol. 44, No. 2, p. 104.
R.G. Grant received Best Student Paper Award.
7. "A Study of Galvanneal Steel Coatings Using Scattering and Transmission Mössbauer Spectroscopy."
R.G. Grant, D.C. Cook and H.E. Townsend.
Proceedings of the 1993 International Conference on the Application of the Mössbauer Effect. Vancouver, Canada, August 8-13 1993, #8-31A, p. 66.

8. "Mössbauer Effect and XRD Studies of Iron-Zinc Binary Alloys."
R.G. Grant and D.C. Cook.
Proceedings of the 1993 International Conference on the Application of the Mössbauer Effect.
Vancouver, Canada, August 8-13 1993, #17-14B, p. 123.
9. "Study of the Shear Stress Failure Point and Crystalline Texture in Galvanneal Coatings Using Mössbauer Spectroscopy."
R.G. Grant and D.C. Cook.
Proceedings of the March Meeting of the American Physical Society,
Pittsburgh, PA, March 21-25 1994, #E29-3.
Bulletin of the APS, vol. 39, No. 1, p. 284.
10. "Identification of Iron-Zinc Phases in Commercially Produced Galvannealed Steel."
R.G. Grant and D.C. Cook.
Proceedings of the 72nd Annual Meeting of the Virginia Academy of Science.
James Madison University, Harrisonburg, VA, May 18-20 1994.
Virginia Journal of Science, vol. 45, No. 2, p. 26.
R.G. Grant received Honorable Mention.
11. "Study of the Iron-Zinc Phases in Corrosion Resistant Industrially Produced Galvanneal Steel."
R.G. Grant and D.C. Cook
Presented at the NATO Advanced Study Institute Program: Interstitial Alloys for Reduced Energy Consumption and Pollution. Il Ciocco, Italy, June 12-24 1994.
12. "Development of a Data-Base of the Microstructural Properties of the Four Iron-Zinc Powder Galvanneal Standards."
R.G. Grant and D.C. Cook.
Presented at the International Symposium on Recent Developments in the Processing Technology and Critical Properties of Zinc-Coated Steel Sheet.
Proceedings of the 33rd Annual Conference of Metallurgists.
Toronto, Canada, August 21-25 1994.
13. "Study of the Crystalline Texture and Shear Stress Failure Point in Galvanneal Coatings Using Mössbauer Spectroscopy."
D.C. Cook and R.G. Grant.
Presented at the International Symposium on Recent Developments in the Processing Technology and Critical Properties of Zinc-Coated Steel Sheet.
Proceedings of the 33rd Annual Conference of Metallurgists.
Toronto, Canada, August 21-25 1994.

14. "Identification and Characterization of the Iron Sites in Fe-Zn Binary Alloys."
R.G. Grant and D.C. Cook.
Proceedings of the November Meeting of the Southeastern Section of the American Physical Society, Newport News, VA, November 10-12 1994, #FE-5.
Bulletin of the APS, vol. 39, No. 8, p. 1827.
15. "In-Situ Identification of the Iron-Zinc Phases in Commercial Galvanneal Steel Coatings."
R.G. Grant and D.C. Cook.
Proceedings of the March Meeting of the American Physical Society,
San Jose, CA, March 20-24 1995, #K23.
Bulletin of the APS, vol. 40, No. 1, p. 284.
16. "Identification of the Fe-Zn Intermetallic Phases in Commercial Galvanneal Steel."
R.G. Grant and D.C. Cook.
To be presented at the 73rd Annual Meeting of the Virginia Academy of Science.
Virginia Military Institute, Lexington, VA, May 24-26 1995.
17. "Iron-Zinc Phase Identification in Commercial Galvanneal Steel."
R.G. Grant and D.C. Cook.
To be presented at the 1994 International Conference on the Application of the Mössbauer Effect. Rimini, Italy, September 10-16 1995.
18. "Iron-Zinc Phase Determination in Commercial Galvanneal Steel."
R.G. Grant and D.C. Cook.
To be presented at the Galvatech '95. 3rd International Conference on Zinc and Zinc Alloy Coated Steel Sheets. Chicago, IL, September 17-21 1995.
19. "Identification of Multiple Iron Sites in Fe-Zn Binary Alloys."
D.C. Cook and R.G. Grant.
To be presented at the Galvatech '95. 3rd International Conference on Zinc and Zinc Alloy Coated Steel Sheets. Chicago, IL, September 17-21 1995.

FINAL TECHNICAL REPORTS:

1. "Identification of the Iron-Zinc Phases in Galvanneal Steel Coatings by Mössbauer Spectroscopy and X-Ray Diffraction. Phase I: Characterization of the Fe-Zn Intermetallic Phases."
D.C. Cook and R.G. Grant. Final Technical Report submitted to International Lead Zinc Research Organization, Inc. in 1993. Grant: ZM-403.

2. "Radiation Detector for On-Line Monitoring of the Zinc-Iron Phases in Galvanneal Steel Coatings. Phase I: Characterization of the Fe-Zn Intermetallic Phases."
D.C. Cook and R.G. Grant. Final Technical Report submitted to Virginia's Center for Innovative Technology in 1993. Grant: MAT-92-007-01.
3. "Identification of the Iron-Zinc Phases in Galvanneal Steel Coatings by Mössbauer Spectroscopy and X-Ray Diffraction. Phase II: Construction and Testing of a Coating Analyzer."
D.C. Cook and R.G. Grant. Final Technical Report submitted to International Lead Zinc Research Organization, Inc. in 1994. Grant: ZM-403.
4. "Radiation Detector for On-Line Monitoring of the Zinc-Iron Phases in Galvanneal Steel Coatings. Phase II: Construction and Testing of a Coating Analyzer."
D.C. Cook and R.G. Grant. Final Technical Report submitted to Virginia's Center for Innovative Technology in 1994. Grant: MAT-93-018.

REVIEWER OF THE FOLLOWING JOURNALS:

Hyperfine Interactions

HONORS AND AWARDS:

Deans list for the 1988-89 and 1989-90 school years.
Member of the National Physics Honors Society.

MEMBERSHIP IN PROFESSIONAL SOCIETIES:

Society of Physics Students
American Physical Society
Virginia Academy of Science
Sigma Xi